

UNIVERSITY OF
BIRMINGHAM

MODELLING OF EMISSIONS, TRANSPORT, AND CHEMISTRY FOR AIR QUALITY MANAGEMENT WITHIN URBAN STREET CANYONS

by

Yuqing Dai

A thesis submitted to the University of Birmingham
for the degree of Doctor of Philosophy

School of Geography, Earth and Environmental Science
College of Life & Environmental Sciences
University of Birmingham

June 2023

UNIVERSITY OF
BIRMINGHAM

University of Birmingham Research Archive

e-theses repository

This unpublished thesis/dissertation is copyright of the author and/or third parties. The intellectual property rights of the author or third parties in respect of this work are as defined by The Copyright Designs and Patents Act 1988 or as modified by any successor legislation.

Any use made of information contained in this thesis/dissertation must be in accordance with that legislation and must be properly acknowledged. Further distribution or reproduction in any format is prohibited without the permission of the copyright holder.

ABSTRACT

This thesis presents a novel, flexible multi-box framework (MBM-FleX) for simulating the transportation and distribution of chemical species in street canyons with varying aspect ratios. The model is computationally resource-efficient and effective in capturing temporal and spatial patterns of reactive species, allowing for comprehensive sensitivity tests to investigate fast non-linear chemistry at the street scale.

The studies within this thesis demonstrate the importance of considering complex photochemistry and shading effects on reactive species in urban canyons, emphasizing the influence of volatile organic compound (VOC) free-radical chemistry on interconversion of odd-oxygen species. In addition, the research highlights the significance of detailed VOC chemistry for regulatory air quality modelling in street canyons, showing that neglecting VOC chemistry may lead to underestimation of nitrogen dioxide (NO_2) concentrations. A field monitoring campaign conducted in a deep street canyon in Naples, Italy, supports the model performance and showcases the impact of urban morphology on air quality. The findings emphasize the importance of considering vertical distribution when assessing health impacts and developing air quality control strategies.

Overall, the thesis advances the understanding of air quality dynamics in urban canyons and presents a valuable tool for effective air quality management in intricate urban environments.

ACKNOWLEDGEMENTS

I wish to express my deepest gratitude to my supervisors, Dr. Xiaoming Cai, Dr. Jian Zhong, and Prof. Rob Mackenzie. Dr. Xiaoming provided enormous support during my master's studies at the University of Birmingham, propelling me into my Ph.D. journey. His altitude to addressing scientific questions has greatly influenced my mindset since the commencement of my doctoral studies. Despite his retirement after my first year, he continued to lend his unwavering support to my academic pursuits. Dr. Jian Zhong's invaluable guidance and insights have been instrumental in enriching my research and fostering critical thinking. His approachable nature has created a supportive environment for growth, for which I am immensely grateful. Prof. Rob Mackenzie consistently demonstrates care for the well-being of every student in our research group. I am particularly impressed with how he handled the lockdown period due to COVID-19. He organized weekly group discussions to maintain our collective momentum, ensuring we had the opportunity to engage with practical topics. These discussions were not only stimulating but also provided a sense of normalcy during an otherwise uncertain period, bolstering my morale and motivation.

I would like to extend special thanks to Prof. Zongbo Shi and Dr. Congbo Song. They have provided me with invaluable suggestions concerning my studies and granted me opportunities to be part of the DY151 cruise. I genuinely relished the scientific journey alongside all of you. I also wish to thank the staff

at GEES who have helped me navigate my Ph.D. journey, including Rosie Day, Claire Thomas, Deanne Brettle, among others.

To all my cherished friends and colleagues - Ruixin Xu, Jiali Feng, Kun Zhang, Andrea Mazzeo, Weiqing Jia, Sophie Mills, Bowen Liu, and many others too numerous to mention individually - my heartfelt appreciation goes out to each of you. Your companionship adds an irreplaceable richness to the inherently fascinating nature of our research. In the words of an old saying, "Even mountains and seas cannot distance people with common aspirations." I sincerely hope for each of you to achieve phenomenal success in your respective life journeys and professional careers.

Finally, my gratitude towards my parents, Doctors Lixin Dai and Aili Si, and my sister Doctor Dandan Dai, is boundless. They have consistently been my rock, guiding me through the darkest hours and toughest days with their kindness and unwavering encouragement. They have made substantial sacrifices to allow me the freedom to choose my own life path. I understand that the opportunity to study abroad for as many years as I have is not common, even with family support. Their love, unconditional and unexpecting of any returns, makes me feel incredibly fortunate. I am deeply appreciative of their love and support, the cornerstone of my journey so far.

LIST OF PUBLICATIONS AND CONFERENCES

Throughout my postgraduate studies at the School of Geography, Earth and Environmental Sciences, University of Birmingham, I had the privilege of presenting my research and collaborating with other scholars on various publications and conference presentations. The following articles and abstracts were accepted for publication and/or presentation during this period, where listed, the co-authors also suggested on research design and paper revising.

Publications

- **Dai, Y.**, Cai, X., Zhong, J. and MacKenzie, A.R., 2022. Chemistry, street canyon geometry, and emissions effects on NO2 “hotspots” and regulatory “wiggle room”. *npj Climate and Atmospheric Science*, *5*(1), p.102.
- **Dai, Y.**, Cai, X., Zhong, J., Mazzeo, A. and MacKenzie, A.R., 2022. Chemistry, transport, emission, and shading effects on NO_2 and O_x distributions within urban canyons. *Environmental Pollution*, *315*, p.120347.
- **Dai, Y.**, Cai, X., Zhong, J. and MacKenzie, A.R., 2021. Modelling chemistry and transport in urban street canyons: Comparing offline multi-box models with large-eddy simulation. *Atmospheric Environment*, *264*, p.118709.
- **Dai, Y**., Mazzeo, A., Zhong, J., Cai, X., Mele, B., Toscano, D., Murena, F. and MacKenzie, A.R., 2023. Modelling of Deep Street Canyon Air Pollution Chemistry and Transport: A Wintertime Naples Case Study. *Atmosphere*, *14*(9), p.1385.
- Jia, B., Tian, Y., **Dai, Y**., Chen, R., Zhao, P., Chu, J., Feng, X. and Feng, Y., 2022. Seasonal variation of dissolved bioaccessibility for potentially toxic elements in size-resolved PM: Impacts of bioaccessibility on inhalable risk and uncertainty. Environmental Pollution, 307, p.119551.

- Xie, Q., Su, S., Chen, J., **Dai, Y**., Yue, S., Su, H., Tong, H., Zhao, W., Ren, L., Xu, Y. and Cao, D., 2021. Increase of nitrooxy organosulfates in firework-related urban aerosols during Chinese New Year's Eve. Atmospheric Chemistry and Physics, 21(14), pp.11453-11465.
- Xie, Q., Su, S., **Dai, Y**., Hu, W., Yue, S., Cao, D., Jiang, G. and Fu, P., 2022. Deciphering 13C and 34S Isotopes of Organosulfates in Urban Aerosols by FT-ICR Mass Spectrometry. Environmental Science & Technology Letters, 9(6), pp.526-532.
- Xie, Q., **Dai, Y**., Zhu, X., Hui, F., Fu, X. and Zhang, Q., 2022. High contribution from outdoor air to personal exposure and potential inhaled dose of PM2. 5 for indoor-active university students. Environmental Research, 215, p.114225.

Conference presentations

- VIRTUAL| Atmospheric Science Conference 2021, Tuesday 6th July 2021.
- Oral Presentation, RMetS Student & Early Career Scientists Conference 2022 4th & 5th July, University of Manchester.

DECLARATION

The research presented in the main chapters of this thesis was carried out collaboratively with Prof. Rob Mackenzie, Dr. Xiaoming Cai, and Dr. Jian Zhong. The large-eddy simulation (LES) results for the regular canyon, along with the reduced chemical scheme (RCS), were generously provided by Dr. Vivien Bright, whereas the LES for the deep canyon was supplied by Dr. Jian Zhong. As the principal author, I designed the research topic, executed the necessary coding, conducted data analysis, and drafted the manuscript. Prof. Rob Mackenzie, Dr. Xiaoming Cai, and Dr. Jian Zhong contributed invaluable inputs to the discussion and meticulously revised the manuscript. In the work presented in Appendix C, the author collaborated with Dr. Andrea Mazzeo, Dr. Benedetto Mele, and Prof. Fabio Murena from the University of Naples Federico II. The colleagues conducted meticulous field measurements related to air pollutants within an exceptionally deep urban canyon in Naples. Acknowledgements pertaining to the use of other resources have been incorporated within each relevant chapter of this thesis.

LIST OF ABBREVIATIONS

Acetaldehyde / ethanal	(CH3CHO)
Ambient Ratio Method	(ARM)
Air Quality Guideline	(AQG)
Aspect Ratio	(AR)
Automatic Urban and Rural Network	(AURN)
Automatic Traffic Counter	(ATC)
Biogenic Volatile Organic Compounds	(BVOCs)
Carbon Monoxide	(CO)
Chemical Transport Models	(CTMs)
Common Representative Intermediates	(CRI)
Community Multi-Scale Air Quality	(CMAQ)
Computational Fluid Dynamics	(CFD)
Computer Program To Calculate Emission From Road Transport	(COPERT)
Damköhler Number	(Da)
Defra Department For Environment, Food And Rural Affairs	(DEFRA)
Ethene / ethylene	(C_2H_4)
(Within a) Factor Of Two	(FAC2)
Formaldehyde / methanal	(HCHO)
Global Air Quality Guidelines	(AQGs)
Highly Oxidized Molecules	(HOMs)
High-Performance Computer	(HPC)
Hydroperoxyl Radical	(HO_2)
Hydroxyl Radical	(OH or HO)
Index Of Agreement	(IOA)
Inertial Sublayer	(ISL)

Intense Emission Condition	(IEC)
Isoprene	(C_5H_8)
Large Eddy Simulation	(LES)
Leeward Shading	(LS)
Master Chemical Mechanism	(MCM)
Miles Per Hour	(mph)
Mixed Layer	(ML)
Multi-Box Model	(MBM)
National Atmospheric Emissions Inventory	(NAEI)
Nitric Acid	(HNO_3)
Nitric Oxide	(NO)
Nitrogen Dioxide	(NO_2)
No Shading	(NS)
Numerical Weather Prediction	(NWP)
Ozone Limiting Method	(OLM)
Ordinary Differential Equations	(ODEs)
One/Two-Dimensional/Three	(1/2/3D)
Oxidants	(O_x)
Ozone	(O_3)
Passive Scalar	(PS)
Particulate Matter	(PM)
Parts Per Billion	(ppb by volume)
Parts Per Trillion	(ppt by volume)
Pearson's Correction Coefficient	(R)
Peroxyacetyl Nitrate	(PAN)
Peroxyacetyl Radical	(PA)
Peroxyl Radicals	(RO_2)

Photochemical Ozone Creation Potential	(POCP)
Photo-Stationary State Defect	(PSSD)
Plume In Grid	(PinG)
Propene	(C_3H_6)
Quasi Steady State Assumption	(QSSA)
Reduced Chemical Scheme	(RCS)
Reynolds Number	(Re)
Reynolds Stress Model	(RSM)
Reynolds-Averaged Navier-Stokes	(RANS)
Root-Mean-Square Deviation	(RMSD)
Roughness Sublayer	(RSL)
Street In Grid	(SinG)
Sub-Grid Scales	(SGS)
Transport For London	(TfL)
Tropospheric Organic Chemistry	(TORCH)
Tropospheric Ultraviolet And Visible	(TUV)
Turbulent Kinetic Energy	(TKE)
Typical Emission Condition	(TEC)
Typical Emission Scenario	(TES)
United Kingdom	(UK)
United Nations	(UN)
Ultra Fine Particle	(UFP)
Urban Boundary Layer	(UBL)
Urban Canopy Layer	(UCL)
Volatile Organic Compounds	(VOC)
Windward Shading	(WS)
World Health Organisation	(WHO)

CONTENTS

ABSTRACT ..... **ii**

ACKNOWLEDGEMENTS ..... **iii**

LIST OF PUBLICATIONS AND CONFERENCES ..... **v**

DECLARATION ..... **vii**

LIST OF ABBREVIATIONS ..... **viii**

CONTENTS ..... **xi**

LIST OF TABLES ..... **xiv**

LIST OF FIGURES ..... **xv**

CHAPTER 1 GENERAL INTRODUCTION ..... **- 1 -**

1.1 Urban atmosphere ..... **- 2 -**
1.1.1 Vertical structure and horizontal scale ..... - 2 -

1.1.2 Urban canyons ..... - 5 -

1.2 Urban air pollution ..... **- 9 -**
1.2.1 Air pollutant compounds ..... - 9 -

1.2.2 Air pollution chemistry ..... - 13 -

1.2.3 Air quality standards and objectives ..... - 19 -

1.3 Air quality modelling ..... **- 22 -**
1.3.1 Model elements ..... - 22 -

1.3.2 Types of air quality models ..... - 24 -

1.3.3 Uncertainty and modelling quality assurance ..... - 32 -

1.4 Research motivation and thesis structure ..... **- 35 -**

CHAPTER 2 COMPARING OFFLINE MULTI-BOX MODELS WITH LARGE-EDDY SIMULATION ..... - 39 -

2.1 Introduction ..... - 41 -

2.2 Methods ..... - 46 -
2.2.1 Description of models ..... - 46 -

2.2.2 Model configurations ..... - 53 -

2.3 Results and Discussion ..... - 60 -
2.3.1 Temporal evolution and the intensity of segregation within the canyon ..... - 60 -

2.3.2 The spatial variation of pollutants in street canyons ..... - 68 -

2.3.3 The model performance with the simple NO_x-O_3 cycle ..... - 75 -

2.4 Conclusions ..... - 79 -

2.5 Supporting Information ..... - 82 -

2.6 Acknowledgements ..... - 83 -

CHAPTER 3 CHEMISTRY, TRANSPORT, EMISSIONS, AND SHADING EFFECTS ON NO_2 AND O_x WITHIN URBAN CANYONS ..... - 84 -

3.1. Introduction ..... - 86 -

3.2. Experimental Section ..... - 90 -
3.2.1 Model description ..... - 90 -

3.2.2 Model configuration ..... - 92 -

3.2.3 Model scenarios ..... - 97 -

3.3 Results and Discussion ..... - 100 -
3.3.1 Effects of shading and solar zenith angles ..... - 100 -

3.3.2 Effects of VOC chemistry ..... - 106 -

3.3.3 Effects of NO_x and VOC emissions ..... - 112 -

3.3.4 Effects of shading intensities ..... - 115 -

3.3.5 Effects of prevailing wind speeds ..... - 117 -

3.4 Conclusions ..... - 120 -

3.5 Supporting Information ..... - 122 -

3.6 Acknowledgements ..... **- 130 -**

CHAPTER 4 CHEMISTRY, CANYON GEOMETRY, AND EMISSIONS EFFECTS ON NO_2 "HOTSPOTS" AND REGULATORY "WIGGLE ROOM" ..... **- 131 -**

4.1 Introduction ..... **- 132 -**

4.2 Methods ..... **- 137 -**
4.2.1 Model Description ..... - 137 -

4.2.2 Model Evaluation ..... - 141 -

4.2.3 Model Scenarios ..... - 144 -

4.3. Results and Discussion ..... **- 148 -**
4.3.1 NO_2 Response Surfaces and Air Quality Management ..... - 148 -

4.3.2 Model Sensitivity ..... - 153 -

4.3.3 Implications for Future Regulatory Practice and Modelling ..... - 158 -

4.4. Supporting Information ..... **- 161 -**
4.4.1 Supplementary Methods ..... - 161 -

4.4.2 Supplementary Discussion ..... - 176 -

4.5 Acknowledgements ..... **- 199 -**

CHAPTER 5 MODELLING OF DEEP CANYON AIR POLLUTION CHEMISTRY AND TRANSPORT: A WINTERTIME NAPLES CASE STUDY ..... **- 200 -**

5.1 Introduction ..... **- 201 -**

5.2 Methodology ..... **- 208 -**
5.2.1 Field data ..... - 208 -

5.2.2. The multi-box framework and some new developments ..... - 212 -

5.2.3. Model configuration and data pre-processing ..... - 215 -

5.2.4. Model simulation and data post-process ..... - 221 -

5.3. Results and Discussion ..... **- 225 -**
5.3.1. Comparing box-model simulations with CFD ..... - 225 -

5.3.2. Concentration fields ..... - 226 -

5.3.3. MBM-FleX results ..... - 228 -

5.3.4. Model simulation sensitivity ..... - 232 -

5.3.5. The performance of MBM-FleX_r ..... - 235 -

5.4. Conclusions ..... **- 236 -**

5.5. Supporting Information ..... **- 238 -**

CHAPTER 6 GENERAL DISCUSSION ..... **- 252 -**

6.1 Thesis Overview and Major Results ..... **- 252 -**

6.2 Limitations and suggestions for future research ..... **- 258 -**

APPENDICES ..... **- 262 -**

Appendix A: Multi-box model parameters ..... **- 262 -**

Appendix B: RCS mechanism ..... **- 264 -**

Appendix C: Fortran90 code for MBM-FleX ..... **- 270 -**

REFERENCES ..... **- 301 -**

LIST OF TABLES

Table 1.1 20
Table 1.2 21
Table 2.1 64
Table 2.2 66
Table 2.3 68
Table 2.4 76
Table 3.1 95
Table 3.2 100
Table 4.1 146
Table 4.2 155
Table 4.3 196
Table 4.4 197
Table 4.5 198
Table 5.1 224
Table 5.2 229
Table 5.3 248
Table 5.4 248
Table 5.5 249
Table 5.6 250
Table 5.7 251

LIST OF FIGURES

Figure 1.1 3
Figure 1.2 7
Figure 1.3 8
Figure 1.4 16
Figure 1.5 24
Figure 1.6 25
Figure 1.7 29
Figure 2.1 51
Figure 2.2 62
Figure 2.3 72
Figure 2.4 74
Figure 2.5 77
Figure 2.6 78
Figure 2.7 82
Figure 2.8 82
Figure 3.1 91
Figure 3.2 104
Figure 3.3 105
Figure 3.4 109
Figure 3.5 110
Figure 3.6 111
Figure 3.7 114
Figure 3.8 115
Figure 3.9 116
Figure 3.10 122
Figure 3.11 123
Figure 3.12 124
Figure 3.13 125
Figure 3.14 126
Figure 3.15 127

Figure 3.16 128
Figure 3.17 129
Figure 3.18 130
Figure 4.1 139
Figure 4.2 142
Figure 4.3 151
Figure 4.4 156
Figure 4.5 157
Figure 4.6 160
Figure 4.7 183
Figure 4.8 183
Figure 4.9 184
Figure 4.10 185
Figure 4.11 186
Figure 4.12 187
Figure 4.13 188
Figure 4.14 189
Figure 4.15 190
Figure 4.16 191
Figure 4.17 192
Figure 4.18 193
Figure 4.19 194
Figure 4.20 195
Figure 5.1 210
Figure 5.2 220
Figure 5.3 231
Figure 5.4 233
Figure 5.5 241
Figure 5.6 242
Figure 5.7 242
Figure 5.8 243
Figure 5.9 244

Figure 5.10 ..... **245**
Figure 5.11 ..... **246**
Figure 5.12 ..... **247**

CHAPTER 1 GENERAL INTRODUCTION

Approximately 68% of the global population is projected to reside in urban areas by 2050 (World Health, 2021), as a consequence of rapid and ongoing urbanization. This trend is expected to generate a considerable increase in anthropogenic emissions (e.g., traffic, domestic), heightened levels of air pollution, and a densification of the urban space (e.g., more urban canyons, a concept that will be defined in section 1.1.2). Although clean air strategies and net-zero policies curtail emissions and enhance air quality, the growing contradiction between urban air quality and the escalating demand for a more habitable environment for urban dwellers has still emerged as a pressing concern.

This thesis primarily focuses on the physical and chemical processes affecting air pollutants in the urban atmosphere. The materials presented in this chapter are cover the basic terminology and concepts explored in subsequent chapters. This fundamental understanding will enable the reader to understand the significance and implications of the research findings presented throughout the thesis. The specific literature reviews for each chapter are presented within their respective sections, and not reproduced here. Some information is reiterated in multiple chapters to enhance readability and provide context for each topic.

1.1 Urban atmosphere

1.1.1 Vertical structure and horizontal scale

The urban boundary layer (UBL) is the bottom portion of the atmosphere near the surface of the Earth (Stull, 2012). In the presence of densely built constructions and intensive human activities, atmospheric processes and climatic characteristics in the UBL are quite different from those of surrounding rural areas. The UBL can be classified into three sublayers based on typical vertical length scales: the roughness sublayer (RSL); the inertial sublayer (ISL); and the mixed layer (ML), listing from bottom to top. The RSL describes the atmosphere layer from the urban surface to two to five times the height of buildings or trees. The airflow within the RSL is very complicated and is greatly affected by individual roughness elements in urban areas. The ISL is a shear-dominated layer above the RSL, with a logarithmic wind velocity profile and a near-uniform vertical distribution of turbulent fluxes. The ML above the ISL is characterised by homogenised atmospheric properties that are less influenced by roughness elements due to forceful thermal turbulence and, in general, accompanying a capping inversion (Oke et al., 2017). During daytime, the typical depth of the UBL is elevated to about 1,000 m over urban areas because of vigorous mixing by thermal heating effects (Figure 1.1a). Cooling effects at night restrict the turbulent mixing capability. The depth of the UBL shrinks to about 50 m to 300 m, depending on the intensity of the nocturnal urban heat island and surface roughness (Figure 1.1b).

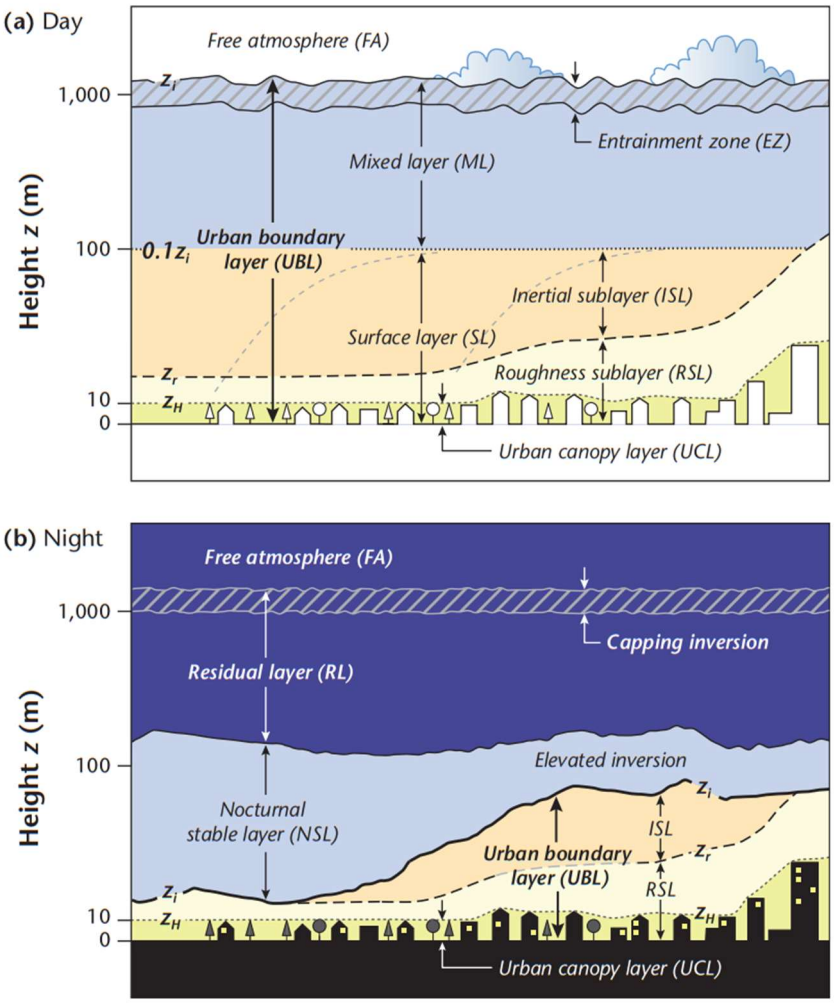


Figure 1.1. Schematic of the typical urban atmosphere (a) in daytime, and (b) at night, z_i is the height of the urban boundary layer, z_H is the height of the urban canopy layer (Oke et al., 2017).

Of the atmospheric motions and their horizontal coverage, the geographical scope of the atmospheric behaviour can be hierarchically divided into four categories: global-scale (> 5×10^3 km); synoptic-scale (hundreds to thousands of kilometres); mesoscale (tens to hundreds of kilometres); and microscale

(0-100 m). Between micro- and mesoscale, the spatial scales may be further partitioned into regional-scale (100-200 km), urban-scale (10-20 km), neighbourhood-scale (1,000-2,000 m), and street-scale (100-200 m) (Britter and Hanna, 2003). Since atmospheric chemistry and aerosol and cloud microphysics evolve over time, the scientific concerns related to these atmospheric phenomena vary across the scales. For instance, the dispersion of air pollution is usually associated with the street- to regional-scale, which climate-relevant processes occur among urban- to global-scale. However, local processes may have important influences on processes at the regional-scale (e.g., impacts of urban heat island on climate change) (Emmanuel and Krüger, 2012), and vice versa. That is, in principle, the chemistry and physics of the atmosphere are coupled across time and space scales; the strength of such coupling is not always well understood. This later chapters of this thesis focus on the extent to which the chemistry of volatile organic compounds (VOCs), usually considered on the regional scale, impacts pollutant dispersion at the street scale.

The urban canopy layer (UCL) is located at the bottom part of RSL, extending from the ground up to the average height of urban constructions or trees (i.e., z_H in Figure 1.1). The UCL is unique because it accommodates most anthropogenic activities (e.g., on-road vehicles) and energy balances. Any changes in the UCL environment will directly affect the living conditions of residents. The air in the UCL generally includes that outdoor and indoor (Mills, 1997), although only outdoor air is considered in the rest of this thesis. The outdoor airflow may be significantly shaped or modified by the morphological

elements in the UCL, such as urban form, street block or canyon, and building facet. A better understanding of the mechanism of local climates and pollution characteristics can lead directly to scientific improvements in urban planning and design, thus enhance the living quality of residents.

1.1.2 Urban canyons

From a geometric perspective, “street canyons” refer to typical urban units characterized by a street lined with continuous in-line buildings on either side (Oke et al., 2017). These canyons create a confined space with limited ventilation capabilities. Street canyons are commonly found in central urban areas with heavy traffic loads. The exchange of air between the canyon and the overlying background, known as ventilation, has been quantified using terms such as "transfer velocity" (SalizzoniSoulhac and Mejean, 2009), “air ventilation rate” (Liu and Leung, 2008), or “exchange velocity” (BrightBloss and Cai, 2013). Strong background wind can significantly accelerate the exchange of air mass between the canyon and background, aiding in the dispersion of emitted pollutants at the street level.

The aspect ratio (AR) is generally used to describe the characteristics of street canyons and is calculated as the ratio of building height (H) to street width (W). Street canyons can be categorized into three main groups (Vardoulakis et al., 2003): avenue street canyons (AR ≤ 0.5), regular street canyons (AR ≈ 1), and deep street canyons (AR ≥ 2). Street canyons may also be further classified according to their continuous length (L): short street canyons (L/H $\approx$ 3), medium street canyons (L/H $\approx$ 5), and long street canyons (L/H $\approx$ 7).

Additionally, symmetric canyons are those with equal building heights on both sides of the street, while asymmetric canyons have a significant discrepancy in building heights between roadsides.

The ambient wind above the canyon rooftop can be divided into three groups based on its prevailing direction to the street axis, including parallel airflow, oblique airflow, and perpendicular (or orthogonal) airflow (Yazid et al., 2014). Figure 1.2 showed several perpendicular airflow regimes over urban street canyons with different AR configurations under the neutral meteorological condition (Oke, 1988). Isolated roughness flow (IRF) appears when the street width is obviously greater than the building height (AR < 0.3), and street canyons are well ventilated. Wake interference flow (WIF) appears when the building intervals become slight closer (0.3 < AR < 0.7). Skimming flow is associated with densely built areas, representing the poorest ventilation inside the street canyon (AR > 0.7).

Air pollution concentrations within street canyons are heavily influenced by circulation patterns. Pollutants from vehicular emissions, for example, disperse across a single air mass within the canyon. This leads to scenarios where the highest concentrations of pollutants are often found in poorly ventilated areas, typically downwind from the emission source. As a result, pedestrians in these areas face increased exposure risks. The geometry of street canyons plays a critical role in shaping air quality within urban environments. Figure 1.2d shows that a primary vortex is formed in the regular (avenue) canyon, driven by the ambient wind in the shear layer

perpendicularly blowing from the leeward side to the windward side cross the canyon axis. Two subscale vortices emerge near the intersection of street and building facets. The main vortex feature was also demonstrated by the neutrally buoyant balloons experiment in the street canyon (AR = 1.4) (DePaul and Sheih, 1986).

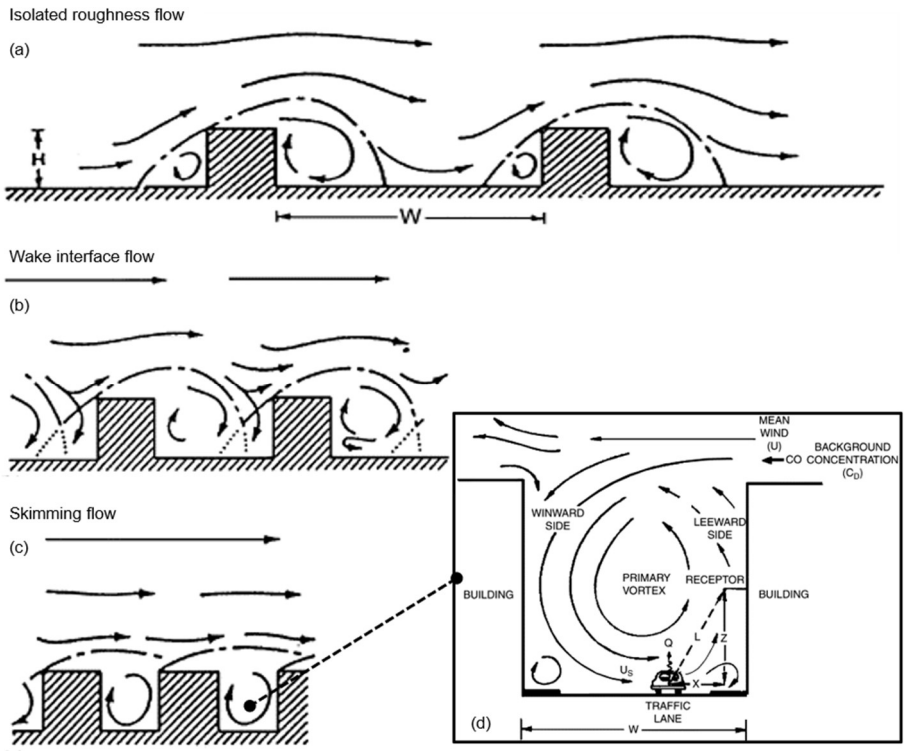


Figure 1.2. Flow regimes in urban street canyons with different aspect ratios (a,b,c, adopted from Oke (1988) and dispersion pattern in a regular street canyon (d, adapted from DabberdtLudwig and Johnson Jr (1973)).

Figure 1.3b depicted the air dispersion pattern in a deep canyon (AR = 2), which clearly exhibits two counter-rotated vortices (ZhongCai and Bloss,

2017). The lower vortex is driven by the air in the shear layer at the bottom of the upper vortex (about the middle position of buildings). As buildings tend to be taller, deep street canyons (with high aspect ratios) tend to experience more limited air circulation. This can lead to the trapping of pollutants and the formation of localized high concentration pockets, posing a greater risk to public health. Moreover, deep street canyons may experience the "canyon vortex" effect, a phenomenon where the limited air exchange causes pollutants to circulate within the canyon, further exacerbating air quality issues, such as in Figure 1.3c (AR = 4.5) (Murena and Mele, 2016).

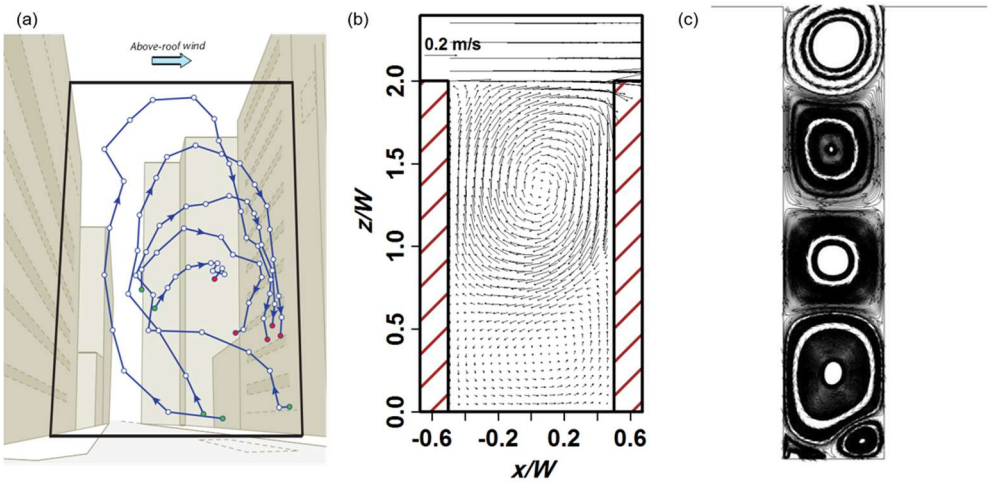


Figure 1.3. Airflow circulation within a (a) street canyon (AR = 1.4) described by the motion of neutrally buoyant balloons (adopted from Oke et al. (2017)); and (b) deep street canyon (AR = 2) revealed by modelling results from large eddy simulation (ZhongCai and Bloss, 2017); and (c) very deep street canyon (AR = 4.5) revealed by modelling results from large eddy simulation (Murena and Mele, 2016).

Other factors that affect pollutant dispersion within the canyon environments include the length, the symmetry, and the configurations of street canyons. For example, urban greening (e.g., in-canyon vegetation) may yield numerous benefits including reduced surface temperature and noise pollution, but it could also trap air masses, thereby increasing the residence time of pollutants and facilitating more extensive chemical reactions and deposition processes (Pugh et al., 2012). Understanding the implications of different canyons on pollutant dispersion is vital for urban planners and policymakers when considering measures to improve air quality and mitigate adverse health effects.

1.2 Urban air pollution

1.2.1 Air pollutant compounds

Air pollutants refer to those substances in the atmosphere that can lead to short-term or long-term adverse effects to humans and the environment, causing the reduction of quality of life (Tiwary and Williams, 2018). Air pollution in urban areas has unique and important characteristics due to elevated primary emissions, sharp concentration gradients, sophisticated coherent and incoherent turbulence patterns, high aerosol surface areas for heterogeneous chemical reactions, heat island effects (e.g., strong daytime heating and weak night-time cooling), and short timescales in chemistry (that is, chemical species persist for a mere few hours due to prevailing wind speeds, thereby constraining the extent of chemical transformation) (Harrison, 2018). The major pollution species subject to regulatory attention and legislation in

the urban atmosphere include particulate matter (PM), nitrogen dioxide (NO_2), ozone (O_3), sulphur dioxide (SO_2), lead (Pb), and volatile organic compounds (VOCs) such as polycyclic aromatic hydrocarbons (PAHs), benzene and 1,3-butadiene. PM here may further be divided into ultrafine particles ($PM_{0.1}$), fine particles ($PM_{2.5}$) and combined coarse and fine particles (PM_{10}). PM_{10} is condensed phase particles with a 50% cut-off aerodynamic diameter of 10 μm in principle, similarly $PM_{2.5}$ is particles with a 50% cut-off aerodynamic diameter of 2.5 μm, and $PM_{0.1}$ refers to nano size particles. PM are either directly emitted by anthropogenic activities (e.g., industrial emissions, constructions, on-road sources) and natural processes (e.g., wildfire, sea salt, pollen) or produced from more complex chemical reactions (e.g., oxidations of NO_2 and SO_2). The particles lead to lung or heart diseases especially for the vulnerable group such as the elderly and children, and smaller size particles have more severe impacts on health, as they could reach deeper into the human body (Lu et al., 2015, Janssen et al., 2011).

NO_2 is a pollution gas that is chemically related to nitric oxide (NO), together they are referred to as nitrogen oxides (NO_x), which is mainly produced by fossil fuel (e.g., petrol and diesel) burning in urban areas. The primary proportion of NO_x in vehicle exhausts is NO because of incomplete combustions. Studies showed that the older engine would decrease NO_2/NO_x ratios but the application of the treatment technologies for particle emissions (e.g., diesel oxidation catalyst) would oxidise more NO to NO_2 (Carslaw et al., 2016, Bishop and Stedman, 2015). Both short- and long-term exposure to NO_2 have direct adverse effects on the respiratory and cardiovascular system. NO_2

is also an important precursor of secondary species such as PM, O_3, and nitric acid (HNO_3), which is able to cause damage to vegetation, materials, and ecosystems (Janssen et al., 2011, Allen et al., 2009).

O_3 in the troposphere has strong reactivity, serving as an effective oxidising agent. Its direct impacts include stimulating the human respiratory system and damaging the growth of vegetation. Although some tropospheric O_3 is transported from the stratosphere to near the ground because of atmospheric processes such as tropospheric folding, it is mainly generated through photochemical reactions involving nitrogen oxides and VOCs. In urban areas with sufficient NO_x emissions, O_3 titrates with NO rapidly, forming high NO_2 concentrations. Due to its relatively long residence time in the atmosphere, it can be transported downwind over long distances and may affect areas with limited or no local sources.

SO_2 is a colourless gas with a pungent odour, mostly sourced from the burning of sulphur-containing fuels. It is an important air pollutant because SO_2 has a strong tendency to react with oxygen (O_2) to produce sulphur trioxide (SO_3) (i.e., stoichiometric reaction). SO_3 reacts with water vapour rapidly and further undergoes homogeneous and heterogeneous nucleation processes to form sulphuric acid aerosol and sulphate. Therefore, SO_2 participates in the formation of sulphuric acid smog and acid rain and thus, has an important impact on the regional environment, such as corrosive effect on marble buildings or sculptures, destruction of vegetation, and impairing the productivity of crops.

VOCs refer to the entire set of vapor-phase atmospheric organics, which have relative small molecular weight, high saturated vapour pressure, low boiling point, and large Henry's constant. VOCs are crucial precursors of photochemical smog, contributing to the formation of tropospheric O_3. VOCs are generally classified into two groups: methane (CH_4) and other non-methane VOCs. CH_4 is the most abundant gaseous organic and is chemically inert in most photochemical reactions. The formation of CH_4 includes reduction of carbon dioxide (CO_2), thermochemical reactions, fermentation of acetic acid, and combustion process. Besides, it is highlighted as a greenhouse gas, contributing to global warming. In contrast to CH_4, the non-methane VOCs usually have short lifetime in the atmosphere. About 10% of global emissions are attributed to anthropogenic activities and about 90% of emissions are attributed to biogenic sources (Seinfeld and Pandis, 2016). VOC species take an important part in atmospheric chemistry.

There are also some trace radicals in the atmosphere, such as hydroxyl (OH) and hydroperoxyl (HO_2). Also, nitrous acid (HONO), while not a radical itself, often participates in atmospheric chemical reactions that generate radicals, thus making HONO a significant species in atmospheric chemistry. Although the concentrations of these species are relatively low compared to constant species, they actively participate in chemical reactions, and significantly impact air quality. The following section of this thesis will consider the major chemical processes involving these radicals.

1.2.2 Air pollution chemistry

Urban chemistry is vital for understanding differences between urban and rural environments. Factors contributing to its importance include emission heterogeneity, emission inventory, wind speed, atmospheric stability, the role of reactive species, and the presence of short-lived species (Harrison, 2018). These factors demonstrate the complex interplay of chemistry, transport, and emissions in urban atmospheres, highlighting the need for targeted research and modelling approaches to effectively study urban air quality. The main chemical reactions in the typical urban atmosphere are described hereafter, including the simple NO_x-O_3 cycle, more complex HO_x (the summation of OH and HO_2) chemistry, and night-time chemistry.

(1) NO_x-O_3 cycle

NO_x is abundant in the urban atmosphere because of vehicle emissions from internal combustion process, namely the Zeldovich mechanism (Mellor et al., 1998):

$$O + N_2 \rightarrow NO + N \quad (1.1)$$

$$N + O_2 \rightarrow NO + O \quad (1.2)$$

Thermal decomposition of molecular oxygen only occurs in very high temperature environments (e.g., engines). The primary NO_2 ratio from the tailpipe ranges from 0.05 ($NO : NO_2 = 0.95 : 0.05$) to 0.30 ($NO: NO_2 = 0.7: 0.3$), depending on the type of vehicle and the degree of wear (Carslaw et al., 2011). When NO concentrations are extremely high, the recombination of NO in generating NO_2 becomes important:

$$NO + NO + O_2 \rightarrow 2NO_2 \quad (1.3)$$

As NO concentrations are diluted to the level at which reaction (1.3) is insignificant, the NO_x-O_3 cycle is dominated through the following photochemical steady state (*PSS*) reactions during the daytime in the absence of VOCs:

$$NO + O_3 \rightarrow NO_2 + O_2 \quad (1.4)$$

$$NO_2 + h\nu \rightarrow NO + O(^3P) \quad (1.5)$$

$$O(^3P) + O_2 + M \rightarrow O_3 + M \quad (1.6)$$

where $h\nu$ is photon energy, $O(^3P)$ represents those O atoms without any excess energy that almost only are able to participate in the reaction (1.6) to produce O_3, and M represents any third molecule (e.g., N_2, O_2) that carries off the excess energy of the reaction (1.6) but is not changed by the collision. The equilibrium of reactions (1.4-1.6) can be defined by Leighton Relationship (Clapp and Jenkin, 2001):

$$[NO_2] = \frac{k_{NO+O_3}}{j_{NO_2}}[NO][O_3] \quad (1.7)$$

where k_{NO+O_3} is chemical reaction rate of the titration between NO and O_3 at a determined temperature, j_{NO_2} is chemical reaction rate of the photodegradation of NO_2 under the sunlight. Overall, the total mixing ratio of oxide (O_x, the summation of NO_2 and O_3) is conserved if there is no other reaction involved.

(2) HO_x chemistry

The highly reactive gas-phase radicals (e.g., OH and HO_2) are very important in the troposphere because they initiate the degradation of most organic species (Bloss, 2009). Figure 1.4 provides a summary of the chemical reactions between OH and VOCs, the dashed lines offer additional propagation processes of radicals in the polluted areas with sufficient NO_x emissions. In the presence of solar radiation at wavelengths less than 310 nm, O_3 is photodegraded into O_2 and O (^1D), subsequently O (^1D) with surplus energy reacts with water vapour (H_2O) producing two OH radicals:

$$O_3 + h\nu(\lambda < 310\text{nm}) \rightarrow O_2 + O(\,^1D) \quad (1.8)$$

$$O(\,^1D) + H_2O \rightarrow OH + OH \quad (1.9)$$

$$O(\,^1D) + M \rightarrow O(\,^3P) + M \quad (1.10)$$

where M represents a molecule that can quench O(^1D), commonly N_2 or O_2. OH can react with carbon monoxide (CO) to form HO_2 through the following reactions:

$$OH + CO \rightarrow H + CO_2 \quad (1.11)$$

$$H + O_2 + M \rightarrow HO_2 + M \quad (1.12)$$

Alternatively, OH can react with hydrocarbons comprising the atoms of carbon (C) and hydrogen (H)(hereafter denoted as RH) to produce organic peroxyl radicals (RO_2):

$$OH + RH \rightarrow H_2O + R \quad (1.13)$$

$$R + O_2 + M \rightarrow RO_2 + M \quad (1.14)$$

In the clean atmosphere with limited NO_x abundance, RO_2 and HO_2 undergo the self-reaction and cross-reaction, generating organic hydroperoxides (ROOH) and hydrogen peroxide (H_2O_2):

$$RO_2 + HO_2 \rightarrow ROOH + O_2 \quad (1.15)$$

$$HO_2 + HO_2 + M \rightarrow H_2O_2 + M \quad (1.16)$$

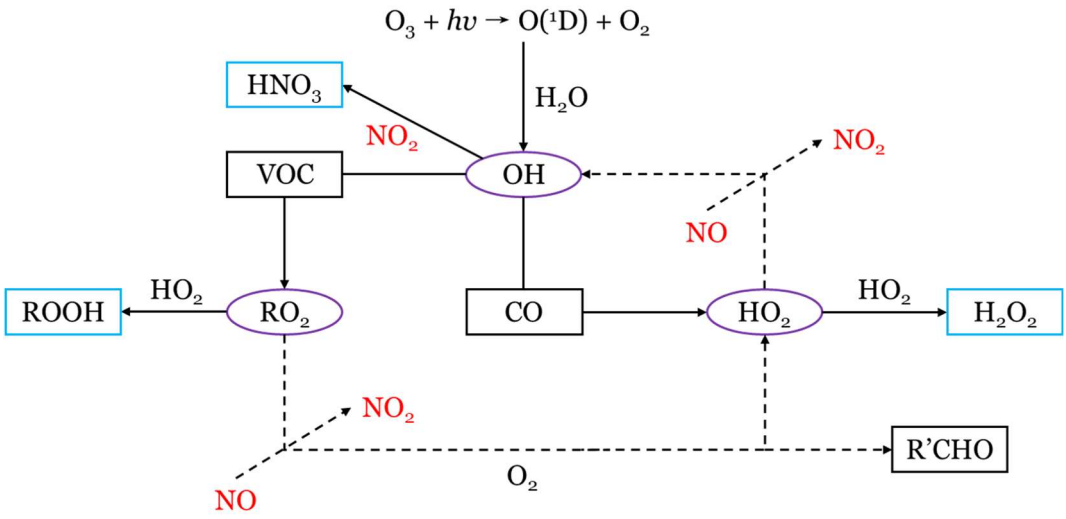


Figure 1.4. VOCs oxidation involving HO_x chemistry, exhibiting the additional propagation processes in polluted urban atmosphere (with sufficient NO_x) with dashed lines, adopted from Bloss (2009).

In this polluted atmosphere with high NO_x abundance, additional radical propagation processes can occur through the following atmospheric chemical reactions:

$$RO_2 + NO \rightarrow RO + NO_2 \quad (1.17)$$

$$RO + O_2 \rightarrow R'CHO + HO_2 \quad (1.18)$$

where RO represents an alkyl radical and R'CHO represents an aldehyde. The product of reaction (1.18) turns more NO to NO_2 and increases OH levels:

$$NO + HO_2 \rightarrow NO_2 + OH \quad (1.19)$$

The aforementioned chemistry cycle is restricted by termination reactions, such as the formation of HNO_3:

$$OH + NO_2 + M \rightarrow HNO_3 + M \quad (1.20)$$

The reaction (1.20) is also the main sink of NO_x in the urban atmosphere, because HNO_3 can easily be converted to the condensed phase. HONO also contributes a large fraction of OH formation in the urban atmosphere, making the chemical reactions become even more complex (Harrison, 2018).

Peroxyacetyl nitrate (PAN) is an important compound in atmospheric chemistry, especially in relation to air pollution and the formation of photochemical smog. The peroxy radicals can undergo intramolecular isomerization to form acyl peroxy radicals, and then the acyl peroxy radicals then react with NO_2 to from PAN:

$$RO_2 \rightarrow CH_3C(O)OO \quad (1.21)$$

$$CH_3C(O)OO + NO_2 \rightarrow CH_3C(O)OONO_2(PAN) \quad (1.22)$$

Considering the loss of PAN, PAN is thermally unstable and can decompose back into its precursors, especially under higher temperature conditions. It can also be broken down by ultraviolet light, leading to the release of acyl peroxy radicals and NO_2:

$$CH_3C(O)OO + NO_2 \rightarrow CH_3C(O)OONO_2\ (PAN) \quad (1.23)$$

$$CH_3C(O)OONO_2 + h\nu \rightarrow CH_3C(O)OO + NO_2 \quad (1.24)$$

(3) Night-time chemistry

(Night-time chemistry is not considered in the remainder of the thesis but is included here for completeness) During night-time, chemical reactions involving energy photons cease, inhibiting the formation of OH radicals as well. Consequently, other chemical reactions become crucial (i.e., reactions (1.25-1.26)), leading to the production of nitrate radicals (NO_3) and ultimately dinitrogen pentoxide (N_2O_5):

$$NO_2 + O_3 \rightarrow NO_3 + O_2 \quad (1.25)$$

$$NO_2 + NO_3 + M \underset{r1}{\overset{r2}{\rightleftarrows}} N_2O_5 + M \quad (1.26)$$

and the most important removal process of N_2O_5 at night may occur on the surface of aerosols through heterogeneous chemistry with water vapor:

$$N_2O_5 + H_2O(l) \rightarrow 2HNO_3(\text{aerosol}) \quad (1.27)$$

R1.25 illustrates the largest source of NO_3 radicals in the atmosphere, which also happens at the daytime. However, the formation of N_2O_5 is significantly suppressed due to the rapid photolysis process of NO_3:

$$NO_3 + h\nu(\lambda < 590\text{nm}) \rightarrow NO_2 + O_3(\,^3P) \quad (1.28)$$

The chemical reactivity of NO_3 radical is less than its analogue, OH, but the concentrations of NO_3 at night-time are much greater than the concentrations of OH at daytime (Brown and Stutz, 2012), making NO_3 the primary oxidant for unsaturated VOCs (carbonyl compounds) during the night. In polluted

atmospheres, such as urban environments, NO_3 may quickly be depleted by primary NO that emitted from vehicles through:

$$NO + NO_3 \rightarrow 2NO_2 \quad (1.29)$$

and the chemical reaction could resist the accumulation of NO_3 and N_2O_5 at night-time (Hester and Harrison, 2009).

1.2.3 Air quality standards and objectives

Air quality has dramatically improved in recent decades in the United Kingdom (UK). The Department for Environment, Food and Rural Affairs (Defra, 2017b) reported SO_2 emissions have reduced by 95%, particulate matter (PM) by 73%, and NO_x by 69% since 1970. However, Air pollution persistently poses the most significant environmental threat to public health, disproportionately impacting children, the elderly, and individuals already at risk (Joint Air Quality Unit, 2017). The ramifications of poor air quality extend beyond human health, detrimentally affecting crop yields. Specifically, emissions like ammonia and nitrogen oxides (NO_x) profoundly disrupt the natural environment and biodiversity, underlining the far-reaching consequences of air pollution (DEFRA, 2023).

Air quality standards function as regulatory instruments to manage pollution activities and maintain air quality at levels considered acceptable and unlikely to jeopardize public health. Typically, these standards rely on scientific and medical evidence (Defra, 2011), establishing thresholds for both short-term exposure to unusually high concentrations and long-term exposure to more moderate levels of pollutants. Table 1.1 provides a comprehensive overview

of the air quality standards set forth by the World Health Organization (WHO) (Hoffmann et al., 2021) and various countries (ZhangHe and Huo, 2012, Firdaus and Ahmad, 2011, HolmanHarrison and Querol, 2015).

Table 1.1. Air quality guidelines from WHO and standards from several countries.

Pollutant		Unit	UK (England)	China (1st)	India (sensitive)	EU	WHO(AQG)
NO_2	1-hour mean	μg/m³	200	200	-	200	-
	24-hour mean		-	-	80	-	25
	annual mean		40	40	30	40	10
SO_2	15 min mean	μg/m³	266	-	-	-	-
	1-hour mean		350	150	-	350	-
	24-hour mean		125	50	30	125	40
	annual mean		20	20	15	-	-
O_3	1-hour mean	μg/m³	-	160	180	-	-
	8-hour mean		120	100	100	120	100
$PM_{2.5}$	24-hour mean	μg/m³	-	35	60	-	15
	annual mean		20	15	40	20	5
PM_{10}	24-hour mean	μg/m³	50	50	100	50	45
	annual mean		40	40	60	40	15
CO	1-hour mean	mg/m³	-	10	2.0	-	-
	8-hour mean		10	-	1.0	-	-
	24-hour mean		-	4	-	10	4
Pb	seasonal mean	μg/m³	-	1	-	-	-
	annual mean		0.25	0.5	0.5	0.5	-
Benzene	24-hour mean	μg/m³	-	0.0025	-	-	-
	annual mean		5	0.001	5	5	-

Air quality objectives denote targeted timelines for reaching specific air quality benchmarks, underlining the significance of mitigating air pollution for public health and environmental preservation. These objectives allow for a

certain number of exceedances, scenarios where pollutant concentrations surpass established limits, recognizing that absolute adherence to standards may not be consistently achievable due to factors such as meteorological conditions. Despite this, the objectives maintain a focus on minimal exceedances, necessitating the amplification of mitigation strategies when limits are frequently exceeded. This approach ensures a persistent pursuit of improved air quality and a reduction in health risks linked to pollution. In the context of the UK, the national air quality objectives, as outlined in the Air Quality Strategy, are encapsulated in Table 1.2.

Table 1.2. Air quality objective and obligations in the UK and in the EU (Defra, 2019a).

Pollutant		UK	Target date	EU	Target date
NO_2	1-hour mean	Not to be exceeded more than 18 times a year	31/12/2005	Not to be exceeded more than 18 times a year	01/01/2010
SO_2	15 min mean	Not to be exceeded more than 35 times a year	31/12/2005	-	-
	1-hour mean	Not to be exceeded more than 24 times a year	31/12/2004	Not to be exceeded more than 24 times a year	01/01/2005
	24-hour mean	Not to be exceeded more than 3 times a year	31/12/2004	Not to be exceeded more than 3 times a year	01/01/2005
O_3	8-hour mean	Not to be exceeded more than 10 times a year	31/12/2005	Not to be exceeded more than 25 times a year, averaged over 3 years	31/12/2010
$PM_{2.5}$	annual mean	Target of 15% reduction in concentrations at urban background	From 2010 to 2020	Target of 20% reduction in concentrations at urban background -	From 2010 to 2020
PM_{10}	24-hour mean	Not to be exceeded more than 35 times a year	13/12/2004	Not to be exceeded more than 35 times a year	01/01/2005

Additionally, the UK government acknowledges that further efforts are required to safeguard people and the environment from the impacts of air pollution and proposes ambitious new targets for $PM_{2.5}$. The newly established obligations for $PM_{2.5}$ include a target of an annual mean concentration of 10 μg m^{-3} across England by 2040, and a reduction in population exposure by 35% by 2040 compared to a 2018 baseline. Interim targets for each long-term goal have also been set out in the Environmental Improvement Plan: to achieve a 12 μg m^{-3} annual mean concentration of $PM_{2.5}$ by January 2028 and to decrease average population exposure to $PM_{2.5}$ by 22% by January 2028, compared to a 2018 baseline (DEFRA, 2023).

1.3 Air quality modelling

1.3.1 Model elements

Measurements of chemical species provide the direct information about pollution levels in the atmosphere. However, these measurements are typically limited to specific temporal and spatial scales and cannot be directly applied to improve pollution control strategies. Air quality modelling integrates scientific understanding of atmospheric processes and serves a crucial role in assessing air quality and evaluating pollution mitigation policies.

To date, numerous air quality models have been developed to describe the temporal and spatial distributions, migration, and transformation pathways of pollutants in the atmosphere, benefiting from their extensive spatial coverage, robust explanatory function (e.g., on sources, causes, and processes), and

predictive capability (DenbyGeorgieva and Lükewille, 2011). In this thesis, modelling refers specifically to process modelling (i.e., physical and chemical processes) rather than data-based, empirical, or machine-learning approaches (i.e., data statistical analysis) (Tiwary and Williams, 2018). Based on geographical scope and typical horizontal resolution, air quality models can be classified by their geographical scope and typical horizontal resolution into global (~5°), continental (~80 km), regional (~20 km), urban (~4 km), and microscale (~5 m) (Seinfeld and Pandis, 2016). Scales smaller than urban, referred to as "local-scale", can be further divided into vehicle wake, street canyons, neighbourhood, city and road tunnels (Kumar et al., 2011). In general, it takes hours to days for the prevailing wind (i.e., airflow above buildings) to blow across a regional domain but only seconds to minutes across a local domain. Figure 1.5 offers the typical elements of a mathematical air quality model (Seinfeld and Pandis, 2016). The air quality model comprises three basic elements: (1) sources (i.e., anthropogenic emissions, natural emissions, and advected emissions); (2) transport influenced by meteorological conditions, which is significantly affected by geographical information; (3) physiochemical transformations, such as chemical reactions and aerosol processes. The subsequent subsection introduces different types of regional and local air quality models and their primary characteristics.

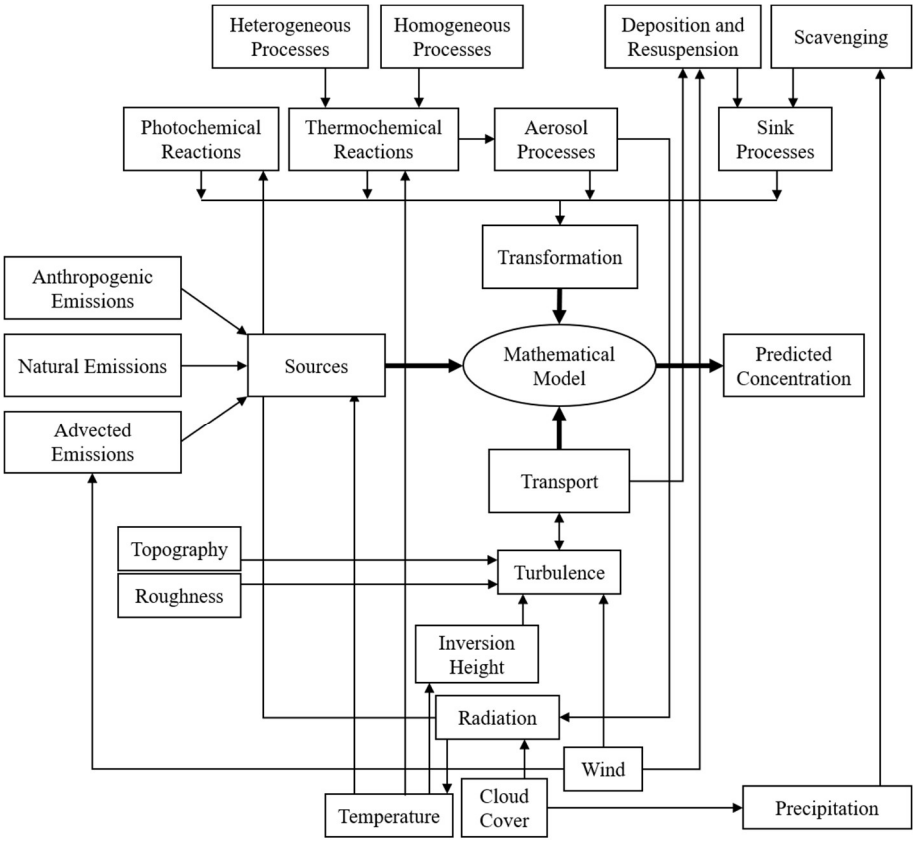


Figure 1.5 Components of a mathematical air quality model, adopted from Seinfeld and Pandis (2016).

1.3.2 Types of air quality models

(1) The Eulerian approach

An Eulerian modelling framework adopts a fixed spatial coordinate, covering a wide domain ranging from a few hundred meters to thousands of kilometres (Seinfeld and Pandis, 2016). The domain generally comprises three-dimensional arrays of boxes with uniform pollutant concentrations in each box, although one- and two-dimensional configurations are also possible (Figure 1.16b) (e.g., Pearce et al. (2021)) and two-dimensional Eulerian

models are used for the most part in this thesis. The atmospheric species transfer mass into and out of a box through its faces.

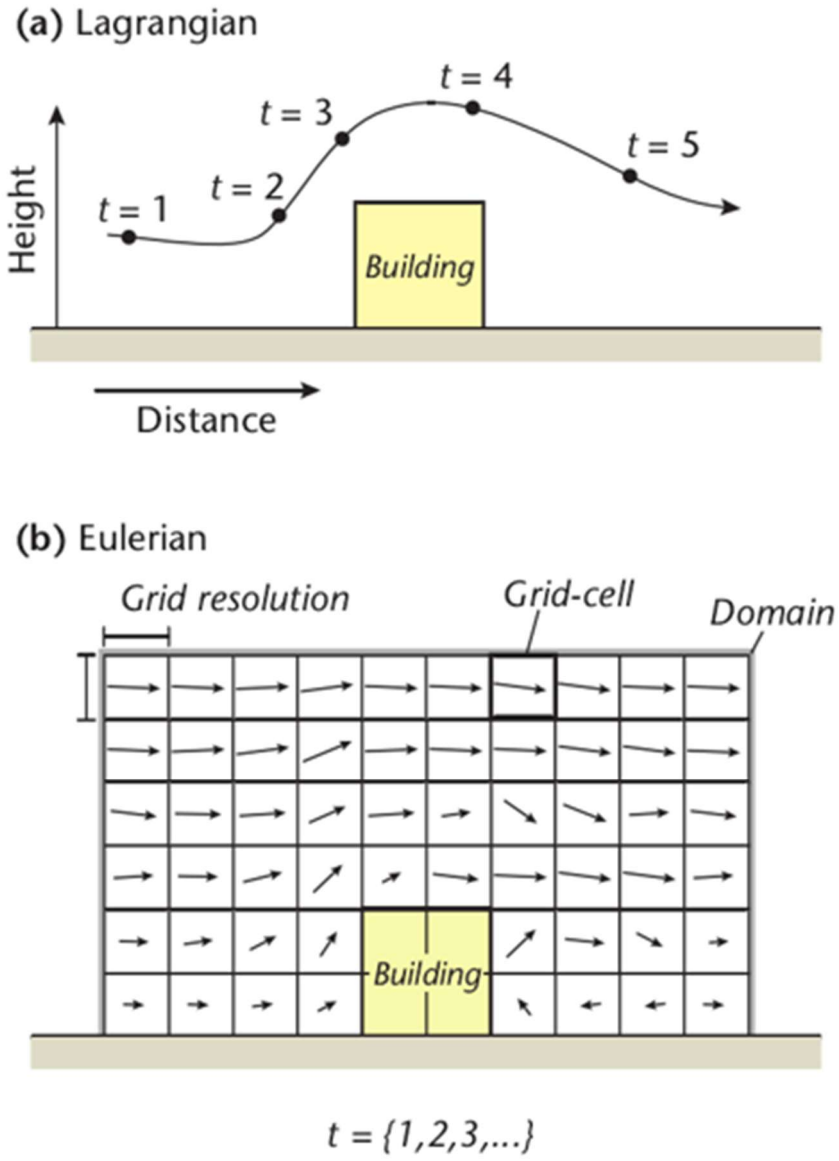


Figure 1.6 Schematic diagram of the Lagrangian and Eulerian based models (Seinfeld and Pandis, 2016).

The size of the box determines the resolution of the model and the accuracy of the simulation. Eulerian models can be applied to simulate the dispersion of pollutants over flat or more complex terrain. However, species injected into each grid are assumed to interact with the rest of in-grid substances immediately and uniformly whereas, in reality, the dispersion may take up to several hours to occupy the whole volume of a grid box depending on its size and roughness (e.g., 50 min for 9 km with 3 m s^{-1} wind speed under flat terrain). Eulerian-based models become computationally expensive as the total number of grid points increases since concentrations within each cell must be calculated simultaneously.

(2) The Lagrangian approach

In contrast to Eulerian modelling, Lagrangian box models adopt horizontally moving domains that correspond to the average wind vector (Figure 1.16a). The main benefit is to continuously follow composition changes within air "parcels" without excessive numerical mixing between parcels, but at the cost that model outputs are not guaranteed to fill a spatial domain unless a reverse-in-time, domain filling method is used to calculate trajectories (Dragani et al., 2002, Sutton et al., 1994). Incorporating emissions into Lagrangian models implies a vertical mixing scale that is usually assumed to be the local height of the planetary boundary layer (PBL). This, in turn, implies a horizontal scale required for mixing throughout the PBL (Emmerson et al., 2004). Since the coherence of air parcels is limited due to atmospheric shear and turbulence, pure Lagrangian methods are often used for relatively short time integrations,

e.g. hour to days (Draxler, 1992). Limited integration times can make it difficult to simulate chemicals with long atmospheric lifetimes; setting long-lived tracers to fixed values is sometimes used when focusing on the partitioning of shorter-lived compounds (Evans et al., 2000).

(3) Simple box model

The box model is a widely adopted, efficient and straightforward approach using simplified parameters to simulate concentrations inside a rectangular box. A typical box model includes emissions, deposition (i.e., wet deposition, dry deposition), physical and chemical transformation, inflows, and outflows (Figure 1.7a). It is assumed that pollutants are instantaneously and uniformly mixed into the box volume, while emissions and meteorology for the dilution process generally remain constant during a determined time-period (e.g., 1 hour). By permitting the mixing depth to be a function of downwind distances, the box model can efficiently conduct simulation on the local-scale areas of interest (Collett and Oduyemi, 1997) and also enable complex schemes to be incorporated accounting for atmospheric chemistry. However, the box model generally is unable to capture any spatial distribution of pollutants within its domain because of its simple nature, which induces non-negligible uncertainty with excessively idealised parameters under sophisticated conditions.

Street network models such as SIRANE (Soulhac et al., 2011) and MUNICH (Kim et al., 2018b) are conceived to simulate pollutant dispersion on the neighbourhood-scale. Such models apply the concept of the street network

with two subdomains: the lower compartment comprising street segments and intersections, and the upper compartment representing the ambient background. Each street segment or intersection is represented by a single box, and main processes occurred in the lower compartment include the advection along the street, diffusion within street intersections, and air exchanges between street segments and the overlying background. Nevertheless, the street network models have inherent restrictions in practice: firstly, it is only suitable for near-flat terrain because the wind field in the boundary layer is assumed to be uniform; secondly, it is unsuitable for the environment with sparse buildings (e.g., parks, squares) because of rapid exchange between the UCL and overlying background; thirdly, it provides a homogenous concentration in each box segment (i.e., cannot distinguish recycled or directly emitted pollution, and cause uncertainty by uniform mixing assumption) (Soulhac et al., 2011).

(4) Gaussian dispersion

The Gaussian approach is probably the most popular way to simulate the concentration of pollutants in urban atmosphere. The approach generally includes two types: plume or puff models. Gaussian plume dispersion (Figure 1.7b) follows a normal distribution along with vertical and horizontal directions with several important hypotheses, including uniform flow, steady meteorology, continuous emission, and mass conservation in the plume (Arya, 1999). Those assumptions indicate that plume models cannot be straightforwardly applied under conditions of complex terrain (including

extremely smooth or rough surface), calm (i.e., low wind speeds), spatially heterogeneous meteorology, and obstacle wake effects without modifications (De Visscher, 2013). Although Gaussian plume models were usually used to model the dispersion of chemical inert species, some plume models such as ADMS-Urban and AERMOD were developed with the capabilities of mathematically treating physical and rapid chemical reactions under steady conditions recently, for instance, using the updated Ambient Ratio Method (ARM2) of hourly NO/NO_2 ratio averages, the Ozone Limiting Method OLM (Cole and Summerhays, 1979), a modified version of PVMRM (PVMRM2), and an explicit NO_x chemistry method (ADMS) (Stocker et al., 2012, Cimorelli et al., 2005).

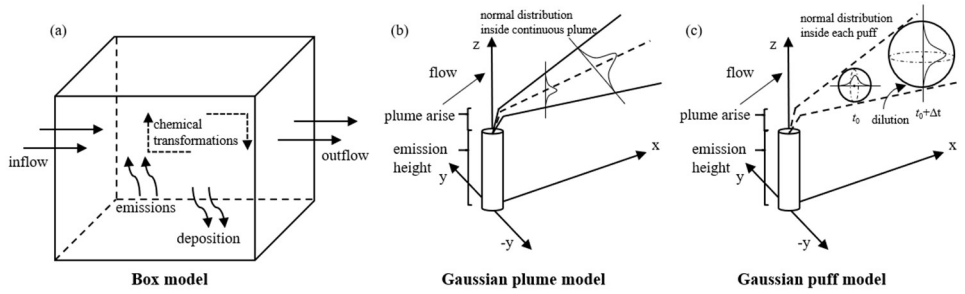


Figure 1.7 Schematic diagram of a typical box model, Gaussian plume model, and Gaussian puff model (adopted from Leelőssy et al. (2014)).

Gaussian puff models (Figure 1.7c) take concepts from both Gaussian and Lagrangian dispersion models, regarding the trajectory of a multitude of puffs with normal distribution in a stochastic random-walk pattern (Leelőssy et al., 2014). As a puff expands in volume, a splitting algorithm may be used to divide

the puff into several pieces. In contrast to plume models, puff models are more appropriate for modelling scenarios with complex trajectories (e.g., non-straight-line emissions), intricate terrain, and calm or recirculated wind flow fields. However, puff models (equation (1.25)) incur much greater computational expense than Gaussian plume models (equation (1.26), with reflection):

$$C(x,y,z) = \frac{Q}{(2\pi)^{3/2}\sigma_x\sigma_y\sigma_z} exp(-\frac{1}{2}(\frac{y-y_0}{\sigma_y})^2)\, exp(-\frac{1}{2}(\frac{x-x_0}{\sigma_x})^2)[exp(-\frac{1}{2}(\frac{z-z_0}{\sigma_z^2})^2) + exp(-\frac{1}{2}(\frac{z+z_0}{\sigma_z^2})^2)] \quad (1.25)$$

$$C(x,y,z) = \frac{Q}{2\pi u\sigma_y\sigma_z} exp(-\frac{y^2}{2\sigma_y^2})[exp(-\frac{(z-H)^2}{2\sigma_z^2}) + exp(-\frac{(z+H)^2}{2\sigma_z^2})] \quad (1.26)$$

where Q is point emission rates, u is the average wind speeds, σ is trajectory/horizontal/vertical dispersion coefficient, x,y,z represent the coordinate of a receptor, x_0,y_0,z_0 represent the previous location of a puff, and H is effective stack height (i.e., emission height plus plume arise). Some Gaussian puff models accommodate chemical reactions following time-stepping algorithms based on Gaussian weighted puff-average concentrations (Chowdhury et al., 2015), thus the air volume by means of chemistry could be divided into three parts: the in-puff volume, the overlapped volume between puffs, and the volume of puffs in contact with the background. The puff injection time affects chemical processes, that is, a reasonable time step of puff emissions enables overlapping and inter-reaction for each puff within one to a few time steps (Korsakissok and Mallet, 2010).

(5) CFD

Computational Fluid Dynamics (CFD) is a powerful technique utilising flexible grids to address dispersion properties of pollutant crossing obstacles or complex urban terrain, and CFD-based models can be divided into Direct Numerical Simulation (DNS), Large Eddy Simulation (LES), and Reynolds Averaged Navier-Stokes (RANS). DNS resolves the whole spatial and temporal scales of motions in the computational mesh. LES models distinguish eddies at coarse and fine scales using spatial filters, then the model simulates eddies at the coarse-scale directly and treats eddies at the fine-scale by using sub-grid scale (SGS) turbulence models (i.e., the Smagorinsky SGS model, dynamic Smagorinsky model, or one-equation SGS model). RANS-based models use approximate time-averaged solutions to model the property of flow turbulence motions. RANS models generally include options to implement one or all of the standard k–ε model (k representing the turbulence energy, and ε representing the dissipation rate), the renormalised-group (RNG) k–ε model, the realisable k–ε model, or a Reynolds stress model (RSM). In contrast to RANS, DNS and LES capture time-varying behaviour, but, because of high computational demands, they have mainly served as a benchmark, replacing experiments in research studies (Versteeg and Malalasekera, 1995, Salim et al., 2011, Cheng et al., 2003).

With the continuous rapid growth in computer hardware, CFD-based models have been extensively used to simulate air pollution in street canyons and industrial areas for research purposes and sometimes for air quality assessment purposes. The most popular CFD codes — including ENVI-met, FLUENT, OpenFOAM, PHOENICS, and STAR-CD — have been employed

frequently in modelling traffic emissions on the street-scale (Nikolova et al., 2011, Di Sabatino et al., 2008, XieHuang and Wang, 2005, Gidhagen et al., 2004). More detailed descriptions of those codes can be found in Xia and Sun (2002). Recent reviews (Lateb et al., 2016, Abhijith et al., 2017) summarised the advantages and limitations of CFD models, and they overviewed a series of studies that attempted to simulate the dispersion of pollutants in open roads or street canyons with green obstacles or green walls. Many previous studies demonstrated that CFD models are suitable for tracking physical and chemical processes of air pollutants on the local scale (BakerWalker and Cai, 2004, BaikKang and Kim, 2007, BrightBloss and Cai, 2013, ZhongCai and Bloss, 2015).

1.3.3 Uncertainty and modelling quality assurance

Air quality model uncertainties refer to the deviations between model predictions and atmospheric observations. These uncertainties can arise from various sources, including inaccuracies in emissions inventories, limitations in the spatial and temporal resolutions of models, simplifications of chemical and physical processes, and uncertainties in meteorological inputs. Generally, those uncertainties can be classified into epistemic uncertainty (i.e., structural uncertainty, parameter uncertainty) and aleatory uncertainty (Knight, 1921). Structural uncertainty refers to incomplete process representations such as mathematical descriptions and chemical schemes; parameter uncertainty is related to uncertain parameters which are adopted for better model adequacy (e.g., deposition velocity, reaction rate coefficient). Aleatory uncertainty

appears randomly and can hardly be reduced, and relates, generally, to uncertain (and sometimes unknowable) inputs and boundary conditions. Specifically, we may further group model uncertainties into:

(1) Incomplete process representations: It has been observed that air quality models sometimes have structural inadequacies, such as simplified chemistry in air quality models or processes controlling diffuse pollution. Criticisms arise when models rely on outdated computational constraints.

(2) Incomplete model parameters: In air quality models, such as the Community Multiscale Air Quality (CMAQ) model, parameter uncertainty is a significant concern when simulating the complex chemical and physical processes that govern the transport and transformation of air pollutants. These models rely on various input data, including meteorological conditions, emissions inventories, and chemical reaction rates, to estimate the concentrations of air pollutants, such as ozone, particulate matter, and nitrogen dioxide. However, due to the simplifications in process representation, and spatial and temporal variability of pollutant sources and environmental conditions, model parameters may not accurately capture real-world conditions. As a result, calibrating and validating air quality models can be challenging.

(3) Uncertain inputs and boundary conditions: Uncertainty arises when transferring information across scales and places. Scale-dependent

parameterizations of inputs and boundary conditions can be a significant source of uncertainty in modelling frameworks, such as atmospheric mesoscale modelling.

(4) Missing factors: The most significant missing factors are the "unknown unknowns" that cannot be anticipated in model uncertainty studies. Ensuring that research programs are agile enough to handle unexpected discoveries is essential for model development in environmental decision making.

Quality assurance in air quality modelling is crucial for guaranteeing the precision, dependability, and trustworthiness of model forecasts. This procedure encompasses a methodical evaluation of model inputs, processes, and outputs. The scientific community employs various steps and methodologies to attain quality assurance in air quality modelling. These measures are integral for safeguarding the model predictions' accuracy and dependability, which serve as the cornerstone for decision-making in the management of air pollution and policy formulation. The processes for modelling quality insurance include:

(1) Sensitivity Analysis: This technique investigates the impact of variations in model inputs or parameters on its output, thereby pinpointing key sources of uncertainty. It offers valuable insights into which components of the model have the greatest influence on the outcome, fostering a better understanding of the system under study.

(2) Model Evaluation: This process involves scrutinizing a model's performance through the comparison of its predictions with independent observations or empirical data. The intent is to identify potential areas for model refinement and decrease uncertainties. Various statistical metrics, including Root Mean Square Deviation (RMSE) and Index of Agreement (IOA) (Chang and Hanna, 2004), can be employed for this purpose and will be elaborated upon in Chapter 4.

(3) Ensemble Modelling: This approach leverages multiple models or model configurations to capture a system's behaviour, aiding in the accounting for uncertainties related to model structure. By considering a range of models, ensemble modelling yields more robust and reliable predictions, capturing a broader spectrum of potential outcomes (Vautard et al., 2009).

(4) Data Assimilation: This method involves the incorporation of observational data into a model with the aim of enhancing model predictions and mitigating uncertainties. By updating model states or parameters in accordance with observed data, data assimilation could lead to more accurate and realistic model forecasts (Carrassi et al., 2018).

1.4 Research motivation and thesis structure

As articulated within the body of this thesis, each chapter has been guided by distinct research motivations. These driving forces have shaped the direction and scope of the investigations and are meticulously delineated within their

respective chapters. However, for the purpose of consolidating the overarching themes of this study, the central research questions, which form the backbone of this thesis, are concisely enumerated as follows:

(1) How does the multi-box photochemical model enhance the simulation of spatial concentration gradients of reactive pollutants within urban street canyons, and in what ways is it superior to traditional one- or two-box models?

(2) What role does shade, influenced by both canyon geometry and solar zenith angle, play in the dispersion and distribution of air pollutants such as nitrogen dioxide (NO_2), ozone (O_3), and their sum (O_x) within the confines of urban street canyons?

(3) Given the introduction of volatile organic compounds (VOCs) and free-radical chemistry into the modelling processes, how is compliance with air quality standards affected, particularly in the context of deep canyons and under conditions of low wind speeds?

(4) How does the prevailing wind velocity modulate the mixing-ratios of NO_2 within street canyons, and how do these effects intertwine with canyon geometry and the intricacies of the chemistry-transport processes?

(5) To what degree of precision can the multi-box model simulate reactive pollutants in regular and in extremely deep urban canyons, and how well do these simulation results correspond with observed data?

(6) How do the outcomes of this research influence urban planning and policymaking, particularly in terms of designing effective air quality control measures that account for the multifaceted influences of street canyon geometry, emissions, shading effects, and photochemical reactions?

The objective of this PhD thesis includes:

(1) Develop a novel multi-box framework to capture the spatial and temporal distribution of reactive species within urban street canyons based on coupled chemical-transport processes. The framework is expected to offer more precise results than traditional zero- and one-dimensional box model but with significant less computational resources than CFD approaches.

(2) Investigate the impact of several factors (such as shading effects, VOC chemistry, and traffic emissions) on the spatial distribution of reactive species within urban canyons with different geometrics. This would enhance our current understanding of air pollutant behaviour in urban environments and assess the implications for regulatory air quality modelling and compliance.

(3) Apply the operational multi-box modelling framework to real deep canyons, evaluate the model performance against observed data, and offer insights for its integration with regional-scale air quality models.

The thesis comprises the following chapters: **Chapter 2** presents a novel multi-box model (MBM-FleX) that captures spatial information on reactive

species within urban street canyons based on coupled chemical-transport processes. In this chapter, the model proves to be a significant step forward from the simple one- and two-box models, providing practical utility for air quality assessment or pollution mitigation management. **Chapter 3** investigates shading effects on NO_2, O_3, and O_x (NO_2 + O_3) within urban street canyons using the MBM-FleX model. The significance of shading effects on the average magnitude and spatial distribution of air pollution within street canyons has been discussed. **Chapter 4** examines the complex chemical-transport processes of NO_2 in street canyons using a multi-box framework with VOC chemistry. In this chapter, the importance of detailed VOC chemistry in modelling air quality and regulatory compliance, particularly in regular and deep canyons, is demonstrated. The study also highlights the potential for chemistry-transport modelling to identify efficient and effective regulatory pathways. **Chapter 5** encompasses a study employing the MBM-FleX framework to simulate the behaviour of reactive pollutants in an extreme deep urban canyon with aspect ratio of 3.7 in Naples, Italy. This work provides implications for practical air quality control and pollution mitigation strategies. **Chapter 6** presents general conclusions and suggestions for future research.

CHAPTER 2 COMPARING OFFLINE MULTI-BOX MODELS WITH LARGE-EDDY SIMULATION

Author Statement

This chapter includes work that was previously published. The details of the publication are as follows:

Dai, Y., Cai, X., Zhong, J. and MacKenzie, A.R., 2021. Modelling chemistry and transport in urban street canyons: Comparing offline multi-box models with large-eddy simulation. Atmospheric Environment, 264, p.118709.

The contributions of the authors are as follows:

Yuqing Dai (the author of this thesis) was responsible for the conceptualization, methodology, coding, data curation, and the original draft preparation. **Rob Mackenzie**, **Xiaoming Cai**, and **Jian Zhong** contributed to reviewing, editing the draft, and supervisory. Additional acknowledgements are presented in Section 2.6 of this chapter.

Abstract

Computational fluid dynamics models are resource-intensive, particularly when complex chemical schemes are implemented, and this computational expense limits their use in sensitivity analyses. We propose a flexible multi-box model that permits spatial disaggregation of sources and depositions to simulate the transportation and distribution of chemical species in street canyons with any aspect ratios for which a large eddy simulation (LES) of the

flow exists. The spatial patterns of reactive species in the multi-box simulations are in good agreement with those from the LES, especially for the deep canyon from which air escapes more slowly. The overestimation of the LES simulation worsens somewhat due to segregations when the chemistry of volatile organic compounds (VOCs) is included but the overall pattern is captured in a modelling framework. By reducing computational costs by several orders of magnitude, the multi-box model allows more sensitivity testing than the LES and is an effective approach to investigate spatial pattern of fast non-linear chemistry or microphysics at the street scale.

***Keywords**:* Air quality; Urban air pollution; Box models; Street canyon; Nitrogen dioxide; Ozone

2.1 Introduction

Street canyons typically combine to build up a semi-enclosed urban environment with high concentrations of anthropogenic pollutants trapped inside, leading to persistent higher exposure risk for pedestrians near the roadside (Oke, 1988, AhmadKhare and Chaudhry, 2005, Vardoulakis et al., 2003). Canyons can be divided into three types in terms of the ratio of building height (H) to street width (W), namely aspect ratio (AR): wide canyons (AR < 0.3), regular canyons (AR ≈ 1), and deep canyons (AR > 1.3) (Vardoulakis et al., 2003). Oke (1988) classified the canyon flows into three isothermal regimes according to AR and L/W (L is the building length along the span-wise direction). These regimes include skimming flow (0.66 < AR < 1.57), wake interference flow (0.1 < AR < 0.66) and isolated roughness flow (AR < 0.1). Besides the isolated roughness flow, wake interference flow, and skimming flow, there is the fourth flow regimes, i.e., multi-vortex flow regime in deep street canyons. If Reynolds (Re) number independence is satisfied, there is only one-vortex when AR is 1 and 3, but two main vortices appear when AR is 5 or more (Yang et al., 2020). However, in wind-tunnel-scale street canyons (H = 6 cm, Re~1.2×10^4), if Re number is not sufficiently large, there are two contra-rotative vortices when AR = 2 and three to five vertically aligned vortices when AR is 3-5 (Li et al., 2008). The main difference between these two groups is whether the requirement of Re-number independence is satisfied or not. ChewAliabadi and Norford (2018b) proposed that the widely adopted criterion Re > 11000 for ensuring Reynolds-number-independence

(Re-independence) is not applicable for 2D street canyons as AR > 1.5. They discovered that only one primary vortex appeared when AR = 2 if Re > 8.7×10^4. Moreover, Yang et al. (2021b) found that isothermal urban airflows for full-scale deep canyons can be independent of Re when Re exceeds 1×10^6 and 1×10^7 when AR is 3 and 5.

Because of much of the human exposure to outdoor air pollutants occurs at the pedestrian level in street canyons, understanding airflow characteristics and distributions of pollutants is of vital importance in evaluating the pollutant health risk and in making policy for targeted air pollution alleviation. The concentration of a passive scalar (PS, an idealised chemically inert substance that negligibly interferes with local fluid dynamics through effects such as buoyancy) can exhibit sharp gradients at the pedestrian level of the street canyons (Murena et al., 2009, Lietzke and Vogt, 2013, FelliniRidolfi and Salizzoni, 2020). Furthermore, the dispersion of atmospheric pollutants within the canyon is accompanied by complex non-linear chemical reactions, evolving on the timescale comparable to the canyon circulation and residence timescale. During the past two decades, studies have focused on the investigation of time-evolution and spatial variations of reactive species, for example, nitric oxide (NO), nitrogen dioxide (NO_2), and ozone (O_3) in street canyons, using coupled computational fluid dynamics (CFD) such as Reynolds-Averaged Navier-Stokes (RANS) and Large-Eddy Simulation (LES) models with different chemical schemes. BakerWalker and Cai (2004) integrated an LES model with a simple NO_x-O_3 cycle (two reactions in sunlight) to simulate the dispersion and spatial distribution of reactive species in a regular street canyon. The

impacts of dynamics on the chemistry had been investigated by introducing the concept of the photo-stationary state defect (PSSD). Low PSSD values indicate equilibrium-like chemistry and were found at the centre of the primary vortex and on the windward corner at the street level. High PSSD values indicate rapidly-changing chemistry and were found at the location near NO_x sources, along the leeward facet (where pollutants were escaping the street canyon), and along the windward wall on the outer edge of the vortex (where fresh air was entrained into the canyon). BaikKang and Kim (2007) adopted the renormalised k-ε RANS model coupled with the simple NO_x-O_3 photochemistry to simulate pollutant dispersion with the effects of street-bottom heating; Kwak and Baik (2012) further incorporated Volatile organic compounds (VOC) chemistry into the model and discussed the sensitivity of O_3 concentrations to NO_x and VOC emissions. KimPark and Kim (2012) examined reactive species in a regular canyon using RANS with a comprehensive tropospheric NO_x-O_3-VOC chemistry from GEOS-Chem. They found a substantial influence of different chemical schemes on O_3 levels and highlight the importance of more explicit chemistry simulation. However, BrightBloss and Cai (2013) found that VOCs could contribute additional but modest NO_2 and O_3 formation (about 12%) in the regular canyon, which is consistent with Garmory et al. (2009). ZhongCai and Bloss (2017) extended the LES model with the NO_x-O_3-VOC chemistry to simulate the spatial distribution of reactive species in an idealised deep urban street canyon. They revealed that volume-averaged NO_2 and the total oxidants (O_x) concentrations significantly increased due to VOCs-relating chemistry. Their works provided a better

understanding of the combined effects of insufficient mixing and non-linear reactions in street canyons with a higher aspect ratio. Zhang et al. (2020) conducted RANS simulations with a simple NO_x-O_3 cycle in street canyons with AR = 1, 3 and 5, but their work neglected the effect of organic free radicals, which is likely important in determining the concentration of reactive species inside deep street canyons. Recently, Wu et al. (2021) developed a platform that integrated a CFD model (i.e., OpenFOAM) and a photochemical mechanism including VOCs for pollutant dispersion in the regular canyon. Although these CFD-based studies provide promising methods in order to simulate physical dispersion and chemical transformation of reactive species within canyons, modelling scenarios in reality are much more sophisticated in terms of, for example, emissions (Wu et al., 2021), wind conditions, roof shapes (Takano and Moonen, 2013), ground or wall heating (Cai, 2012b), and the presence of green infrastructures such as trees with varying leaf area density (Gromke et al., 2008, Gromke and Ruck, 2007, Abhijith et al., 2017). The domain/model configurations need to be adjusted from case to case, and using a CFD model is, in general, very computationally expensive for the study of such a wide range of scenarios, especially when explicit VOC chemical reactions are included.

A more convenient and efficient way is adopting offline simulations, as is routinely employed at regional and global scales (e.g., Jacobson and Jacobson (2005); Kukkonen et al. (2012)). The zero-dimensional one-box model can easily adopt complex chemistry without intensive computational resources. It also exhibited satisfactory performance compared to the LES (BrightBloss and

Cai, 2013), despite relatively higher modelled NO, NO_2 and hydroxyl radical (OH) concentrations. ZhongCai and Bloss (2016b) implemented a coupled two-box model with NO_x-O_3-VOC chemistry for simulating pollutants in a deep canyon. They highlight that the one-box treatment would miscalculate flow structure and pollutant gradients, and, hence, underestimate the exposure risk of pedestrians to NO_2 in the deep canyon. However, these simplified box models are still too coarse to evaluate air quality conditions at the pedestrian level. They would systematically neglect substantial concentration contrasts near the centre of the carriageway and cannot capture the horizontal distribution of pollutants, which is as important as vertical features in street canyons. The lack of available process-based methods makes it difficult to investigate systematically coupled chemistry-transport effects in street canyons.

In this study, a multi-box model with a flexible number of boxes and flexible chemical schemes has been developed for air pollution simulations in street canyons. The model design, mathematical formulation, and configurations for testing are described in Section 2.2. In Section 2.3, the modelling results of reactive species from the multi-box models with a reduced NO_x-O_3-VOC chemistry and a simple NO_x-O_3 cycle are evaluated against the published modelling data from the LES dynamical models at the box grid resolution, for idealised regular and deep street canyons. The time-evolution of concentrations, segregation effects due to overly fast chemistry in the multi-box case, and spatial variations inside canyons are discussed in detail. The conclusions and future perspective are summarised in Section 2.4.

Although not the focus of the current paper, we note that aerosol microphysics introduces non-linear processes in street canyons in a similar way to chemistry (Gelbard and Seinfeld, 1980, JacobsonTabazadeh and Turco, 1996, Jacobson and Seinfeld, 2004, Zhong et al., 2020a, Zhong et al., 2020b, Zhong et al., 2018); the modelling framework described below could be extended to include detailed size-dependent aerosol microphysics in the future.

2.2 Methods

2.2.1 Description of models

(1) The multi-box models

The principle of the multi-box model is to split the volume of street canyons into several boxes, where each box ideally reflects a resolved airflow arising from the aspect ratio or physical obstructions in street canyons (e.g., Figure 2.1). In the two-dimensional framework, assuming the background wind above the roof level blows across the street canyon from left to right, boxes inside the model are indexed based on their locations in Cartesian coordinates, starting from the bottom-left to the top-right, e.g., $\mathrm{Box}_{[1,1]}$ represents the leeward corner of a canyon. Pollutant transfer between adjacent boxes is determined by the mean wind advection and by turbulent diffusion across the mesh interface. Vertical (denoted by capital "*G*") and horizontal (denoted by capital "*F*") mixing-ratio fluxes (ppb m s^{-1}) for pollutant, q, into $\mathrm{Box}_{[k,i]}$ (i.e., "k" represents vertical index position, "i" represents horizontal index position) can be formulated as:

$$F_{e,[k,i]} = u_{e,[k,i]}\left(C_{q,[k,i-1]} - C_{q,[k,i]}\right) \quad (2.1)$$

$$F_{a,[k,i]} = \begin{cases} U_{a,[k,i]} C_{q,[k,i-1]}, U_{a,[k,i]} \geq 0 \\ U_{a,[k,i]} C_{q,[k,i]}, U_{a,[k,i]} < 0 \end{cases} \quad (2.2)$$

$$G_{e,[k,i]} = w_{e,[k,i]} \left(C_{q,[k-1,i]} - C_{q,[k,i]} \right) \quad (2.3)$$

$$G_{a,[k,i]} = \begin{cases} W_{a,[k,i]} C_{q,[k-1,i]}, W_{a,[k,i]} \geq 0 \\ W_{a,[k,i]} C_{q,[k,i]}, W_{a,[k,i]} < 0 \end{cases} \quad (2.4)$$

where $G_{a,[k,i]}$ (ppb m s^{-1}) and $F_{a,[k,i]}$ (ppb m s^{-1}) are mixing-ratio fractional fluxes due to advective transfer (i.e., flow resolved by the LES); $G_{e,[k,i]}$ (ppb m s^{-1}) and $F_{e,[k,i]}$ (ppb m s^{-1}) are mixing-ratio fluxes due to turbulent diffusion formulated by the Fick's law. $W_{a,[k+1,i]}$ (m s^{-1}) and $U_{a,[k,i+1]}$ (m s^{-1}) are the advective transfer velocities in the vertical and horizontal directions, respectively; and $w_{e,[k+1,i]}$ (m s^{-1}) and $u_{e,[k,i+1]}$ (m s^{-1}) are transfer velocities due to turbulent diffusion. By assuming all fluxes as vectors with positive values along the coordinate directions, the concentration in Box$_{[k,i]}$ can be calculated from the following equation:

$$\frac{dC_{q,[k,i]}}{dt} = E_{q,[k,i]} - \frac{G_{a,[k,i+1]} + G_{e,[k,i+1]}}{l_i} + \frac{G_{a,[k,i]} + G_{e,[k,i]}}{l_i} - \frac{F_{a,[k+1,i]} + F_{e,[k+1,i]}}{h_k} + \frac{F_{a,[k,i]} + F_{e,[k,i]}}{h_k} + \Delta S_{q,[k,i]} + \Delta V_{q,[k,i]} \quad (2.5)$$

where $C_{q,[k,i]}$ (ppb) is the mixing-ratio of the q^{th} species in Box$_{[k,i]}$, $E_{q,[k,i]}$ (ppb s^{-1}) is the emission rate of the q^{th} species into Box$_{[k,i]}$, h_k (m) and l_i (m) are the box height and box width respectively, $\Delta S_{q,[k,i]}$ (ppb s^{-1}) is the net production rate of the q^{th} species due to chemistry in Box$_{[k,i]}$, and $\Delta V_{q,[k,i]}$ (ppb s^{-1}) is the net deposition term of the q^{th} species in Box$_{[k,i]}$. Allowing computations with more species, and where the associated $\Delta S_{q,[k,i]}$ terms reflect more complicated non-linear chemistry, is one of the prime motivations for the development of

the box model. By default, the boundary layer above the street canyon is assumed as one compartment, representing relatively steady background conditions over a long period (e.g., 1 hour). The 4th order Runge-Kutta method is adopted in the multi-box model to solve the ordinary differential equations (ODEs) numerically. To facilitate a systematic investigation, we use two dimensionless ratios to represent the size of grid boxes to the entire street canyon:

$$\alpha_k = \frac{h_k}{h_0} \tag{2.6}$$

$$\beta_i = \frac{l_i}{l_0} \tag{2.7}$$

where h_0 (m) and l_0 (m) are the canyon height and street width, respectively. Then the volume-averaged concentrations of q^{th} species ($C_{q,\text{m×n-box}}$) for the entire canyon with m × n boxes is:

$$C_{q,m\times\text{n-box}} = \sum_{k=1;i=1}^{\text{k=m;i=n}} \alpha_k \beta_i C_{q,[\text{k,i}]} \tag{2.8}$$

If the volume is equal for all the boxes in street canyons, that is, i.e., $\alpha_1 = \alpha_2 = \ldots = \alpha_k = \frac{1}{m}$ and $\beta_1 = \beta_2 = \ldots = \beta_i = \frac{1}{n}$, then the equation (2.8) can be rewritten to:

$$C_{q,m\times\text{n-box}} = \frac{\sum_{k=1;i=1}^{\text{k=m;i=n}} C_{q,[\text{k,i}]}}{m\times n} \tag{2.9}$$

Additionally, a dimensionless factor $\gamma_{q,[\text{k,i}]}$ is adopted to account for the heterogeneous on-road emission of the q^{th} species:

$$\gamma_{q,[\text{k,i}]} = \frac{\alpha_k \beta_i E_{q,[k,i]}}{\sum_{k=1;i=1}^{\text{k=m;i=n}} \alpha_k \beta_i E_{q,[\text{k,i}]}} \tag{2.10}$$

Up to n continuous line sources could be added into the k^{th} (k = 1, 2, …, m) layer of the canyon, which is helpful for elevated road or rail sources and for biogenic emissions from street trees. $\gamma_{q,[k,i]}$ = 0 or $\gamma_{q,[k,i]}$ = 1 indicates that no emission or all vehicle emissions have been injected into $Box_{[k,j]}$.

In order to derive net chemical terms especially for short-lived reactive species such as hydroxyl radical (OH) and hydroperoxyl radical (HO_2), the ODEs of a chemical system for q^{th} species can be written as:

$$\frac{d}{dt} C_{q,[k,i]} = P_{q,[k,i]} - L_{q,[k,i]} C_{q,[k,i]} \tag{2.11}$$

where $P_{q,[k,i]}$ and $L_{q,[k,i]}$ are the chemical production and loss rates in the specific $Box_{[k,i]}$. If that chemical kinetics remain constant during a given timestep, Δt, equation (2.11) may be solved numerically with the quasi-steady-state approximation (QSSA):

$$C_{q,[k,i],t_0+\Delta t} = \frac{P_{q,[k,i],t_0}}{L_{q,[k,i],t_0}} + \left(C_{q,[k,i],t_0} - \frac{P_{q,[k,i],t_0}}{L_{q,[k,i],t_0}} \right) e^{-L_{q,[k,i],t_0} \Delta t} \tag{2.12}$$

where t_0 represents the starting point of each time interval during simulations. The chemical lifetime of q^{th} species, $\tau_{q,[k,i]}$, in the $Box_{[k,i]}$ is:

$$\tau_{q,[k,i]} = \frac{1}{L_{q,[k,i]}} \tag{2.13}$$

If $\tau_{q,[k,i]} < 0.1\Delta t$, chemical reactions are extremely fast compared to Δt, which means the chemical-steady-state can be adopted:

$$C_{q,[k,i],t_0+\Delta t} = \frac{P_{q,[k,i],t_0}}{L_{q,[k,i],t_0}} \tag{2.14}$$

If $\tau_{q,[k,i]} > 100\Delta t$, chemical reactions take through much slower compared to Δt, and the forward Eulerian formula can be used:

$$C_{q,[k,i],t_0+\Delta t} = C_{q,[k,i],t_0} + \left(P_{q,[k,i],t_0} - L_{q,[k,i],t_0} C_{q,[k,i],t_0}\right)\Delta t \quad (2.15)$$

If $0.1\Delta t < \tau_{q,[k,i]} < 100\Delta t$, then the chemical timescale has a comparable magnitude with Δt, and equation (2.12) is employed for the calculation. However, solving equation (2.12) incurs substantial computational costs in practice. Alexandrov et al. (1997) proposed an alternative way for the optimisation of the QSSA algorithm, which rationally expands the exponential term based on the Taylor expansion in the second order:

$$e^{-L_{q,[k,i],t_0}\Delta t} \approx \frac{1}{1+L_{q,[k,i],t_0}\Delta t+0.5(L_{q,[k,i],t_0}\Delta t)^2} \quad (2.16)$$

and the equation (2.12) can be reformatted as:

$$C_{q,[k,i],t_0+\Delta t} = \frac{C_{q,[k,i],t_0}+\left(1+0.5L_{q,[k,i],t_0}\Delta t\right)P_{q,[k,i],t_0}\Delta t}{1+L_{q,[k,i],t_0}\Delta t+0.5(L_{q,[k,i],t_0}\Delta t)^2} \quad (2.17)$$

In the one- and multi-box models, reactive species have been divided into two categories in terms of their chemical lifetime. For the regular and deep canyons, an empirical timestep value of 0.03 s was used with the equation (2.15) for numerical integration of long-lived species (e.g., NO, NO_2, O_3), and a value of 0.003 s with the equation (2.17) was used for short-lived species (e.g., HO, HO_2). They are the same as those used in the LES (ZhongCai and Bloss, 2015, BrightBloss and Cai, 2013) based on the timescale of the turbulent eddies, which also indicates that no species are fully in steady state in urban street canyon environment.

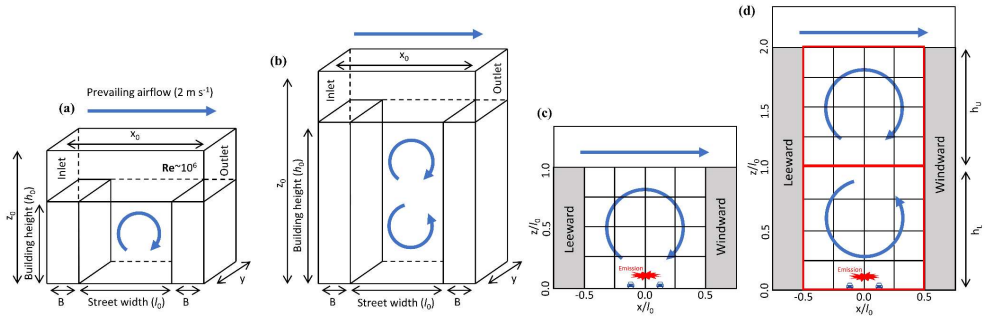


Figure 2.1. Schematic diagram of (a) the LES domain for a regular urban street canyon where x_0 = 24 m, y_0 = 40 m and z_0 = 90 m, and canyon geometries l_0 = h_0 = 18 m, wall width B = 3 m, modified from BrightBloss and Cai (2013); (b) the LES domain for a deep canyon x_0 = 36 m, y_0 = 40 m and z_0 = 112 m, and canyon geometries l_0 = 18 m, h_0 = 36 m and B = 9 m, modified from ZhongCai and Bloss (2015); (c) the equivalent multi-box (16) model for the regular canyon; (d) the two-box model denoted by the red frame, where the height of upper (h_U) and lower compartments (h_L) is 9 m, and the multi-box (32) model for the deep canyon. See text for details.

The multi-box model is written in R version 3.6.2 (R Core Team, 2019) and Fortran 90 (using the Intel Fortran (IVF) Compiler) in the origin version 1.0, including three modules: the main program, the dynamical submodule, and a chemical submodule. Modularisation allows the model to be easily modified or updated for various research purposes, e.g., to investigate the impact of different chemical mechanisms on air quality in street canyons or to investigate in-canyon particle microphysics (c.f., Nikolova et al. (2016)).

(2) The one- and two-box models

Additionally, a typical one-box model is used as a reference in this study, and the mathematical expression is (Liu and Leung, 2008):

$$\frac{dC_{q,0}}{dt} = E_{q,0} - \frac{w_{t,0}}{h_0}\left(C_{q,0} - C_{q,b}\right) + \Delta S_{q,0} + \Delta V_{q,0} \quad (2.18)$$

where a subscript "0" indicates that signs have the same meaning as those in the multi-box model but for a whole space of the street canyon in volume. The parameter $w_{e,0}$ (m s^{-1}) represents the "exchange velocity" between the street canyon and boundary layer above the rooftop. A two-box model is also used only for simulations in the deep street canyon, the mathematical expressions are (Murena, 2012, ZhongCai and Bloss, 2016b):

$$\frac{dC_{q,L}}{dt} = E_{q,L} - \frac{w_{t,L}}{h_L}\left(C_{q,L} - C_{q,U}\right) + \Delta S_{q,L} + \Delta V_{q,L} \quad (2.19)$$

$$\frac{dC_{q,U}}{dt} = \frac{w_{t,L}}{h_U}\left(C_{q,L} - C_{q,U}\right) - \frac{w_{t,U}}{h_U}\left(C_{q,U} - C_{q,b}\right) + \Delta S_{q,U} + \Delta V_{q,U} \quad (2.20)$$

where subscripts "L" and "U" indicate that signs have the same meaning as aforementioned but for the lower and upper compartments (i.e., including 16 boxes in the red box to solve the main vortices) of the deep street canyon in volume, respectively. $w_{e,\mathrm{L}}$ (m s^{-1}) represents the "exchange velocity" between two in-canyon compartments, and $w_{e,\mathrm{U}}$ (m s^{-1}) represents the "exchange velocity" between the upper compartment and the overlying background.

(3) Large-eddy simulation

The LES results of reactive species were taken from BrightBloss and Cai (2013) for an idealised regular canyon, and from ZhongCai and Bloss (2017) for a deep canyon. Their studies applied OpenFoam *v*2.1.1 (JasakJemcov and Tukovic, 2007) to resolve turbulence at large spatial and temporal scales and to simulate incompressible airflow with a high Reynolds number (Re ~1×10^6) in street canyons under the neutral atmosphere. The unresolved sub-grid scales

(SGS) processes were treated using the one-equation SGS turbulence model, and the logarithmic law of the rough-wall (Schlichting and Gersten, 2016) was used for the near-wall treatment. Symmetry boundary conditions were used for the domain overlying the canyon, and cyclic boundary conditions were employed in x- and y-directions. A constant pressure gradient in the upper background was assumed to produce a flow perpendicular to the canyon axis. The simulations of the LES were conducted with only dynamics for about 5 hours in order to obtain a dynamical-steady flow field, which was further adopted as the initial turbulence condition.

For the regular canyon, the resolved turbulent kinetic energy (TKE) has been evaluated against wind-tunnel experiments (CuiCai and J. Baker, 2004) and the scalar has been validated by CaiBarlow and Belcher (2008); for the deep canyon, the flow field agreed well with water-channel (Li et al., 2008) and wind tunnel (Kovar-Panskus et al., 2002) experiments. The deposition of air pollutants is not considered in the LES modelling. The method for integrating VOC chemistry in the LES modelling is similar to that of the multi-box simulations described above and has been detailed in ZhongCai and Bloss (2017). The methods for initialising and processing the LES (e.g., emission, time step) are also adopted directly for the multi-box model and are described in the following section.

2.2.2 Model configurations

(1) Street canyon geometry

The LES domains adopted for regular (AR = 1) and deep (AR = 2) canyons were presented in Figure 2.1(a) and Figure 2.1(b), respectively. In the LES, mesh resolutions were 0.3 m, 1.0 m and 0.3 m in the x, y, z directions, respectively, inside street canyons. That is, there are respectively 3,600 and 7,200 cells inside regular and deep canyons in the LES simulations. For the layer above the canyon in the LES simulation, Δz gradually increased by a factor of 1.15 from the rooftop to the domain top (z_0 = 18-90 m and z_0 = 36-112 m for regular and deep canyons). Figure 2.1(c) and Figure 2.1(d) are the respective counterparts in multi-box models for the cross-section canyons. The building height and street width are 18 m ($h_0 = l_0$) for the regular street canyon and are 36 and 18 m ($h_0 = 2l_0$) for the deep street canyon. The red frame in Figure 2.1(d) presents a two-box model with $h_L = h_U$ = 18 m. One primary clockwise vortex form in the simulations of the regular canyon as the background skimming wind perpendicularly blows along the x-direction across the canyon axis; however, in the deep street canyon, a clockwise vortex in the upper compartment and a weak counter-clockwise vortex in the lower compartment are formed. In the multi-box model, the in-canyon volumes have been divided into identical 16 and 32 boxes for the regular and deep canyons, respectively (namely the 16- and 32-box models). This implies that each grid has a volume of 4.5 m × 1 m × 4.5 m = 20.25 m^3.

(2) Dynamical parameters for air mass exchange

The exchange velocity ($w_{e,0}$) for the one-box model, and the advective and turbulent velocities for the multi-box model, are of the utmost importance in

determining the intensity of in-canyon mixing, and transport and rates of escape of atmospheric pollutants to the overlying background. The values of $w_{e,0}$ = 0.022 m s^{-1} and $w_{e,0}$ = 0.012 m s^{-1} are respectively adopted for the cross-section 18 m × 18 m regular and 18 m × 36 m deep canyons (as in Figure 2.1) in the one-box model, corresponding to a reference wind velocity of 2 m s^{-1} in the above rooftop layer under the neutral conditions (Cai, 2012a; Zhong et al., 2017). The values of $w_{e,L}$ = 0.0229 m s^{-1} and $w_{e,U}$ = 0.0156 m s^{-1} are used for the two-box simulation in the deep canyon, respectively.

In order to quantify the transport due to advection ($W_{a,[k,i]}$ and $U_{a,[k,i]}$, denote "advective velocities" in this study) and mixing due to turbulence ($w_{e,[k,i]}$ and $u_{e,[k,i]}$, denote "turbulent velocities") in the multi-box model, firstly vertical mixing-ratio fluxes including advective fluxes and turbulent fluxes of PS at the interface of boxes were extracted from the LES modelling results, and the averaged values over a period of the last 60 minutes were used for calculations. The total horizontal fluxes were then derived based on the flux balance of each grid on the Eulerian coordinates under an assumed equilibrium state over the period. These LES-derived fluxes describe the transmission of PS between any two adjacent boxes in street canyons. However, the velocities from the LES simulations (representing "real" wind conditions) cannot be used directly, because they need to be adjusted to calculate the mass transfer between coarser grids. Therefore, pollutant advective velocities ($U_{a,[k,i]}$ and $W_{a,[k,i]}$) are obtained using the vertical advective fluxes ($F_{a,[k,i]}$ and $G_{a,[k,i]}$) and the grid concentrations (i.e., an volume-averaged value at the grid resolution of the multi-box model)

following the equation (2.2) and equation (2.4), and vertical mixing-ratio turbulent velocities ($w_{e,[k,i]}$ and $u_{e,[k,i]}$) are obtained using vertical turbulent fluxes ($F_{e,[k,i]}$ and $G_{e,[k,i]}$) and concentration gradients based on the equation (2.1) and equation (2.3). In this way, the mass fluxes of the multi-box and LES models are consistent at the same box interface under the equilibrium state. It is noted that the derivation for horizontal fluxes may have uncertainties because emissions from a single line source are simply assumed to be injected into one grid in the multi-box model, whereas a Gaussian distribution over the carriageway was assumed in the LES model. A coarser grid resolution can reduce this type of error. Therefore, in this study, the 16- and 32-box models are used to evaluate reactive species in regular and deep urban street canyons, and the details of advective and turbulent velocities are presented in Appendix A (Table S1 and Table S2). Model performance under higher horizontal resolutions is left to be evaluated in future work.

Due to the very similar magnitude of advective fluxes entering and escaping the street canyon in the neutral atmosphere (SalizzoniSoulhac and Mejean, 2009), the escaping canyon fluxes due to vertical advection are rotated into the horizontal direction, and thus the multi-box model considers only turbulent terms at the rooftop. Turbulent velocities as described above could be negative (although usually of small magnitude in such cases), indicating counter-gradient turbulent diffusion under the box-model framework (Figure 2.1c and Figure 2.1d). This may cause the model to crash during a box model timestep if concentrations become negative. In order to address this issue, a

minimum positive value of 1.0×10^{-4} m s^{-1} is applied to the turbulent velocity, implying a very small turbulent flux compared to the advective flux for the interface under such conditions.

(3) Emissions and chemical mechanism

Traffic-related pollutants were emitted by two consecutive line-sources at 1 m height and at 2.5 m to the left and right of the street centre axis for the LES models. Therefore the emissions were evenly injected into $Box_{[1,2]}$ and $Box_{[1,3]}$ at the street level for the multi-box models ($\gamma_2 = \gamma_3 = 0.5$). The emission rates of NO, NO_2, carbon monoxide (CO), ethene (C_2H_4), propene (C_3H_6), formaldehyde (HCHO) and acetaldehyde (CH_3CHO) were calculated based on the UK Road Vehicle Emission Factors (Boulter et al., 2009), which were 558, 62, 1356, 56, 24, 32 and 15 g km^{-1} hr^{-1}, representing a typical weekday traffic scenario of 1500 vehicles per hour with an average speed of 30 miles per hour (mph), which equate to 900, 100, 3593, 347, 150, 96 and 98 ppb s^{-1} for the LES cell; to 4.0, 0.44, 16, 1.55, 0.67, 0.88 and 0.42 ppb s^{-1} for the 16- (and 32-) box grid; and to 0.252, 0.028, 1.0, 0.097, 0.042, 0.055 and 0.026 ppb s^{-1} for the one-box grid in the regular canyon and for the two-box grid in the deep canyon. Moreover, PS that only undergoes physical processes was injected at the same rate with NO_x (= NO + NO_2) to investigate the sole effect of canyon dynamics on the model performance.

The Reduced Chemical Scheme (RCS) was developed by BrightBloss and Cai (2013), based on the Common Representative Intermediates mechanism version CRI *v2-R5* (Watson et al., 2008). The RCS retains the compounds that

have important effects on core chemical intermediates in urban street canyons and includes 51 gas-phase species and 136 chemical reactions. The chemical kinetics are calculated at 20°C under a standard atmosphere pressure (e.g., photodegradation rate of 9.20×10^{-3} s^{-1} for NO_2), and they are adopted for simulating the daytime chemistry in the present study. The comparison between RCS and the benchmark Master Chemical Mechanism (12691 chemical reactions of 4351 species for MCM*v*3.0) (Saunders et al., 2003) showed that the maximum differences were 3%, 13%, 16%, and 12% for NO, NO_2, O_3 and OH during a four-hour simulation, which was comparable to, or smaller than, the errors from emissions and detection techniques (Boulter et al., 2009, Heard and Pilling, 2003). The total computation time of the multi-box model with RCS is about 6 minutes, which is higher than that of the one-box (~1 s) and two-box models (~8 s), but is significantly faster compared to those of the LES (around 10 days) (ZhongCai and Bloss, 2017).

(4) Model initialisation and output post-processing

The initial concentrations of the multi-box model are consistent with those in LES conditions for two types of canyons, which were taken from the field study of the Tropospheric Organic Chemistry (TORCH) experiment (Lee et al., 2006). These observations represent a typical atmospheric condition in rural London, UK, during the summer of 2003. The models have been operated for 30 min "spin-up" period without any emission in order to initialise the chemical intermediates, then traffic emissions are switched on and concentrations of all species at t = 30 min are used as the cyclic "fixed" background conditions for a

next 210 min modelling duration (i.e., t = 30-240 min) in a time step of 0.03 s. The solar radiation intensity remains constant during the model operation. "*zero background*" for PS is assumed during the LES and box operations.

The concentrations from box models were stored in an interval time step of 1 min for time-evolution analysis. The final hour of the modelling results (i.e., t = 180-240 min) was extracted for the calculation. Details about LES outputs pre-processing can be found in BrightBloss and Cai (2013) (for the regular canyon) and ZhongCai and Bloss (2015) (for the deep canyon), respectively. Subsequently, the modelling results of LES were averaged equivalent to the coarse resolution of box models for the purpose of evaluating the spatial distributions of air pollutants with the multi-box models. In order to investigate the impacts of incomplete mixing on the sub-grid scale variability due to chemistry, a widely-used dimensionless parameter *intensity of segregation* (KrolMolemaker and de Arellano, 2000) is adopted in this study:

$$I_{S(q_1+q_2)} = \frac{\langle q_1^* q_2^* \rangle}{\langle q_1 \rangle \langle q_2 \rangle} \tag{2.21}$$

where $I_{S(q_1+q_2)}$ represents the intensity of segregation between chemical species q_1 and q_2, angle brackets refer to the volume-averaged conservation quality, defined by equation (2.8) for the multi-box model, $<q_1^* q_2^*>$ represents the volume-averaged covariance between q_1 and q_2, and an asterisk means the deviation from the averaged value. So, for a general case, we have $\langle q_1 \rangle = \sum \alpha_k \beta_i C_{q_1,[k,i]}$, $\langle q_2 \rangle = \sum \alpha_k \beta_i C_{q_2,[k,i]}$, $q^*_{1,[k.i]} = C_{q_1,[k,i]} - \langle q_1 \rangle$, $q^*_{2,[k,i]} = C_{q_2,[k,i]} -$

$\langle q_2 \rangle$, and $\langle q_1^* q_2^* \rangle = \frac{1}{16} \sum q_{1,[k,i]}^* q_{2,[k,i]}^*$. The volume-averaged second-order reaction rate ($<k_{(q_1+q_2)}>$) can be written as:

$$\left\langle k_{(q_1+q_2)} \right\rangle = k_{(q_1+q_2)} \left(1 + I_{S(q_1+q_2)}\right) \tag{2.22}$$

where $k_{(q_1+q_2)}$ is the original reaction rate in the sufficiently well-mixed one-box model. Therefore, $I_{S(q_1+q_2)}$ can also be thought of as quantifying the deviation from chemical equilibrium due to the spatial segregation associated with atmospheric dynamics. For any species in the one-box model, $I_{S(q_1+q_2)}$ equals to zero because there is no spatial segregation inside the box. A positive $I_{S(q_1+q_2)}$ indicates that $<k_{(q_1+q_2)}>$ in the 16-box model is larger than $k_{(q_1+q_2)}$ in the one-box model because of the segregation effect. When $q_1 = q_2$, $I_{S(q_1+q_2)}$ represents the spatial variability of any specific pollutant in respect to its canyon volume-averaged concentration.

2.3 Results and Discussion

2.3.1 Temporal evolution and the intensity of segregation within the canyon

Figure 2.2 shows temporal evolution of the volume-averaged pollutant mixing-ratios of the LES, and multi- and one-box models under the same raw emissions, meteorological conditions, and RCS chemistry as the LES model, in idealised regular (a, b) and deep (c, d) street canyons, respectively. Modelling results of the two-box model are available only for the deep canyon. The LES-RCS data for the regular and deep canyons are from BrightBloss and Cai (2013) and ZhongCai and Bloss (2017), respectively. The box models produce

less temporal variability; reactive species slowly move toward a chemical-transport equilibrium. The O_3 concentrations drop sharply after zero-emission "spin-up" period due to NO and O_3 titration, accelerating the formation of NO_2 in street canyons. The OH and HO_2 concentrations rapidly relax to equilibrium when traffic emissions are switched on, the maintenance of a steady-state HO_2 by oxidation of VOCs contributes to an additional NO_2 fraction. The chemical species in the regular canyon achieve a transport-chemistry balance more quickly (i.e., about 90 min for NO and NO_2) than in the deep canyon (e.g., around two hours for NO and NO_2) in both one- and multi-box models, and the LES, because of more effective ventilation for canyons with a lower AR. The concentrations of selected species at the equilibrium state over the final hour of model operation are discussed below for a better understanding of the coupled dynamical and chemical processes in street canyons.

Table 2.1 illustrates the time-averaged mixing-ratios of PS, NO, NO_2, O_3, OH, HO_2, NO_x (= NO + NO_2), O_x (= NO_2 + O_3) and NO_2/NO ratios from the models coupled with the RCS chemistry during the final simulation period ($180 \leq t \leq 240$ min) in the regular and deep street canyons, respectively. For the regular canyon, LES outputs are slightly different from those in BrightBloss and Cai (2013), because of the dynamics-driven variability in concentrations and the difference in averaging times (i.e., $180 \leq t \leq 240$ min in the current study vs. $150 \leq t \leq 210$ min). The modelled mean PS concentrations of box models are in good agreement with those of the LES-based models (differences within ±0.5%). The spatially-averaged NO concentrations over the canyon are underestimated up to 4% by the box models, while levels of other species are

all overestimated to different extents, in particular with OH levels (overestimated up to around 38%). The overestimations of O_3 are about 5.7% and 2.8% by the one- and 16-box models compared to more accurate LES modelling results.

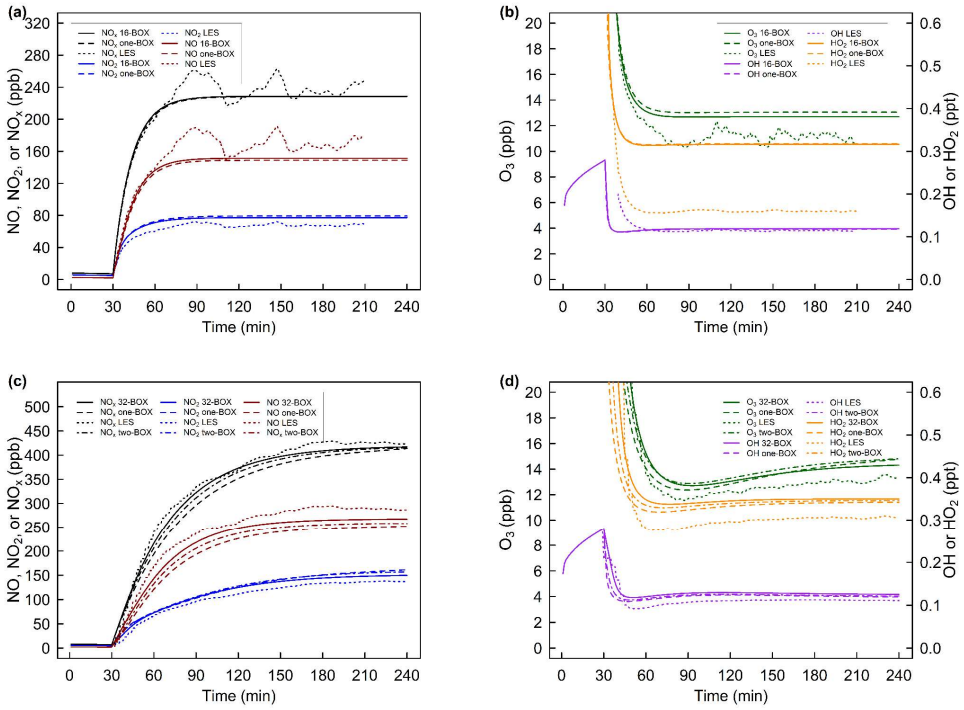


Figure 2.2. Temporal variation of the spatially averaged mixing-ratio of NO, NO_2, NO_x, O_3 (ppb), OH and HO_2 (ppt) calculated using the LES, multi-box and a typical one-box models for the regular (a, b) and deep (c, d) street canyons. Two-box simulations are conducted only in the deep canyon, see text for details.

Previous modelling results (BrightBloss and Cai, 2013) showed that the NO_x modelled by the zero-dimensional one-box model were about 8 ppb (3.3%) higher than by the LES, O_3 concentrations were underestimated by 6%, and NO was overestimated by around 1%. One explanation for the difference between

the results of the present and the previous studies is that the value of $w_{e,0}$ adopted for representing the canyon ventilation is ~5% higher in this study (i.e., $w_{e,0}$ = 0.22) compared to their work (i.e., $w_{e,0}$ = 0.21), resulting in a higher abundance of O_3 in the street canyon due to inward transport in from the background. The NO and NO_2 concentrations would be changed accordingly. It should be noted that NO_x increases by about 1.6% in the box models, which means NO_x loss processes (e.g., production of nitric acid and organic nitrates) are more effective in the LES model. The O_x levels are respectively 9.0% and 11.1% higher in the 16- and one-box models because the efficient mixing of background O_3 and in-canyon NO produces more NO_2 than under less efficient mixing conditions, which is further discussed in the following section.

For the deep canyon, it is noted that the coarse resolution leads to a systematic underestimation of about 3.0% in PS by the one-box model and of about 2% by the two-box model (Table 2.1); additionally, Table 2.2 presents the mixing-ratio of pollutants from the LES, 32-box and two-box models in the upper and lower compartments of the deep canyon, respectively. The 32-box model performs better than the two-box model in simulating PS in both compartments. This may be attributed to the definition of the exchange velocity (e.g., $w_{e,0}$, which is calculated based on the gradient between the whole canyon-averaged and the ambient concentrations) and other dynamical parameters. For example, the exchange velocities for the two-box and multi-box models are calculated based on the gradient between the concentrations in the rooftop boxes and the overlying background. This more local concentration gradient provides a better description for the flux balance

in the multi-box model and thus, better modelling results (i.e., closer to the LES outputs).

Table 2.1. Time-averaged mixing-ratios from LES, the multi (16/32)-box model, and the one-box and two-box models with RCS chemistry for urban street canyons.

		Mixing-ratio (ppb)							[(b)-(a)]/(a) (%)	[(c)-(a)]/(a) (%)	[(d)-(a)]/(a) (%)
		(a) LES	(b) 16/32-box	(c) Two-box	(d) One-box	(b) - (a)	(c) - (a)	(d) - (a)			
The regular street canyon (AR = 1)	PS	223.86	224.33	-	223.85	0.47	-	-0.01	0.21	-	-0.004
	NO	154.66	151.28	-	148.87	-3.38	-	-5.79	-2.19	-	-3.74
	NO_2	70.12	77.19	-	79.35	7.07	-	9.23	10.08	-	13.16
	O_3	12.35	12.70	-	13.05	0.35	-	0.70	2.83	-	5.67
	OH^*	0.086	0.119	-	0.118	0.033	-	0.032	38.37	-	37.21
	HO_2^*	0.253	0.316	-	0.318	0.063	-	0.065	24.90	-	25.69
	NO_x	224.78	228.47	-	228.22	3.69	-	3.44	1.64	-	1.51
	O_x	82.47	89.89	-	92.4	7.42	-	9.93	9.00	-	11.05
	NO_2/NO	0.45	0.51	-	0.53						
The deep street canyon (AR = 2)	PS	430.23	423.53	421.53	417.06	-6.7	-8.7	-13.17	-1.56	-2.02	-3.06
	NO	289.10	266.48	257.48	250.11	-22.62	-31.62	-38.99	-7.82	-10.94	-13.49
	NO_2	136.07	147.84	154.57	156.52	11.77	18.5	20.45	8.65	13.60	15.03
	O_3	13.14	14.19	14.62	14.46	1.05	1.48	1.32	7.99	11.26	10.05
	OH^*	0.11	0.13	0.12	0.12	0.02	0.01	0.01	18.18	9.09	9.09
	HO_2^*	0.31	0.35	0.34	0.34	0.04	0.03	0.03	12.90	9.68	9.68
	NO_x	425.17	414.32	412.05	406.63	-10.85	-13.12	-18.54	-2.55	-3.09	-4.47
	O_x	149.21	162.03	169.19	170.98	12.82	19.98	21.77	8.59	13.39	13.44
	NO_2/NO	0.47	0.55	0.60	0.63						

* Mixing-ratio of OH and HO_2 are presented in part per trillion (ppt).

The difference in the flux-balanced exchange velocities may also have important impacts on the chemistry in the canyon. The multi-box models include horizontal transport that can compensate errors in modelling the

canyon-averaged concentration, as less PS levels (around 1.5%) are underestimated by the 32-box model. The box models overestimate reactive species except for NO compared to the LES, which is consistent with the tendencies in the regular canyon. The absolute errors between the LES and box models are larger for NO, NO_2 and O_3 but are smaller for OH and HO_2 in the deep canyon, partly due to poor ventilation. Moreover, different chemical regimes may exist in the canyon in terms of multi-vortices formed in the canyon, generating a complex outcome for the whole-canyon averages. O_x is overestimated, as in the regular canyon, but NO_x is underestimated partly because of the advective, and turbulent velocities used in the model.

The concentration differences show a consistent pattern going from the complete-mixing (i.e., one-box resolution) to resolved transport-and-mixing (i.e., LES resolution) conditions for most reactive pollutants. That is, the multi-box model in general presents closer-to-LES results than the one-box model. For example, instant mixing in street canyons accelerates more NO conversion to NO_2. Hence, NO_2 is overestimated around 13% by the one-box model but 10% by the 16-box model in the regular canyon; and it is overestimated about 15% by the one-box model, 13.6% by the two-box model, but 8.6% by the 32-box model in the deep canyon (Table 2.1 and Table 2.2). The NO_2/NO ratios gradually reduce from 0.53 to 0.45, and from 0.63 to 0.47 in the regular and deep street canyons from the one-grid approximation to the highest resolution, respectively. For the modelled concentrations of HO_x (= OH + HO_2), the results of all the box models are very close to each other. The

rationale behind this similarity is discussed below using the intensity of segregation.

Table 2.2. Time-averaged mixing-ratios from LES, the 32-box model, and the two-box model with RCS chemistry in the deep canyon.

		Mixing-ratio (ppb)					[(b)-(a)]/(a) (%)	[(c)-(a)]/(a) (%)
		(a) LES	(b) 32-box	(c) Two-box	(b) - (a)	(c) - (a)		
The upper compartment	PS	321.23	315.93	313.65	-5.30	-7.58	-1.65	-2.36
	NO	198.14	182.87	178.03	-15.27	-20.11	-7.71	-10.15
	NO_2	118.44	125.78	129.02	7.34	10.58	6.20	8.93
	O_3	15.21	16.29	16.96	1.08	1.75	7.10	11.51
	OH^*	0.11	0.12	0.12	0.01	0.01	9.09	9.09
	HO_2^*	0.33	0.36	0.37	0.03	0.04	9.09	12.12
	NO_x	316.58	308.65	307.05	-7.93	-9.53	-2.50	-3.01
	O_x	133.65	142.06	145.97	8.41	12.32	6.29	9.22
	NO_2/NO	0.60	0.68	0.72				
The lower compartment	PS	539.23	531.13	529.42	-8.10	-9.81	-1.50	-1.82
	NO	380.06	350.09	336.93	-29.97	-43.13	-7.89	-11.35
	NO_2	153.69	169.90	180.12	16.21	26.43	10.55	17.20
	O_3	11.06	12.09	12.29	1.03	1.23	9.31	11.12
	OH^*	0.11	0.12	0.12	0.01	0.01	9.09	9.09
	HO_2^*	0.28	0.33	0.33	0.05	0.05	17.86	17.86
	NO_x	533.75	519.99	517.05	-13.76	-16.7	-2.58	-3.13
	O_x	164.75	181.99	192.41	17.24	27.66	10.46	16.79
	NO_2/NO	0.40	0.48	0.53				

* Mixing-ratio of OH and HO_2 are presented in part per trillion (ppt).

Table 2.3 compares the percentage intensities of segregation between any two selected chemical species from the LES and multi-box models in regular and

deep street canyons. It shows that the most spatially variable air pollutant in the canyon is NO (i.e., indicated by $I_{S(NO+NO)}$) and the least spatially variable pollutant is OH (i.e., indicated by $I_{S(OH+OH)}$) in general. Not surprisingly almost all intensities of segregation in the deep street canyon are considerably higher (e.g., 26% for $I_{S(NO+NO)}$) than those in the regular canyon (e.g., 3% for $I_{S(NO+NO)}$), which are supported by ZhongCai and Bloss (2017). It indicates that NO concentrations become more heterogeneous due to the perturbed in-canyon vortices, but OH is less affected in terms of their abundance and lifetime in street canyons. It is also found that within both types of canyons the values of $I_{S(q_1+q_2)}$ in the multi-box models mostly have a same sign with those in the LES, which is positive for "emitted-inside-canyon" species (i.e., NO, NO_2) and is negative for "entrained-from-background" and "formed in situ" species (i.e., O_3, OH, HO_2), indicating similar chemical behaviours (e.g., generation or depletion) of these species in the LES and multi-scale models.

For atmospheric pollutants that directly react with each other, the intensities of segregation of the multi-box models have a trend toward "zero" compared with the LES. For example, NO and O_3 titration rates are slower by 2.79% and 10.02% in regular and deep canyons under the "true" condition, but slower by only 1.34% and 9.35% respectively under the "multi-box" approximation at the current resolution. That is, the performance of multi-box model is in between the LES (i.e., close to the "true" flow, insufficient mixing with hundreds of thousands of boxes) and the one-box model (i.e., instant and homogeneous mixing with no segregation). The reactions of O_3 and HO_2

producing OH have been accelerated by 1.74% and 2.36% in the LES, but only by 0.42% and 1.56% in the multi-box models.

Table 2.3. The percentage intensities of segregation between pairs of reactive species from the LES and multi-box models (BOX) for the regular and deep canyons. Bold symbols represent species that directly react with each other in the models, and negative values are shown in red.

		LES					BOX				
		NO	NO_2	O_3	OH	HO_2	NO	NO_2	O_3	OH	HO_2
The regular street canyon (AR = 1)	NO	3.02	-	-	-	-	2.97	-	-	-	-
	NO_2	1.38	0.83	-	-	-	1.61	1.15	-	-	-
	O_3	**-2.79**	-1.64	3.54	-	-	**-1.34**	-0.36	1.61	-	-
	OH	**-0.81**	**-0.27**	**0.76**	0.43	-	**-0.08**	**-0.03**	**0.07**	0.004	-
	HO_2	**-1.43**	**-0.71**	**1.74**	**0.60**	**1.12**	**-0.56**	**-0.20**	**0.42**	**0.02**	**0.15**
The deep street canyon (AR = 2)	NO	26.15	-	-	-	-	26.35	-	-	-	-
	NO_2	10.21	4.18	-	-	-	11.50	5.58	-	-	-
	O_3	**-10.02**	-4.35	5.09	-	-	**-9.35**	-3.86	4.45	-	-
	OH	**-2.75**	**-1.06**	**1.09**	0.31	-	**0.22**	**0.15**	**-0.09**	0.01	-
	HO_2	**-5.13**	**-2.12**	**2.36**	**0.57**	**1.15**	**-3.54**	**-1.45**	**1.56**	**-0.03**	**0.57**

2.3.2 The spatial variation of pollutants in street canyons

Figure 2.3 illustrates vertical profiles ($0 < z/l_0 < 0.25$, $0.25 < z/l_0 < 0.5$, $0.5 < z/l_0 < 0.75$, $0.75 < z/l_0 < 1.0$) of time-averaged PS, NO, NO_2, O_3, OH and HO_2 in the regular canyon (black lines), along with the leeward (blue lines) and

windward walls (red lines) in order to further ascertain the performance of the multi-box model. In order to compare the model performance of the LES and multi-box model at the same grid resolution, the quantities of the LES were averaged over the entire street width ($-0.5 < x/l_0 < 0.5$) and the nearest box grid resolution adjacent to the canyon walls (i.e., $-0.5 < x/l_0 < -0.25$ for the leeward, $0.25 < x/l_0 < 0.5$ for the windward), respectively. The distributions of chemical species from the 16- and 32-box models are presented in Chapter 2.5 Supporting Information Figure 2.7 and Figure 2.8, respectively. Over the final hour of the simulation, it is clear that the vertical distributions of PS from the 16-box model are in good agreement (within 5 ppb) with those from the LES, with higher concentrations elevated on the leeward side of the street corner (305.0 ppb) and considerably lower concentrations on the windward side (172.2 ppb) due to the in-canyon air circulation. The agreement for PS indicates that the multi-box model with LES-driven dynamics captured the major flow pattern well (i.e., a primary vortex) within the regular street canyon.

The agreement for PS also implies that the discrepancies in the abundance of reactive species between the multi-box and the LES models are mainly attributed to NO_x-O_3-VOC chemical reactions, though their vertical and horizontal features are also well-reproduced by the multi-box model. NO concentrations are well-simulated in $Box_{[1,4]}$ (difference within 1 ppb) but are slightly underestimated at other grid points, especially for the leeward side (difference around 8 ppb, ~3%). Due to less segregation for the 16-box model, there is a more effective O_3 titration in the canyon, which depletes more NO

turning to NO_2, thus causing an underestimation of NO and an overestimation of NO_2 contents in the 16-box model. Errors in NO_2 concentrations become smaller on the windward side but become larger on the leeward side from the street level to the canyon rooftop. The maximum overestimation of NO_2 is 15.6 ppb (19.1%) at $0 < z/l_0 < 0.25$ of the leeward side ($Box_{[1,1]}$) and 9.9 ppb (12.6%) at $0.5 < z/l_0 < 0.75$ of the windward side ($Box_{[3,4]}$). The O_3 concentrations are underestimated on the windward side with the maximum box-minus-LES value of 2.2 ppb (24.3%) at $0 < z/l_0 < 0.25$ ($Box_{[1,1]}$) due to effective titration with recirculated NO under the sufficient mixing condition. However, there is an clear overestimation in O_3 contents on the leeward side with the maximum difference of -3.6 ppb (19.1%) at $0.75 < z/l_0 < 1.0$ ($Box_{[1,4]}$). The explanation could be that more O_3 accumulated on the leeward side because of the rapid photodegradation of overproduced NO_2 due to segregation effects on the windward side. Moreover, overestimating NO_2 concentrations in the presence of constant NO levels could potentially skew the atmospheric chemistry, leading to increased HO_2 production primarily through reactions with OH, subsequently producing nitric acid. Concurrently, the heightened consumption of OH in reactions with the excessive NO2 could deplete OH concentrations, assuming steady-state conditions for other OH sources and sinks. However, this scenario could also trigger a series of feedback mechanisms, mainly through NO reactions with HO_2 forming additional NO_2 and O_3. The increased O_3 could further enhance OH production via photolysis and reactions with water vapour. Elevated OH levels may intensify the formation of RO_2 from VOCs, with subsequent reactions

potentially converting RO_2 back to HO_2. Consequently, OH levels might initially decrease due to increased consumption in reactions with NO_2, but feedback mechanisms involving O_3 and VOCs could potentially lead to elevated levels of both OH and HO_2. These chemical reactions may explain that HO_x concentrations (about 0.03 ppt for OH, 0.07 ppt for HO_2) are overestimated by the multi-box model compared to the LES in this study.

The Damköhler number (Da) is a widely used ratio of the chemical reaction rate to the diffusion rate (or, equivalently, the ratio of diffusion timescale to reaction timescale) for determining the importance of segregation effects on reactive species (DriscollChen and Yoon, 1992). If Da << 1, the dynamics achieve “equilibrium” much faster than the reaction, leading to minimal segregation effects for the pollutant; if Da >>1, the reaction may be considered to reach equilibrium instantaneously compared to the relatively slower diffusion rates. That is, dynamics for the pollutants with substantial segregation effects must be considered in a coupled manner (GarmoryRichardson and Mastorakos, 2006). ZhongCai and Bloss (2017) reported the Da numbers of NO, NO_2, O_3, OH and HO_2 in the street canyon, which were 3.4, 5.8, 69, 1.44×10^5 and 4.44×10^4, respectively. The chemical reaction rates of HO_x are much quicker than the diffusion rates across the model grid (Da >> 1). This explains that HO_2 is 0.02 ppt higher on the windward side compared to the leeward side, and vertical distributions of OH and HO_2 from the 16-box model are not significant compared to the outputs of the LES.

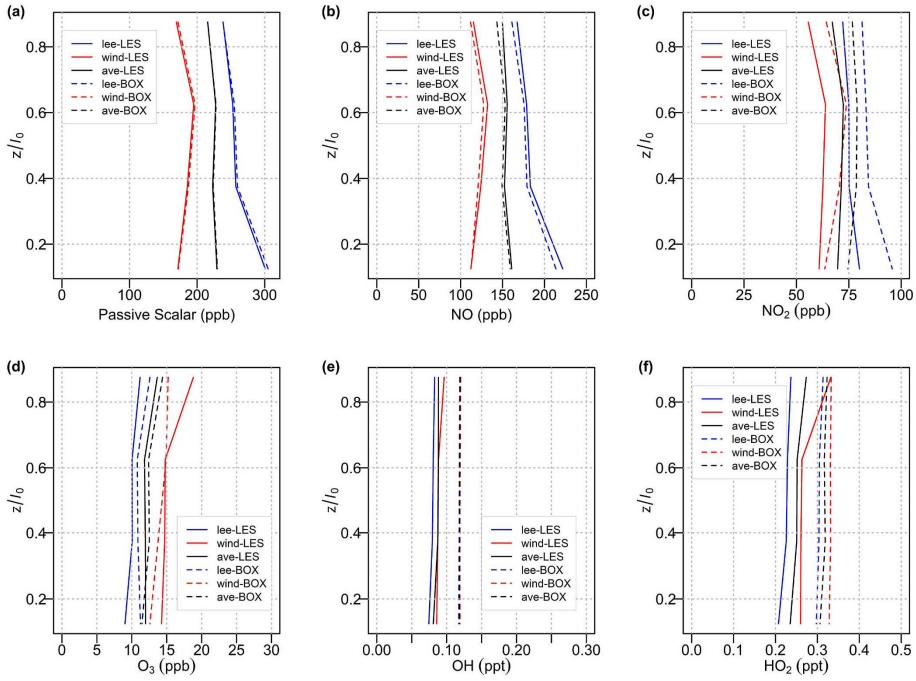


Figure 2.3. Vertical profiles of the time-averaged mixing ratios of PS, NO, NO_2, O_3, OH and HO_2 in the regular street canyon ($-0.5 < x/l_0 < 0.5$) represented by the black lines, along with the leeward wall ($-0.5 < x/l_0 < -0.25$) represented by the blue lines, and along with the windward wall ($0.25 < x/l_0 < 0.5$) represented by the red lines. Solid and dash lines indicate modelling results from LES and multi-box models, respectively (For interpretation of the references to color in this figure legend, the reader is referred to the Web version of the article).

Figure 2.4 shows the vertical distributions of selected species in the deep canyon and along with the leeward and windward facets. The PS concentrations of the 32-box model are well-matched to those of the LES model in both vertical and horizontal directions, with an underestimation of around 10 ppb (2.4%) on the leeward side and of 25 ppb (2.5%) on the windward side. Cumulative traffic emissions produce very high PS mixing-ratios in the lower part of the canyon ($0 < z/l_0 < 1.0$). The concentration

of PS decreases smoothly with height on the leeward side but sharply varies on the windward side, e.g., concentrations are higher on the windward side when $0 < z/l_0 < 1.0$ but on the leeward side when $1.0 < z/l_0 < 2.0$. This indicates noticeable segregation between the lower and upper compartments of the deep street canyon due to the presence of two counter-rotating vortices that are captured by the LES and multi-box models. The upper vortex is driven by the ambient wind in the shear layer at the rooftop (z/l_0 = 2.0) so that the characteristics of the vertical profiles are similar to those of the regular canyon, while the lower vortex is driven by the upper vortex at approximately z/l_0 = 1.0 (or slightly lower) (ZhongCai and Bloss, 2015, Eliasson et al., 2006).

Considering the chemically reactive species, NO concentrations are slightly underestimated on both sides of the canyon as for the regular canyon, with the maximum difference of 74.9 ppb (9.5%) in $Box_{[1,4]}$ on the windward corner. NO_2 is overestimated by the 32-box model, especially for the windward side (~6%). The O_3 concentrations are slightly underestimated by the 32-box model in the upper vortex on the windward side (~5%), and then are overestimated when air parcel moves to the upper leeward side and to the lower vortex (~10%). Although HO_x concentrations are still higher in the 32-box model compared to the LES, the spatial profiles of HO_2 are well reproduced due to a longer diffusion time in the deep canyon in contrast to the regular canyon. Errors in modelled concentrations (solid and dash lines with the same color) always become larger at $0 < z/l_0 < 1.0$ but become closer at $1.0 < z/l_0 < 2.0$. For example, the 32-box model overestimates NO_2 and O_3 by

14.9% and 27.4% on the leeward side, and by 18.1% and 23.1% on the windward side at the street level ($0 < z/l_0 < 0.25$), but those differences decrease to 8.1%, 17.8%, 14.4% and -10.0% at the rooftop level ($0.75 < z/l_0 < 1.0$), respectively. Therefore, when applying the grid assumption to simulate reactive species in street canyons, it is necessary to consider the inherent uncertainty due to chemical reactions being too fast in particular at the street level, which may lead to an overestimation of pedestrian exposure risks.

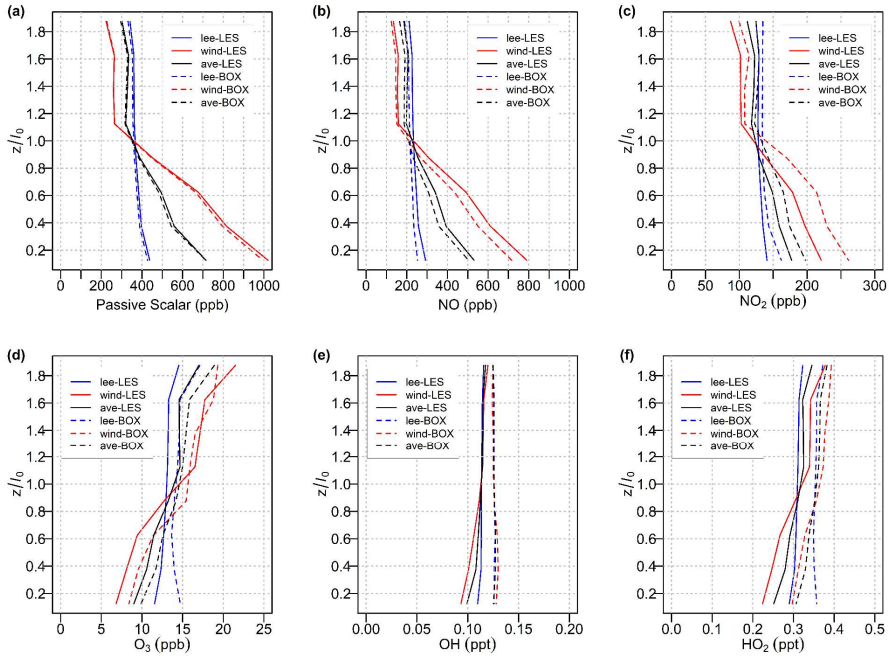


Figure 2.4. Vertical profiles of the time-averaged mixing-ratios of PS, NO, NO_2, O_3, OH and HO_2 in the deep street canyon ($-0.5 < x/l_0 < 0.5$) represented by the black lines, along with the leeward wall ($-0.5 < x/l_0 < -0.25$) represented the by blue lines, and along with the windward wall ($0.25 < x/l_0 < 0.5$) represented by the red lines. Solid and dash lines indicate modelling results from LES and multi-box models, respectively.

2.3.3 The model performance with the simple NO_x-O_3 cycle

The performance of the multi-box models has been further evaluated with the simplified NO_x-O_3 chemical reactions:

$$NO + O_3 \rightarrow NO_2 \quad (2.23)$$

$$NO_2 + h\nu \xrightarrow{O_2} NO + O_3 \quad (2.24)$$

where $h\nu$ represents solar photons. The production and photodegradation coefficients of NO_2 are taken from the RCS chemistry, which are 4.01×10^{-4} ppb^{-1} s^{-1} and 9.20×10^{-3} s^{-1}, respectively. The quasi-steady state assumption (QSSA) is adopted for the calculation. The computation time for the multi-box model using the simple NO_x-O_3 cycle is much quicker (~40 s) than that using RCS chemistry. Table 2.4 illustrates the time- and spatial-averaged mixing-ratios of NO, NO_2, O_3, NO_x, O_x and NO_2/NO ratios with solely NO_x-O_3 reactions during the final hour in the regular and deep canyons. The modelled NO_x concentrations of the LES model are about 1.9% lower in the regular canyon but are slightly higher in the deep canyon compared to the box models, partly because of strong turbulent fluctuations in the LES. As expected, NO_2 concentrations gradually reduce by 10-13% in the regular canyon without involving OH/HO_2 chemicals, thereby decreasing O_x contents to a similar magnitude. This reduction is rather significant (37-41%) in the deep canyon, resulting in dramatically lower NO_2/NO ratios, which is demonstrated by ZhongCai and Bloss (2017). In comparison with the LES outputs, O_3 concentrations are underestimated by the box models to different extents in both regular and deep canyons, which differs from its trends of overestimation

with the RCS chemistry. Overall the multi-box models performed better than the one-box and two-box models in simulating all reactive species except O_3.

Table 2.4. Time-averaged mixing-ratios from LES, the multi (16/32)-box model, and the one-box and two-box models with the simple NO_x-O_3 chemistry for urban street canyons.

		Mixing-ratio (ppb)							[(b)-(a)]/(a) (%)	[(c)-(a)]/(a) (%)	[(d)-(a)]/(a) (%)
		(a) LES	(b) 16/32-box	(c) Two-box	(d) One-box	(b) - (a)	(c) - (a)	(d) - (a)			
The regular street canyon (AR = 1)	NO	165.10	165.27	-	163.24	0.17	-	-1.9	0.10	-	-1.13
	NO_2	62.58	66.81	-	68.72	4.22	-	6.14	6.75	-	9.81
	O_3	10.60	10.19	-	10.43	-0.4	-	-0.17	-3.89	-	-1.60
	NO_x	227.69	232.08	-	231.97	4.39	-	4.28	1.93	-	1.88
	O_x	73.18	77.00	-	79.16	3.81	-	5.97	5.21	-	8.16
	NO_2/NO	0.38	0.40	-	0.42						
The deep street canyon (AR = 2)	NO	352.57	344.33	336.85	333.14	-8.2	-15.7	-19.4	-2.34	-4.46	-5.51
	NO_2	85.43	86.30	90.29	92.03	0.87	4.86	6.60	1.02	5.69	7.72
	O_3	6.89	6.38	6.62	6.45	-0.5	-0.27	-0.44	-7.35	-3.95	-6.43
	NO_x	438.00	430.63	427.14	425.17	-7.37	-10.9	-12.8	-1.68	-2.48	-2.93
	O_x	92.32	92.69	96.91	98.48	0.37	4.59	6.15	0.40	4.97	6.67
	NO_2/NO	0.24	0.25	0.27	0.28						

Modelling differences between the four models shrink when using the very simplified chemical reactions in contrast to the NO_x-O_3-VOC chemical scheme. More specifically, Figure 2.5 presents vertical profiles of the difference of NO, NO_2 and O_3 concentrations under different chemical schemes using the multi-box models and the LES, respectively. It clearly exhibits the direct contributions from the VOCs mechanisms spatially, which, in general, shows more substantial influences on the modelling results of the multi-box model

compared to those of the LES. The contributions of VOCs are significantly enhanced in the deep street canyon compared to the regular canyon; involving VOCs tends to have greater impacts on local emitted species such as NO and NO_2 in the lower compartments (i.e., $0 < z/l_0 < 1.0$) and on remote species such as O_3 in the upper compartments (i.e., $1.0 < z/l_0 < 2.0$). Although there are some differences between the performance of the multi-box models and the LES, the multi-box models reproduce well the contribution of VOCs to the vertical distribution of NO_2 and O_3.

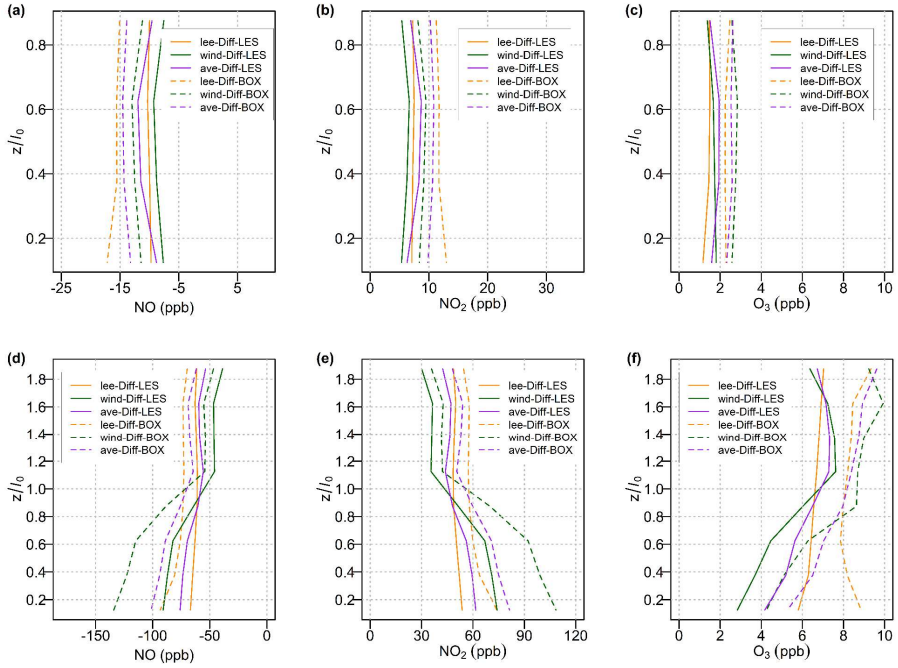


Figure 2.5. Vertical profiles of the difference of NO, NO_2 and O_3 concentrations under different chemical schemes (modelling results with the VOC chemistry minus results with the simple NO_x-O_3 chemistry) in regular (a, b, c) and deep (d, e, f) street canyons ($-0.5 < x/l_0 < 0.5$) represented by the purple lines, along with the leeward wall ($-0.5 < x/l_0 < -0.25$) represented the by orange lines, and along with the windward wall ($0.25 < x/l_0 < 0.5$) represented by the green lines. Solid and dash lines indicate modelling results from LES and multi-box models, respectively.

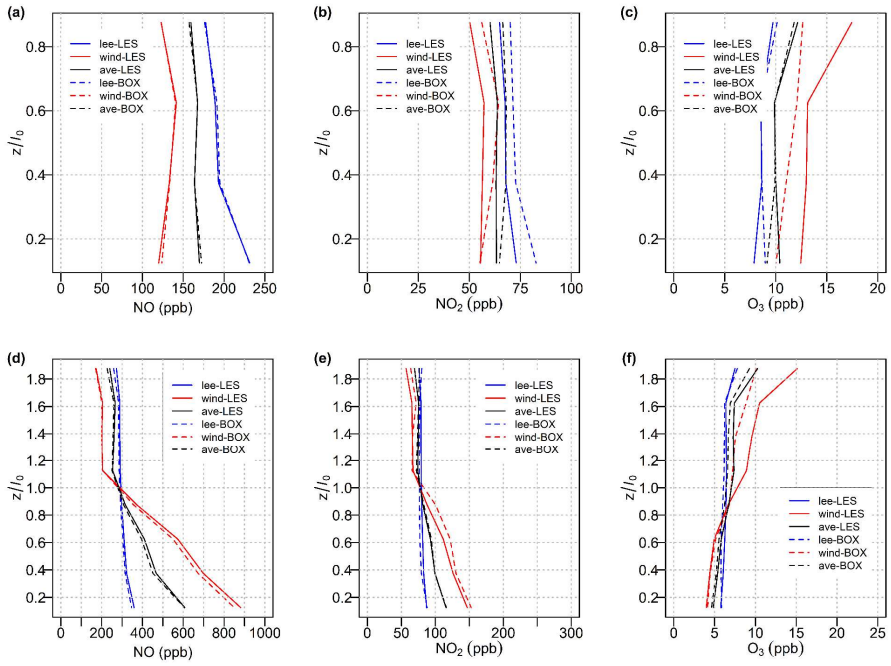


Figure 2.6. Vertical profiles of the time-averaged mixing-ratios of NO, NO_2, and O_3 in regular (a, b, c) and deep (d, e, f) street canyons ($-0.5 < x/l_0 < 0.5$) represented by the black lines, along with the leeward wall ($-0.5 < x/l_0 < -0.25$) represented the by blue lines, and along with the windward wall ($0.25 < x/l_0 < 0.5$) represented by the red lines. Solid and dash lines indicate modelling results from LES and multi-box models, respectively.

Figure 2.6 illustrates the vertical distributions of NO, NO_2, and O_3 in the regular (a, b, c) and deep (d, e, f) street canyons (i.e., horizontal-averaged concentration cross $-0.5 < x/l_0 < 0.5$) and along the canyon walls (i.e., $-0.5 < x/l_0 < -0.25$ and $0.25 < x/l_0 < 0.5$). In the regular canyon, NO is well-simulated with negligible difference between two models. The vertical profile of NO_2 is overestimated by the 16-box model due to segregation. Nevertheless, extent of overestimation in NO_2 becomes smaller compared to the simulations with NO_x-O_3-VOC chemistry, leading to relatively lower O_3 concentrations along the leeward wall.

However, underestimation of O_3 becomes larger on the windward side, with a maximum difference of 4.8 ppb at the rooftop ($0.75 < z/l_0 < 1.0$). In the deep canyon, we also obtained satisfied vertical distributions of all three species from the 32-box model compared to those in the LES. Concentration gradients of NO_2 and O_3 lessen when applying the simple NO_x-O_3 cycle, especially for the street level. NO_2 is still overestimated on the windward side and underestimated on the leeward side, but to a much acceptable degree compared to the scenario with the RCS (Figure 2.4). The trends of O_3 are the same as that of the regular canyon in the upper vortex ($1.0 < z/l_0 < 2.0$), e.g., an underestimation on the windward side and overestimation on the leeward side but are consistent with the LES in the lower vortex ($0 < z/l_0 < 1.0$). This indicates that the modelling domain with VOC emissions (e.g., high coverage of vegetation) should consider using air quality models with resolution as high possible to diminish the segregation effects in chemistry.

2.4 Conclusions

A process-based multi-box photochemical street-canyon model, with a flexible number of boxes and based on a set of transport parameters calculated from the LES outputs is developed in this study. The performance of this street-scale chemical transport model coupled with NO_x-O_3-VOC chemistry (or a simplified NO_x-O_3 cycle), for modelling reactive species in the regular (AR = 1) and deep (AR = 2) street canyons, is compared to the published LES data and to one- and two-box simulations. Results show that the model configured with a single box captures the average state of air pollutants in street canyons, and the results

are consistent with previous studies (BrightBloss and Cai, 2013, ZhongCai and Bloss, 2016b). Compared with the benchmark LES simulation, the multi-box model reproduces well the spatial contrast in pollutant concentrations inside the street canyons in particular with a chemically inert passive scalar. Namely, the spatial concentration patterns have been captured for the regular street canyon (i.e., single primary vortex), as well as for the deep street canyon (i.e., two counter-rotating vortices). For the regular canyon, it is found that the NO and O_3 titration reaction becomes more effective due to less segregation along the windward facet, leading to an underestimate of O_3 and an overestimate of NO_2 levels. On the leeward side, the overestimated NO_2 results in an overestimation of O_3 through photolysis. An additional overestimation of NO_2 is attributed to OH/HO_2 chemistry. The impact of segregation effects on the reactive species is substantial, in particular for short-lived species. The OH and HO_2 concentrations are overestimated by the multi-box model, their vertical variations are not very significant compared to the LES because of their very short chemical timescales.

In a deep canyon with poor ventilation, the relationship of reactive species in the upper compartment between the 32-box and LES models is consistent with those in the regular canyon. However, in the lower compartments of the canyon, O_3 is always overestimated, and there are obvious variations of OH and HO_2 concentrations along the vertical direction. Additionally, under the simple NO_x-O_3 cycle, the differences between the multi-box model and the LES become smaller particularly for the deep canyon. Although the effects of VOC chemistry on reactive species such as NO_2 are underestimated compared to

the LES, the multi-box models capture the vertical contribution of VOCs to these pollutants in street canyons and are a significant step forward from the simple one- and two-box models. The multi-box model is less computationally efficient than the typical one-box (~1 s) and two-box models (~8 s), but it can offer spatial information on reactive species within street canyons based on coupled chemical-transport processes (with VOC chemistry) in a fairly short computational times (~6 min) compared to the LES (e.g., ~10 days in ZhongCai and Bloss (2017)). Overall, the multi-box model enables insightful investigations into the multiple processes as well as their complex interactions and is of practical utility for air quality assessment or pollution mitigation management in street canyons.

Although not the focus of the current chapter, we note that aerosol microphysics introduces non-linear processes in street canyons in a similar way to chemistry; the modelling framework described below could be extended to include detailed size-dependent aerosol microphysics in the future. Further works may also focus on adopting the multi-box model to simulate air pollution in street canyons with spatially segregated emissions due to the presence of vegetation. More detailed chemical schemes (e.g., Master Chemical Mechanism, MCM*v*3.0 (Saunders et al., 2003)) can be incorporated into the model. The evaluation of modelling results with field measurements is recommended. A more challenging task is to merge the effects of airflow parallel to the street axis on the diffusion and transformation of chemical species, which would enable for a wider range of model applications.

2.5 Supporting Information

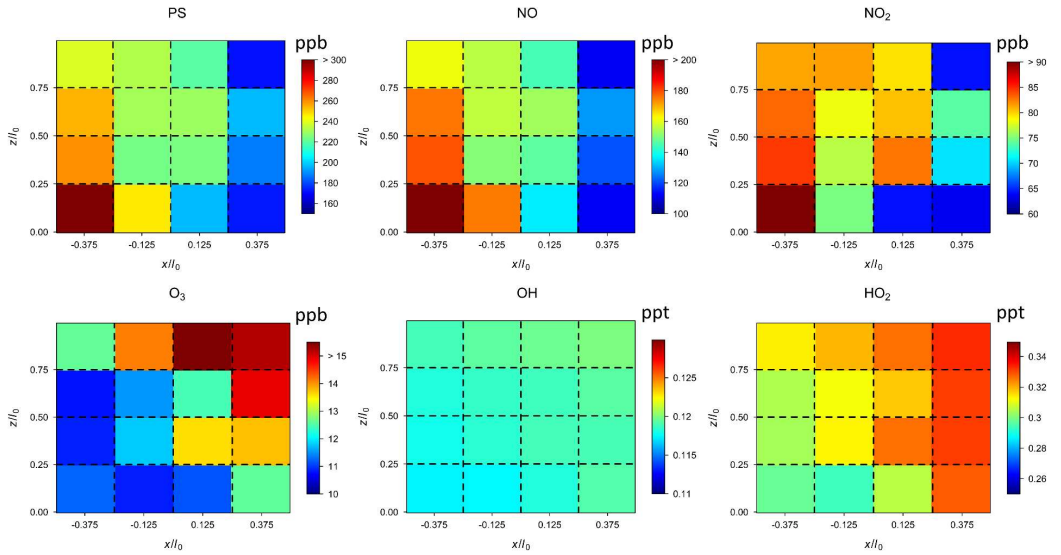


Figure 2.7. The distributions of pollutants in the regular street canyon from the 16-box model.

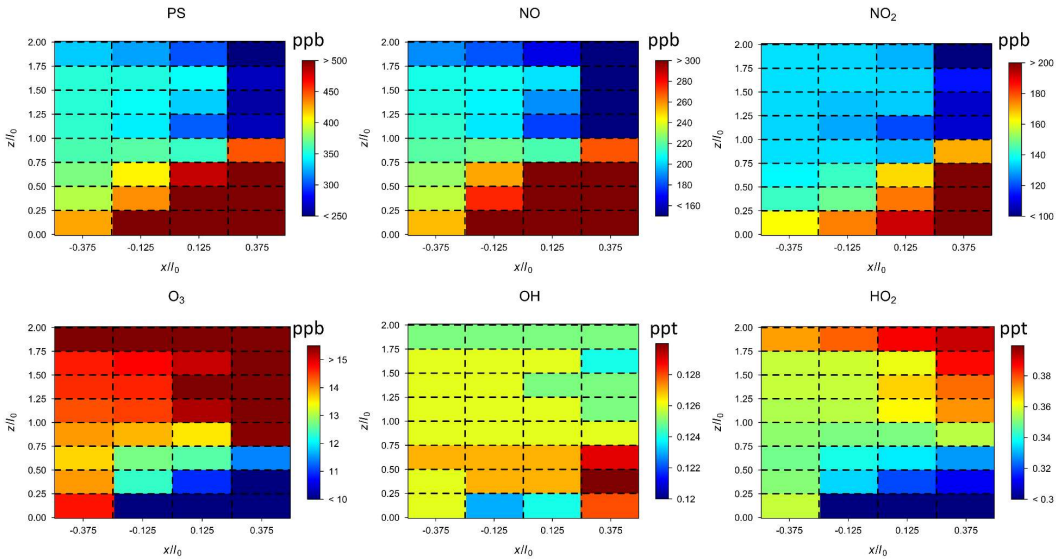


Figure 2.8. The distributions of pollutants in the deep street canyon from the 32-box model.

2.6 Acknowledgements

The authors thanks Dr Vivien Bright for provision of the reduced chemical scheme (RCS). YD would like to thank the University of Birmingham's BlueBEAR HPC service (http://www.bear.bham.ac.uk) for providing the computational resource. ARMK acknowledges funding support of the Natural Environment Research Council (grants NE/S013814/1, NE/S003487/1). The comments of the anonymous reviewers are gratefully acknowledged.

CHAPTER 3 CHEMISTRY, TRANSPORT, EMISSIONS, AND SHADING EFFECTS ON NO_2 AND O_x WITHIN URBAN CANYONS

Author Statement

This chapter contains work that has been previously published. The publication details are as follows:

Dai, Y., Cai, X., Zhong, J., Mazzeo, A. and MacKenzie, A.R., 2022. Chemistry, transport, emission, and shading effects on NO_2 and O_x distributions within urban canyons. Environmental Pollution, 315, p.120347.

The contributions of the authors are as follows:

Yuqing Dai (the author of this thesis) was responsible for the conceptualization, methodology, coding, data curation, and the original draft preparation. **Rob Mackenzie** and **Jian Zhong** contributed to reviewing, editing the draft, and supervisory. **Xiaoming Cai** and **Andrea Mazzeo** contributed to reviewing and editing the draft. Additional acknowledgements are presented in Section 3.6 of this chapter.

Abstract

The capacity to predict NO_2 and the total oxidant ($O_x = NO_2 + O_3$) within street canyons is critical for the assessment of air quality regulations aimed at enhancing human wellbeing in urban hotspots. However, such assessment requires the coupling of numerous processes at the street-scale, such as

vehicular emissions and tightly coupled transport and photochemical processes. Photochemistry, in particular, is often ignored, heavily simplified, or parameterized. In this study, MBM-FleX — a process-based street canyon model that allows fast computation of various emission profiles and sun-lit conditions with tightly coupled physical (transport and mixing) and chemical processes and without loss of sufficient spatial resolution — was used to simulate shading effects on reactive species within urban canyons. Driven by pre-generated large-eddy simulation of flow, MBM-FleX results show that shading effects on volatile organic compound (VOC) free-radicals significantly affect the interconversion of odd-oxygen species that cannot be captured by the simple NO_x-O_3 chemistry, for example, reducing NO_2 by limiting the formation of hydroperoxyl radicals. Consistent with previous results in simpler model systems, the inclusion of VOC free-radical chemistry did not appreciably alter the sensitivity of NO_2 to shading intensity in regular canyons, but a non-linear relationship between NO_2 and shading intensity is found in deep canyons when the air residence time grew. When solar incidence simultaneously passes through multiple vortices in street canyons, VOC chemistry and shade may considerably influence model results, which may therefore affect the development of urban planning strategies and personal exposure evaluation.

3.1. Introduction

Urban air pollution is critically important to human wellbeing given that the urban population is expected to grow rapidly to 68% in the world by 2050 (United Nations, 2018) and human exposure to air pollution can lead to increases in respiratory morbidity and mortality (Murray et al., 2020, Zeng et al., 2020, Anenberg et al., 2018). For instance, nitrogen dioxide (NO_2) is a vital contributor to urban air pollution as a gaseous pollutant and as a precursor to aerosol formation, and its concentration can become significant high in some urban "hotspots" such as street canyons, which describe a narrow street flanked by incessant obstructions on both sides, forming a stagnant environment with, in general, heavy emissions and reduced dispersion. Street canyons are becoming increasingly prevalent as urban areas grow denser (Joint Air Quality Unit, 2017). They can be categorized into three groups based on their aspect ratios (AR, defined as the ratio of canyon height to street width): avenue canyons with $AR \leq 0.5$; regular canyons with $AR \approx 1.0$ and no significant openings on the facade; and deep canyons with $AR \geq 2.0$ (Vardoulakis et al., 2003). The characteristic of airflow field and the dispersion pattern within urban canyons are sensitive to Reynolds number (Re) (ChewAliabadi and Norford, 2018b), roof shape (Takano and Moonen, 2013), in-canyon trees and green infrastructure (Gromke and Ruck, 2007, Abhijith et al., 2017, Yazid et al., 2014), street orientation, and ARs (AhmadKhare and Chaudhry, 2005, Chatzidimitriou and Yannas, 2017). The ventilatory capacity of canyons generally decreases with increased ARs, leading to poorer air quality at the

pedestrian level and hence serious public health consequences for citizens exposed to such circumstances (SolazzoVardoulakis and Cai, 2011).

Nitrogen oxides (NO_x, a summation of nitrogen oxide NO and NO_2) and ozone (O_3) undergo closely coupled dynamics and chemical processes within the urban canyon environment (Garmory et al., 2009), which have motivated research studies. Salmond et al. (2013) conducted a field monitoring campaign and suggested that the presence of leaves on trees would resist vehicular emissions moving upward to the rooftop along the leeward facade, giving marked impacts on in-canyon dynamics and chemistry. A variety of parametric (e.g., canyon box models) and numerical (e.g., Computational fluid dynamics (CFD)) models integrated with chemical schemes have been used to simulate the behavior of air pollutants (e.g., temporal and spatial distributions, mass exchanges with the overlying background) within street canyons (BrightBloss and Cai, 2013, ZhongCai and Bloss, 2016a, ZhongCai and Bloss, 2017, Wu et al., 2021, KimPark and Kim, 2012, Kwak and Baik, 2012). Particles in street canyons raised similar issue of transport and aerosol microphysics (e.g., Zhong et al. (2018)). However, most of these studies hypothesized constant photolysis rates within street canyons primarily due to expensive computational cost in numerical models. Given that the photolysis rate of NO_2 can be 20-40% of the theoretical value on overcast (Finlayson-Pitts and Pitts Jr, 1999) or hazy (Li et al., 2018) days, our knowledge of shading effects on air pollution within street canyons remain limited.

Although CFD-based air quality models offer the most convincing physical

simulations based on current understanding, they require enormous computational resources in general, which increases by several orders of magnitude when complex volatile organic compound (VOC) free-radical schemes are involved. Hence, many earlier simulations either employed the simple NO_x-O_3 chemistry for a broad variety of modelling scenarios or VOC schemes for a restricted number of scenarios to save computing time (Liu et al., 2021, ZhongCai and Bloss, 2016a). Previously, studies applied large-eddy simulation (LES) and Reynolds-averaged Navier-Stokes (RANS) models coupled with a simple NO_x-O_3 chemistry to investigate shading effects on air pollutants in street canyons (GraweCai and Harrison, 2007, Liu et al., 2021). However, the absence of VOC chemistry can introduce substantial uncertainty into model performance (KimPark and Kim, 2012, KwakBaik and Lee, 2013), leading to sub-optimal or even mistaken strategies for air quality regulation (Dai et al., 2022b).

Using a zero-dimensional, one-box, model (i.e., the well-mixed assumption for reactive species) cannot address all aspects of air quality within street canyons due to the presence of strong concentration gradients, which means that pollution "hotspots" will be undiagnosed, and too-rapid chemical dilution will occur, leading to underestimated segregation effects (ZhongCai and Bloss, 2014, Monks et al., 2015). We have developed a process-based Eulerian multi-box model ("MBM-FleX") with flexible grid resolution to simulate temporal and spatial evolutions of air pollutants inside street canyons. The model uses a small number of boxes sufficient to resolve explicitly major vortices in the flow and so represent the dominant dynamical processes of advection and

turbulent mixing. Compared to online LES-with-chemistry, this model design boosts computational speed very significantly and so allows computational resource to be reallocated to the investigation of broader emissions conditions and more complete VOC free-radical chemistry. MBM-FleX takes LES-derived airflow patterns in idealised regular (AR = 1) and deep (AR = 2) canyons as input, and yields a good temporal and spatial agreement with LES for a passive tracer and for reactive species (e.g., NO, NO_2, and O_3) (Dai et al., 2021b). The MBM-FleX model yields comparable results regarding the spatial features of air pollutants with an extremely low computational cost for typical regular (~3 min) and deep (~6 min) canyon simulations to the LES (~10 days) (Dai et al., 2021b) using a high-performance computer (HPC). Model-observation evaluations are comparable to those of other air quality models (e.g., CiTTy-Street, ADMS-urban) (Pugh et al., 2012, Hood et al., 2021, Dai et al., 2022b).

Here we extended the MBM-FleX to simulate shading effects on NO_2 and O_3 inside the street canyon with different aspect ratios. It is also useful to consider the total oxidant O_x, which equals the sum of NO_2 and O_3, since these values are preserved in GraweCai and Harrison (2007) under different shading conditions. The solar-induced heating of ground and building facets induced by the solar radiation may “assist” or “oppose” air circulation, depending on the angle of solar zenith and the canyon geometry (Cai, 2012b, Paolini et al., 2014). Such thermal impacts on air flow remain highly contentious. With a temperature differential of around 10 Kelvin, previous studies indicate that the co-effects of wind-driven dynamic force due to enhanced or reduced circulation and the heating (i.e., ground and wall) alter the in-canyon flow

characteristics and hence the distribution of air pollutants inside the canyons substantially (Liu et al., 2021, Yang et al., 2021a, Hang et al., 2020). Therefore, here we disentangle shading effects on atmospheric photochemistry (*J*-values) from intricate transport-chemical interactions.

3.2. Experimental Section

3.2.1 Model description

Figure 3.1 presents the multi-box framework (MBM-FleX) by which the cross-sectional space of an urban street canyon has been divided into 16 and 32 boxes with an equal grid size for regular (AR = 1) and deep (AR = 2) canyons, respectively. The size and number of model boxes can vary flexibly depending on particular interests in air quality "hotspots" within canyons (Dai et al., 2021b). NO_x, carbon monoxide (CO), and VOCs from anthropogenic (e.g., vehicles) and natural sources can be injected into two central boxes that represent a dual carriageway and, if necessary, into any boxes where line emissions may occur continuously. Currently, this two-dimensional (2D) MBM-FleX is settled to the case of a perpendicular background wind to the street axis because cross-canyon flow generates the most vigorous in-canyon circulations and is hence the most appropriate location to start an investigation.

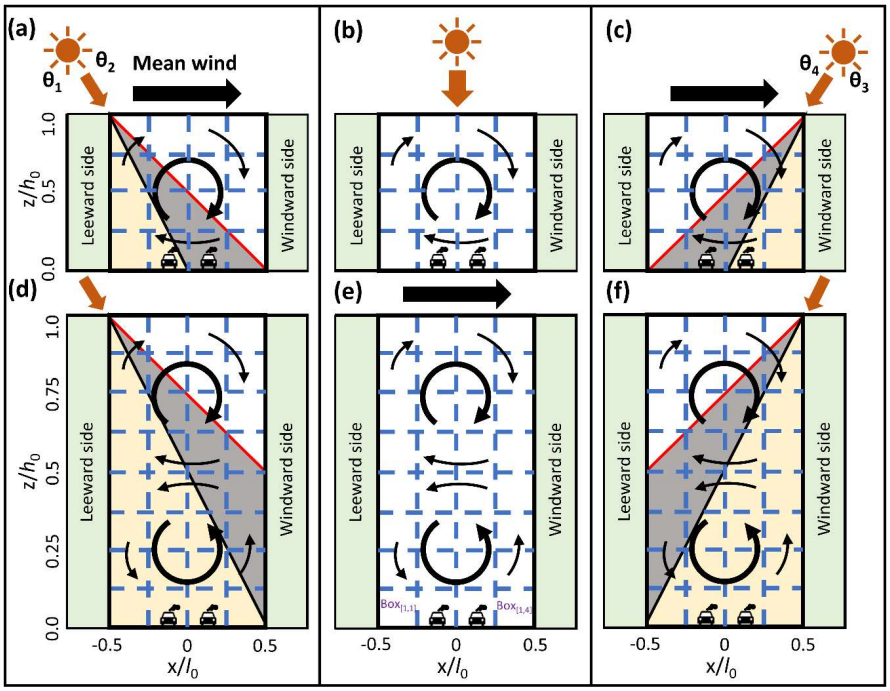


Figure 3.1. The effects of sun position on regular and deep two-dimensional canyons: (a, d) leeward shading (LS) occurs when the sun is on the leeward side of canyons; (b, e) no shading (NS) when there is no shadow within canyons; (c, f) windward shading (WS) occurs when the sun is on the windward side of canyons. The canyon width l_0 = 18 m, and the building height h_0 = 18 m for the regular canyon and h_0 = 36 m for the deep canyon, respectively. θ_1-θ_4 represent different angles of solar zenith, resulting in half-shaded regular and deep canyons, respectively. When AR = 1 canyon is half-shaded, AR = 2 canyon is in deep shade (grey shading); when AR = 2 canyon is half-shaded, AR = 1 canyon is partially shaded (yellow shading). In-canyon vortices are also shown (curved arrows).

Assuming the prevailing wind blows from the screen-left to the screen-right, we index the in-canyon m×n boxes using "k" for the ordinate and "i" for the abscissa directions, starting from the bottom-left (i.e., $Box_{[1,1]}$) toward top-right (i.e., $Box_{[m,n]}$). Thereby, concentrations of q^{th} species within $Box_{[k,i]}$

and within the entire canyon are represented by $C_{q,[k,i]}$ and $C_{q,0}$, respectively. Pollutant mass exchange between neighbouring boxes within street canyons occurs through two key physical processes: advective transport, which is represented by an upwind scheme (referred to "advective velocity"), and turbulent mixing that defined by Fick's law (referred to as "turbulent velocity"); mass exchange between canyons and the overlying background is dominated by turbulent transfer (BrightBloss and Cai, 2013, ZhongCai and Bloss, 2017). A linear relationship is assumed between in-canyon dynamics and prevailing wind velocities (Murena et al., 2011, BarlowHarman and Belcher, 2004a). A flowchart (Figure 3.10) in Supporting Information, Chapter 3.5, is presented to describe the components of the MBM-FleX, and more information including mathematical descriptions has been detailed in a previous work (Dai et al., 2021b). The code is available in both R (e.g., version 3.6.2, R Core Team (2019)) (https://github.com/ddyyqq112233/StreetX-CTM) and Fortran 90 (using the Intel Fortran (IVF) Compiler), respectively.

3.2.2 Model configuration

(1) Street canyon geometry

Canyon geometries are taken from previous LES configurations, with the regular canyon having a street width of l_0 = 18 m and a building height of h_0 = 18 m, and with the deep canyon having l_0 = 18 m and h_0 = 36 m, respectively (GraweCai and Harrison, 2007, Cai, 2012b, Cai, 2012a). A cartesian grid used here has an x-axis that is perpendicular to the canyon and a z-axis that is vertical to the canyon. Therefore, the box resolution for both

regular (4 × 4, 16 boxes) and deep (4 × 8, 32 boxes) canyons in x, z directions was Δx = 4.5 m, Δz = 4.5 m, respectively, which means that each MBM-FleX box contains 225 LES mesh elements within street canyons.

(2) Airflow within canyons

Airflow field in street canyons is difficult to simulate, and it varies with factors such as building geometry, in-canyon trees, and Re number. A primary clockwise vortex and two counter-rotating vortices are observed within regular and deep canyons, respectively (BrightBloss and Cai, 2013, ZhongCai and Bloss, 2017, Garmory et al., 2009, BaikKang and Kim, 2007), however, a single-vortex flow regime may also be found in deep canyons when the independence of Re is fulfilled (Yang et al., 2021b, Yang et al., 2020, ChewAliabadi and Norford, 2018b). In this study, we applied dynamical parameters (Tables S1-S2 in Appendix A) derived from available LES results for idealised regular and deep canyons without any in-canyon obstructions or green walls (c.f., BrightBloss and Cai (2013)), which represent flow characteristics with Re of $\sim 10^6$ at a prevailing wind speed of U_0 = 2 m s^{-1} in the neutral atmosphere. This also indicates the inlet boundary conditions are pre-defined, as used in the LES configuration, including a cyclic condition for the airflow in the both the x- and y- directions. The near-wall treatment (Schlichting and Kestin, 1961) was used for the flow, and a zero-flux condition was applied to all chemical species on the solid boundaries. More details and parameter derivation processes are presented in ZhongCai and Bloss (2017) and Dai et al. (2021b).

(3) Chemical mechanism

Two chemical schemes are applied into model simulations accounting for urban canyon chemistry, the first is a purely inorganic NO_x-O_3 chemistry that consists of reactions (3.1)-(3.3), below (Carpenter et al., 1998):

$$NO_2 + h\nu(\lambda < 410\text{nm}) \rightarrow NO + O(^3P) \quad (3.1)$$

$$O(^3P) + O_2 + M \rightarrow O_3 + M \quad (3.2)$$

$$O_3 + NO \rightarrow NO_2 + O_2 \quad (3.3)$$

here $h\nu$ represents the energy absorbed by the reactants where h is Planck's constant and ν is the frequency of the absorbed light, M signifies a third-body molecule that absorbed surplus energy, reuniting O_2 and $O(^3P)$ (i.e. O atoms without any excess energy that almost only are able to participate in the reaction 3.2) to produce an O_3 molecule. The other is a reduced chemical scheme (RCS) with 51 gas-phase species and 136 reactions derived from the Common Representative Intermediates mechanism version (CRI*v*2-R5) (Watson et al., 2008), including production of NO_2 by interaction of NO with hydroperoxyl radicals (HO_2) and peroxyl radicals (RO_2, where R is an organic molecule). Initially, model simulations were confined to midsummer daytime, and photolysis rates were derived using a two-stream isotropic scattering model at a 0.5 km altitude and a middle latitude (i.e. Birmingham, UK) under clear conditions (Table 3.1). BrightBloss and Cai (2013) presented full RCS details and its evaluation against CRI*v*2-R5 and the Master Chemical Mechanism (MCM*v*3) (Saunders et al., 2003).

Table 3.1. Photochemical reactions and their reaction rate coefficients (*J*-values) at 293 K included in the Reduced Chemical Scheme (RCS).

Order	Reactions	*J*-values	Type
1	$O_3 \rightarrow OH + OH$	3.40×10^{-6}	Inorganic
2	$H_2O_2 \rightarrow OH + OH$	7.11×10^{-6}	Inorganic
3	$NO_2 \rightarrow NO + O_3$	9.20×10^{-3}	Inorganic
4	$NO_3 \rightarrow NO$	2.34×10^{-2}	Inorganic
5	$NO_3 \rightarrow NO_2 + O_3$	1.83×10^{-1}	Inorganic
6	$HONO \rightarrow OH + NO$	2.02×10^{-3}	Inorganic
7	$HNO_3 \rightarrow OH + NO_2$	6.30×10^{-7}	Inorganic
8	$HCHO \rightarrow CO + HO_2 + HO_2$	3.05×10^{-5}	Organic
9	$HCHO \rightarrow H_2 + CO$	4.61×10^{-5}	Organic
10	$CH_3CHO \rightarrow CH_3O_2 + HO_2 + CO$	5.07×10^{-6}	Organic
11	$CARB_7 = CH_3CO_3 + HCHO + HO_2$	3.36×10^{-6}	Organic
12	$HOCH_2CHO = HCHO + CO + HO_2 + HO_2$	1.77×10^{-5}	Organic
13	$UCARB10 = CH_3CO_3 + HCHO + HO_2$	1.62×10^{-5}	Organic
14	$CARB6 = CH_3CO_3 + CO + HO_2$	1.26×10^{-4}	Organic
15	$UCARB12 = CH_3CO_3 + HOCH_2CHO + CO + HO_2$	1.62×10^{-5}	Organic
16	$CH_3NO_3 = HCHO + HO_2 + NO_2$	8.96×10^{-7}	Organic
17	$CH_3OOH = HCHO + HO_2 + OH$	5.44×10^{-6}	Organic
18	$CH_3CO_3H = CH_3O_2 + OH$	5.44×10^{-6}	Organic
19	$HOCH_2CO_3H = HCHO + HO_2 + OH$	5.44×10^{-6}	Organic
20	$RU14OOH = UCARB12 + HO_2 + OH$	1.37×10^{-6}	Organic
21	$RU14OOH = UCARB10 + HCHO + HO_2 + OH$	4.07×10^{-6}	Organic
22	$RU12OOH = CARB6 + HOCH_2CHO + OH$	5.44×10^{-6}	Organic
23	$RU10OOH = CH_3CO_3 + HOCH_2CHO + OH$	5.44×10^{-6}	Organic
24	$HOC2H4OOH = HCHO + HCHO + HO_2 + OH$	5.44×10^{-6}	Organic
25	$RN9OOH = CH_3CHO + HCHO + HO_2 + OH$	5.44×10^{-6}	Organic

(4) Emissions

In this study, we take a busy midsummer weekday traffic scenario for a reference run (denoted as "RR") with U_0 = 2 m s^{-1} and 1,500 on-road vehicles

per hour at an average speed of 30 mph in Birmingham, UK, which is consistent with previous LES configurations (see, ZhongCai and Bloss (2017), BrightBloss and Cai (2013)); the primary NO_2: NO_x ratio (f_{NO_2}) is taken as 0.1, as has been used in previous works (BrightBloss and Cai, 2013, ZhongCai and Bloss, 2014, ZhongCai and Bloss, 2015). The emission rates of NO_x, VOCs, and CO are 620, 127, and 1,356 g km^{-1} hr^{-1}, which equate respectively to 4.44, 16, and 3.52 ppb s^{-1} for a model grid and are denoted as the "Typical Emission Scenario" (TES); VOC fractions are determined based on the annual emission mass, photochemical ozone creation potential (POCP) weighted mass and OH reactivity (BrightBloss and Cai, 2013, Boulter et al., 2009), which is 44% (1.55 ppb s^{-1}) for ethene (C_2H_4), 19% (0.67 ppb s^{-1}) for propene (C_3H_6), 25% (0.88 ppb s^{-1}) for formaldehyde (HCHO), and 12% (0.42 ppb s^{-1}) for acetaldehyde (CH_3CHO); only NO_x emissions are considered for the simple NO_x-O_3 chemistry.

(5) Other configurations and data processing

The initial concentrations of chemical species at t = 0 min (e.g., 1.3 ppb for NO, 6.78 ppb for NO_2, and 49.99 ppb for O_3) are obtained from the Tropospheric ORganic Chemistry experiment (TORCH) field campaign in suburban London (Lee et al., 2006). The multi-box models have been 'spun-up' for 30 min without any emissions to generate important atmospheric intermediates, and all chemical species at t = 30 min are adopted as the boundary condition (e.g., 2.5 ppb for NO, 5.6 ppb for NO_2, and 51.2 ppb for O_3) in the layer above the street canyon. Subsequently, the model is run over 210 min with emissions and chemistry, using a 0.03 s timestep, to achieve dynamical steady-state and

chemical quasi-equilibrium.

Additionally, buildings, road surfaces, and in-canyon vegetations provide substantial area for reactants to deposit. Reactants may undergo chemical transformations upon deposition, potentially forming new compounds or being removed from the atmospheric phase. For example, NO_2 can undergo heterogeneous reactions to produce nitric acid (HNO_3) and other nitrogen-containing compounds. Including deposition terms in the model ensures that these surface interactions are considered, leading to more accurate predictions of reactant concentrations. However, due to the lack of deposition rates, the deposition term has been omitted in the current analysis.

3.2.3 Model scenarios

Table 3.2 summaries all simulated scenarios in the regular and deep canyons. Here we consider three typical scenarios for the relative direction of wind perpendicular to idealised 2D urban canyons and the sunshine throughout the daytime: (1) the leeward shading "LS" (Figure 3.1a and 3.1d) indicates that street canyons beneath the top-right triangle are shaded; (2) no shading "NS" (Figure 3.1b and 3.1e) indicates that no shading effects in street canyons; and (3) the windward shading "WS" (Figure 3.1c and 3.1f) indicates that street canyons beneath the top-left triangle are shaded. In cases LS and WS, the angle of sun zenith is assumed to stay at 45 degree, θ_1 (i.e., red line in Figure 3.1a and Figure 3.1d) and θ_3 (i.e., red line in Figure 3.1c and 3.1f), for regular and deep canyons, respectively, consequently the regular canyon has been half-shaded, and three quarters of the deep canyon have been shaded (see, grey plus yellow

areas). A critical factor to consider in this 2D geometry is the solar zenith angle. For each shading scenario (LS and WS) for the regular and deep canyons, we adjusted the solar zenith angle respectively to 67.5 degree, θ_2 and θ_4, to investigate its impact on chemical processes, that is, the shaded area shrinks to the yellow area from red lines to black oblique lines. Although clouds scatter solar radiation and have daytime radiative cooling effects on urban areas (MorrisSimmonds and Plummer, 2001, Nilsson and Niklasson, 1995, Weng and Fu, 2014), that is not our focus here; we assume clear conditions (i.e., cloud free, no precipitation) throughout model simulations. Therefore, the distinct shading areas defined by the shading scenario and the solar zenith angle are highly temporal-dependent. Modelling results estimated by the MBM-FleX at t = 240 min are used for further analysis.

The first-order rate coefficients for photochemistry (J-values) are assigned individually in each box of the MBM-FleX. For the no shading "NS" modelling scenarios, raw J-values in Table 3.1 are applied for RCS photochemical reactions and the value of reaction (3.1) is applied for the simple NO_x-O_3 chemistry in the unshaded areas, respectively. According to Finlayson-Pitts and Pitts Jr (1999), these values are scaled by 25% in the fully shaded grids and are scaled to the proportion of shading areas in the partially shaded grids, which is given by:

$$J_r = 0.25 \times J_r \times SA_f + \left(1 - SA_f\right) \times J_r = J_r\left(1 - 0.75 \times SA_f\right) \quad (3.4)$$

where J_r is J values for the r^{th} photochemical reaction, SA_f is the fraction of the shaded area in the grid. Non-photochemical reaction rate coefficients are kept

unchanged since the solar heating only raises air temperature by around 2-3 Kelvin (Liu et al., 2021, Bourbia and Awbi, 2004). VOC chemistry is an important contributor to the formation of NO_2 and O_3 in deep canyons (see ZhongCai and Bloss (2017)). The difference between to the two chemical schemes (i.e., reactions (3.1)-(3.3) vs. the VOC scheme) in unshaded conditions has been discussed elsewhere (Dai et al., 2022b); here our focus is on how the choice of chemical scheme influences the calculated shading effects.

In this study, we also discuss the effect of shading magnitude on concentrations within street canyons. Here the origin *J*-values in unshaded grids are multiplied by a factor of 0%, 25%, 50%, and 75% in the fully shaded grids, respectively. In order to investigate the influence of prevailing wind speed (U_0) on shading effects, *J*-values are held at a quarter of their original magnitudes in those fully shaded grids, while U_0 has been altered by ±40% from the RR (U_0 = 2 m s^{-1}) to 1.2 m s^{-1} (denoted as "LR") and 2.8 m s^{-1} (denoted as "HR"), respectively. Moreover, vehicular emissions are influenced by both traffic conditions and lane loading capability (e.g., the width of the carriageway). While maintaining U_0 = 2 m s^{-1} (thus, dynamical patterns within the canyon) and 25% *J*-values in the fully shaded grids, NO_x and VOC emission rates are normalised (i.e., $E_q/E_{q,\mathrm{TES}}$, where q refers to the q^{th} species) by a factor of 0.05-1.0 in a step of 0.05 (i.e., 0.05, 0.10, …, 0.95, 1.0), respectively, which comprises overall 400 model simulations with different NO_x/VOC ratios.

Table 3.2. Summary of all scenarios simulated in the idealised regular and deep canyons. Note that the model operations have been conducted for each combination of variables, respectively.

V1 Shading scenarios (9)
NS: no shade
LS: leeward shading with a solar zenith angle of 45 degree
LS: leeward shading with a solar zenith angle of 67.5 degree
WS: windward shading with a solar zenith angle of 45 degree
WS: windward shading with a solar zenith angle of 67.5 degree
V2 Chemical scenarios (2)
Simple NO_x-O_3 cycle
Reduced Chemical Scheme with volatile organic compound (VOC) free radical reactions
V3 Emission scenarios (400)
NO_x emissions: 20 scenarios from low to high emissions
VOC emissions: 20 scenarios from low to high emissions
V4 Shading intensities (5)
J-values: 100%; 75%; 50%; 25%; 0%
V5 Prevailing wind speed (3)
Prevailing wind speed: 1.2 m s^{-1}; 2 m s^{-1}; 2.8 m s^{-1}

3.3 Results and Discussion

3.3.1 Effects of shading and solar zenith angles

Half of the regular canyon and three quarters of the deep canyon is shaded when the solar zenith angle is at θ_1 for LS and θ_3 for WS. In such condition, Figure 3.2 and Figure 3.3 respectively present the spatial distribution of

concentrations for NO_2 and O_3, and their disparities between shaded and unshaded (NS) scenarios along the leeward ($-0.5 < x/l_0 < -0.25$) and windward ($0.5 < x/l_0 < -0.25$) facades of the regular and deep canyons. The canyon averaged NO_2 and O_3 (and thus, O_x) differences alter very slightly (< 1 ppb in both regular and deep canyons) as the solar zenith angle moves from LS (solid lines) to WS (dashed lines), which suggests little difference in pollution mass transfer from street canyons to the upper background when the solar zenith angle is such that the regular canyon is half-shaded. However, LS and WS obviously affect the spatial distribution of pollutants within street canyons. Following the course of the primary vortex in the regular canyon (Figure 3.2), NO_2 and O_3 differences due to the shading grow more pronounced when the air passes through the shaded area, but soon lessen quickly as the air reaches the unshaded area. Therefore, LS has a greater influence on ground concentrations on the leeward side ($Box_{[1,1]}$), while WS has a greater influence on the windward side ($Box_{[1,4]}$). Moreover, shifting from the LS to WS in the regular canyon, the ground NO_2 differences with respect to the unshaded run range from 5.0 ppb (5.3%) to 2.8 ppb (2.9%) on the leeward side and from 1.2 ppb (1.9%) to 6.1 ppb (9.5%) on the windward side; while the ground O_3 difference decreases range from -7.5 ppb (-67.4%) to -5.1 ppb (-46.0%) on the leeward side and from -2.8 ppb (-22.2%) to -7.7 ppb (-61.2%) on the windward side, respectively. With the air moving toward the unshaded area near the rooftop, concentration differences is smaller than those at the pedestrian level due to the enhanced photodissociation, which is consistent with LES modelling (c.f., GraweCai and Harrison (2007)).

In the deep canyon (Figure 3.3), the upper vortex is formed by the turbulent effect induced by wind shear near the building rooftop (ZhongCai and Bloss, 2015), just as for the regular canyon, resulting in similar (but more pronounced) NO_2 and O_3 patterns under the different shading scenarios. For the LS, NO_2 and O_3 concentration differences are up to 7.2 ppb (5.4%) and -9.7 ppb (-67.4%) in $Box_{[1,6]}$ on the leeward side. For the WS, the differences are up to 8.5 ppb (7.9%) and -10.4 ppb (-63.3%) in $Box_{[4,6]}$ on the windward side, respectively. The differences decline rapidly in the lower compartment within which a minor counterclockwise vortex is generated by wind shear at the middle of the canyon, and the shading effects become less important as the lower compartment has been fully shaded under both LS and WS. NO_2 decreases somewhat (< 2 ppb) as a result of reduced contributions from VOC chemistry; that is, the production of HO_2 and RO_2 has been reduced under the shading scenarios. O_3 levels at the lower compartment stay rather stable because its production and maintenance in this area are not significantly hindered by the lack of direct sunlight. The concentration of O_x decreases slightly (< 2 ppb) because of the formation of nitric acid (HNO_3) insides deep canyons.

Considering the solar zenith angle at which the deep canyon is half-shaded (θ_2 and θ_4), Figure 3.4 shows the spatial distribution of concentration differences for NO_2, O_3, and O_x within the regular canyon along the leeward and windward facades. In comparison to the "half-shaded regular canyon" scenario (Figure 3.2), the spatial distribution of pollutant differences is similar, although ground NO_2 and O_3 differences are somewhat decreased under

varying shading conditions. When full sunlight crosses through both the upper clockwise and lower anti-clockwise vortices of the deep canyon (Figure 3.5), NO_2 and O_3 reduce substantially under the shading scenarios, leading to larger concentration differences. From LS (θ_2) to WS (θ_4), ground NO_2 differences slightly increase from -1.4 ppb (-0.9%) to -3.2 ppb (-2.0%) on the leeward side and from -13.8 ppb (-5.2%) to -16.1 ppb (-6.1%) on the windward side. Ground O_3 differences change from -11.0 ppb (-75.4%) to -8.1 ppb (-55.6%) on the leeward side and from -5.0 ppb (-59.5%) to -6.4 ppb (-77.1%) on the windward side, respectively.

Our results show that shading effects modify the spatial distribution of reactive species within street canyons depending on the canyon geometry and solar zenith angle. Interestingly, although NO_2 photodegradation rate has been reduced from 9.20×10^{-3} s^{-1} to 2.30×10^{-3} s^{-1} when the deep canyon is half-shaded, NO_2 concentrations within the deep canyon become lower by up to ~9% because of the shade. Also, O_x is a useful measure of the street canyon chemistry and its difference due to the shade decreases slightly in the regular canyon but decreases substantially up to 23 ppb (~7%) inside the deep canyon, which can be attributed to the inclusion of VOC chemistry as it becomes more important when air residential time is longer. This is further discussed in the following section by model simulations using the simple NO_x-O_3 chemistry.

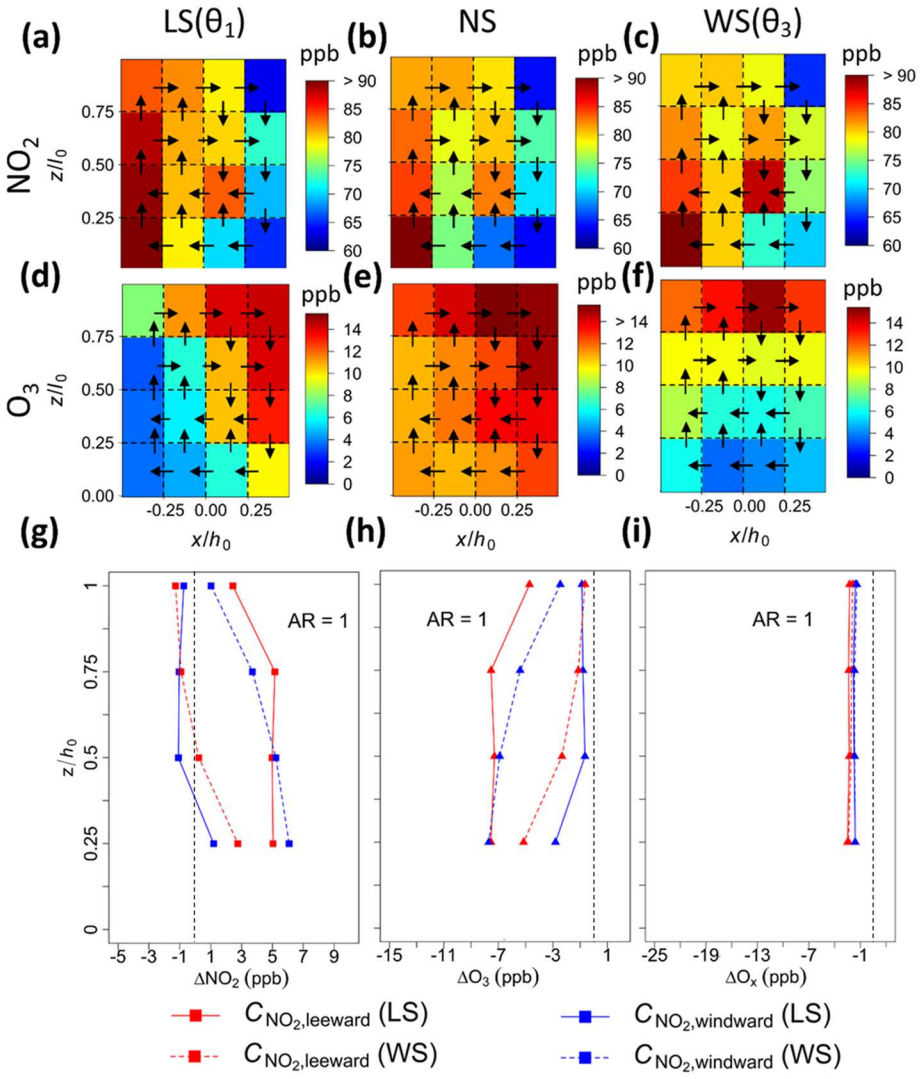


Figure 3.2. The spatial distribution of NO_2 and O_3 (ppb) under the lee-side (θ_1) and wind-side (θ_3) shading with a quarter of original *J*-values of RCS chemistry in the regular canyon (hereafter, first and second rows). Line graph panels a-c present concentration differences with respect to a no-shading simulation (values of shaded situations LS and WS subtracted from those of the unshaded scenarios NS) for NO_2, O_3, and O_x in the regular canyons, respectively. The solar zenith angle is such that the regular canyon is half-shaded. Subscripts "leeward" and "windward" represent the magnitude of differences along with the leeward wall ($-0.5 < x/l_0 < -0.25$) and the windward wall ($0.25 < x/l_0 < 0.5$), respectively. Arrows give an illustration of the advective flow in the canyon. See text for details. Dashed line indicates there is no difference between modelling scenarios.

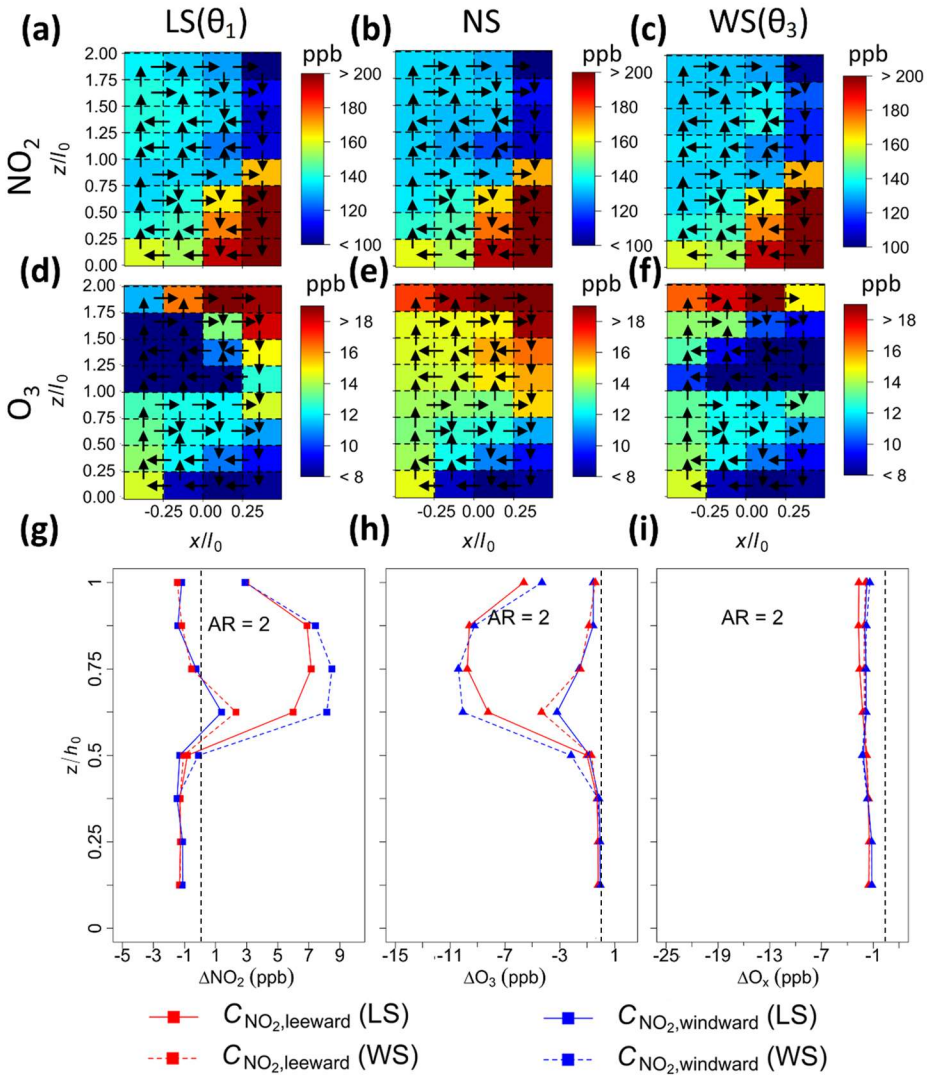


Figure 3.3. The spatial distribution of NO_2 and O_3 (ppb) under the lee-side (θ_1) and wind-side (θ_3) shading with a quarter of original *J*-values of RCS chemistry in the deep canyon. Line graph panels a-c present concentration differences with respect to a no-shading simulation (values of shaded situations LS and WS subtracted from those of the unshaded scenarios NS) for NO_2, O_3, and O_x in the deep canyon. The solar zenith angle is such that the regular canyon is half-shaded. Subscripts "leeward" and "windward" represent the magnitude of differences along with the leeward wall ($-0.5 < x/l_0 < -0.25$) and the windward wall ($0.25 < x/l_0 < 0.5$), respectively. Arrows give an illustration of the advective flow in the canyon. See text for details. Dashed line indicates there is no difference between modelling scenarios.

3.3.2 Effects of VOC chemistry

Inclusion of VOCs emissions from on-road vehicles can affect photochemical reactions, especially in deep urban canyons with longer residence times of air pollutants (ZhongCai and Bloss, 2017). CFD-based models, in general, simulate air quality within street canyons or across densely built regions coupled only to a simple NO_x-O_3 cycle to conserve computational resources. Shading affects not only NO_2 photolysis, but also several VOC free-radical reactions (e.g., Table 3.1). Using simple NO_x-O_3 chemistry at different solar zenith angles, Figure 3.6 gives the spatial distribution of concentration differences between the shaded scenarios and the unshaded scenario for NO_2, O_3, and O_x in regular and deep canyons. Figure 3.12 provides the percentage underestimation of NO_2, O_3, and O_x concentrations spatially within street canyons due to shading effects (see Figures 3.12-3.15 for the spatial distribution of absolute values). Considering the shading scenarios, the loss of photon flux causes NO_2 to rise regardless of the solar zenith angle, which can also be observed when VOC chemistry is negligible (e.g., see Figure 3.2a and Figure 3.3a for NO_2 distributions in the regular canyon). When only the simple chemistry is considered, O_x can be regarded as a passive tracer, since changes in NO_2 are compensated by opposite changes in O_3. O_x concentrations are always conserved between the shaded scenarios and the unshaded scenario (Figures 3.6c, 3.6f, 3.6i, 3.6l). Therefore, the magnitudes of O_3 depletion are similar to that of increased NO_2 but opposite in sign (e.g., positive NO_2 and negative O_3 differences accordingly of 5 ppb along the leeward wall under the LS) (GraweCai and Harrison, 2007). Although the spatial distribution of

concentration differences between shading and unshaded scenarios still varies with solar zenith angle, these changes in concentration are less important for NO_2 (up to ~10%) but remain substantial for O_3 (up to ~75%).

Our results indicate not only that simulations using the RCS scheme capture O_3 production or depletion more precisely (Muilwijk et al., 2016), but also the importance of shading effects on NO_2. Reduced photolysis rates constrain the generation of hydroperoxyl radicals (HO_2), thus limiting the synthesis of NO_2 through the oxidation of NO. NO_2 concentrations decrease by 0.1%-7% due to the shading effects when VOC chemistry becomes important (see, Figure 3.5g). Therefore, the RCS model describes the proper mechanics of O_x depletion as a function of the local availability of VOC free radicals and the solar energy, which cannot be simulated by using the simple NO_x-O_3 cycle.

Absolute values of NO_2 and O_3 can be considerably underestimated without considering VOC chemistry, for example, the averaged NO_2 increases from 85 ppb to 136 ppb (37%) and O_3 from 7 ppb to 13 ppb (46%) in the idealised deep canyon (ZhongCai and Bloss, 2017). One might ask whether these disparities, caused by different chemical schemes, can be offset by shading effects. Without shading (i.e., NS), underestimates of NO_2 by using the simple NO_x-O_3 cycle are ~13% and ~41% in the regular and deep canyons compared to those of using VOC chemistry; and underestimates of O_3 are ~20% and ~55%, respectively (Figure 3.5). Considering the effect of including shading on the underestimates of simple chemistry, the magnitude of the underestimate varies with solar zenith angle and canyon geometry. When the regular canyon

has been half-shaded, O_3 underestimates change remarkably to ~35% and ~22% in regular and deep canyons, respectively; when the deep canyon has been half-shaded, the canyon averaged underestimations are similar to those of NS in the regular canyon but decrease to ~37% for NO_2 and to ~31% for O_3 in the deep canyon, respectively. It is worth noting that the underestimate of O_3 varies spatially within street canyons (e.g., ~50% at the pedestrian level and ~15% at the rooftop of the deep canyon). There is no single and simple factor that can be used to bridge the gap between concentration differences due to different chemical schemes, with or without shading, which emphasizes the need to include shading effects along with VOC free-radical chemistry in future air quality simulations.

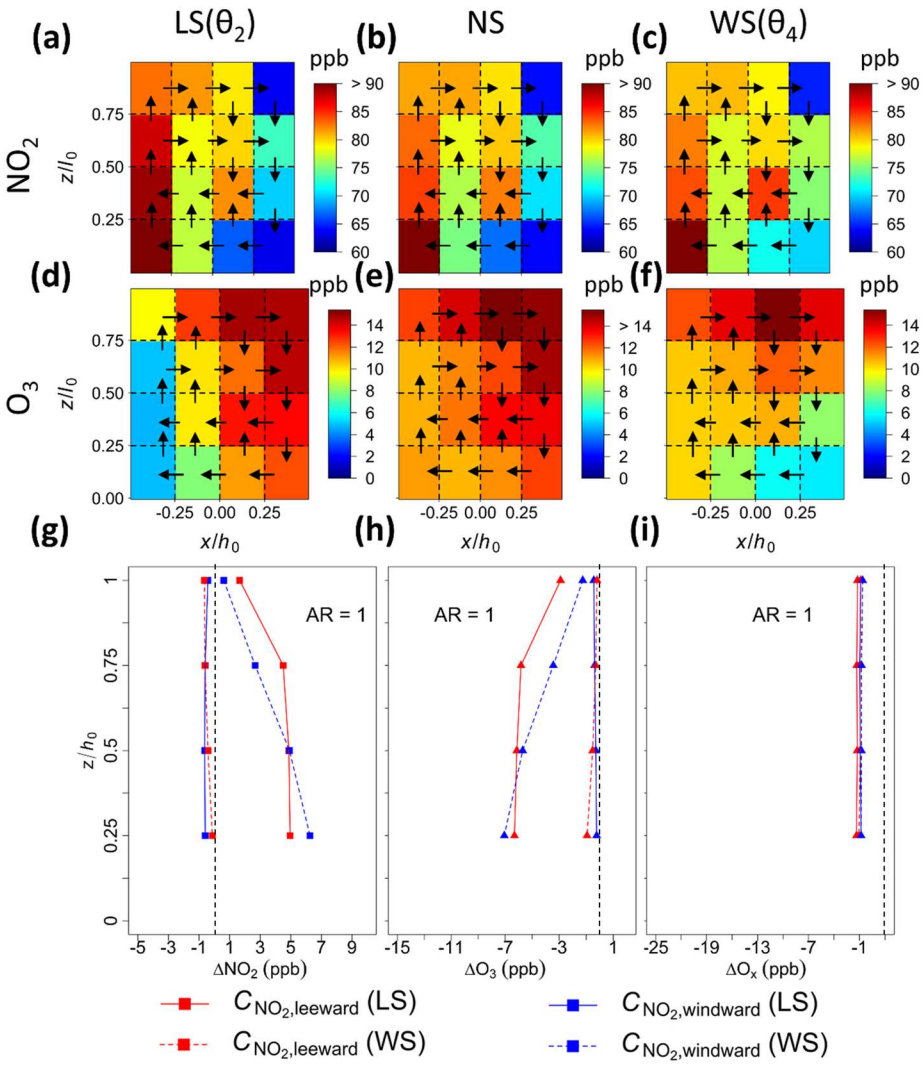


Figure 3.4. The spatial distribution of NO_2 and O_3 (ppb) under the lee-side (θ_2) and wind-side (θ_4) shading with a quarter of original *J*-values of RCS chemistry in the regular canyon. Line graph panels a-c present concentration differences with respect to a no-shading simulation (values of shaded situations LS and WS subtracted from those of the unshaded scenarios NS) for NO_2, O_3, and O_x in the regular canyons, respectively. The solar zenith angle is such that the deep canyon is half-shaded (θ_2 and θ_4). Subscripts "leeward" and "windward" represent the magnitude of differences along with the leeward wall ($-0.5 < x/l_0 < -0.25$) and windward wall ($0.25 < x/l_0 < 0.5$), respectively. Arrows give an illustration of the advective flow in the canyon. See text for details. Dashed line indicates there is no difference between modelling scenarios.

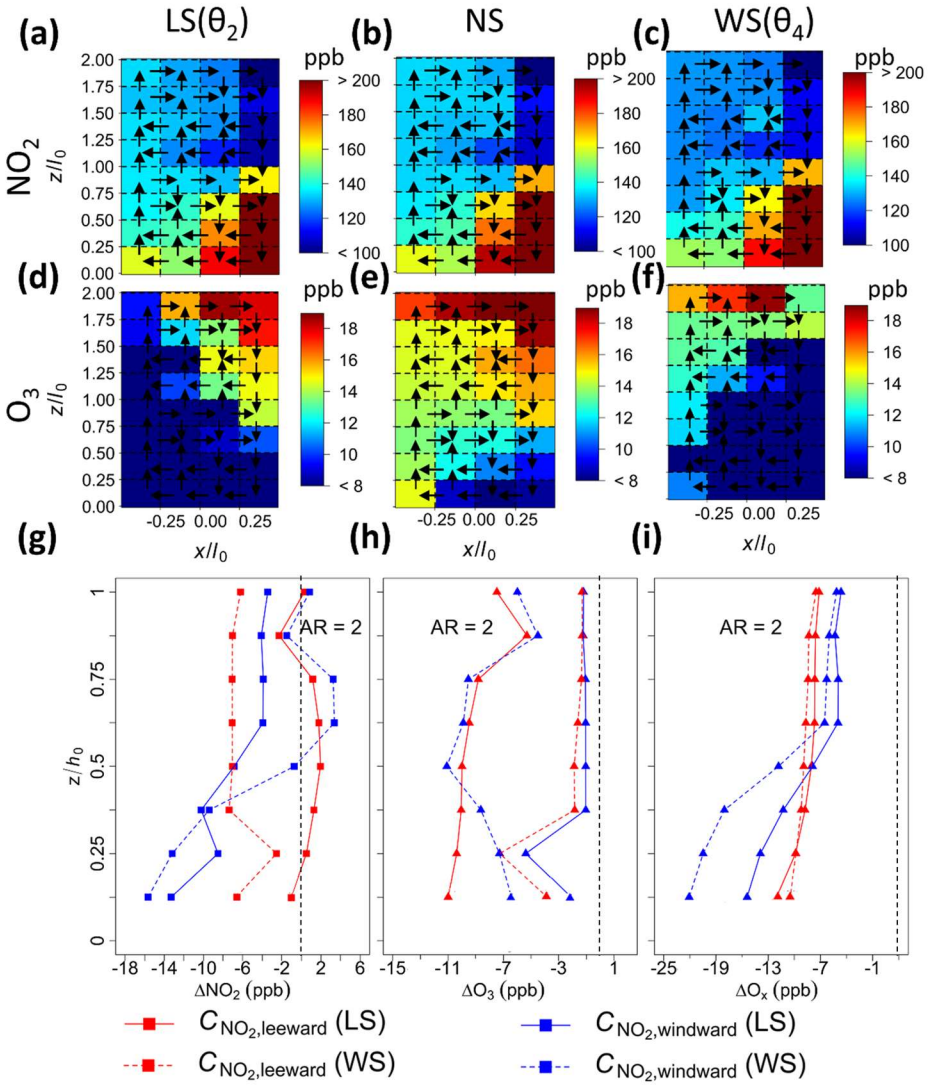


Figure 3.5 The spatial distribution of NO_2 and O_3 (ppb) under the lee-side (θ_2) and wind-side (θ_4) shading with a quarter of original *J*-values of RCS chemistry in the deep canyon. Line graph panels a-c present concentration differences with respect to a no-shading simulation (values of shaded situations LS and WS subtracted from those of the unshaded scenarios NS) for NO_2, O_3, and O_x in the regular canyons, respectively. The solar zenith angle is such that the deep canyon is half-shaded (θ_2 and θ_4). Subscripts "leeward" and "windward" represent the magnitude of differences along with the leeward wall ($-0.5 < x/l_0 < -0.25$) and windward wall ($0.25 < x/l_0 < 0.5$), respectively. Arrows give an illustration of the advective flow in the canyon. See text for details. Dashed line indicates there is no difference between modelling scenarios.

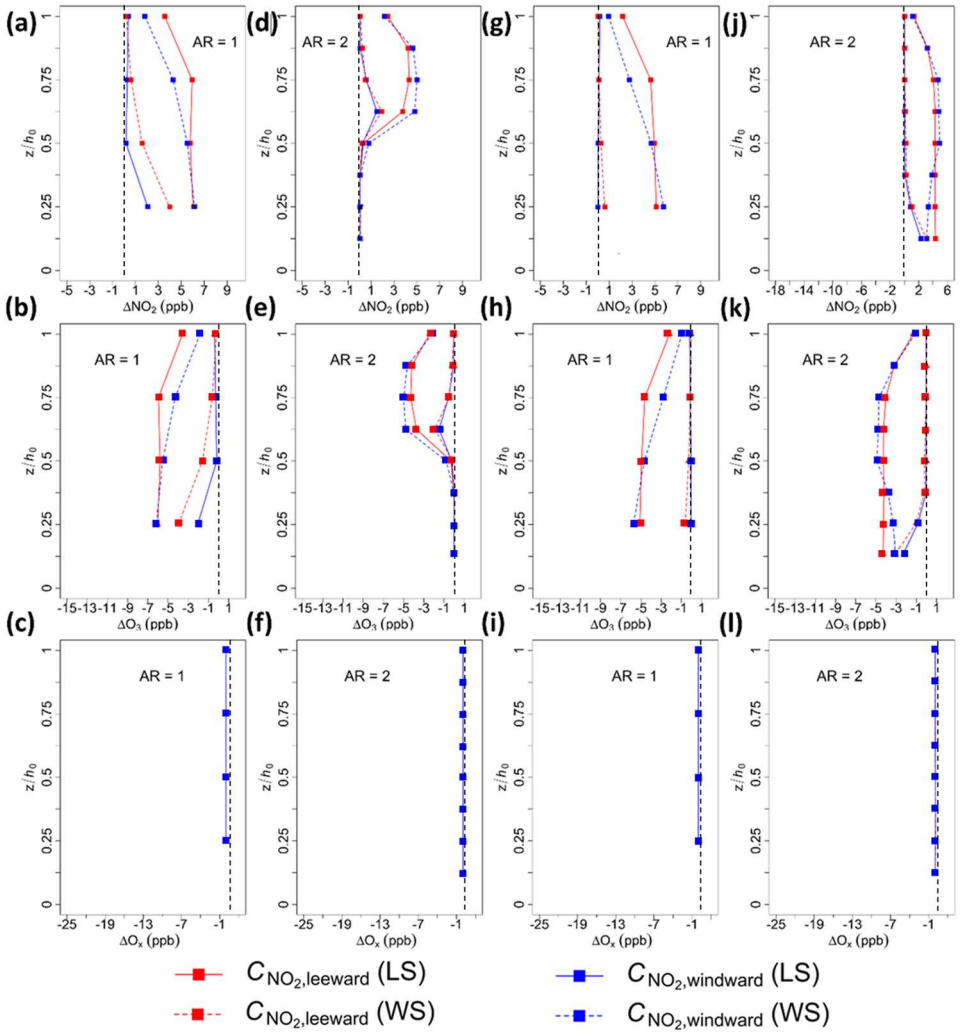


Figure 3.6. The vertical distribution of concentration differences for NO_2, O_3, and O_x in ppb by using the **simple NO_x-O_3 chemistry** in regular (a, b, c, g, h, i) and deep (d, e, f, j, k, l) street canyons. All differences are with respect to a no-shading simulation. The solar zenith angle is such that the regular canyon is half-shaded (θ_1 and θ_3) for figures a-f; and the angle is such that the deep canyon is half-shaded (θ_2 and θ_4) for figures g-l. Subscripts "lee" and "wind" represent the magnitude of differences along with the leeward wall ($-0.5 < x/l_0 < -0.25$) and windward wall ($0.25 < x/l_0 < 0.5$), respectively. Dashed line indicates there is no difference between modelling scenarios.

3.3.3 Effects of NO_x and VOC emissions

The response of atmospheric chemistry to anthropogenic emissions is complex and highly non-linear (Colbeck and MacKenzie, 1994, Seinfeld and Pandis, 2008). It is therefore likely that shading effects will vary with on-road conditions such as vehicle types and emission factors. While greater percentage uncertainties in O_3 concentrations are found under a typical traffic condition (as discussed above), their absolute values are not significant. Nonetheless, shifting traffic emissions also alter the chemistry in the urban environment, potentially yielding more O_3 to the critical level higher than 40 ppb and causing adverse effects on public health and plants (Satsangi et al., 2004, BortierDe Temmerman and Ceulemans, 2000). Therefore, we examined various emission conditions to investigate their impacts on shading effects. Here we adopt percentage differences to assess shading effects on NO_2 and O_3 levels within urban canyons because varying traffic emissions lead to different absolute values of air pollution. Results are illustrated in Figure 3.7 and Figure 3.8 using isopleths similar to those used in O_3-NO_x-VOC sensitivity studies (Sillman, 1999).

Figure 3.7 shows that NO_x and VOC emissions have considerable impact on shading effects in a non-linear fashion when the solar zenith angle is such that the regular canyon is half-shaded, but the pattern changes little with the shading scenarios (i.e., LS and WS). Lower traffic emissions lead to stronger relative changes due to shading on NO_2 by up to ~10% and ~5% in regular and deep canyons, respectively, but result in weaker shading effects on O_3 by up to

~23% and ~13%, respectively. The shading effects on NO_2 are more sensitive to NO_x than they are to VOC emissions, particularly under a high-NO_x circumstance within street canyons, but shading becomes more susceptible to VOCs when NO_x emissions are low. The shading effects on O_3 change very slightly with VOC emissions but increase greatly with increasing NO_x emissions. When the solar zenith angle is such that the deep canyon is half-shaded and the regular canyon is less shaded (Figure 1), the sensitivity of shading effects to emissions decreases in the regular canyon (e.g., varying < 2% for in-canyon NO_2; Figure 3.8) but significantly increases in the deep canyon. In the NO_x-sensitive (or VOC-saturated) zone, the shading effect increases with increasing NO_x emissions and shows relatively little change in response to increased VOC emissions.

The solid line in each panel of Figure 3.7 and Figure 3.8 depicts emission conditions leading to the critical level of NO_2 (105 ppb) and O_3 (40 ppb) without shading, whereas the dashed line gives the critical-level emission conditions with shading. The disparity between the lines indicates that model simulations without shading provide imprecise determination of compliance, particularly for O_3 concentrations within the urban canyon environment. Despite that results indicate that neglecting shade has a little effect on compliance with the air quality threshold for the canyon-average value, it should be noted that half-shading situations with very high VOC:NO_x ratios might be significant if internal combustion vehicles are phased out, removing NO_x but leaving VOC emissions from solvent evaporation and biogenic VOCs, which could be discussed further. Model results for the regular canyon in our

work vary from those of a prior work (GraweCai and Harrison, 2007) because to the existence of VOC free-radical interactions that violate O_x conservation, which suggests the shading effects and VOC free-radical chemical reactions need to be considered properly particularly for the deep canyon modelling.

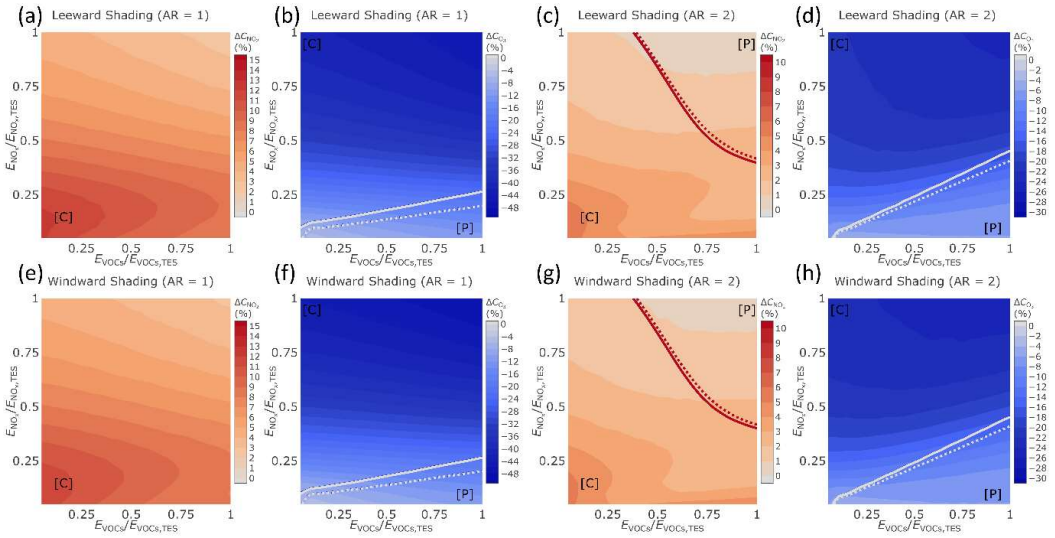


Figure 3.7. The percentage difference (%) in canyon-averaged NO_2 and O_3 due to the shading effects (one quarter of original *J*-values in fully shaded grids) for RCS chemistry in regular and deep canyons at different NO_x and VOC emission rates. The solar zenith angle is such that the regular canyon is half-shaded (θ_1 and θ_3). The solid contour represents the critical level of NO_2 (105 ppb) and O_3 (40 ppb) under the unshaded scenario, and the dash contour represents the critical level under the shaded scenario. The Region "[P]" represents the polluted air zone where air pollution concentrations exceed the objective, and the Region "[C]" represents the clear air zone where the air quality is in compliance with the objective.

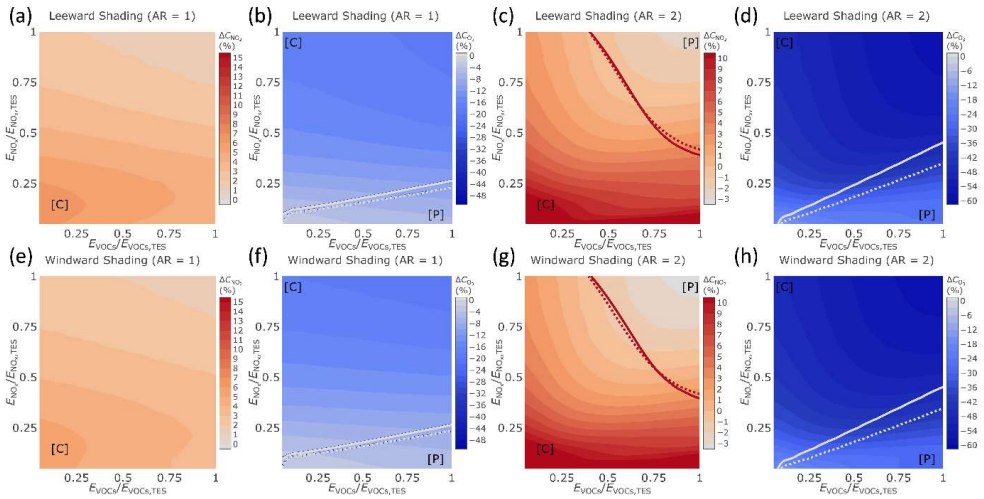


Figure 3.8. The percentage difference (%) in canyon-averaged NO_2 and O_3 due to the shading effects (one quarter of original *J*-values in fully shaded grids) for RCS chemistry in regular and deep canyons at different NO_x and VOC emission rates. The solar zenith angle is such that the deep canyon is half-shaded (θ_2 and θ_4). The solid contour represents the critical level of NO_2 (105 ppb) and O_3 (40 ppb) under the unshaded scenario, and the dash contour represents the critical level under the shaded scenario. The Region "[P]" represents the polluted air zone where air pollution concentrations exceed the objective, and the Region "[C]" represents the clear air zone where the air quality follows the objective.

3.3.4 Effects of shading intensities

Figure 3.9 and Figure 3.16 provide the concentration difference for NO_2 and O_3 between the shaded scenarios (LS and WS) and NS under different chemical schemes with the photolysis rate of various percentages of their original values in shaded grids of street canyons. In the regular canyon, as with GraweCai and Harrison (2007), the shade overall causes increased canyon averaged NO_2 and decreased O_3 (i.e., $C_{NO_2,0}$ and $C_{O_3,0}$, denoted by black lines in our figures) due to

reduced efficiencies of NO_2 photolysis (reaction (3.1), above) and, hence, reduced O_3 formation (Figures 3.9a, 3.9c, 3.16a, 3.16c). There is a nearly linear relationship between concentration differences and the shading magnitude, as those in GraweCai and Harrison (2007), for all shading scenarios and locations shown except NO_2 in the deep-canyon, half-shading scenario (Figure 3.9b).

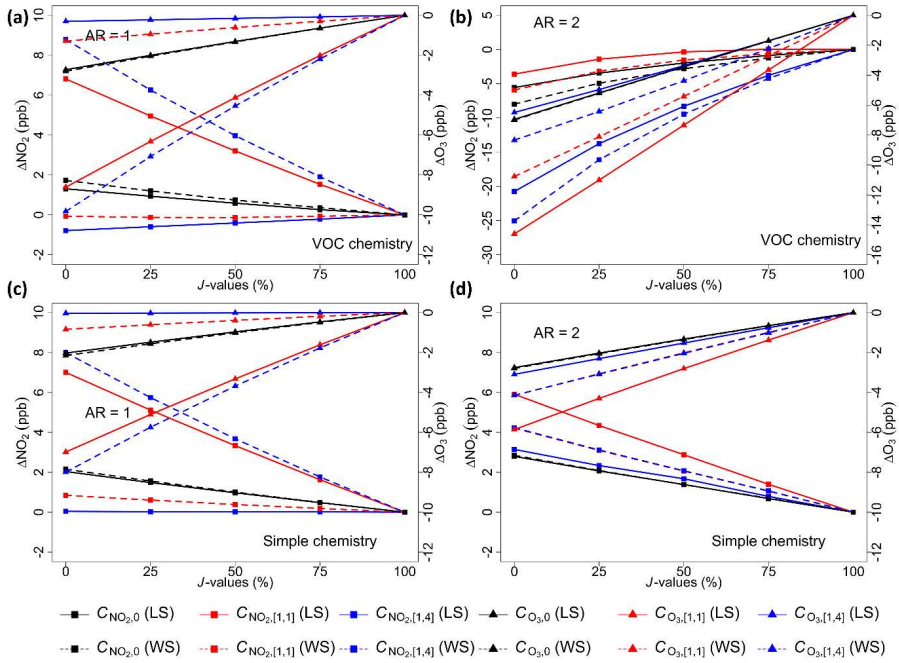


Figure 3.9. Concentration differences in NO_2 and O_3 (ppb) under different photolysis rates in RCS and simple NO_x-O_3 chemistry that denoted by percentages of their original values in regular and deep canyons, respectively. The sun zenith angle is such that the deep canyon is half-shaded and the regular canyon lightly shaded (θ_2 and θ_4). Line colours indicate different locations of street canyons (the entire canyon and the pavement); line types indicate concentrations of different shading scenarios (LS and WS) minus those of NS; and squares and triangles represent NO_2 and O_3, respectively. Note the change of y-axis scales between top-right and bottom-right panels.

In the deep canyon, where chemistry has more time to take place, the relationship between the shading magnitude and NO_2 differences depends on both the solar zenith angle and chemical schemes. Figure 3.9d and Figure 3.17d indicate that the efficiency of NO_2 dissociation alone cannot be responsible for non-linear effects. With VOC free-radical chemistry, a near linear relationship between NO_2 and O_3 concentration differences and the shading magnitude is found when the regular canyon has been half-shaded (i.e., the solar zenith angle is θ_1 or θ_3, Figure 3.17b). However, when the deep canyon is half-shaded (i.e., the solar zenith angle is θ_2 or θ_4), the linear hypothesis between concentrations and the shading magnitude is still valid for O_3 but is not valid for NO_2, because NO_2 differences increase non-linearly with the photolysis efficiency and vary very little throughout a range of shading magnitudes on the lee-side façade in the deep canyon. Therefore, using the simple NO_x-O_3 chemistry can lead to erroneous estimates of air quality and subsequent health impacts, as the simple linear assumption between NO_2 and shade intensity is no longer applicable when VOC free-radical chemistry is involved. This is particularly important for urban networks in mid-latitude with a high density of tall buildings because of sufficient shade and poor ventilation, which highlights the necessity of considering VOC reactions for physicochemical process simulations in the real atmosphere.

3.3.5 Effects of prevailing wind speeds

The prevailing wind speed (U_0) affects the mass exchange efficiency between the street canyon and the overlying background, leading to changes in resident

time of chemical species and in the distribution of pollutant concentrations within street canyons (Murena et al., 2011). Higher U_0 (e.g., 2.8 m s^{-1}) enables not only enhanced rooftop ventilation but also more rapid in-canyon air circulation between shaded and unshaded areas inside the urban canyon (GraweCai and Harrison, 2007), while lower U_0 (e.g., 1.2 m s^{-1}) allows chemistry to occur for longer time (Park et al., 2015). Albeit that using scaled dynamical parameters cannot describe in-canyon airflow characteristics absolutely accurately, the objective here is to investigate in broad terms the impact of canyon ventilation on the shading effects associated with solar zenith angle and canyon geometry. When the regular canyon is half-shaded, absolute shading-non-shading differences for NO_2 and O_3 are small (as shown in Figure 3.18). Increased U_0 leads to markedly lower NO_2 and higher O_3 inside street canyons due to a stronger mixing between the canyon and the background (ZhongCai and Bloss, 2016b). Therefore, considering the percent variance, in the regular canyon, NO_2 reduces somewhat (to ~1%) as a result of shading effects due to decreased efficiency of formation through VOC chemistry at lower U_0, while NO_2 concentrations rise by 5% at higher U_0, because VOC chemistry. Differences in O_3 decrease from ~38% to ~29% with increasing wind speeds. In the deep canyon, the impact of changes in prevailing wind velocity on the shading effects is quite small (< 2%) for NO_2 and O_3 due to its impacts on both physical and chemical processes. When the deep canyon is half-shaded (Figure 3.18), the pattern of concentration changes inside the regular canyon is very similar to that of the "half-shaded regular canyon" condition (i.e., from -1% to 2% for NO_2 and from -20% to -15% for

O_3). The differences drop substantially with increased U_0 in particular for ground NO_2 on the windward side (e.g., from -38 ppb and -32 ppb to -8 ppb for WS and LS, respectively), however, these changes in percentage are small (from ~-8% to ~-4%), because ground NO_2 concentrations can be extremely high (e.g., up to ~230 ppb) in the deep canyon at low U_0 (Murena et al., 2009, ZhongCai and Bloss, 2015). The shading effects on the canyon average O_3 decrease slightly (< 3%) as U_0 increases, but larger wind impacts are observed at different locations inside the canyon (e.g., ~15% along the windward side). Consequently, the impact of prevailing wind speed on shading effects cannot be disregarded because location-specific concentrations need to be predicted accurately to develop targeted and effective strategies.

In this study, MBM-FleX provides a possible method for coupling different chemical schemes to simulate reactive species in urban canyons. Inevitably, the current model has some limitations. Firstly, the dynamical parameters need to be derived from advection and turbulence based on the pre-operated LES results, which indicates that the airflow characteristics are predefined in the MBM-FleX. Secondly, while the resolution of the model is adjustable, a high resolution leads to less segregation effects (ZhongCai and Bloss, 2014, Li et al., 2021) but exponentially increasing the number of dynamical parameters. There is always a trade-off between the amount of meshes and the computation time. Thirdly, MBM-FleX is only applicable when the predominant wind direction is perpendicular to the street axis. In light of these complications, more studies into the shading effects on air quality at street-to-regional scale is necessary to improve the rationale of urban design.

3.4 Conclusions

The poorly ventilated nature of urban canyons leads to frequent occurrences of severe air pollution, thus affecting the health of pedestrians that exposed in such environments. Therefore, urban canyons become "hotspots" areas for air quality regulations. A processed-based multi-box model (MBM-FleX) coupled with chemical schemes was implemented to investigate shading effects on NO_2, O_3, and O_x ($NO_2 + O_3$) within urban street canyons. Our results reveal sometimes large differences between the shaded and unshaded scenarios, demonstrating that the interaction of shading effects, chemical processes, emissions, and tracer transport alter the average magnitude and spatial distribution of air pollution within street canyons. When the solar zenith angle is such that a regular canyon (aspect ratio~1) is half-shaded, NO_2 and O_3 differences caused by the shading effects become more significant as air blows through the shaded areas, but quickly reduced when the air moves into the unshaded areas due to enhanced photochemistry. In the deep street canyon, considering the same angle of incident sunlight, the concentration differences rapidly lessen and the shading effects become less significant in the lower compartment as it is completely shaded on both lee- and wind-side directions. The spatial distribution of pollutants in the regular canyon overall are similar when solar zenith angle changes in this study, while concentration differences within the deep canyon increase significantly.

With the simple NO_x-O_3 chemistry, shade slows the photodegradation of NO_2, causing NO_2 concentrations to increase inside street canyons, while O_3

concentrations always vary in an opposite manner due to O_x conservation. Our results reveal that VOC chemistry can be of importance in modelling shading effects in terms of its impact on, in particular, O_x concentrations in street canyons, which becomes crucial when the generation of NO_2 from the oxidation of NO with hydroperoxyl radical (HO_2) is limited. Additionally, the difference in O_3 between shaded and unshaded scenarios is linearly related to shading intensity, but the shaded-unshaded difference in NO_2 is not linearly related to shading intensity, especially in deep canyons with longer time for photochemistry to occur. Prevailing wind speeds also have a location-specific influence on concentration differences due to the shade. These difficulties suggest that one cannot simply use a proxy to simulate shading effects on street-canyon air quality. The relatively strong effect on street canyon ozone could also have implications for the production of Highly Oxidized Molecules (HOMs), and so for new particle formation, but this requires further investigation with an extend chemistry scheme that includes the ozonolysis of alkenes and aromatics (e.g., Rissanen et al. (2014)) and is outside the scope of the present study.

Ultimately, the results above should be modelled in combination with effects on tracer transport, such as the impact of heating (e.g., Cai (2012b)) and enhanced wall roughness (e.g., in-canyon green infrastructures, Buccolieri et al. (2018)). Nevertheless, this study provides an initial quantification of shading effects on reactive air pollutants under various solar zenith angles, chemical schemes, traffic conditions, canyon geometry, and shading intensities. The findings provide steer for developing air quality models and

proposing air quality solutions for urban hotspots. The technique utilised in this study is applicable for assessing the shading effects in the non-neutral atmosphere when pre-generated LES parameters are available to provide the dynamical input parameters, it allows a fast computation of a large number of scenarios without loss of sufficient spatial resolution and representation of transport, mixing, and chemical processes, and can be further expanded into a user friendly toolkit for street network air quality simulations.

3.5 Supporting Information

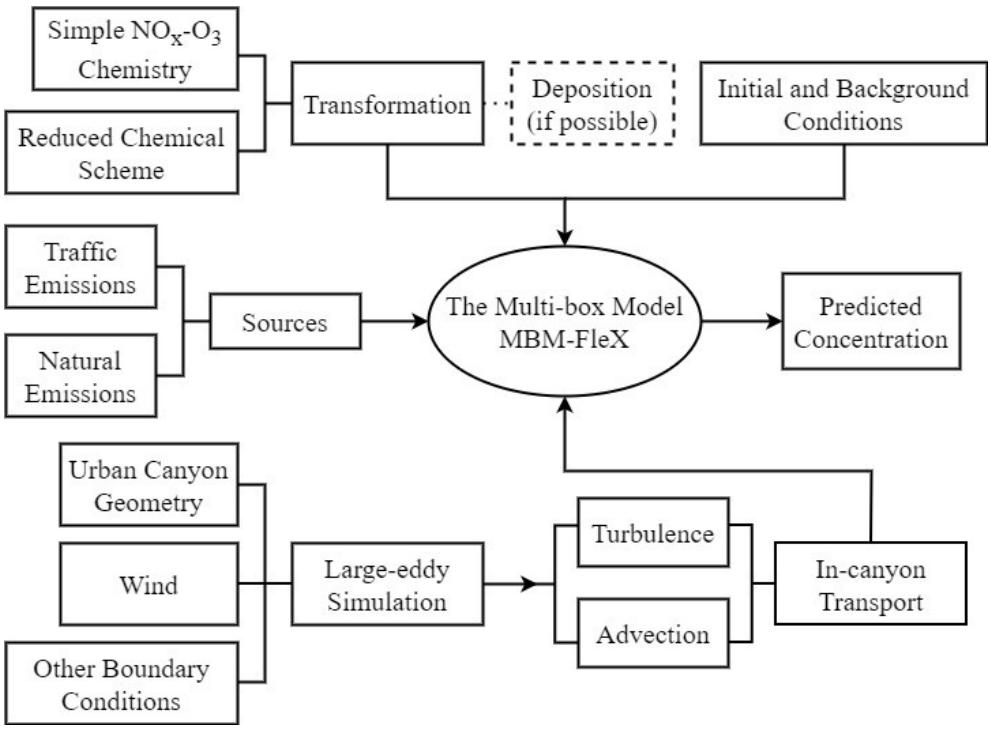


Figure 3.10. Components of the multi-box model MBM-FleX for urban canyon air quality modelling.

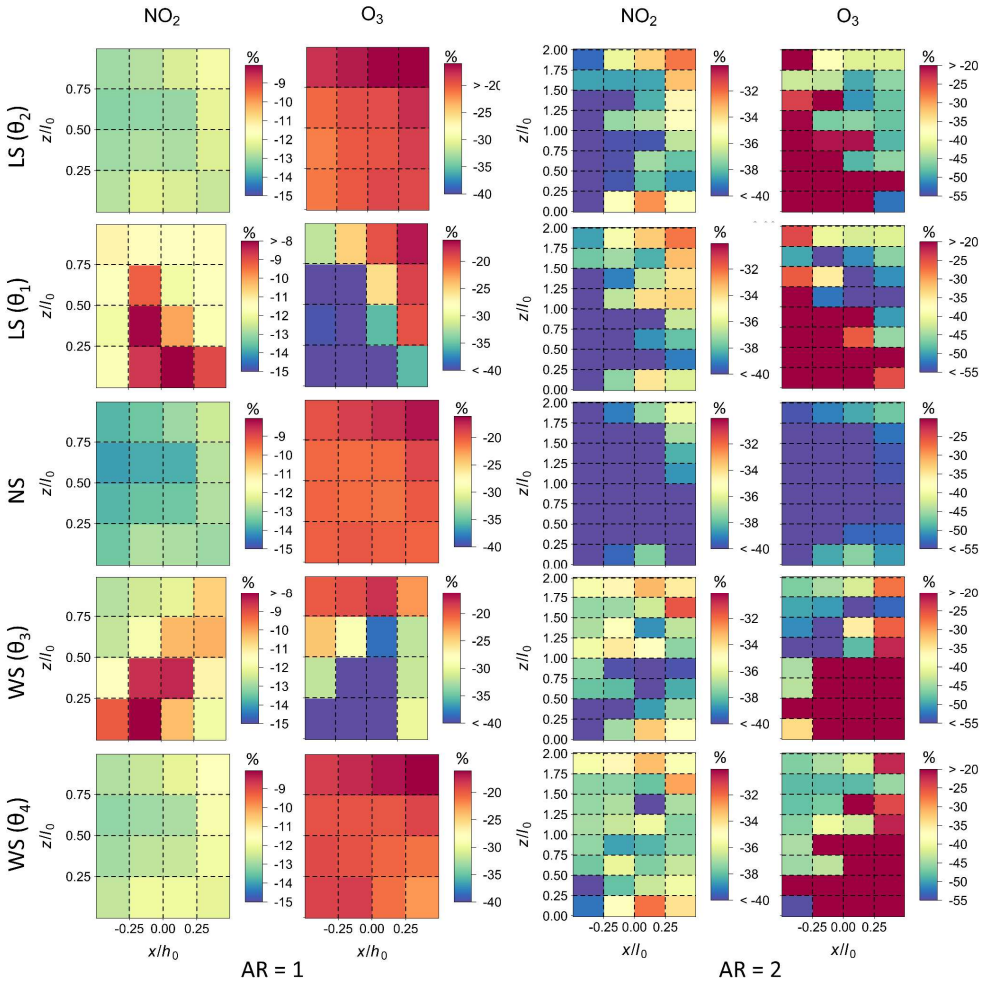


Figure 3.11. The underestimation of NO_2 and O_3 concentrations in percentage (%) by the multi-box models with the simple NO_x-O_3 chemistry compared to those of VOC free-radical chemistry under different shading scenarios and solar zenith angles (θ_1 to θ_4), respectively.

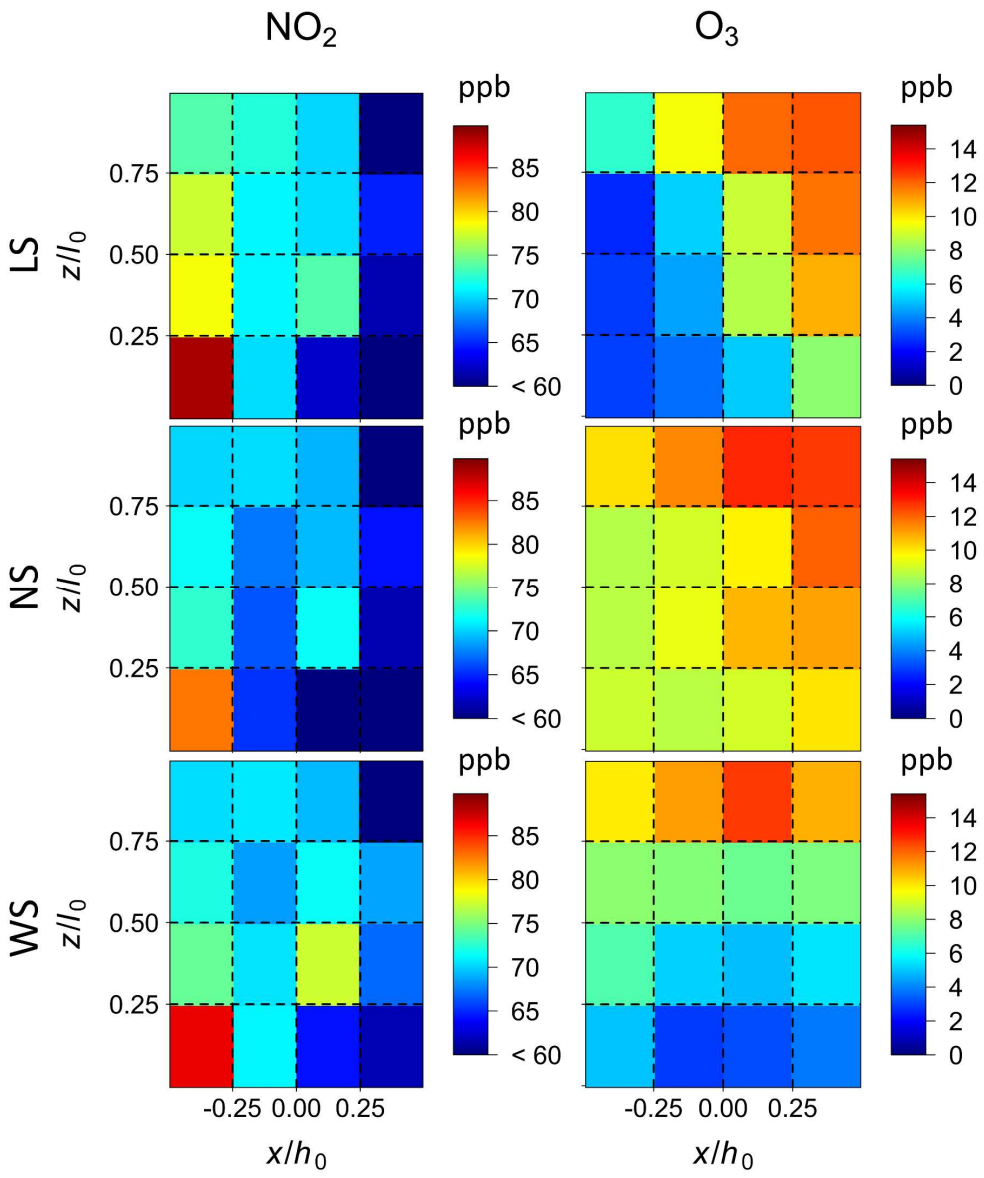


Figure 3.12. The spatial distribution of NO_2 and O_3 concentrations (ppb) with a quarter of original *J*-value of the simple NO_x-O_3 chemistry in fully shaded grids in the regular street canyon. The solar zenith angle is such that the regular canyon is half-shaded (θ_1 and θ_3). Subscripts "leeward" and "windward" represent magnitude of differences along with the leeward wall ($-0.5 < x/l_0 < -0.25$) and the windward wall ($0.25 < x/l_0 < 0.5$), respectively. LS, WS, and NS represent different shading scenarios. See text for details.

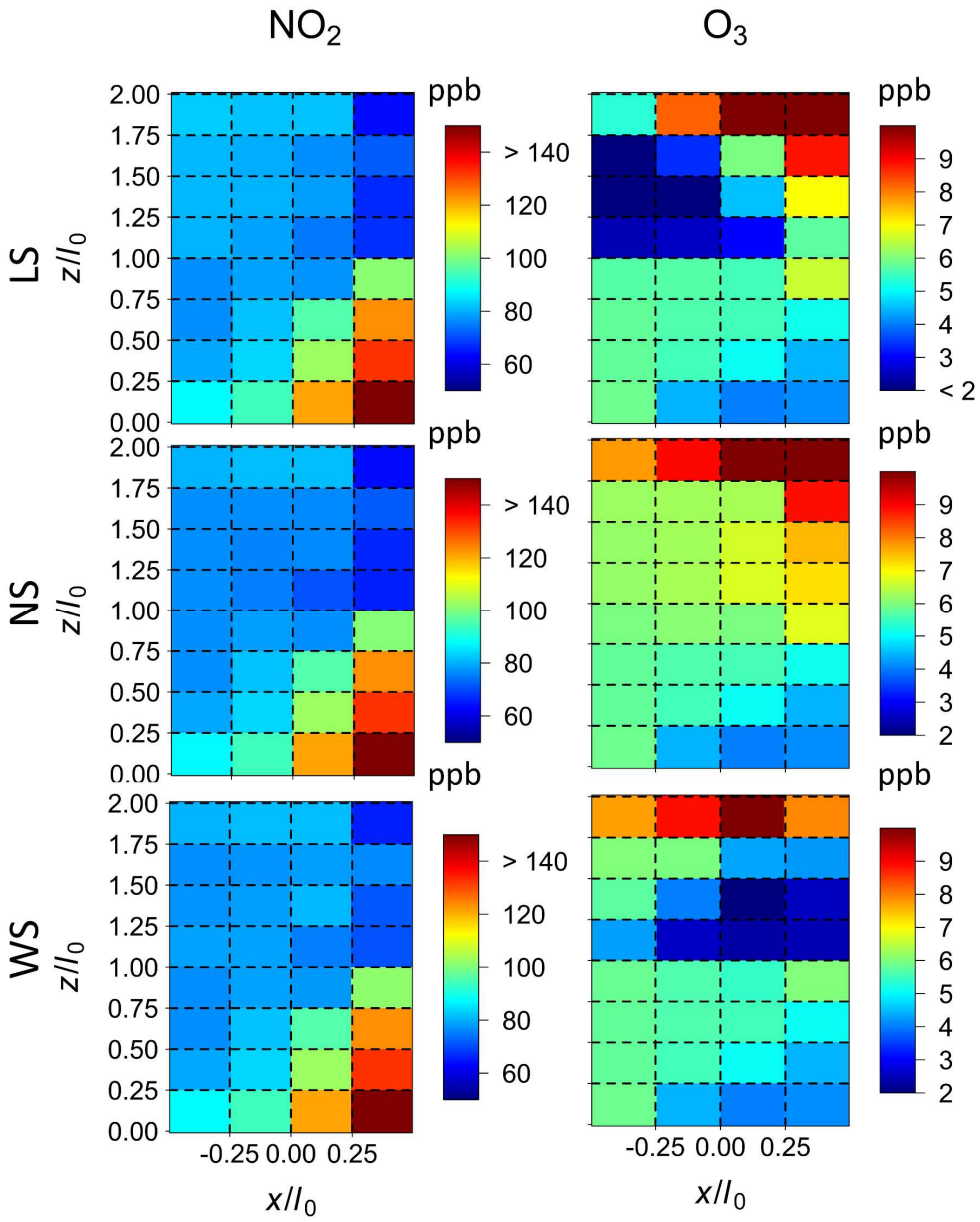


Figure 3.13. The spatial distribution of NO_2 and O_3 concentrations (ppb) with a quarter of original *J*-value of the simple NO_x-O_3 chemistry in fully shaded grids in the deep street canyon. The solar zenith angle is such that the regular canyon is half-shaded (θ_1 and θ_3). Subscripts "leeward" and "windward" represent magnitude of differences along with the leeward wall ($-0.5 < x/l_0 < -0.25$) and the windward wall ($0.25 < x/l_0 < 0.5$), respectively. LS, WS, and NS represent different shading scenarios. See text for details.

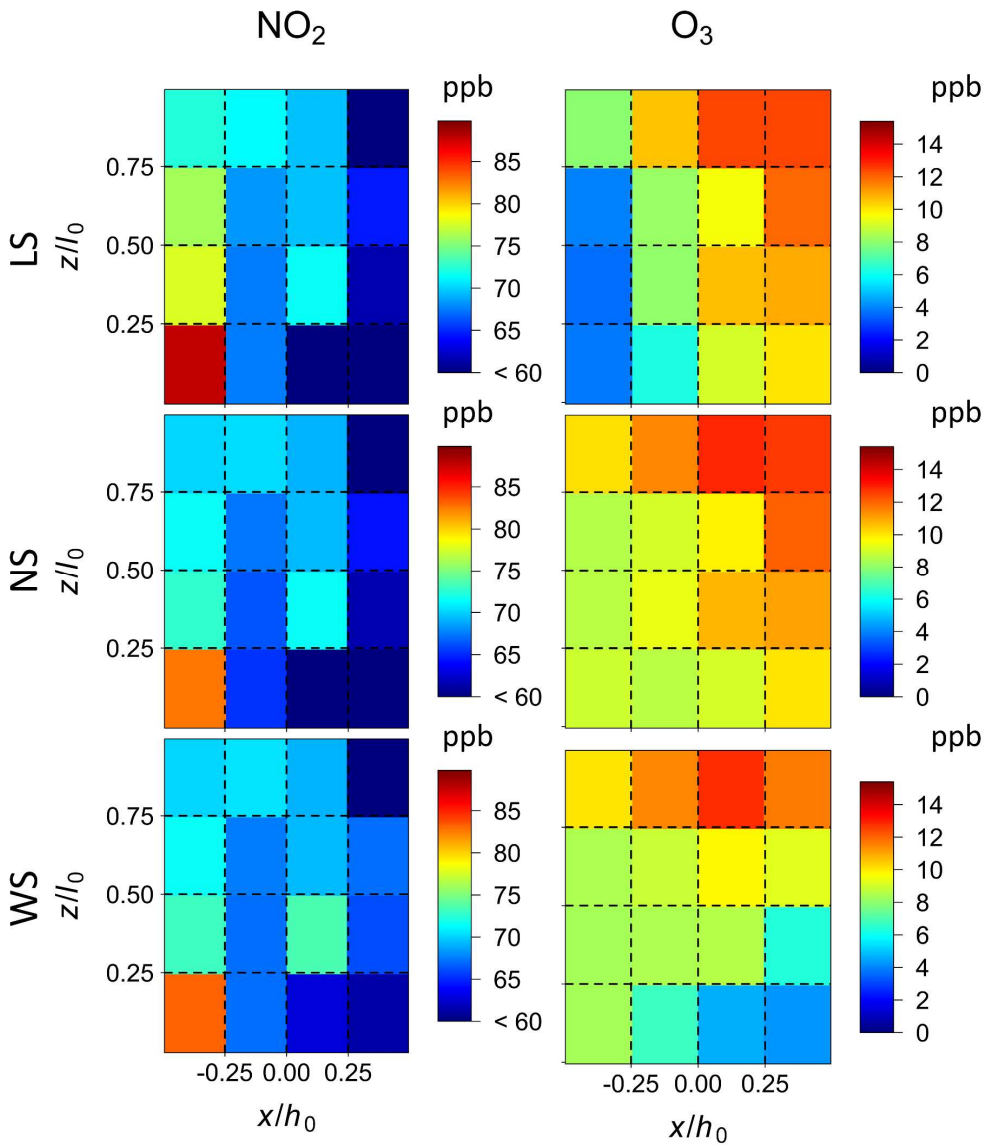


Figure 3.14. The spatial distribution of NO_2 and O_3 concentrations (ppb) with a quarter of original *J*-value of the simple NO_x-O_3 chemistry in fully shaded grids in the regular street canyon. The solar zenith angle is such that the deep canyon is half-shaded (θ_2 and θ_4). Subscripts "leeward" and "windward" represent magnitude of differences along with the leeward wall ($-0.5 < x/l_0 < -0.25$) and the windward wall ($0.25 < x/l_0 < 0.5$), respectively. LS, WS, and NS represent different shading scenarios. See text for details.

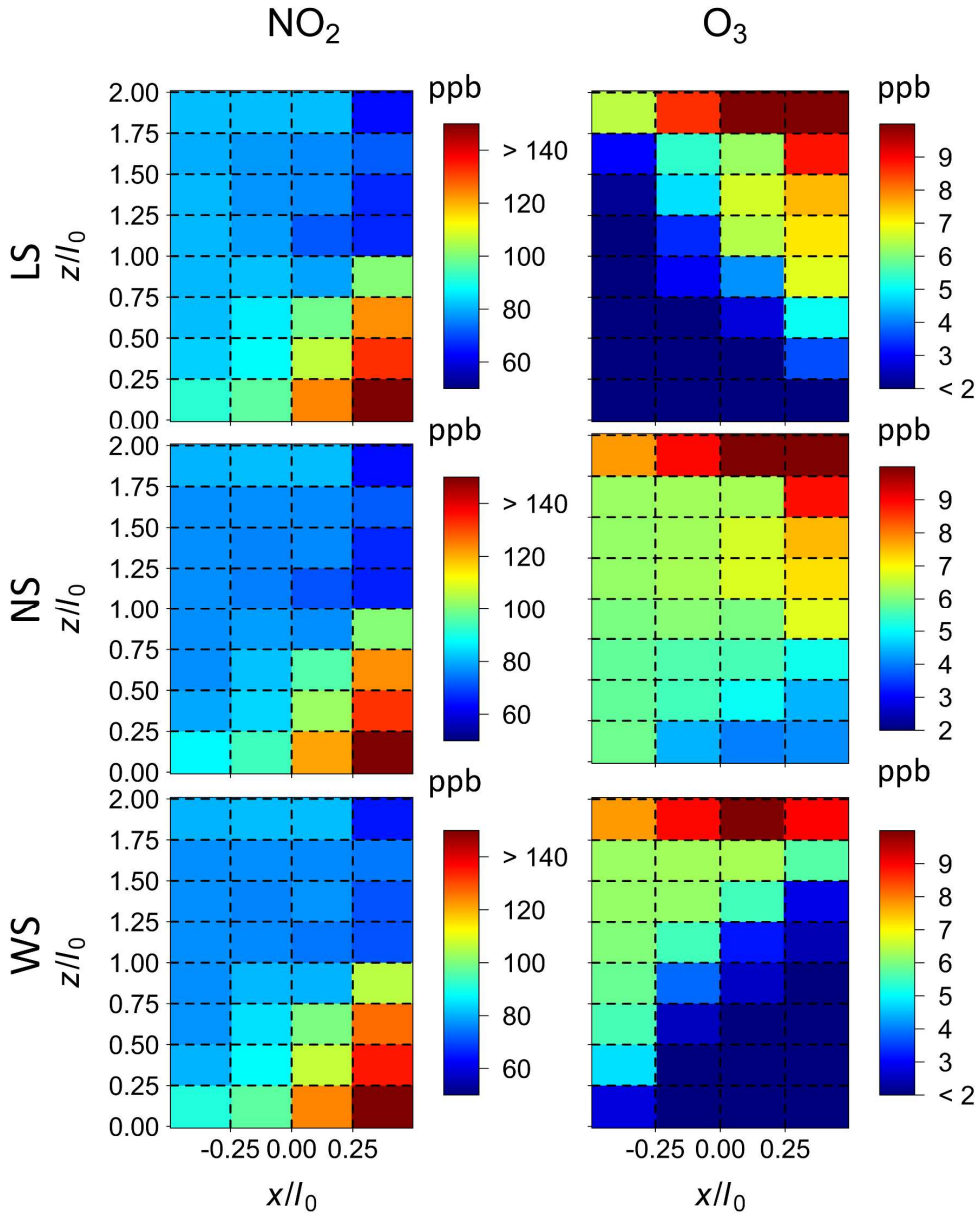


Figure 3.15. The spatial distribution of NO_2 and O_3 concentrations (ppb) with a quarter of original *J*-value of the simple NO_x-O_3 chemistry in the deep street canyon. The solar zenith angle is such that the deep canyon is half-shaded (θ_2 and θ_4). Subscripts "leeward" and "windward" represent magnitude of differences along with the leeward wall ($-0.5 < x/l_0 < -0.25$) and the windward wall ($0.25 < x/l_0 < 0.5$), respectively. LS, WS, and NS represent different shading scenarios. See text for details.

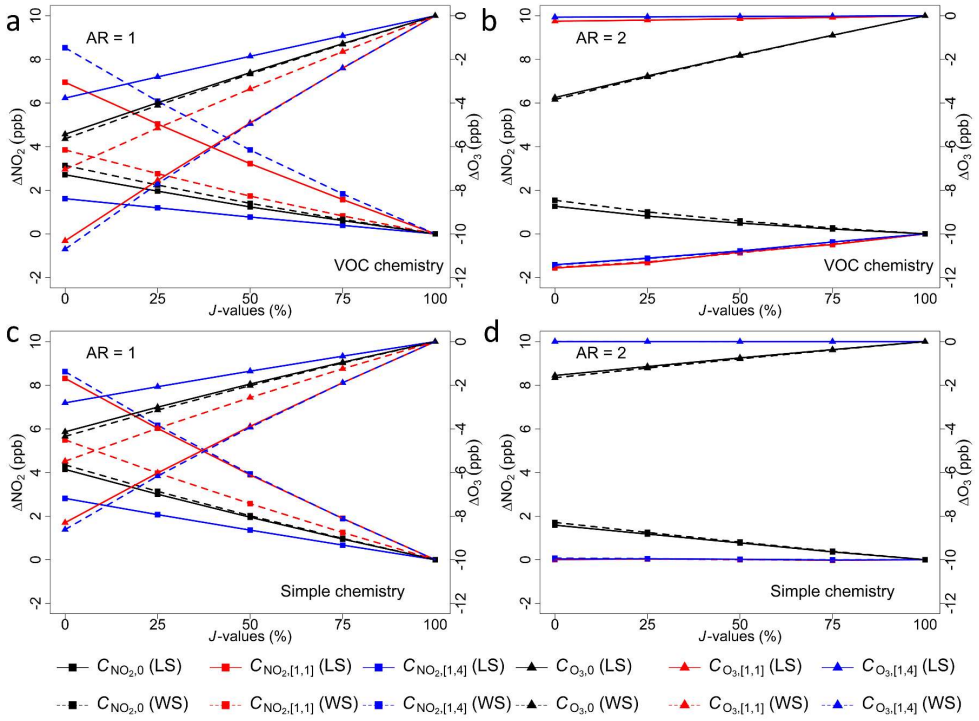


Figure 3.16. Concentration differences in NO_2 and O_3 (ppb) under different photolysis rates in RCS and simple NO_x-O_3 chemistry that denoted by percentages of their original values in regular and deep canyons, respectively. Hereinafter all differences are with respect to the no-shading simulation. The sun zenith angle is such that the regular canyon is half-shaded and the deep canyon deeply shaded (θ_1 and θ_3). Line colours indicate different locations of street canyons (the entire canyon and the pavement); line types indicate concentrations of different shading scenarios (LS and WS) minus those of NS; and squares and triangles represent NO_2 and O_3, respectively.

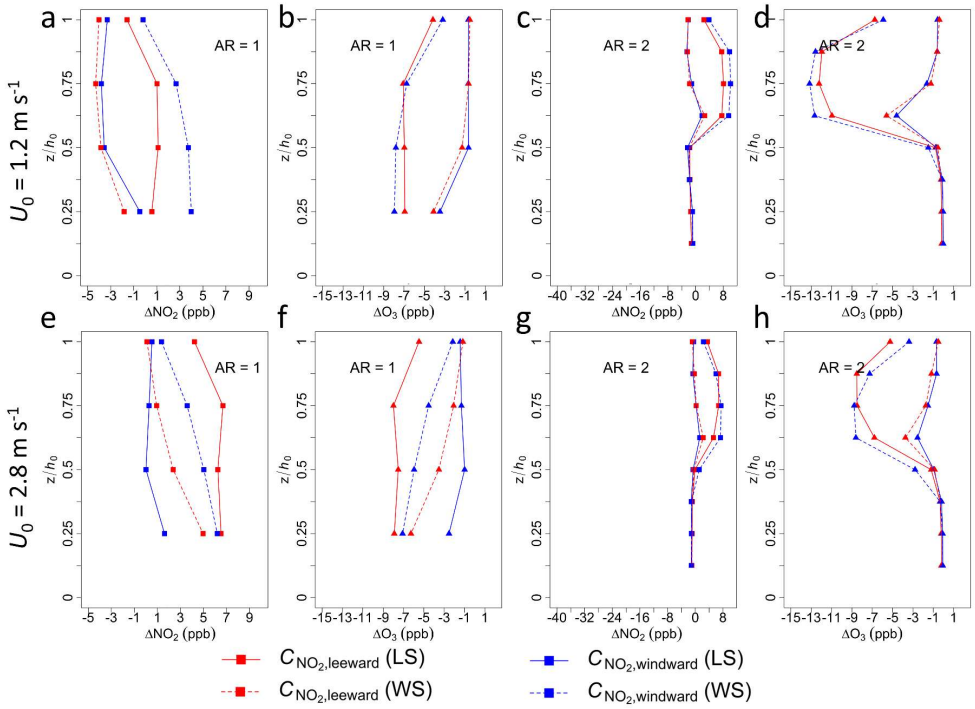


Figure 3.17. The spatial distribution of concentration differences in NO_2 and O_3 (ppb) with a quarter of original *J*-values of RCS chemistry in fully shaded grids in regular and deep canyons at different prevailing speeds (U_0). The solar zenith angle is such that the regular canyon is half-shaded. Subscripts "leeward" and "windward" represent magnitude of differences along with the leeward wall ($-0.5 < x/l_0 < -0.25$) and the windward wall ($0.25 < x/l_0 < 0.5$), respectively.

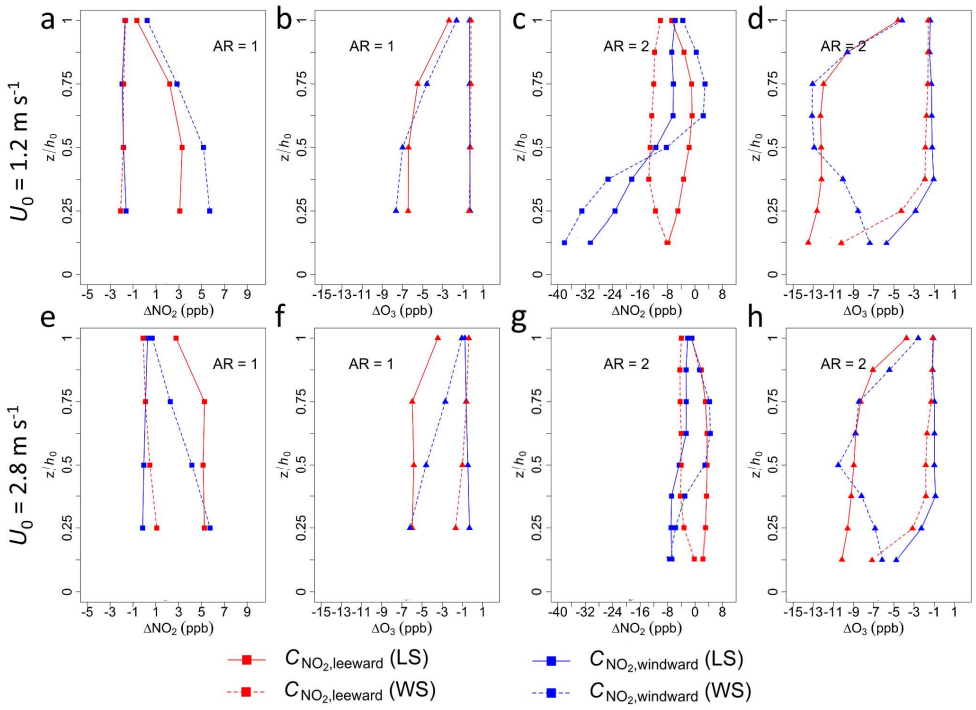


Figure 3.18. The spatial distribution of concentration differences in NO_2 and O_3 (ppb) with a quarter of original *J*-values of RCS chemistry in fully shaded grids in regular and deep canyons at different prevailing speeds (U_0). The solar zenith angle is such that the deep canyon is half-shaded. Subscripts "leeward" and "windward" represent magnitude of differences along with the leeward wall ($-0.5 < x/l_0 < -0.25$) and the windward wall ($0.25 < x/l_0 < 0.5$), respectively.

3.6 Acknowledgements

The authors thank the University of Birmingham's BlueBEAR HPC service (http://www.bear.bham.ac.uk) for offering high-performance computational resource. We thank Dr. Vivian Bright for providing the reduced chemical scheme (RCS). A.R.M.K. thanks the UK Natural Environment Research Council for support through grants NE/S00582X/1 and NE/S003487/1.

CHAPTER 4 CHEMISTRY, CANYON GEOMETRY, AND EMISSIONS EFFECTS ON NO_2 "HOTSPOTS" AND REGULATORY "WIGGLE ROOM"

Author Statement

This chapter encompasses work that has been previously published. The details of the publication are as follows:

Dai, Y., Cai, X., Zhong, J. and MacKenzie, A.R., 2022. Chemistry, street canyon geometry, and emissions effects on NO_2 "hotspots" and regulatory "wiggle room". npj Climate and Atmospheric Science, 5(1), p.102.

The contributions of the authors are as follows:

Yuqing Dai (the author of this thesis) was responsible for the conceptualization, methodology, coding, data curation, and the original draft preparation. **Rob Mackenzie** and **Jian Zhong** contributed to reviewing, editing the draft, and supervisory. **Xiaoming Cai** contributed to reviewing and editing the draft. Additional acknowledgements are presented in Section 4.5 of this chapter.

Abstract

The extent to which nitrogen dioxide (NO_2) undergoes complex chemical-transport processes near strong nitrogen-oxide sources in street canyons is not fully understood. A multi-box framework with volatile organic compound (VOC) chemistry has been evaluated against large-eddy simulation (LES) data

and observations, and then used to simulate NO_2 at street-canyon "hotspots". 42000 sensitivity studies — varying nitrogen oxides (NO_x) and VOC emission strength, and primary NO_2 fraction (f_{NO_2}) emitted within each of five streetscape cases — show the importance of detailed VOC chemistry, even in regular canyons (aspect ratio, AR = 1) when the ambient wind is weak. For a midsummer central London scenario, the inclusion of chemistry moves the canyon from compliance to out-of-compliance with the 1-hour NO_2 standard. Ignoring street-canyon chemistry can lead, therefore, to false positives in regulatory air quality modelling. Neglecting VOC chemistry can underestimate NO_2 by 6%-22% in regular canyons, and even more (-51%-31%) in deep canyons (AR = 2), particularly with lower f_{NO_2} values resulting from gasoline-dominated vehicle fleets or by tighter control of primary NO_2 from diesels. The very significant changes in regulatory "wiggle room" across sensitivity studies demonstrate the utility of this kind of chemistry-transport modelling for identifying efficient and effective regulatory pathways.

4.1 Introduction

Poor outdoor air quality has been linked to a mortality burden of between 28,000 and 36,000 every year in the UK (COMEAP, 2018) and 4.2 million deaths brought forward globally (World Health, 2018); it also significantly increases the risk of respiratory diseases and has impacts on cognitive performance in particular with vulnerable groups (ZhangChen and Zhang, 2018, Kim et al., 2018a, Domingo and Rovira, 2020). Nitrogen dioxide (NO_2) is one of the most harmful urban air pollutants, with direct adverse impacts on human health; it

also contributes to the formation of harmful secondary pollutants such as ozone (O_3), peroxyacetyl nitrate (PAN) and particulate matter (PM). PAN, in turn, is important as a "reservoir" compound, transporting and then releasing reactive nitrogen downstream of its sources (LaFranchi et al., 2009, Singh and Hanst, 1981). Moreover, although this work primarily concentrated on NO_2, it is important to underscore the more significant contribution of PM to premature death in the UK.

Tail-pipe emissions from internal combustion engines are the dominant primary source of NO_2 in most urban areas (Davison et al., 2021). Subsequently, secondary NO_2 is generated from nitric oxide (NO) through its rapid reactions with O_3, hydroperoxy (HO_2), and organic peroxyl radicals (RO_2). The radicals are generated from the photo-oxidation of volatile organic compounds (VOCs), which derive predominantly from tail-pipe emissions in cold conditions (Valach et al., 2015, George et al., 2015), augmented by evaporative (Geng et al., 2009, Liu et al., 2019) and biogenic emissions (Valach et al., 2014, Seco et al., 2011, SahuTripathi and Yadav, 2017) in warmer conditions. For cities in the global North, traffic emissions are estimated to be responsible for more than 60% of NO_x concentrations at roadside in urban areas (DEFRA, 2017a, Fu et al., 2020, Veratti et al., 2020). Although prominent downward trends in the annual NO_2 concentrations have been observed in many megacities (e.g., London, Beijing) under tight emission control strategies, evidence indicates that there is no safe threshold of exposure to air pollutants (Good et al., 2016) and the Global Air Quality Guidelines (AQGs) have been updated by World Health Organization (WHO) in 2021, suggesting that annual

NO_2 levels should not exceed 10 μg m^{-3} (a 75% reduction), while the 1-hour limit (200 μg m^{-3}) remains valid (World Health, 2021). Breaches of NO_2 levels against standards still occurred in congested areas with inadequate ventilation (i.e., regions with poor mixing with the overlying atmosphere — "street canyons" for example). More residents in urban areas will be affected by air quality issues as buildings in urban areas become denser (Joint Air Quality Unit, 2017) and as urban populations increase (Cohen, 2006).

The term "street canyon" refers to a narrow street flanked by continuous in-line buildings (OkeMills and Voogt, 2017). According to the aspect ratio (AR, the ratio of building height to street width), street canyons can be categorized as "avenue" (AR ≤ 0.5), "regular" (AR ≈ 1), and "deep" (AR ≥ 2) canyons (Vardoulakis et al., 2003). Previous wind/water-tunnel-scale studies found that one vortex and multiple counter-rotated vortices in idealised regular and deep urban canyons with symmetrical geometries, flat roofs, and a high Reynold (Re) number (~10^6), respectively (ZhongCai and Bloss, 2015, BrightBloss and Cai, 2013). However, there is a continuing about the threshold value for the formation of multi-vortices and Re-independence in street canyons. ChewAliabadi and Norford (2018b) reported that a single vortex may form in the deep canyon (c.f., AR = 2) if Reynold (Re) number is around 10^5; full-scale urban canyon simulations showed that only a primary vortex is generated in street canyons with AR equals to one and three, and two vortices are formed when AR equals to five and six, while the essential Re for Re-independent airflows is ~10^6 and ~10^7 for canyons with AR = 3 and AR = 5, respectively (Yang et al., 2021b, Zhang et al., 2019). These controversies

suggest that CFD results should be re-visited in the future by comparison with observations and are beyond the scope of this study.

NO_2 builds up in heavily trafficked street canyons because of intensive vehicle emissions and inefficient exchange of air with the ambient background aloft. This exchange of air, or ventilation, has been quantified as a rate with units of velocity, called a "transfer velocity" (SalizzoniSoulhac and Mejean, 2009), "air ventilation rate" (Liu and Leung, 2008), or "exchange velocity" (BrightBloss and Cai, 2013). The distribution of NO_2 in street canyons is complicated by chemical reactions. NO, NO_2, and O_3 rapidly adjust towards a photo-stationary state (see, for example, Hewitt and Jackson (2008), BakerWalker and Cai (2004)) (Supporting Information, Chapter 4.4, reactions 4.10 and 4.11). As air flows around urban street canyons, NO_x (i.e., the sum of NO and NO_2)-O_3 and organic free-radical chemistry (hereafter denoted as "free-radical chemistry") also take place. Previous studies have stressed the critical role of VOC abatement and hence free-radical chemistry in controlling NO_2 and O_3 in VOC-sensitive urban areas at the regional scale (Lyu et al., 2019, YangLiu and Li, 2020, Wang et al., 2019). However, the impact of VOC on NO_2 concentrations at the street scale has been very sparingly studied. Computational fluid dynamics (CFD) based models such as Reynolds-averaged Navier-Stokes (RANS) and large eddy simulation (LES) have very occasionally been used for simulating reactive species (e.g., NO, NO_2, O_3) in street canyons by coupling dynamics and chemistry (Tominaga and Stathopoulos, 2011, BakerWalker and Cai, 2004, BaikKang and Kim, 2007, Salim et al., 2011, Han et al., 2018, Wu et al., 2021). These models can provide very detailed airflow characteristics and a very

high-resolution distribution of reactive species in street canyons (Takano and Moonen, 2013, Tominaga and Stathopoulos, 2011, Murena et al., 2009). Nevertheless, it is difficult to incorporate complex chemical schemes into these simulations due to computational resource constraints, very substantially restricting their scope to survey the parameter space through sensitivity studies. Gaussian models can be extended to allow fast computation of the dispersion of pollutants within street canyons, but they are less process-based and have limited ability to represent complex chemical reactions in the atmosphere. Although single-box models (e.g., Pugh et al. (2012)) allow more complicated chemistry and/or microphysics to be incorporated, they cannot calculate within-canyon concentration gradients and chemical segregation (Vinuesa and de Arellano, 2005, Pugh et al., 2011, Sykes et al., 1994, Soulhac et al., 2011), that give rise to highly localized pollution "hotspots".

In the present study, we used a two-dimensional (2D) multi-box framework that removes the well-mixed assumption presented in single-box calculation, to simulate NO_2 mixing-ratios within urban street canyons. VOC chemistry was incorporated into the model without unmanageable loss of computational speed (Dai et al., 2021b). Overall the model offers the spatial distribution of pollutants with a fairly short computational time (e.g., ~6 min for a deep canyon and ~3 min for a regular canyon) compared to the LES (~10 days). Here the model results at the pedestrian level were evaluated against available observations. By taking into account a large portfolio of emission scenarios, different routes for reducing NO_2 in street canyons were explored. The model results show the extent to which it is important to include free-radical

chemistry, as distinct from the purely inorganic NO_x-O_3 scheme, thereby supporting strategies for efficient and effective air pollutant management.

This article is organized as follows: the Methods section in Chapter 4.2 comprises of three sub-sections, i.e., "model description" describes the multi-box model used in this work and its basic components; "model evaluation" compares the model results to measurements within four realistic street canyons; "model scenarios" presents the details of the model configuration for different emission and meteorological scenarios. Three sub-sections in the Results and Discussion in Chapter 4.3 demonstrate the analysed results in street canyons, the influence of emission heterogeneity and meteorology on model results, and implications for future modelling and air quality regulatory policy, respectively.

4.2 Methods

4.2.1 Model Description

Figure 4.1 presents schematics of a typical one-box model and the multi-box models for street canyons with different geometries. The compartment with thick black lines represents the entire canyon (denoted by "Box_0") with a flat roof-shape. The compartment overlying the building roofs represents the ambient background above the urban canopy layer (UCL). The canyon volume is split into several boxes (dashed blue lines) to give Eulerian grid resolutions of, in this case, "16-box" for the regular (AR = 1) canyon and "32-box" for the deep (AR = 2) canyon. Using the subscripts "*k*" pointing to the location along the ordinate direction and "*i*" to the location along the direction of the abscissa,

the multi-box model can specify the position of any box within the canyon (denoted by "$Box_{[k,i]}$"). Assuming that a non-zero component of the ambient wind on the rooftop blows from left to right perpendicularly to the street axis, in-canyon boxes are indexed from the bottom-left, increasing upwards and rightwards (e.g., k = 1 represents the pedestrian level, and i = 1 represents model boxes near the leeward building facet). Emissions of NO_x (E_{NOx}) and VOCs (E_{VOCs}) from anthropogenic or natural sources can be injected into any box in the multi-box model. The mixing-ratios of the q^{th} species in Box_0 and in $Box_{[k,i]}$ are denoted as $C_{q,0}$ (ppb) and $C_{q,[k,i]}$ (ppb), respectively.

Turbulent mixing between the canyon and background is parameterized using "exchange rates" in the one- and multi-box models (Pugh et al., 2012, ZhongCai and Bloss, 2016a, Soulhac et al., 2011, Vardoulakis et al., 2003), respectively; in-canyon dynamics for the multi-box model comprise advection and turbulent diffusion, which are described by a set of parameters (Appendix A Tables S1-S2), namely "advective velocity" and "turbulent velocity" (Dai et al., 2021b). These velocities are derived from previously computed LES data with the high Reynolds number ($\sim 10^6$) turbulent airflow for idealised regular and deep canyons under a prevailing wind velocity (U_0) of 2 m s^{-1} in the neutral atmosphere (BrightBloss and Cai, 2013, ZhongCai and Bloss, 2015), and a linear relationship is assumed for in-canyon dynamics with respect to U_0 in this study (Murena et al., 2011, BarlowHarman and Belcher, 2004a). The mathematical description of the box models is presented in Chapter 4.4 Supporting Information.

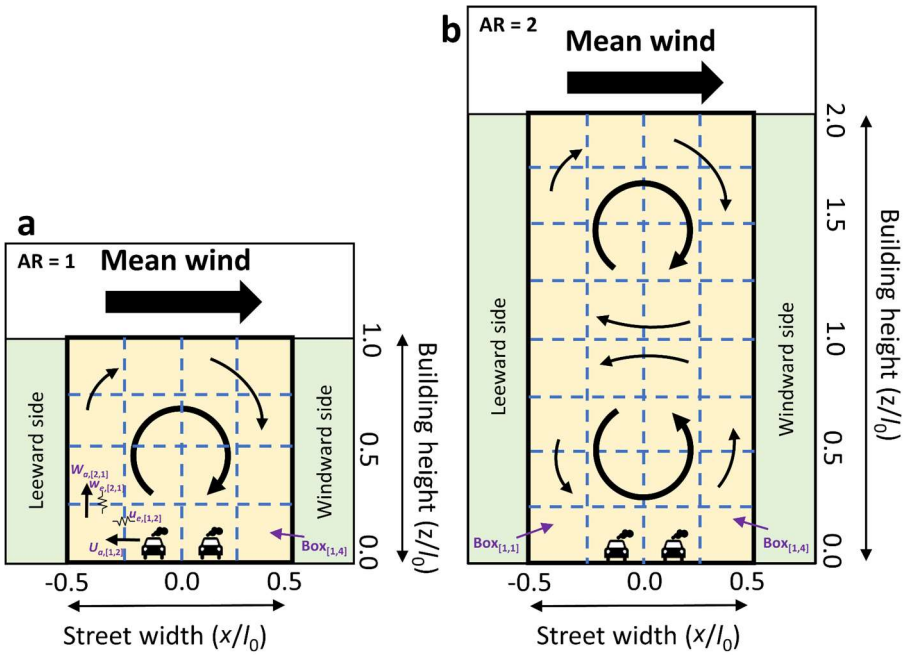


Figure 4.1. A conceptual view of box models for regular and deep street canyons. The bold black frame represents a typical one-box model, the air is assumed to be well-mixed and thus, pollutants are homogeneously distributed; the dashed blue lines grided the single box into several compartments of equal volume, which represents 16- and 32-box models, respectively, in this example. A primary vortex exists within the regular canyon and two counter-rotated vortices exist within the deep canyon; the well-mixed assumption is applied for each box.

Modularization of the model code allows easy modification of chemical kinetics cell by cell for applications under complex scenarios (e.g., accounting for shaded areas or stagnant corners), and even the addition of particle microphysics instead of, or in addition to, gas-phase chemistry (cf., Zhong et al. (2018)). In the present study, consistent chemical reaction rate coefficients are assumed within street canyons (i.e., one set of kinetic coefficients across the whole canyon). As with calculation of the flow, there is a trade-off between

computation time and the complexity of the chemical scheme. The chemical scheme should be as complicated as is required for the problem being studied, but not more complicated than necessary (ZhongCai and Bloss, 2016a). The near-explicit Master Chemical Mechanism (MCM) (Saunders et al., 2003) or GECKO-A mechanism generator (AumontSzopa and Madronich, 2005) could be used to provide very detailed description of species-specific chemical evolution. To save computation time, we opt for a Reduced Chemical Scheme (RCS) (BrightBloss and Cai, 2013) including 51 gas-phase species and 136 chemical reactions that was developed from a subset of the MCM *v*3.1 with a comparable performance (~10%) against full MCM *v*3.1 on NO, NO_2, O_3 and OH(BrightBloss and Cai, 2013). The RCS was used for simulating the daytime NO_x-O_3-VOC chemistry in the urban canyon environment by the multi-box models, photolysis coefficients were calculated using the Tropospheric Ultraviolet and Visible (TUV) Radiation Model *v*4.1 (Madronich and Flocke, 1999), representing for conditions during the summer daytime in a typical street canyon at a mid-latitude urban area. Detailed information is provided otherwhere (BrightBloss and Cai, 2013), and the full RCS mechanism including the chemical reaction rates is presented in Chapter Appendices. Compared to the simple inorganic NO_x-O_3 cycle, the complicated chemistry of the RCS (i) incorporates generation of NO_2 by reaction of NO with HO_2 and RO_2 (where R is an organic moiety); (ii) incorporates production of organic nitrates and PAN; (iii) incorporates segregation; and (iv) allows some questions of VOC speciation to be addressed. Additionally, the RCS only considers gaseous chemistry and does not take into account heterogeneous reactions within

street canyons, which is sufficient for our purposes in this work. However, notably our model indicates a potential pathway to investigate the effects of chemistry on changes in air pollution by flexibly coupling specific chemical schemes.

4.2.2 Model Evaluation

Having previously demonstrated that the passive tracer and NO_2 from the multi-box models matched well with those of the LES from which the flow was diagnosed (Dai et al., 2021b), in this study, we evaluated the results of the one- and multi-box models against field observations. We use observations from the "Optimization of Modelling Methods for Traffic Pollution in Streets" (TRAPOS) — specifically from Schildhornstrasse (Berlin, Germany), Goettingerstrasse (Hanover, Germany), and Jagtvej (Copenhagen, Sweden) — and from Marylebone Road (UKA00315) and North Kensington (UKA00253) in central London, UK, which are parts of the national automatic monitoring network (AURN). The multi-box model with 16 in-canyon boxes performed well when evaluated using six widely-accepted metrics (Cai and Steyn, 2000, Willmott et al., 1985, Willmott, 1981, WillmottRobeson and Matsuura, 2012) (see Table 4.5 in Supporting Information). Metrics from Hood et al. (2021), which is representative of the state-of-art, are also provided; more information can be found in Supporting Information in Chapter 4.4.

Figure 4.2 presents a comparison of normalized modelled NO_x and NO_2 against observations (equation (4.20) in Supporting Information) under various prevailing wind velocities (U_0) in Marylebone Road, respectively. The 16-box

model, in general, performed better with respect to NO_x and NO_2 compared to the typical one-box model due to its finer spatial resolution. For the windward condition (i.e., monitors located on the windward side of the canyon), modelled mixing-ratios of NO_x and NO_2 were higher than observed values (Figures 4.2a and 4.2c). As U_0 increased from 2 m s^{-1} to 8 m s^{-1}, modelled mixing-ratios decreased significantly and monotonically, while observations dropped only slightly.

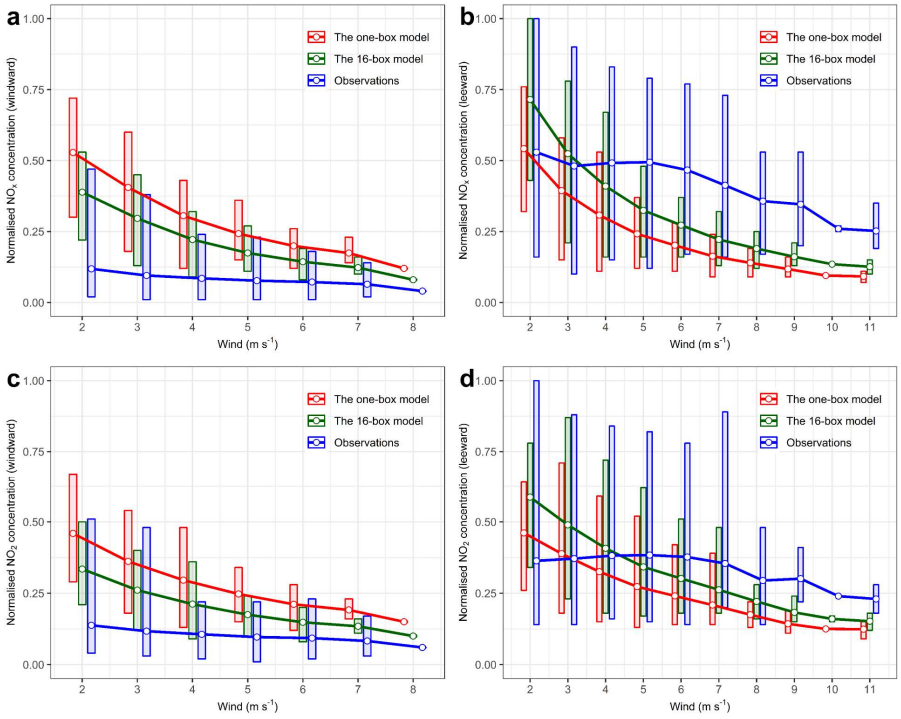


Figure 4.2. Comparison of model results against observations. Comparison of normalized modelled NO_x and NO_2 concentrations against observations in Marylebone Road at various prevailing wind velocities (U_0) for the windward (**a**, **c**) and leeward (**b**, **d**) conditions. The error bars represent the range of data at the same U_0, and thus a similar airflow pattern within the street canyon. The points represent the average values for each group.

The discrepancies between model predictions and measurements could attributable to (1) the exchange velocity between the canyon and overlying background was much greater in reality than that used in the simulations because the monitoring cabinets in Marylebone Road are located where the actual AR of the canyon is less than unity, and the building roofs are rounded rather than rectangular; (2) the mechanical generation of turbulence overlying the UCL has been underestimated because the LES domain does not adequately represent the entire atmospheric boundary layer, resulting in the dynamics of the inner- and outer-layer being attenuated compared to reality (GryllsSuter and van Reeuwijk, 2020).

As the exchange velocity increases, more recirculating pollutants are removed from the canyon. The effects of the background air become more important in determining mixing-ratios of air pollutants on the windward side, which leads to a tendency for simulated and observed values to converge. For the leeward condition, observations exhibit very complex patterns (Figures 4.2b and 4.2d) possibly due to the blocking effect of trees (Buccolieri et al., 2018). The box models remained sensitive to U_0; only a very slight decrease with wind speed was found in the observations. Consequently, the contrast between simulations and observations became larger under high U_0 scenarios. Figure 4.9 in Supporting Information presents a comparison of normalized modelled NO_x against observations under different U_0 in three TRAPOS sites, respectively. While the 16-box model retains an advantage over the one-box model, the results show a substantial relationship between in-canyon concentrations and background wind velocities.

There are many potential sources of uncertainty complicating the comparison of models and observations, which are discussed in Supporting Information "Method". We also note that adopting empirical parameters (Supporting Information Table 4.4) for the multi-box model can compensate for such uncertainties and significantly improve the model performance for place-specific simulations (Table 4.5, see Supporting Information for details). Overall, the multi-box model offers an improvement on the state-of-art for efficient simulation of the spatial distribution of reactive species within regular and deep canyons when tested against observations (Table 4.5), current regulatory approaches or the LES results in Supporting Information (Dai et al., 2021b).

4.2.3 Model Scenarios

In this study, we neglect any complications induced by in-canyon vegetation, street furniture, heating or mechanical turbulence, and concentrate only on the same idealised (non-vegetated) regular and deep canyons as in previous studies (BrightBloss and Cai, 2013, ZhongCai and Bloss, 2015). Previous literature showed that NO_2 pollution was worst on the upward-vortex side at the pedestrian level of street canyons (ZhongCai and Bloss, 2015, BrightBloss and Cai, 2013, MoradpourAfshin and Farhanieh, 2017, BaikKang and Kim, 2007). We therefore explore the variability of NO_2 mainly concentrating for the reporting of our results in these areas — that is, $C_{NO_2,[1,1]}$ for the regular canyon and $C_{NO_2,[1,4]}$ for the deep canyon (as illustrated in Figure 4.1) — through a series of scenarios (Table 4.1). The spatial distribution of air

pollutants in street canyons are provided in Supporting Information "Discussion", Chapter 4.4.

We use an idealised Marylebone Road as our base regular street canyon (i.e., the building height and street width are 34 m), and then represent an idealised deep street canyon by doubling the building height to 68 m to investigate the effect of canyon geometry on pollutant mixing-ratios. As the primary driver for the ventilation of pollutants, the velocity of the prevailing wind (U_0) has significant impacts on air quality in street canyons, determining the intensity of vortices and, thus, the distribution of mixing-ratios within canyon; the emission heterogeneity may influence reactive species due to physical processes and segregation effects (ZhongCai and Bloss, 2014). Taking a typical U_0 of 2 m s^{-1}, uniform emissions into the central carriageway ($Box_{[1,2]}$ and $Box_{[1,3]}$) and simple volume-splitting (i.e., boxes are equal in size) as the base case (Case 0), we performed model sensitivity studies (Case 1-4) to simulate the effect of U_0 (±40%) and to investigate crudely the impact of a central reservation or hedgerow on NO_2 in street canyons. Model results are discussed below, and details are presented in Supporting Information.

Initial conditions of NO, NO_2, O_3, and carbon monoxide (CO) were taken from in situ measurements from North Kensington (UKA00253) and were 2.6, 8.3, 32.0, and 151.4 ppb, respectively, representing a daytime summer atmosphere in London urban background for the year 2019. The model operated without any emissions for the first 30-minute "spin-up" period that allowed sufficient time for turbulent dynamics to reach a quasi-equilibrium state for the

preparation of key chemical intermediates (CaiBarlow and Belcher, 2008, BrightBloss and Cai, 2013), and the mixing-ratios of all species at t = 30 min were used as background conditions. After the "spin-up" period, emissions were switched on and the multi-box model, as a representative of a typical urban unit, exchanges mass fluxes with the background continuously through the shear layer at the roof level. The averaged mixing-ratio of pollutants at a quasi-equilibrium state (here t = 180-240 min) were used for analysis (ZhongCai and Bloss, 2016b).

Table 4.1. Summary of the multi-box model simulations for reactive species[a]

	Configuration
Case 0	U_0 = 2.0 m s^{-1}; 1.0 × ($w_{e,0}$, |W_a, U_a|,|w_e, u_e|); $\gamma_{q,[1,2]} = \gamma_{q,[1,3]}$ = 0.5
Case 1	U_0 = 1.2 m s^{-1}; 0.6 × ($w_{e,0}$, |W_a, U_a|,|w_e, u_e|); $\gamma_{q,[1,2]} = \gamma_{q,[1,3]}$ = 0.5
Case 2	U_0 = 2.8 m s^{-1}; 1.4 × ($w_{e,0}$, |W_a, U_a|,|w_e, u_e|); $\gamma_{q,[1,2]} = \gamma_{q,[1,3]}$ = 0.5
Case 3	U_0 = 2.0 m s^{-1}; ($w_{e,0}$, |W_a, U_a|,|w_e, u_e|); $\gamma_{q,[1,1]} = \gamma_{q,[1,2]} = \gamma_{q,[1,3]} = \gamma_{q,[1,4]}$ = 0.25
Case 4	U_0 = 2.0 m s^{-1}; ($w_{e,0}$, |W_a, U_a|,|w_e, u_e|); $\gamma_{q,[1,1]} = \gamma_{q,[1,4]}$ = 0.5

[a] U_0: prevailing wind velocity in the background; ($w_{e,0}$, \|W_a, U_a\|,\|w_e, u_e\|): in-canyon physical parameters for the multi-box models ($W_{a,[k,i]}$ and $U_{a,[k,i]}$ (m s^{-1}) are pollutant transfer velocities due to advective transportation respectively in the vertical and horizontal directions; and $w_{e,[k,i]}$ and $u_{e,[k,i]}$ (m s^{-1}) are transfer velocities due to turbulent mixing); $\gamma_{q,[1,i]}$ (i = 1, 2, 3, 4): the proportion of vehicle emissions in $Box_{[1,i]}$ to the total emissions (see Support Information Chapter 3.4). From Case 1 to Case 4, model sensitivities were conducted to investigate the effects of the prevailing wind, emission heterogeneity on in-canyon NO_2.

A typical emission condition (TEC) is defined with emission rates of 525.3, 1032.4, and 170.2 g km^{-1} h^{-1} for NO_x, CO and VOCs, respectively, which represents a generic UK situation (i.e., not Marylebone Road) of weekday on-road traffic volume of 1500 vehicle hr^{-1} with an average speed of 40 km hr^{-1} based on National Atmospheric Emissions Inventory (NAEI). The equivalent rates of emission of the q^{th} species into a box grid is calculated as a mixing-ratio rate of change (denoted by "$E_{q,\mathrm{TEC}}$"). We use a normalized emission rate (i.e., $E_q/E_{q,\mathrm{TEC}}$, denoted by "E_q^{norm}") to describe the variations in total emissions across the sensitivity study. It is assumed that the percentages of ethene (C_2H_4), propene (C_3H_6), formaldehyde (HCHO), and acetaldehyde (CH_3CHO) in the total VOC mix initially are 44%, 19%, 25%, and 12%, respectively, as calculated on the basis of annual mass emissions from road transport, photochemical ozone creation potential (POCP), and hydroxyl radical (OH) reactivity (Boulter et al., 2009, BrightBloss and Cai, 2013). The reactivity and POCP enable the consideration of a wider array of VOCs, beyond those explicitly represented in simplified or lumped chemical schemes. These schemes in atmospheric chemistry modelling typically aggregate diverse VOCs sharing analogous chemical characteristics to expedite computational processes. However, such simplification may engender potential inaccuracies in prognosticating the consequent atmospheric repercussions of emissions. Although biogenic VOC emissions are not included in this research, they are expected to have a negligible effect on target pollutants such as NO_2 and PAN (see further discussion in Supporting Information).

In each case, we model 8400 (20 × 20 × 21) emission scenarios in a trivariate space (i.e., $E^{\text{norm}}_{\text{NO}_x}$, $E^{\text{norm}}_{\text{VOCs}}$, primary NO_2 fractions (NO_2:NO_x, denoted by f_{NO_2})) where $E^{\text{norm}}_{\text{NO}_x}$ = 0.1, 0.2, …, 1.9, 2.0 and $E^{\text{norm}}_{\text{VOCs}}$ = 0.1, 0.2, …, 1.9, 2.0, reflecting tidal traffic volumes (150-3000 vehicles hr^{-1}, or equivalent emissions). Smaller values of $E^{\text{norm}}_{\text{VOCs}}$ can also be interpreted as approaching the simple inorganic NO_x-O_3 cycle, and so also test the effect of VOC chemistry on the model results. The values of f_{NO_2} are lower in areas dominated by petrol engines but can be very high in megacities with large number of diesel engines (Carslaw et al., 2016), hence, f_{NO_2} = 0.1, 0.11, …, 0.29, 0.3 can be interpreted as representing the efficiency of emissions control technology or, approximately, the effect of engine type on NO_2 in street canyons.

4.3. Results and Discussion

4.3.1 NO_2 Response Surfaces and Air Quality Management

Figure 4.3 shows the modelled mixing-ratios of NO_2 on the upward-flowing side of the main circulatory vortex, at the pedestrian level of regular and deep street canyons. The figure shows a 2D slice through the parameter space at the typical VOC emission rate ($E^{\text{norm}}_{\text{VOCs}}$ = 1) and U_0 = 2 m s^{-1}. The solid line dividing the polluted air zone (P) and the clean air zone (C) is the UK hourly air quality objective for NO_2 (105 ppb corresponding to 200 μg m^{-3} based on the conversion factor estimated at 20 ℃ and 1 atm), which we will describe below as the "compliance line". The dotted and dashed lines show the compliance line from other relative VOC emission values projected onto the $E^{\text{norm}}_{\text{VOCs}}$ = 1 surface: we refer to the dotted $E^{\text{norm}}_{\text{VOCs}}$ = 0.1 compliance line as the "low free-radical

chemistry" line (i.e., more complicated chemistry is essentially near-absent, as in most current regulatory models), and the dashed $E_{\mathrm{VOCs}}^{\mathrm{norm}}$ = 2 as the "intense free-radical chemistry" line. The compliance lines reveal a complex relationship between emission factors and free-radical chemistry. It should of course be borne in mind that increases or decreases in NO_x and VOC emissions as well as changes in primary NO_2 are often simultaneous in reality, but the lines in Figure 4.3 show the extent to which compliance to the air quality standard depends on assumptions about chemistry which are routinely absent from regulatory modelling. Similarly, the much more computationally intensive LES might typically investigate 6 or 10 of the 8,400 scenarios tested by the multi-box model (e.g., Kwak and Baik (2012), KimPark and Kim (2012), KwakBaik and Lee (2013)), and so could miss the general patterns captured in Figure 4.3.

The impact of emissions and primary NO_2 in the presence of free VOC radical-chemistry presents a challenge to policy makers pursuing effective mitigation options. Consider a regular canyon with an intense emission condition (IEC) of 3,000 vehicle hr^{-1} with $E_{\mathrm{NO_x}}^{\mathrm{norm}}$ = 2 and $f_{\mathrm{NO_2}}$ = 0.26 (with $E_{\mathrm{VOCs}}^{\mathrm{norm}}$ = 1 for illustration purposes in Figure 4.3a), that is, modelling a putatively perfect AR = 1 canyon in Marylebone Road in central London. Under these conditions, the site is not compliant: the site conditions are above and to the right of the compliance line (Figure 4.3a). NO_2 mixing-ratio reductions are then strongly dependent upon total NO_x emissions and $f_{\mathrm{NO_2}}$. Reducing solely $E_{\mathrm{NO_x}}$ by ~10% (the horizontal arrow) or $f_{\mathrm{NO_2}}$ from 0.26 to 0.23 (the vertical arrow) brings NO_2 into compliance. However, if free-radical chemistry is effectively ignored, the site

is below and to the left of the dashed line and so already in compliance. This would be, in effect, a false positive outcome arising from the neglect of chemistry in the model. If organic chemistry is twice as intense (i.e., $E_{VOCs}^{norm} = 2$), the site is very far from compliance, and reaching compliance would require reducing E_{NO_x} by ~25% or f_{NO_2} from 0.26 to 0.12, with concomitantly large implications for control technology and regulation. The compliance line shifts nonlinearly in terms of free-radical chemistry from the intense situation (dashed line) to the "*zero*" situation (dotted line) as E_{VOCs} are reduced, implying that reducing E_{VOCs} alone results in progressively less effective NO_2 mitigation, leading to a VOCs-saturated and NO_x-sensitive condition. Therefore, multi-variate synergistic controls (e.g., the oblique arrow in Figure 4.3a, with a shorter distance between the IEC and the limitation) offer a more effective way of reducing NO_2 in street canyons. However, note that the optimum path for air quality ameliorations varies significantly based on the geometry of canyons and should be evaluated carefully in each instance. The distance between the present emission scenario and the three-dimensional compliance surface may help stakeholders in designing more effective strategies for improving air quality in urban areas (e.g., Figure 4.8).

The situation is more complicated when the building height is doubled, as this greatly reduces the exchange velocity and increases the residence time of air pollutants, allowing more time for chemistry to take place (ZhongCai and Bloss, 2015, Park et al., 2015). For the deep canyon (Figure 4.3b), E_{NO_x} requires to be reduced absolutely (~65%) as NO_2 is extremely high. Neglecting free-radical chemistry makes a very significant difference to modelled NO_2 and,

hence, to the position of a site relative to the compliance line (dotted line in Figure 4.3b). For our hypothetical deep London canyon, the NO_x reduction required would be underestimated by almost 50% for modelling that ignores chemistry (i.e., the dotted compliance line at f_{NO_2} = 0.26) and this underestimation gets markedly worse for lower values of f_{NO_2}.

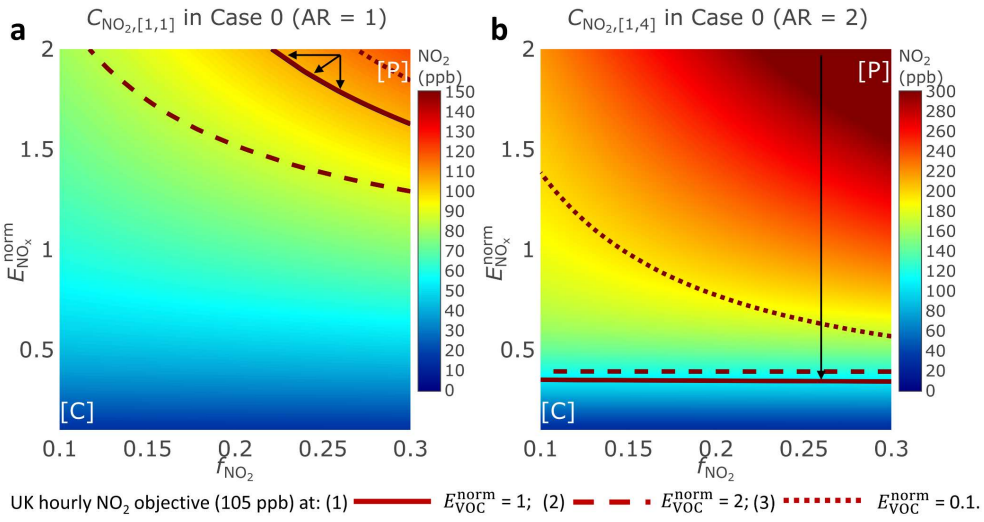


Figure 4.3. Emissions effects on upward-vortex side NO_2 mixing-ratios at the pedestrian level in urban canyons. The upward-vortex side NO_2 mixing-ratios (ppb) at the pedestrian level of the regular (**a**) and deep (**b**) canyons at E^{norm}_{VOCs} = 1 in Case 0 (U_0 = 2 m s^{-1}). f_{NO_2} is the primary NO_2 fraction, $E^{norm}_{NO_x}$ and E^{norm}_{VOCs} are the ratios of NO_x and VOC emission rates to their typical emission condition (TEC), respectively. All simulated patterns change when E_{VOCs} is changed, and the compliance line shifts to the dotted and dashed lines when E^{norm}_{VOCs} changes to 0.1 and 2, respectively. The regions "[P]" and "[C]" divided by the compliance line represent the polluted and clean air zone, respectively. The arrows represent control strategies for NO_2 reduction under an intense emission condition (IEC), see text for details.

The region "C" of compliant air quality in the two-dimensional E_{NO_x}— f_{NO_2} space (Figure 4.3) can be thought of as comprising the "wiggle room" (χ) of different E_{NO_x} and f_{NO_2} scenarios that provided tolerable air quality in street canyons (see further discussion in Supporting Information). When the compliance line is linear with respect to E_{NO_x}, region "C" is a simple shape (e.g., the solid and dashed lines in Figure 4.3b) and air quality management options are simple to describe. When the compliance line is either not linear or becomes far apart for the different chemistry intensities (e.g., Figure 4.3a), then visual inspection of phase space is the best way to consider management options.

Numerically integrating this region to calculate the area of compliant parameters collapses the complexity of Figure 4.3a into a single number but that number provides a useful metric for quantifying the effect of free-radical chemistry on in-canyon NO_2; the changing magnitude of χ reflects the sensitivity of NO_2 to key emission variables such as E_{NO_x} and E_{VOCs} (see Supporting Information). The metric, χ, is computed as a dimensionless value of emissions in Table 4.2 within the 2D space of Figure 4.3. The difference in the metric between the "low free-radical chemistry" scenario (E_{VOCs}^{norm} = 0.1) and the "intense free-radical chemistry" (E_{VOCs}^{norm} = 2) provides an upper limit to the extent to which neglect of free-radical chemistry overestimates the compliant phase space available in the street canyon, and so measure the potential for false positives in the regulatory modelling. For instance, introducing free-radical chemistry (E_{VOCs}^{norm} = 1) to the standard case, Case 0, decreases the air

quality management "wiggle room", χ, by only ~3.5%, but introducing free-radical chemistry to the low wind speed case, Case 1, decreases χ by 46%. For the deep canyon, the effect of free-radical chemistry is between 60% and 70% for all wind speeds (Table 4.2).

The dotted ("low free-radical chemistry", $E_{\mathrm{VOCs}}^{\mathrm{norm}}$ = 0.1) compliance line in the deep canyon is non-linear, that is, its gradient becomes steeper where f_{NO_2} is less than ~0.2. Recalling that the range of f_{NO_2} can come about by increasing the fraction of gasoline-driven vehicles in fleet, this non-linearity indicates that neglecting free-radical chemistry introduces a large error in χ for areas dominated by gasoline-engines. When $E_{\mathrm{VOCs}}^{\mathrm{norm}}$ = 2 in the deep canyon, conversion of NO_2 to organic nitrates and PAN (Appendix B Table S3, reaction (125)) results in a slight increase in χ (Figure 4.3b, Table 4.2). Figures 4.14 and 4.15 in Supporting Information present the isopleths of the mixing-ratio of PAN as a function of E_{NO_x} and E_{VOCs} at the pedestrian level in regular and deep canyons, respectively. Since the production of PAN cannot be simulated by a simple NO_x-O_3 cycle, ignoring free-radical chemistry may result in an underestimate of the significance of PAN in street canyons. The model results show a clear spatial distribution of PAN in regular and deep street canyons, respectively; high PAN concentrations in the presence of low NO_x and high VOC emissions imply that lowering NO_x must be accompanied by a concerted effort on VOC emissions to limit PAN production in the UCL. Additional information is available in Supporting Information (i.e., model sensitivity).

4.3.2 Model Sensitivity

Sensitivity runs (Figures 4.10-4.11 in Supporting Information; Table 4.2) determine the impacts of prevailing wind velocity (U_0) on NO_2 mixing-ratios. Air quality within the modelled urban canyons improves considerably, up to ~25%, with better ventilation, and deteriorates sharply, by up to ~60%, when U_0 is low (Supplementary Figures 4.10-4.11). This behavior is in-line with previous modelling results (ZhongCai and Bloss, 2016b) and observations (Gidhagen et al., 2004). In our model, the airflow inside street canyons is assumed to be linearly scaled to U_0, but the effects on NO_2 are highly non-linear with respect to emission profiles and monitoring locations within street canyons (Supplementary Figures 4.12-4.13) because of the tight coupling of chemistry-transport processes. In the regular canyon, χ drops very rapidly in Case 1 compared to Case 0 (Table 4.2) because the low U_0 implies a longer residence time for air parcels, making free-radical chemistry more important.

Figure 4.4 and Figure 4.5 show the effect of emission heterogeneity on NO_2 mixing-ratios near the carriageway. The mixing-ratio of NO_2 shows little change ($\chi \approx$ that in Case 0) at the upward-vortex side as vehicle emissions shift from the central street toward the pavement, but it becomes very different at the downward-vortex side, especially in the deep canyon (see Figure 4.11 in Supporting Information). This asymmetry has clear implications for coordinated urban planning of transport and the built environment. The emission heterogeneity may also alter the mass fluxes escaping the canyons and thus, the overall mixing-ratio of pollutants within canyons. This becomes even more important when the blocking effect of central barriers and the segregation impact are considered, which merits future investigation.

Table 4.2. The "wiggle room" (χ, dimensionless) under the hourly NO_2 compliance line[a]

E_{VOCs}^{norm} [b]	Regular canyon (AR = 1)			Deep canyon (AR = 2)		
	0.1	1.0	2.0	0.1	1.0	2.0
Case 0	1.89	1.82	1.48	0.73	0.24	0.29
Case 1[c]	1.46	0.78	0.54	0.41	0.16	0.22
Case 2[c]	>1.9[a]	>1.9[a]	>1.9[a]	1.01	0.34	0.32
Case 3[d]	1.87	1.80	1.43	0.71	0.24	0.28
Case 4[d]	1.86	1.77	1.39	0.69	0.23	0.27

[a]The maximum value for χ in the AR = 1 phase space is 1.9; higher values indicates that parameter values beyond the state space investigated would be compliant; [b]E_{VOCs}^{norm} represents the ratio of VOC emission rates to its typical emission condition (TEC); [c]Varying prevailing wind velocity; [d]Varying distribution of vehicle emissions.

An alternative view of VOC free-radical chemistry effects is provided in Figure 4.6, which is produced from NO_2-E_{VOCs} "slices" through the full NO_2–E_{VOCs}–E_{NO_x}– f_{NO_2} phase space. For clarity, we normalize the E_{VOCs} values to $E_{VOCs,TEC}$ (i.e., E_{VOCs}^{norm}) and normalize NO_2 mixing-ratios to their values at E_{VOCs}^{norm} = 1. Each area divided by vertical dotted lines represents one VOC emission scenario as labelled in Figure 4.6. The range of boxes represents the variability in NO_2 (%) under different E_{NO_x} and f_{NO_2} conditions, and the points and lines represent the variability in NO_2 (%) for the IEC situation. Model errors that would occur from using the simple NO_x-O_3 scheme are closely approximated by the y-axis range of the boxes, and are highly dependent upon E_{NO_x}, E_{VOCs}, f_{NO_2}, and street canyon geometries. The degree of model error, due to using the

simple chemistry, is not linearly related to these emission parameters due to the chemical complexity.

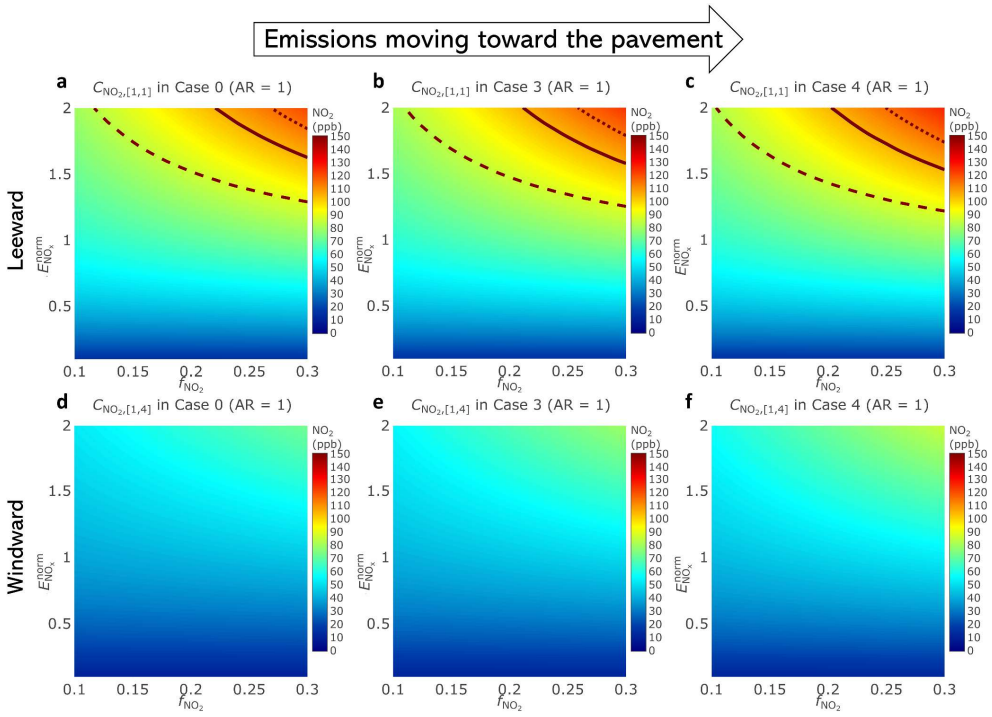


Figure 4.4. Emission heterogeneities on NO_2 mixing-ratios in the regular canyon. The mixing-ratios (ppb) of NO_2 on the leeward side ($C_{NO_2,[1,1]}$) and windward side ($C_{NO_2,[1,4]}$) of the regular canyon at $E^{norm}_{VOCs} = 1$ under different emission heterogeneities. f_{NO_2} is the primary NO_2 fraction, and $E^{norm}_{NO_x}$ is the ratio of NO_x emission rates to the TEC of a typical emission condition. The solid line represents the UK air quality hourly NO_2 limit (105 ppb), and this contour line shifts to the dotted and dashed lines when E^{norm}_{VOCs} changes to 0.1 and 2, respectively.

In Case 0, the effect of neglecting VOC free-radical chemistry underestimates NO_2 by 5.9% to 22.1% (8.8% for the IEC) in the regular canyon, and becomes even more significant (-51.3% to 30.9%, -25.2% for the IEC) in the deep canyon. Lowering U_0 greatly enhances the residence time of reactive species

and increases the range of under- or over-estimation in NO_2 (Case 1), making free-radical chemistry more important even in the regular canyon (-39.5% to 6.9%, -15.4% for the IEC). The effect of emission heterogeneity on NO_2 is minor in the regular canyon (Cases 3 and 4) under most circumstance but cannot be ignored in the deep canyon (Figure 4.6).

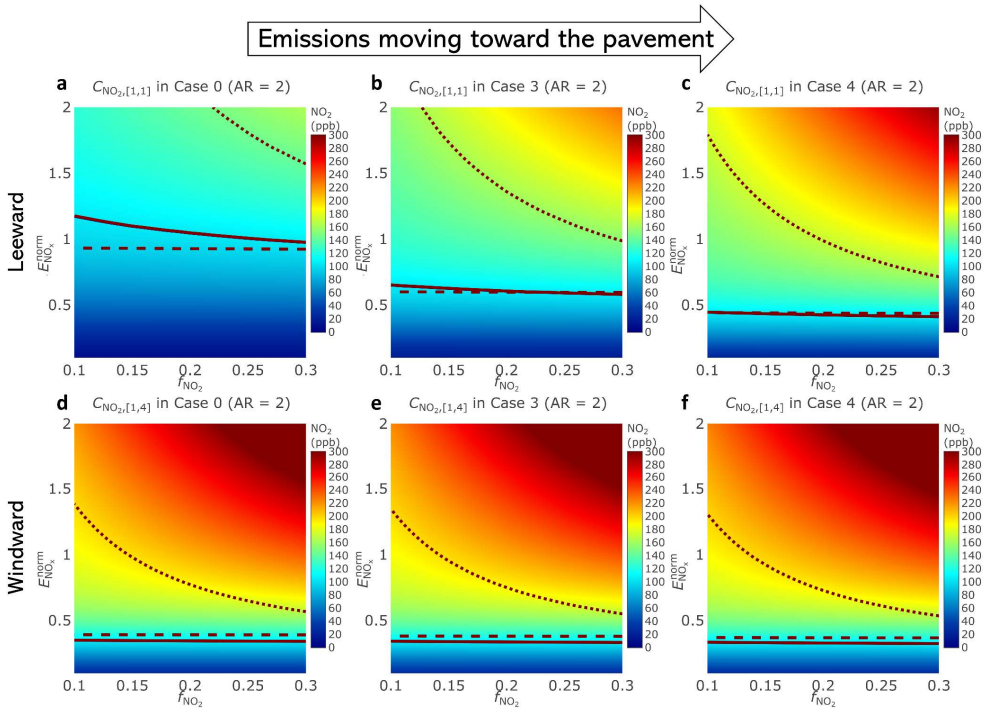


Figure 4.5. Emission heterogeneities on NO_2 mixing-ratios in the deep canyon. The mixing-ratios (ppb) of NO_2 on the leeward side ($C_{NO_2,[1,1]}$) and windward side ($C_{NO_2,[1,4]}$) of the deep canyon at E^{norm}_{VOCs} = 1 under different emission heterogeneities. f_{NO_2} is the primary NO_2 fraction, and $E^{norm}_{NO_x}$ is the ratio of NO_x emission rates to the TEC of a typical emission condition. The solid line represents the UK air quality hourly NO_2 limit (105 ppb), and this contour line shifts to the dotted and dashed lines when E^{norm}_{VOCs} changes to 0.1 and 2, respectively.

4.3.3 Implications for Future Regulatory Practice and Modelling

Chemical (and microphysical) complexities in street canyons have been accommodated using one- and 1D two-box models of street canyons to date (Nikolova et al., 2016, Pugh et al., 2012, ZhongCai and Bloss, 2016b). The magnitude of underestimation or overestimation of NO_x and NO_2 levels by the typical one-box model is quantified in Supporting Information. The one-box model significantly under- and over-estimated mixing-ratios on the upward- and downward-vortex sides of street canyons, respectively (Figure 4.18). The inaccuracy varies with U_0 but is more strongly dependent upon emission source strength and heterogeneity. In general, the one-box model performs closer to multi-box model results for NO_x in less polluted areas (i.e., low E_{NO_x} and E_{VOCs}), but its performance on reactive species such as NO_2 does not improve correspondingly, due to non-linear chemistry. Previous studies have built empirical equations that are derived from long-term in-situ observations (Kakosimos et al., 2010, Westmoreland et al., 2007, MaseyHamilton and Beverland, 2018) for NO_2 calculation from NO_x in some operational models (e.g., STREET (Johnson et al., 1973), AEOLIUS (Buckland and Middleton, 1999), OSPM (Berkowicz, 2000, Vardoulakis et al., 2007)). Our results, however, indicate that such data-driven correlations would vary substantially across sites based on emissions (see, for example, Figures 4.10-4.13) and should be used with care in regulatory practice and modelling. Additional explanation is given in Support Information.

The results presented here, particularly our discussion of regulatory "wiggle room", χ, should not be interpreted as a tolerance of emissions, but rather as an acknowledgement that air quality management operates in the frame of available technologies and publicly acceptable regulation (DEFRA, 2023, DEFRA, 2019b). Although our focus has been on NO_2 and PAN, VOCs contribute significantly to the generation of other secondary pollutants such as O_3 and aerosols (Mozaffar et al., 2020, Wu and Xie, 2017, Wang et al., 2018) and the management required to control those may be different. The impact of VOC free-radical chemistry on NO_2 concentrations in a regular canyon has been uncertain: it has been calculated previously to be rather limited (~10%) (BrightBloss and Cai, 2013, Garmory et al., 2009), or more significant (KimPark and Kim, 2012). By developing a computationally efficient model with spatial resolution and free-radical chemistry, we draw out the impact of chemistry more clearly through an exploration of the model phase space. Our findings indicate that NO_2 productions through VOC chemistry may be substantial or insignificant, depending in predictable ways on emission characteristics.

It is also worth noting that the effect of VOC chemistry on NO_2 at the pedestrian "hotspot" is likely much greater than the effect on the whole canyon volume. By focusing on "compliant" parameter sets producing model results below the UK 1-hour air quality standard, tens of thousands of model integrations can be described visually in a succinct way and even collapsed to a single integral metric, χ, which warns when neglect of radical chemistry is most misleading. The strong dependence of our results on aspect ratio and wind speed demonstrate starkly the need for emissions control given the densification of

urban living (NæssSaglie and Richardson, 2020, Stone Jr et al., 2007) and the global terrestrial stilling (i.e., a reduction in land surface wind velocity of ~8%) which has been observed during recent decades (Zeng et al., 2019, Vautard et al., 2010, Tian et al., 2019, McVicar et al., 2012).

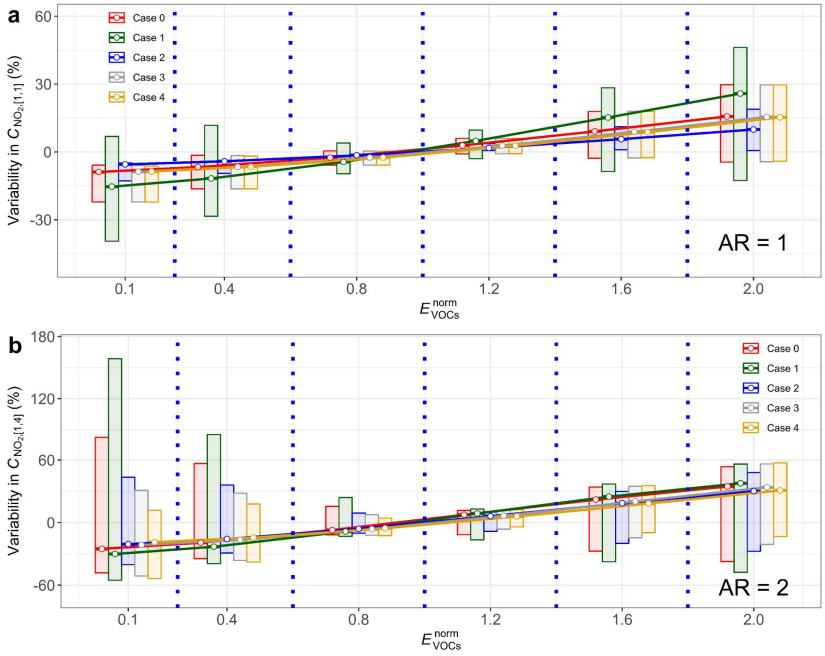


Figure 4.6. The NO_2 variability under different emission scenarios. The variability in the mixing-ratio of NO_2 (%) under different normalised NO_x emissions ($E^{norm}_{NO_x}$), VOC emissions (E^{norm}_{VOCs}), and primary NO_2 fractions (f_{NO_2}) in regular (a) and deep (b) street canyons, respectively. Each area that divided by vertical blue dotted lines represent one VOC emission scenario as labelled. The points and solid lines represent the variability in NO_2 for the intense emission condition (IEC) on a putative perfect AR = 1 "Marylebone Road" ($E^{norm}_{NO_x}$ = 2, f_{NO_2} = 0.26).

Taking a broader perspective on the "wiggle room", this dimensionless factor can be used in a variety of more-or-less rigorous ways. Estimating the location

of particular street canyons on the contour plot qualitatively is useful in order to develop efficient synergistic pathways for air quality regulations. The metric can be expanded to create a "wiggle volume" if necessary to fit in three-dimensional (3D) parameter-space that can be explained in great detail (Figure 4.8). The local slope components of χ reflects the effectiveness of limiting a parameter (e.g., emissions) to improve air quality. Furthermore, χ could also be extended to be employed at larger scales, since cooperative control strategies for regional NO_x and VOC emissions are urgently needed, but research has not yet fully quantified their social costs (Shen et al., 2021, Ding et al., 2021).

4.4. Supporting Information

4.4.1 Supplementary Methods

(1) Model formulation

In a typical one-box model, the mixing-ratio of any chemical species in street canyons can be mathematically expressed as (Liu and Leung, 2008):

$$\frac{dC_{q,0}}{dt} = E_{q,0} - \frac{w_{e,0}}{h_0}\left(C_{q,0} - C_{q,b}\right) + \Delta S_{q,0} + \Delta V_{q,0} \quad (4.1)$$

where $C_{q,0}$ (ppb) and $C_{q,b}$ (ppb) are the mixing-ratios of q^{th} chemical species respectively in Box_0 and in the rooftop background, t (s) is the time in second, h_0 (m) is the building height near the carriageway, $w_{e,0}$ (m s^{-1}) is the exchange velocity between the street canyon and the overlying background, $E_{q,0}$ (ppb s^{-1}) is the rate of the q^{th} species from continuous line sources that injected into Box_0 in a mixing-ratio tendency depending on the model grid size (e.g., h_0 for

the one-box model), $\Delta S_{q,0}$ (ppb s^{-1}) is the net chemical production and loss rate, and $\Delta V_{q,0}$ (ppb s^{-1}) is the net deposition rate of the q^{th} species in Box_0.

In the multi-box model, advective mass transport (denoted by a subscribe "a") and turbulent mixing with a bulk format of the Fick's law (denotes by a subscript "e") are two key dynamics in street canyons and also, determines air exchange velocities between the canyon and the overlying background (CuiCai and J. Baker, 2004, Eliasson et al., 2006, CaiBarlow and Belcher, 2008). We build up a series of "advective velocities" and "turbulent velocities" to calculate mixing-ratio communications between any two adjacent boxes in the regular and the deep canyons, respectively. The expressions of vertical and horizontal mixing-ratio fluxes across the interface of grids are:

$$F_{e,[k,i]} = u_{e,[k,i]}\left(C_{q,[k,i\text{-}1]} - C_{q,[k,i]}\right) \tag{4.2}$$

$$F_{a,[k,i]} = \begin{cases} U_{a,[k,i]}C_{q,[k,i\text{-}1]}, U_{a,[k,i]} \geq 0 \\ U_{a,[k,i]}C_{q,[k,i]}, U_{a,[k,i]} < 0 \end{cases} \tag{4.3}$$

$$G_{e,[k,i]} = w_{e,[k,i]}\left(C_{q,[k\text{-}1,i]} - C_{q,[k,i]}\right) \tag{4.4}$$

$$G_{a,[k,i]} = \begin{cases} W_{a,[k,i]}C_{q,[k\text{-}1,i]}, W_{a,[k,i]} \geq 0 \\ W_{a,[k,i]}C_{q,[k,i]}, W_{a,[k,i]} < 0 \end{cases} \tag{4.5}$$

where $F_{e,[k,i]}$ (ppb m s^{-1}) and $F_{a,[k,i]}$ (ppb m s^{-1}) are horizontal mixing-ratio fluxes describing turbulent diffusion and advective transfer, respectively, and $G_{e,[k,i]}$ (ppb m s^{-1}) and $G_{a,[k,i]}$ (ppb m s^{-1}) are the corresponding vertical mass fluxes for these processes. $C_{q,[k,i]}$ (ppb) represents the mixing-ratio of the q^{th} species in $Box_{[k,i]}$. The terms $U_{a,[k,i]}$ (m s^{-1}) and $u_{e,[k,i]}$ (m s^{-1}) are pollutant transfer velocities respectively due to advective transportation and turbulent

mixing in the horizontal direction; $W_{a,[k,i]}$ (m s^{-1}) and $w_{e,[k,i]}$ (m s^{-1}) are transfer velocities respectively due to advection and turbulence in the vertical direction. Defining all fluxes as vectors which are positive upwards and rightwards, the mixing-ratio of the q^{th} species in $Box_{[k,i]}$ is:

$$\frac{dC_{q,[k,i]}}{dt} = E_{q,[k,i]} - \frac{G_{a,[k,i+1]}+G_{e,[k,i+1]}}{l_i} + \frac{G_{a,[k,i]}+G_{e,[k,i]}}{l_i} - \frac{F_{a,[k+1,i]}+F_{e,[k+1,i]}}{h_k} + \frac{F_{a,[k,i]}+F_{e,[k,i]}}{h_k} + \Delta S_{q,[k,i]} + \Delta V_{q,[k,i]} \quad (4.6)$$

where $E_{q,[k,i]}$ (ppb s^{-1}) is the emission rate of the q^{th} species in $Box_{[k.i]}$, l_i (m) and h_k (m) are the width and height of $Box_{[k.i]}$, $\Delta S_{q,[k,i]}$ is the net chemical production and loss rate, and $\Delta V_{q,[k.i]}$ (ppb s^{-1}) is the net deposition rate of the q^{th} species in $Box_{[k.i]}$.

The multi-box model adopts stable background conditions in the overlying shear layer above the roof over a long operating time (e.g., in the order of one hour), while mixing-ratios vary dynamically at a fast time step (e.g., seconds) in street canyons. Due to the very similar magnitude of advective fluxes entering and escaping street canyons with AR ≥ 1 in the neutral atmosphere (SalizzoniSoulhac and Mejean, 2009), the escaping canyon fluxes due to vertical advection are rotated into the horizontal direction for the mixing-ratio balance near the rooftop, and thus the multi-box model applies only turbulent terms at the rooftop (Dai et al., 2021b).

Ideally, the box geometry should mirror the compartmentalisation of the in-canyon flow arising from physical obstructions and asymmetric heating (ZhongCai and Bloss, 2016b). Therefore we allow grid sizes to vary in the vertical and cross-canyon directions. Accordingly, we define two

dimensionless ratios to denote the size of mesh to the total canyon volume with $m \times n$ boxes within street canyons:

$$\alpha_k = \frac{h_k}{h_0} \tag{4.7}$$

$$\beta_i = \frac{l_i}{l_0} \tag{4.8}$$

where h_0 (m) is the canyon height, l_0 (m) is the street width, h_k (m) is the grid height on k^{th} (k = 1, 2,..., m) layer and l_i (m) is the grid width on i^{th} (i = 1, 2,..., n) column. Using a multi-box model with only four grids as an example (Figure 4.7), $\alpha_1 = \beta_1 = 0.5$ indicates that four boxes in the street canyon have equal volumes. An α_1 value of 0.3 and β_1 of 0.7 describes the splitting in which $Box_{[1,1]}$ and $Box_{[1,2]}$ occupy 21% and 49% volume of the canyon, respectively. An α_1 value of 0.7 and β_1 of 0.3 represent that $Box_{[1,1]}$ and $Box_{[2,2]}$ occupy 21% and 9% volume of the canyon, respectively. Moreover, air pollutants may be injected into different boxes in street canyons due to, for example, street reservation and hedgerow. Here we use a dimensionless factor $\gamma_{q,[k,i]}$ (k = 1,2,..., m; i = 1, 2,..., n) to depict the spatially heterogeneous line emissions of the q^{th} species within the multi-box model. Hence, on the k^{th} layer of the canyon:

$$\gamma_{q,[k,i]} = \frac{\alpha_k \beta_i E_{q,[k,i]}}{\sum_{o=1;j=1}^{o=m;j=n} \alpha_o \beta_j E_{q,[o,j]}} \tag{4.9}$$

$E_{q,[k,i]}$ (ppb s^{-1}) is the emission rate of the q^{th} species in $Box_{[k,i]}$. A $\gamma_{q,[k,i]}$ value of 0 means that no emission activities of the q^{th} species occurred in $Box_{[k,j]}$; and a $\gamma_{q,[k,i]}$ value of 1 means that all emissions are injected into $Box_{[k,i]}$.

Considering model dynamics, for the one-box model, an exchange rate $w_{e,0}$ is adopted to describe mass transfer of pollutants between street canyons and

overlying background; for the multi-box models, $|W_a, U_a|$ is used as the assemble of pollutant transfer velocities due to advective transport, and $|w_e, u_e|$ is the set of pollutant transfer velocities due to turbulence in street canyons. These dynamical parameters derived from the LES (Appendix A Table S1 and Table S2) under an ambient prevailing wind velocity (U_0) of 2.0 m s^{-1} in the neutral atmosphere (ZhongCai and Bloss, 2017, BrightBloss and Cai, 2013) are used to describe airflow characteristics in the idealised regular and deep canyons without any obstacles, respectively. Detailed information about the derivation process and the comparison between the multi-box model and the LES results are presented in (Dai et al., 2021b). It is worth noting that dynamical parameters must be modified in a physically consistent way to guarantee continuity of the airflow, and extrapolations to AR-specific canyons must be conducted with caution, for instance, the advective process becomes important for avenue street canyons (LiuLeung and Barth, 2005, Pearce et al., 2021). For time-dependent dynamical processes of the multi-box model, the multi-variable 4^{th} order Runge-Kutta method has been used to solve the ordinary differential equations (ODEs) numerically (Williamson, 1980).

The multi-box model permits flexible chemical schemes from highly lumped to nearly explicit. In the current version, the multi-box model supports two chemical mechanisms described as follows:

(1) Simple NO_x-O_3 photochemistry with the Leighton relationship (i.e., photo-stationary state assumption) that used by previous LES studies (BaikKang and Kim, 2007, BakerWalker and Cai, 2004):

$$NO + O_3 \rightarrow NO_2 \quad (4.10)$$

$$NO_2 + h\nu \overset{O_2}{\rightarrow} NO + O_3 \quad (4.11)$$

where $h\nu$ is photon energy.

(2) A Reduced Chemical Scheme (RCS) that developed by BrightBloss and Cai (2013) for simulating reactive species in street canyons during daytime. As with almost all grid-based models, we assume that chemical species undergo sufficient mixing in an empirical integration time interval of 0.03s for long-lived species (e.g., NO_2, O_3), and of 0.003s for short-lived species (e.g., OH, HO_2) in each box according to the framework of the multi-box model (ZhongCai and Bloss, 2017).

(2) Model evaluation

For the model evaluation, the Schildhornstrasse site has a carriageway width of 18 m, a canyon width of 26 m, and an average building height of 21 m (AR ≈ 0.81). The street is oriented 120° to the north, and it carries around 45,000 vehicles per day. The air quality monitor is located on the south-westerly side of the carriageway at the height of 2.5 m. The Goettingerstrasse has a street width of 25 m and a canyon height of 20 m (AR ≈ 0.8). The street is oriented 165° to the north and carries around 30,000 vehicles per day. A continuous operating monitor is settled on the south-westerly side of the street at the height of 1.5 m. The two-line Jagtvej street has a traffic intensity of 22,000 vehicles per day, with a street width of 25 m and a canyon height of 18 m (AR ≈ 0.72). The street aligns about 30^0 with respect to the north, and hourly pollutants are measured at 3.5 m height on the south-easterly side of the road,

5.7 m from the canyon facet. For these TRAPOS sites, annual diurnal vehicle profiles of buses, vans, cars, and trucks were counted for weekdays, Saturdays, and Sundays, respectively. In our study, hourly NO_x emissions that taken from National Atmospheric Emissions Inventory (NAEI) for central London (51.522°N, 0157°E) in the year 2008 were used for the model evaluation (Bush et al., 2010). Emission rates of NO_x into street canyons were 8.2 mg m^{-2} hr^{-1} and they were scaled according to traffic volume, which are consistent with those evaluations of Pugh et al. (2012). The background values and meteorological conditions (i.e., wind direction, wind velocity) were measured from surrounding buildings and suburban areas. Further descriptions about the TRAPOS sites were also provided in Hood et al. (2021) and the website (https://www2.dmu.dk/atmosphericenvironment/Trapos/).

Marylebone Road is a major thoroughfare in the City of Westminster that carries around 90,000 vehicles per day, and it has been generally identified as a near-regular and symmetrical street canyon edged by continuous buildings frontage, with an AR of about a unity ($h_0 \approx l_0 \approx 34$ m, measured from Google Earth). The air sampling monitor is located on the southside near the central carriageway, with a sampling inlet at a height of approximately 4 m. North Kensington is an urban background site to the west of Marylebone Road. Routine hourly measured NO, NO_2, O_3 and CO from 1st January 2010 to 23rd June 2019 were taken from both sites for the model evaluation. Two-direction hourly traffic counts of the same period for Marylebone Road were extracted from the Automatic Traffic Counter (ATC) Database and provided by Transport for London (TfL). They were used to calculate vehicle emissions,

which implies a linear relationship between vehicle counts and pipe emissions. Note that those data with missing values over five minutes within an hour were excluded.

Having established that VOC chemistry contributes only a small fraction of NO_2 in the regular canyon under high U_0 (Supplementary Figure 4.10), the simple NO_x-O_3 cycle — i.e., equation 4.10 and equation 4.11, with a NO_2 production coefficient k_1 of 4.01×10^{-4} ppb^{-1} s^{-1} and a photodegradation coefficient k_2 of 9.20×10^{-3} s^{-1} — is adopted for the model evaluation in order to save computational time. Annual fleet-averaged emission inventories (hot exhaust only), including the primary NO_2 fraction (f_{NO_2}) for central London are drawn from UK National Atmospheric Emissions Inventory (NAEI), which have been listed in Table 4.3 in Supporting Information. Hourly meteorological data, including wind velocity, wind direction, cloud condition, and weather events are retrieved from London Heathrow Airport, representing the synoptic flow condition in the background overlying the canyon roof.

To narrow the scope, daytime meteorological data from 9: 00 a.m. to 15:00 p.m. under the "clear sky" without weather events (e.g., precipitation, snow) are extracted for the monitoring sites (with available meteorological data). The vortex studies are limited to situations where the ambient wind blows perpendicularly to the street canyon axis, eliminating the effects from along street advection. Therefore, wind directions with an angle not exceeding 25° perpendicular to the street axis and wind velocities equal to or higher than 2 m s^{-1} are used for the analysis. For example, on the Marylebone Road, wind

directions within 140°-190° for two-consecutive-hour represent the "leeward condition" (i.e., the air quality monitor situated on the leeward side), and within 320°-10° represent the "windward condition", respectively. The background mixing-ratios are assumed to be uniformly distributed through the whole domain initially and employed as inlet boundary conditions during each model operation period (i.e., one hour).

The normalisation (i.e., min-max feature scaling) for Figure 4.2 in the main text is calculated as follows:

$$C_q^{\text{norm}} = \frac{C_q - min(C_q)}{max(C_q) - min(C_q)} \quad (4.12)$$

where C_q^{norm} is the normalised mixing-ratio of q^{th} species, max(C_q) and min(C_q) are the maximum and minimum values of the entire dataset (comprising modelling results and observations). The discussion is presented in the main text. Six commonly-used statistics are adopted to evaluate modelled mixing-ratios against observations, including fraction of predictions within a factor or two (FAC2), root-mean-square deviation (RMSD), unsystematic RMSD ($RMSD_u$), systematic RMSD ($RMSD_s$), Pearson's correction coefficient (R), and index of agreement (IOA) (Cai and Steyn, 2000, Willmott et al., 1985, Willmott, 1981, WillmottRobeson and Matsuura, 2012). The mathematical expressions of those indicators are provided as equations 4.13-4.20. FAC2 is the fraction of model predictions that satisfy within the range of 0.5 to 2, and RMSD calculates the average difference between matched pairs of estimators and observations. If the value of RMSD tends to be zero, the modelled data match well with observations. The metric, R, measures the goodness-of-fit of the best linear

relationship between modelled and observed mixing-ratios, and IOA indicates the degree of convergence between modelled data and observations. The closer the value of FAC2, R or IOA to unity represents a better model performance.

$$0.5 \leq \frac{P_r}{O_r}(\text{FAC2}) \leq 2.0 \tag{4.13}$$

$$\text{RMSD} = \sqrt{\frac{\sum_{r=1}^{N}(P_r - O_r)^2}{N}} \tag{4.14}$$

$$\text{RMSD}_u = \sqrt{\frac{\sum_{r=1}^{N}(P_r - \hat{P}_r)^2}{N}} \tag{4.15}$$

$$\text{RMSD}_s = \sqrt{\frac{\sum_{r=1}^{N}(\hat{P}_r - O_r)^2}{N}} \tag{4.16}$$

$$\text{R} = \frac{1}{N-1}\sum_{r=1}^{N}\left(\frac{P_r - \overline{P}}{\delta_P}\right)\left(\frac{O_r - \overline{O}}{\delta_O}\right) \tag{4.17}$$

$$\text{IOA} = \begin{cases} 1 - \frac{\sum_{r=1}^{N}|P_r - O_r|}{2\sum_{r=1}^{N}|O_r - \overline{O}|}, \sum_{r=1}^{N}|P_r - O_r| \leq 2\sum_{r=1}^{N}|O_r - \overline{O}| \\ \frac{2\sum_{r=1}^{N}|O_r - \overline{O}|}{\sum_{r=1}^{N}|P_r - O_r|} - 1, \sum_{r=1}^{N}|P_r - O_r| > 2\sum_{r=1}^{N}|O_r - \overline{O}| \end{cases} \tag{4.18}$$

where P_r and O_r denote the r^{th} rank of values from the modelling and observations, respectively; N is the total number of a continuous dataset; a bar represents the mean value (e.g., $\overline{P_r}$); $\widehat{P_r}$ is derived from:

$$\hat{P}_r = a + b \times O_r \tag{4.19}$$

a is intercept and b is the slope. Then, we have a following relationship:

$$\text{RMSD}^2 = \text{RMSD}_u{}^2 + \text{RMSD}_s{}^2 \tag{4.20}$$

The modelling evaluation statistics for urban street canyons are shown in Table 4.5 in Supporting Information for NO_x on TRAPOS sites, and for NO_x and

NO_2 mixing-ratios on Marylebone Road, respectively. Although all monitoring sites have lower AR values than a typical regular (AR = 1) canyon, which generally means more efficacious ventilation, for Schildhornstrasse, Goettingerstrasse and Marylebone Road, the high-resolution 16-box model performs better with respect to NO_x compared to the typical one-box model. For Jagtvei, the correction (R value) of the 16-box model for NO_x is slightly less than that of the one-box model, but the systematic RMSD is reduced substantially from 46 ppb to 29 ppb. The performance of two models with respect to simulate NO_2 mixing-ratios on Marylebone Road is very similar. Overall, evaluation results above are comparable with those of in Hood et al. (2021).

Our model evaluation indicates the complexity of advective transportation and turbulent diffusion, which has a discernible impact on air quality on the leeward side of a regular canyon. Marylebone Road is subject to many complications (e.g., vegetations, barriers, bus stops) that make the real road very different from an idealised street canyon (Hood et al., 2021). The presence of significant leafy vegetation on the leeward side may considerably constrain dynamical processes and resist airflow moving upwards to the roof, resulting in severe air pollution on the leeward side of the regular canyon (Wang et al., 2020, MoradpourAfshin and Farhanieh, 2017, Salmond et al., 2013), but note that the effectiveness of vegetation on dispersion remains highly controversial (Jeanjean et al., 2015, Abhijith et al., 2017). There are some other sources of uncertainties in model evaluations, such as unrepresented mechanical turbulence, ground heating, wall heating, and

shading. For example, turbulent diffusion is often more appreciable under "opposing" wall heating conditions (Cai, 2012b); two opposing rotating vortices may also form in a regular canyon due to building roof configurations and floor heated effects (Takano and Moonen, 2013, XieHuang and Wang, 2005). These uncertainties may be accommodated in the future by building a library of dynamic parameters for the multi-box model from LES runs.

Additionally, although already a marked improvement on single-box approaches, the performance of the multi-box models on simulating NO_x and NO_2 in Marylebone Road may be improved further. By substituting observed concentrations into equations 4.2-4.5, while retaining mass fluxes from the LES, we can calculate a revise set of place-specific empirical parameters (Table 4.4), and all evaluating statistics are greatly improved as shown in Supplementary Table 4.5 (i.e., model 16-box-ps, denoted in red). In the future, building empirical equations could help to make the multi-box model independent of the LES operations.

(3) Model sensitivity

We set up a series of sensitivity scenarios (see Table 4.1, main text) to investigate NO_2 mixing-ratios in street canyons. Assuming that the rooftop exchange velocity and in-canyon dynamics are linearly proportional to the prevailing wind velocity (U_0), cases set up with the magnitude of U_0 ranging from 1.2 m s^{-1} (Case 1) to 2.8 m s^{-1} (Case 2). Although the maximum of wind speeds is not very large, it provides a 40% increases in canyon ventilation when compared to the typical condition (U_0 = 2 m s^{-1}) that was used in

previous LES (c.f., BrightBloss and Cai (2013)), resulting in substantial improvements in street canyon air quality. We assume that vehicle emissions are uniformly injected into boxes near central canyons (i.e., $Box_{[1,2]}$, $Box_{[1,3]}$ in Figure 4.1, main text) for the model evaluation and Case 1-2.

In order to investigate the effects of emission heterogeneity on NO_2 mixing-ratios, we adopted another two cases (Case 3 and Case 4) as shown in Table 4.1 of the main text. Keeping total vehicle emissions constant, Case 3 represents that line traffic emissions emitted equally across the domain into $Box_{[1,1]}$, $Box_{[1,2]}$, $Box_{[1,3]}$ and $Box_{[1,4]}$, respectively; Case 4 represents that emissions emitted at the domain edges into $Box_{[1,1]}$ and $Box_{[1,4]}$ only (i.e., no emissions in $Box_{[1,2]}$ and $Box_{[1,3]}$).

Figure 4.10 illustrates the effects of U_0 on the NO_2 mixing-ratios (ppb) on the leeward ($C_{NO_2,[1,1]}$) and windward ($C_{NO_2,[1,4]}$) sides of the regular canyon at a typical VOC emission rate (i.e., normalised VOC emission E_{VOCs}^{norm} = 1) from the 16-box model, for Case 1 (a, d, U_0 = 1.6 m s^{-1}), Case 0 (b, e, U_0 = 2.0 m s^{-1}), Case 2 (c, f, U_0 = 2.4 m s^{-1}), respectively. For box locations at the pedestrian level of the regular canyon, the dashed line (i.e., the hourly NO_2 limit) shifts from the bottom-left towards the top-right from Case 0 to Case 2, and the clean zone (Region "C") gradually dominates the modelling scenarios. The modelled NO_2 on the leeward side from the 16-box model is, in general, higher than those on the windward side in terms of the presence of primary vortex (c.f., BrightBloss and Cai (2013)). Because of efficient ventilation promoted by U_0, $C_{NO_2,[1,1]}$ for the "intense emissions condition (IEC)" is 193.7, 121.2, 90.6 ppb, and $C_{NO_2,[1,4]}$

is 115.6, 72.7, 54.7 ppb from Case 1 to Case 0, and to Case 2, respectively. Similarly, for the deep canyon (Supplementary Figure 4.9), $C_{NO_2,[1,1]}$ for the IEC is 218.4, 163.6 and 126.0 ppb, and $C_{NO_2,[1,4]}$ is 528.3, 321.5 and 261.2 ppb from Case 1 to Case 2, respectively, suggesting higher risks of breaching the hourly NO_2 limit due to pollutants being trapped in the deep canyon. The multi-box modelling results show that the emission heterogeneity may cause differences in NO_2 levels near the carriageway in both regular and deep canyons (Figure 4 and Figure 5 in main content). For the IEC at E_{VOCs}^{norm} = 1 as an example, from Case 0 to Case 3 and Case 4, $C_{NO_2,[1,1]}$ are 121.2, 123.9 and 126.7 ppb and $C_{NO_2,[1,4]}$ are 72.7, 79.2 and 85.7 ppb in the regular canyon; $C_{NO_2,[1,1]}$ are 163.6, 230.1 and 294.2 ppb, and $C_{NO_2,[1,4]}$ are 351.5, 359.2, 366.9 ppb in the deep canyon, respectively. The results imply that the mixing-ratio of NO_2 on the downward-vortex side is more affected by the emission heterogeneity than those of the upward-vortex side.

Additionally, Figures 4.14 and 4.15 in Supporting Information depict the isopleths of the mixing-ratio of peroxyacetyl nitrate (PAN) in the regular and deep canyons, respectively, corresponding to NO_x and VOC emissions. PAN is a highly hazardous and lachrymatory air pollutants that is produced by photochemical reactions between VOCs and NO_x. PAN has a distinct spatial distribution at the pedestrian level similar to that of NO_2, rising on the upward-vortex side and decreasing on the downward-vortex side of street canyons. The horizontal distribution of PAN is consistent with the LES findings. For example, ZhongCai and Bloss (2017) observed a percentage gradient of about

7.6% in the deep canyon (AR = 2), which corresponds to 1.27 ppb on the upward-vortex side and 1.18 ppb on the downward-vortex side, averaged within the multi-box grid resolution. Significantly more PAN is produced with low U_0 because chemical reactions have more time to occur, especially in the deep canyon; raising U_0 lowers the mixing-ratio of PAN in the canyons. With high VOC and low NO_x emissions, higher PAN concentrations are found, which is in line with previous modelling studies and observations. For example, the observed PAN in southern California could increase up to 65 ppb during the summer (Lashgari, 2005); a greater reduction in NO_x than VOCs can lead to less NO-O_3 titrations (resulting in high NO_2 to NO ratios due to reaction between peroxyacetyl radical ($CH_3C(O)O_2$) and NO, c.f., Xu et al. (2021)) and favour the formation of free-radicals and thus, PAN in the atmosphere (Wang et al., 2017, Qiu et al., 2020, QiuMa and Li, 2019); previous 0D chemistry box model results showed that severe PAN levels (e.g., more than 50 ppb) may occur in street canyons if emission conditions (e.g., significantly higher VOCs than NO_x) are met (Seinfeld and Pandis, 2008, Liu and Leung, 2008).

Biogenic volatile organic compounds (BVOCs) emitted by urban vegetations, such as isoprene (C_5H_8) and monoterpenes (α-pinene and β-pinene, both $C_{10}H_{16}$), may undergo photochemical reactions, resulting in the formation of secondary air pollutants such as O_3, peroxy nitrates, and particulates. Their contributions may grow to be very substantial on a regional scale (Chameides et al., 1988, Donovan et al., 2005, Calfapietra et al., 2013). Three reactions (Appendix B Table S3, reactions 36-38) have been included in the chemical scheme used in this study (i.e., RCS) to account for BVOC chemistry, both α-

pinene and β-pinene were omitted from the mechanism represented by the surrogate species isoprene. In the main text, only vehicle emissions are considered. To investigate the effect of BVOCs on the street canyon chemistry, we briefly examined the sensitivity of several key air pollutants to BVOC emissions for regular and deep canyons under the typical emission condition (TEC) with f_{NO_2} = 0.26 in Case 0 (U_0 = 2 m s^{-1}). The emission rate of BVOCs (as a total of isoprene and monoterpenes) is taken from Owen et al. (2003), which is 1000 g km^{-2} h^{-1} for rural land classes (the emissions in dense urban areas are even lower). Table 4.5 presents the differences in percentage between the model results at the "hotspot" that include and exclude BVOC emissions. The results indicate that natural BVOC emissions from urban vegetations have very little effect (< 1%) on air pollutants such as NO_2, O_3, and PAN in urban street canyons.

4.4.2 Supplementary Discussion

(1) Distribution of pollutants in street canyons

Figures 4.16 and 4.17 in Supporting Information provide the spatial distribution of NO, NO_2, O_3 and PS concentrations in the regular and deep street canyons, respectively. These figures represent a modelling scenario under the TEC (E_{VOCs}^{norm} = 1.0, $E_{NO_x}^{norm}$ = 1.0) that described above with a f_{NO_2} = 0.26 and a typical prevailing wind speed (U_0 = 2 m s^{-1}). In the regular canyon, NO concentrations are slightly lower than NO_2 in this idealised modelling scenario due to high f_{NO_2}, the involvement of VOC chemistry, and also background conditions. The concentration differences between leeward and windward

sides are significant than their vertical variations for NO, NO_2, and PS. The maximum value is found at the corner of leeward side for NO_2 and PS, but is found at the rooftop of leeward side of the street canyon for NO.

In the deep street canyon, Figure 4.17 shows that two counter-rotating vortices exist in the canyon, this can be expected due to the LES configuration in previous studies (ZhongCai and Bloss, 2017, ZhongCai and Bloss, 2015). NO concentrations are lower than NO_2 but they have a comparable spatial patterns within the canyon. Additionally, the vertical variations are quite small along the leeward facet but become more pronounced on the windward side. NO and NO_2 concentrations are substantially elevated at the pedestrian level on the windward side compared to those on the leeward side, and they drop sharply by as much as ~80% with increasing height. Eventually, NO and NO_2 levels on the windward side become lower than those on the leeward side.

(2) Inaccuracy of the one-box case

The mixing-ratios of the q^{th} species at the pedestrian level (i.e., $C_{q,[1,1]}$ and $C_{q,[1,4]}$) are vital for evaluations of the actual hazard of pollutants to residents near the carriageway. Considering data post-processing, the differences of modelled mixing-ratios between the one-box model and a m×n-box model on the leeward and windward sides are respectively:

$$\Delta C_{q,[1,1]} = C_{q,0} - C_{q,[1,1]} \tag{4.21}$$

$$\Delta C_{q,[1,n]} = C_{q,0} - C_{q,[1,n]} \tag{4.22}$$

then the percentage of overestimation or underestimation by the one-box model at the pedestrian level can be written as:

$$\varphi_{q,[1,1]} = \frac{\Delta C_{q,[1,1]}}{C_{q,[1,1]}} \times 100\% \quad (4.23)$$

$$\varphi_{q,[1,n]} = \frac{\Delta C_{q,[1,n]}}{C_{q,[1,n]}} \times 100\% \quad (4.24)$$

To clarify, for example, if $\varphi_{q,[1,1]}$ = 0%, then the mixing-ratio of the q^{th} species in the one-box .model is the same as that of $Box_{[1,1]}$; a positive value of $\varphi_{q,[1,1]}$ indicates that, compared to the multi-box model which offers benchmark model results, the one-box model overestimates the mixing-ratio on the leeward side; and $\varphi_{q,[1,n]}$ indicates a similar meaning to $\varphi_{q,[1,1]}$ but for the windward side of street canyons.

Figure 4.18a in Supporting Information presents the results of $\varphi_{NO_2,[1,1]}$ and $\varphi_{NO_2,[1,4]}$, and similarly, Figure 4.18c provides the results of $\varphi_{NO_x,[1,1]}$ and $\varphi_{NO_x,[1,4]}$ in the regular and deep canyons under different U_0 (i.e., Cases 0-2). Supplementary Figures 4.18b and 4.18d illustrate the extent to which the one-box model underestimates or overestimates NO_x and NO_2 in the regular and deep canyons under different emission heterogeneities (i.e., Cases 3-4) at a constant prevailing wind velocity of U_0 = 2.0 m s^{-1}. The variation of the points in each case represents the underestimation or overestimation under different emission conditions (i.e., including all 8400 scenarios). Here, NO_x can be regarded as a chemically inert passive tracer because chemical reactions alter the fraction of NO and NO_2 but have little effect on NO_x (i.e., only a small fraction of NO_x has been converted into nitric acid). In other word, the spatial

distribution of NO_x mostly attributes to the in-canyon physical process, while NO_2 depends on both physical and chemical processes. The findings demonstrate that the model error introduced by a simple one-box model is strongly reliant on the prevailing wind speed, the emission heterogeneity, and the canyon geometry; different distributions of NO_2 and NO_x in Figure 4.18 illustrate the impacts of chemical processes on the model performance. Consequently, no single correction factor is capable of reconstructing multi-box models from the one-box results.

(3) Inaccuracy of empirical conversion of NO_x to NO_2

Although the semi-empirical models such as AEOLIUS (Buckland and Middleton, 1999) and STREET (DabberdtLudwig and Johnson Jr, 1973) lack the ability to describe those reactive species that carry out free-radical reactions, an oxidant-partitioning model can be used to calculate the chemical reactions between NO, NO_2 and O_3. The mathematical description is (DEFRA, 2005):

$$C_{\mathrm{NO_2}} = C_{\mathrm{NO_2},b} + (C_{O_3,b} - C_{O_3}) + f_{\mathrm{NO_2}} \times (C_{\mathrm{NO}_x} - C_{\mathrm{NO}_x,b}) + C^* \quad (4.25)$$

where C^* is the regional oxidant contribution excluding background contributions, and other parameters have been defined above. Accordingly, the empirical equation applied for areas in central London is (MaseyHamilton and Beverland, 2018):

$$C_{\mathrm{NO_2}} = -0.0001 \times \left(C_{\mathrm{NO}_x}\right)^2 + 0.2737 \times C_{\mathrm{NO}_x} + 18.648, R^2 = 0.997 \quad (4.26)$$

the unit of the concentrations of NO_x and NO_2 is in μg m^{-3}. Using spatial distribution of NO_x to derive those of NO_2 empirically will ignore the coupling effect of physical and chemical processes in urban street canyons. In order to assess the differences in model results between the process-based scheme (i.e., RCS chemistry) and empirical calculations, we applied the equation (4.26) to calculate NO_2 in street canyons using the modelled NO_x from the multi-box models. Subsequently, the unit of NO_2 concentrations is converted into ppb at 20°C and 1 atm. Assuming the NO_2 values of the multi-box models as the benchmark, Figure 4.19 in Supporting Information provides the variability of model errors in percentage using the empirical equation (4.26) at the pedestrian level of the regular and deep canyons under different E_{NO_x}, E_{VOCs}, and f_{NO_2}. Our results show that even with minimal involvement of VOC radical chemistry (i.e., E_{VOCs}^{norm} = 0.1), the range of uncertainty varies significantly with E_{NO_x} and f_{NO_2}. The empirical calculation of NO_2 is also influenced by the prevailing wind velocity, the emission heterogeneity, and the canyon geometry. For example, high U_0 (e.g., Case 2) can reduce the model error up to ~40% compared to low U_0 situations for the IEC; the model error induced by the emission heterogeneity is not significant (~5%) in the regular canyon, but it becomes more significant (up to ~17%) in the deep canyon. The results given here indicate that the accuracy of using empirical equations for predicting reactive species is largely dependent on pollutant discharge conditions, and therefore such equations must be utilized with caution and judged against case-by-case criteria.

(4) An integral metric

Recognizing the sensitivity of the compliance line to the intensity of VOC free-radical chemistry, and by inspection of Figures 4.3-4.5 and Supplementary Figures 4.10 and 4.11 we offer the following integral as a measure of the overall impact of organic chemistry or the canyon geometry on the regulatory "wiggle room", χ, available in a particular location:

$$\chi = \int_{min(\psi_1)}^{max(\psi_1)} min\left(\psi_2 \middle| q^{\text{th}}(\psi_3), max(\psi_2)\right) d\psi_1 \tag{4.27}$$

where ψ_1, ψ_2, and ψ_3 represent any three adjustable parameters, which control the concentration of q^{th} species, $\psi_2|_{q^{\text{th}}(\psi_3)}$ represent the "compliance line" of q^{th} species over the entire 2D ψ_1-ψ_2 phase space as a function of ψ_1 at constant ψ_3, and the "min" and "max" functions represent the minimum and the maximum of values of parameters within the parameter space studied. Although the hyper-volume for the full multi-dimensional ψ_1 to ψ_3 phase space under the "compliance surface" for q^{th} species can be computed, for simplicity χ is calculated here as a family of metrics based on a 2D slice of the ψ_1 to ψ_2 phase space at each fixed ψ_3 value in order to assess the extent to which it varies with ψ_3. Therefore, from the various permutations of equation (4.27), we choose equation (4.28) because it foregrounds the parameters most directly related to NO_2:

$$\chi = \int_{min\left(f_{\text{NO}_2}^{\text{norm}}\right)}^{max\left(f_{\text{NO}_2}^{\text{norm}}\right)} min\left(E_{\text{NO}_x}^{\text{norm}} \middle| \text{NO}_2 = 105(E_{\text{VOCs}}^{\text{norm}}), max\left(E_{\text{NO}_x}^{\text{norm}}\right)\right) df_{\text{NO}_2}^{\text{norm}} \tag{4.28}$$

where $f_{\text{NO}_2}^{\text{norm}}$ represents the normalized f_{NO_2} to its value at f_{NO_2} = 0.2, that is, min ($f_{\text{NO}_2}^{\text{norm}}$) = 0.5 and max($f_{\text{NO}_2}^{\text{norm}}$) = 1.5, and χ is mathematically equal to the

E_{NO_x}–f_{NO_2} phase space under the compliance line plus the remaining space of compliance. Therefore, a high magnitude of χ represents the presence of more space for E_{NO_x} and f_{NO_2} binding in street canyons to bring NO_2 into compliance; otherwise, a small increment in E_{NO_x} or f_{NO_2} may greatly increase the risk of exceeding the hourly NO_2 limit. The differences in χ (i.e., $\Delta\chi$) due to the varying E_{VOCs}, the canyon geometry, and other available parameters can be interpreted by their influence on the position of the compliance line and, therefore, the concentration of NO_2 throughout the whole E_{VOCs}–E_{NO_x}–f_{NO_2} phase spaces. However, note that even if $\Delta\chi \approx 0$, a visual inspection of phase space is still essential to investigate the sensitivity of NO_2 to E_{NO_x} and f_{NO_2}.

The variation of χ values with respect to ψ_3 (e.g., E_{VOCs} in the main text) may be used to characterize the sensitivity of NO_2 to any change in ψ_3. For instance, for a central London scenario (AR = 1) in Case 0 (U_0 = 2 m s^{-1}), we computed χ values when ψ_3 was set to E_{NO_x} and f_{NO_2} (hereafter denoted as "$\chi(E_{NO_x})$" and "$\chi(f_{NO_2})$"), respectively. The results are presented in Figure 4.20. The wiggle room, χ (i.e., ψ_3 is E_{VOCs} as in the equation (4.28) and the main text), rises by 22% from E_{VOCs}^{norm} = 2.0 to E_{VOCs}^{norm} = 0.1; $\chi(E_{NO_x})$ grows by 47% from $E_{NO_x}^{norm}$ = 2.0 to $E_{NO_x}^{norm}$ = 1.3; and $\chi(f_{NO_2})$ increases by 19% from $f_{NO_2}^{norm}$ = 1.5 to $f_{NO_2}^{norm}$ = 0.6. However, the slope of three curves indicates that while $E_{NO_x}^{norm}$, E_{VOCs}^{norm}, and $f_{NO_2}^{norm}$ continue to decline, the rise in wiggle room grows slower, suggesting that these critical emission parameters should be managed in concert to ensure more effective air quality improvement.

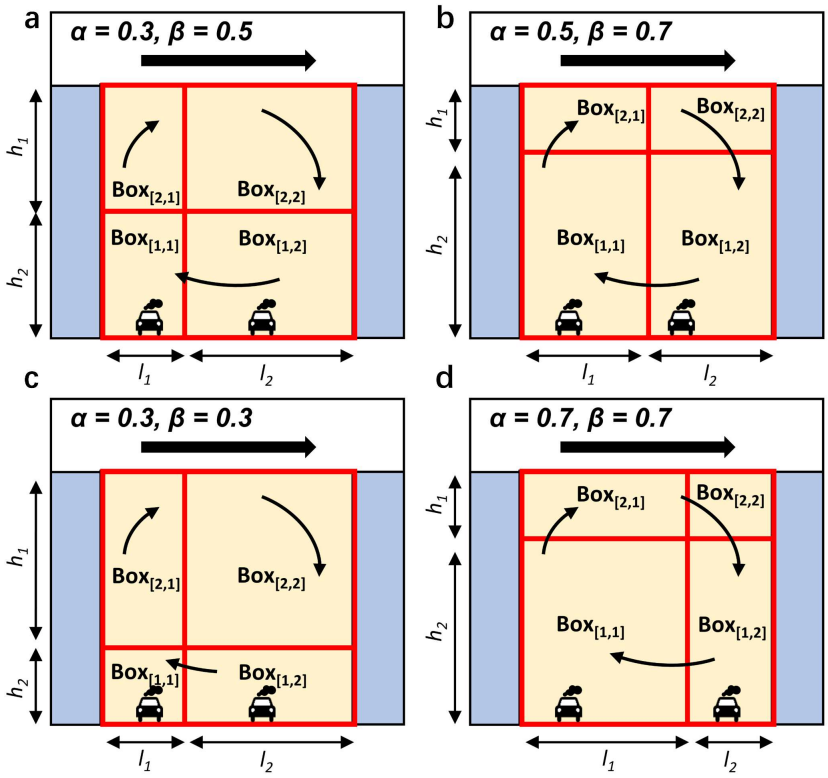


Figure 4.7. The multi-box model framework. **a-d.** Conceptual diagram of the 4-box model with different boxes in size for the regular street canyon.

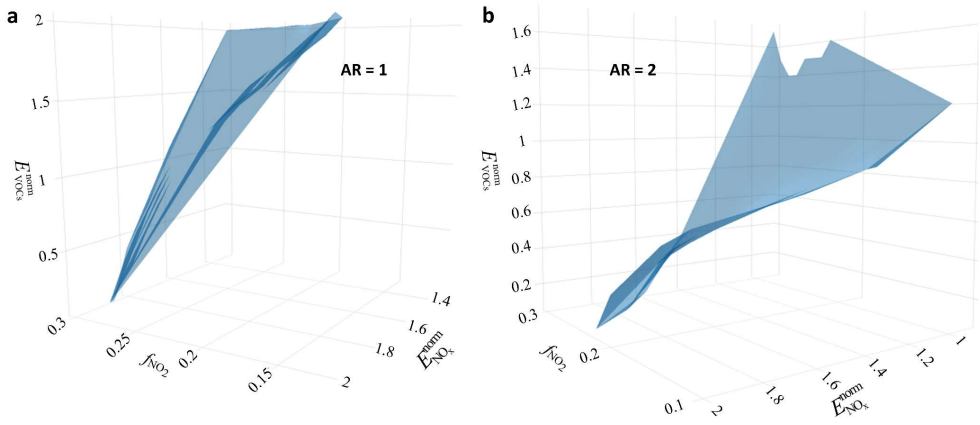


Figure 4.8. Compliance surface of NO_2 in street canyons. The mixing-ratio compliance surface (105 ppb) of NO_2 on the upward-vortex side of a regular canyon (**a**, AR = 1) and a deep canyon (**b**, AR = 2) under a typical prevailing wind velocity of U_0 = 2 m s^{-1} (Case 0).

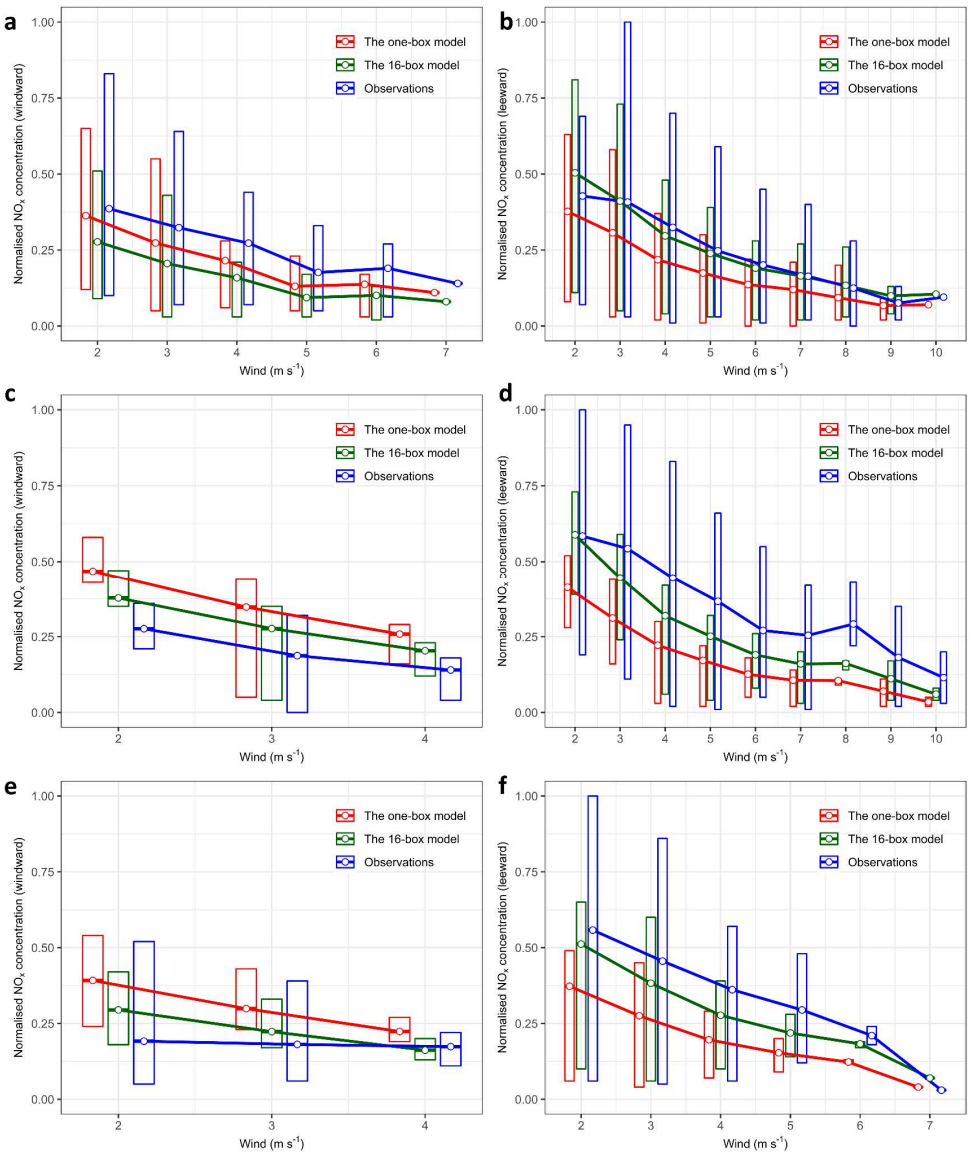


Figure 4.9. Comparison of model results against observations. Comparison of normalized modelled NO_x concentrations against observations in Jagtvej (**a**, **b**), Goettingerstrasse (**c**, **d**), and Schildhornstrasse (**e**, **f**), respectively. The error bars represent the range of data at the same U_0, and thus a similar airflow pattern within the street canyon. The points represent the average values for each group.

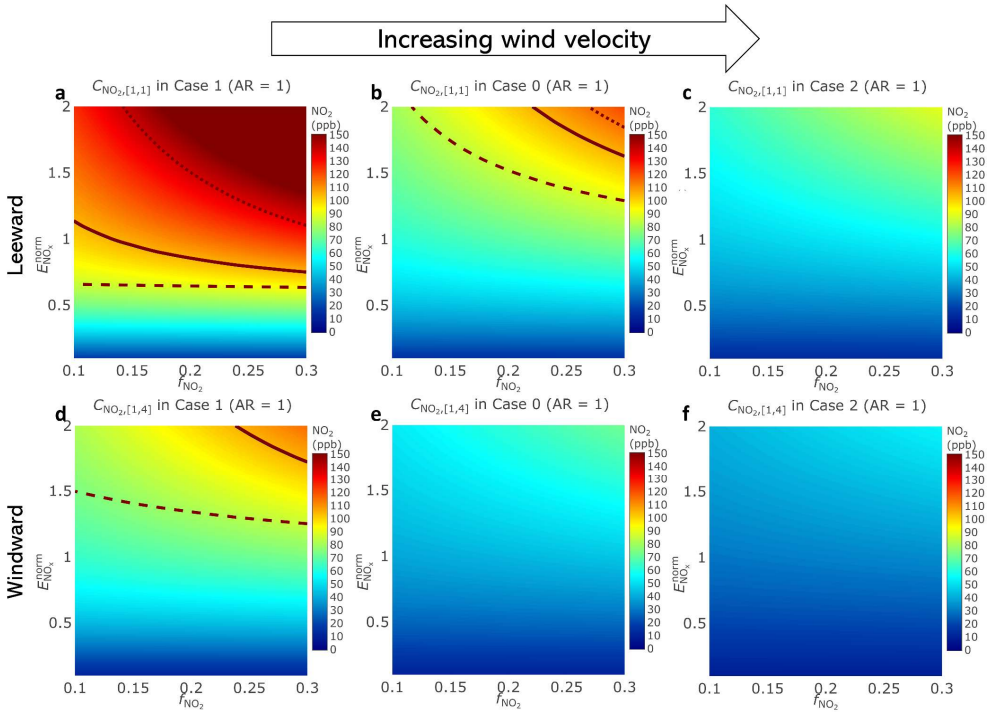


Figure 4.10. Wind effects on upward-vortex side NO_2 mixing-ratios at the pedestrian level in the regular canyon. The mixing-ratios (ppb) of NO_2 on the leeward side ($C_{NO_2,[1,1]}$) and windward side ($C_{NO_2,[1,4]}$) of the regular canyon at E^{norm}_{VOCs} = 1 under different external wind velocities (U_0 = 2 m s^{-1} for Case 0 (**b**, **e**); U_0 = 1.2 m s^{-1} for Case 1 (**a**, **d**); U_0 = 2.8 m s^{-1} for Case 2 (**c**, **f**)). f_{NO_2} is the primary NO_2 fraction, and $E^{norm}_{NO_x}$ is the ratio of NO_x emission rates to the TEC of a typical emission condition. The solid line represents the UK air quality hourly NO_2 limit (105 ppb), and this contour line shifts to the dotted and dashed lines when E^{norm}_{VOCs} changes to 0.1 and 2, respectively.

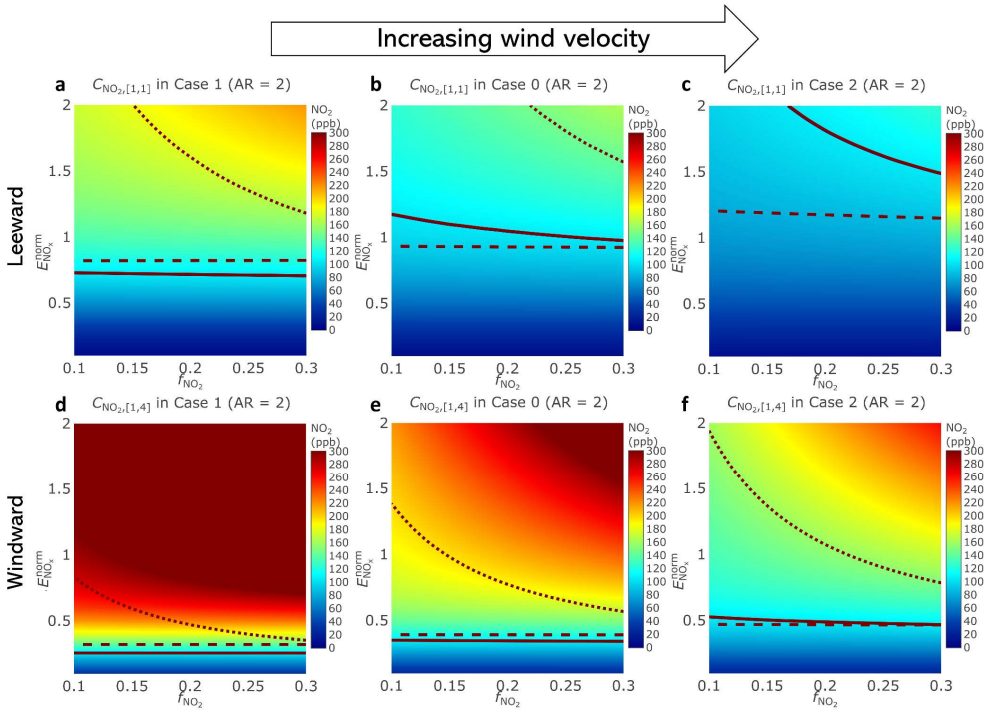


Figure 4.11. Wind effects on upward-vortex side NO_2 mixing-ratios at the pedestrian level in the deep canyon. The mixing-ratios (ppb) of NO_2 on the leeward side ($C_{NO_2,[1,1]}$) and windward side ($C_{NO_2,[1,4]}$) of the deep canyon at E^{norm}_{VOCs} = 1 under different external wind velocities (U_0 = 2 m s^{-1} for Case 0 (**b**, **e**); U_0 = 1.2 m s^{-1} for Case 1 (**a**, **d**); U_0 = 2.8 m s^{-1} for Case 2 (**c**, **f**)). f_{NO_2} is the primary NO_2 fraction, and $E^{norm}_{NO_x}$ is the ratio of NO_x emission rates to the TEC of a typical emission condition. The solid line represents the UK air quality hourly NO_2 limit (105 ppb), and this contour line shifts to the dotted and dashed lines when E^{norm}_{VOCs} changes to 0.1 and 2, respectively.

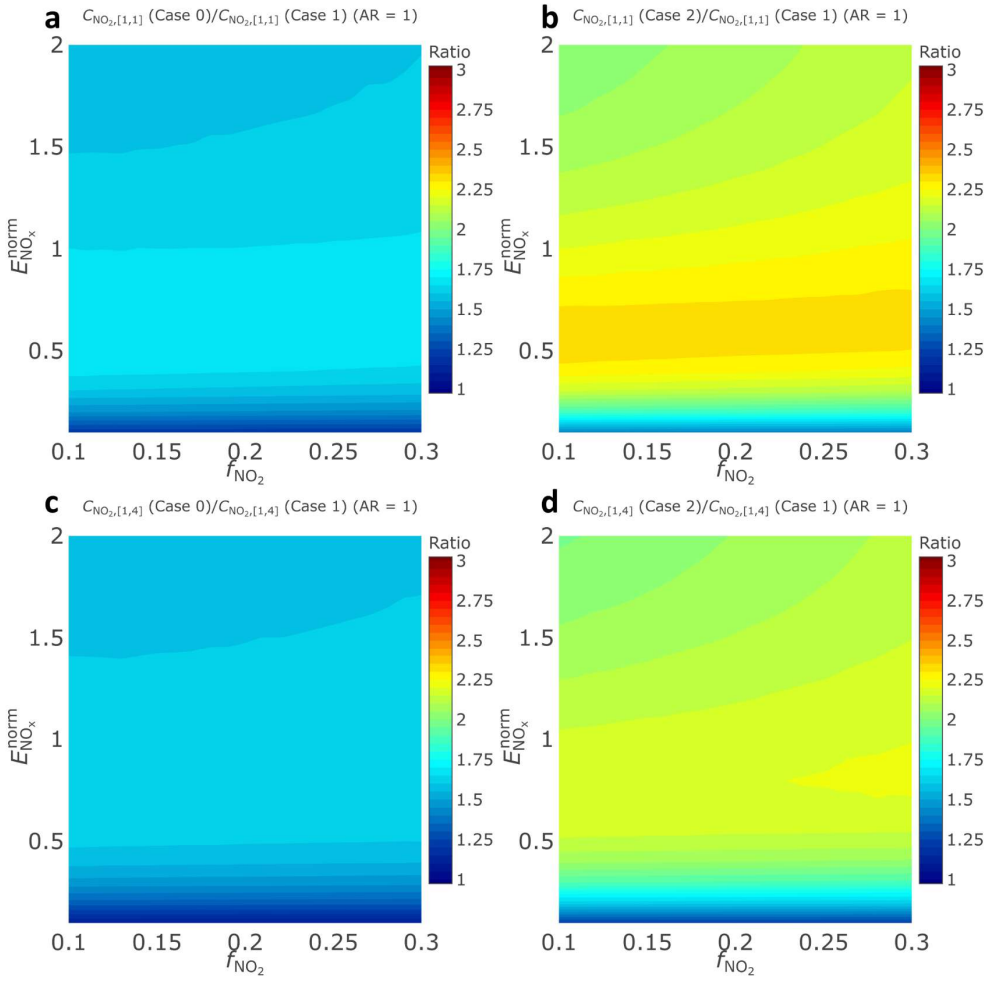


Figure 4.12. Wind effects on relative NO_2 at the pedestrian level in the regular canyon. **a-d.** The ratios of NO_2 mixing-ratios under different external wind velocities (U_0) from Case 0 (U_0 = 2 m s^{-1}) to Case 2 (U_0 = 2.8 m s^{-1}) to those of Case 1 (U_0 = 1.2 m s^{-1}) in the regular canyon at a typical VOC emission rate (E^{norm}_{VOCs} = 1). f_{NO_2} is the primary NO_2 fractions, and $E^{norm}_{NO_x}$ is the ratio of NO_x emission rates to the TEC of a typical emission scenario.

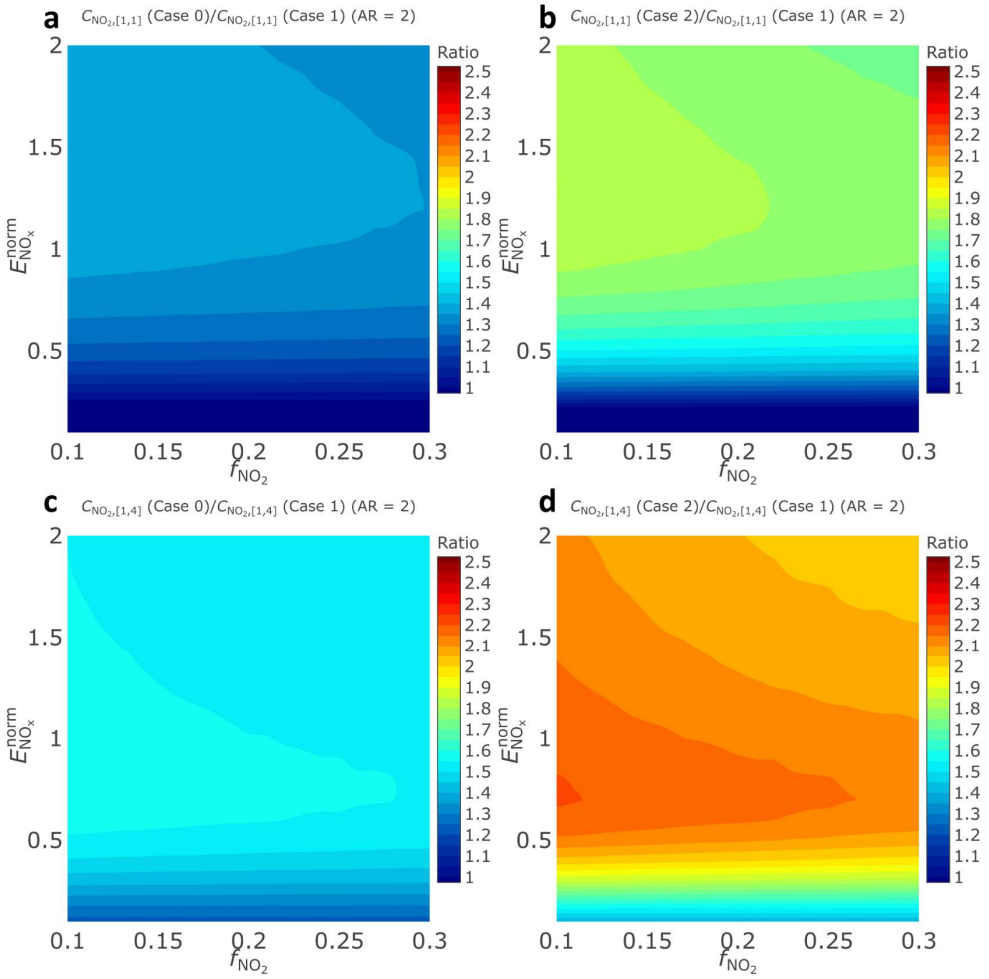


Figure 4.13. Wind effects on relative NO_2 at the pedestrian level in the deep canyon. **a-d.** The ratios of NO_2 mixing-ratios under different external wind velocities (U_0) from Case 0 (U_0 = 2 m s^{-1}) to Case 2 (U_0 = 2.8 m s^{-1}) to those of Case 1 (U_0 = 1.2 m s^{-1}) in the deep canyon at a typical VOC emission rate (E^{norm}_{VOCs} = 1). f_{NO_2} is the primary NO_2 fraction, and $E^{norm}_{NO_x}$ is the ratio of NO_x emission rates to the TEC of a typical emission scenario.

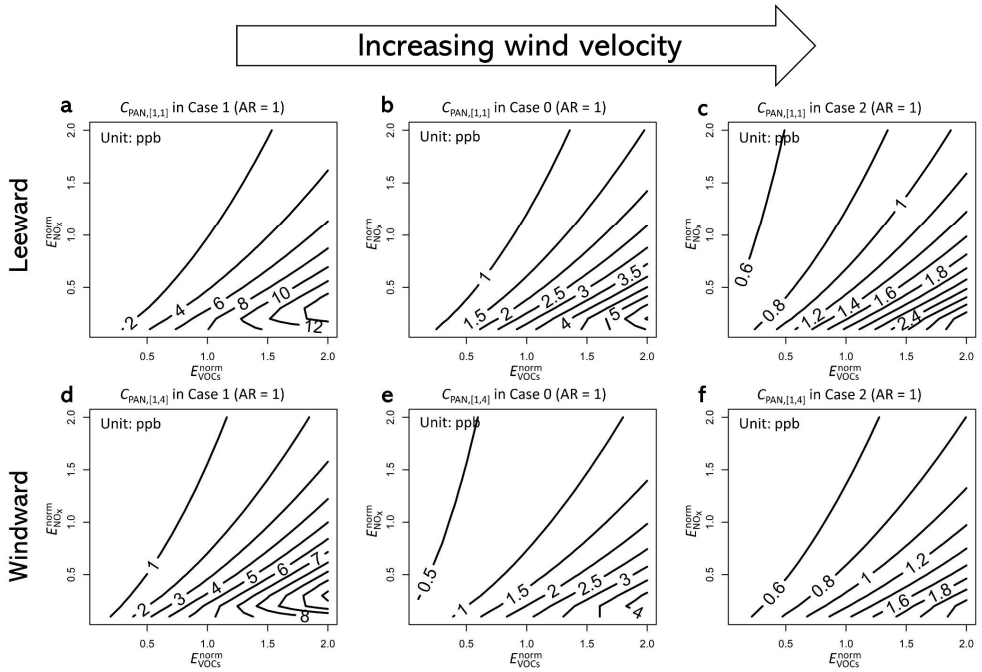


Figure 4.14. Emissions effects on upward-vortex side PAN mixing-ratios at the pedestrian level in the regular canyon. Isopleths showing the mixing-ratios (ppb) of peroxyacetyl nitrate (PAN) as a function of NO_x and VOCs emissions on the leeward side ($C_{PAN,[1,1]}$) and windward side ($C_{PAN,[1,4]}$) of the regular canyon at f_{NO_2} = 0.26 under different external wind velocities (U_0 = 2 m s^{-1} for Case 0 (**b**, **e**); U_0 = 1.2 m s^{-1} for Case 1 (**a**, **d**); U_0 = 2.8 m s^{-1} for Case 2 (**c**, **f**)). E^{norm}_{VOCs} and $E^{norm}_{NO_x}$ are the ratios of VOCs and NO_x emission rates to the TEC of a typical emission condition, respectively.

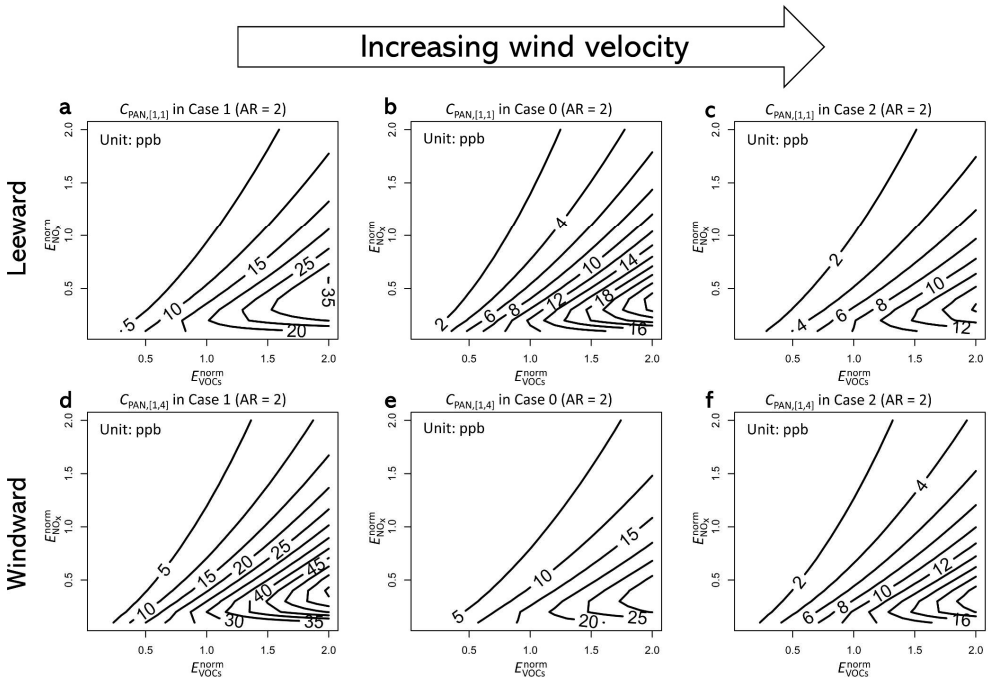


Figure 4.15. Emissions effects on upward-vortex side PAN mixing-ratios at the pedestrian level in the deep canyon. Isopleths showing the mixing-ratios (ppb) of peroxyacetyl nitrate (PAN) as a function of NO_x and VOCs emissions on the leeward side ($C_{PAN,[1,1]}$) and windward side ($C_{PAN,[1,4]}$) of the deep canyon at f_{NO_2} = 0.26 under different external wind velocities (U_0 = 2 m s^{-1} for Case 0 (**b**, **e**); U_0 = 1.2 m s^{-1} for Case 1 (**a**, **d**); U_0 = 2.8 m s^{-1} for Case 2 (**c**, **f**)). E_{VOCs}^{norm} and $E_{NO_x}^{norm}$ are the ratios of VOCs and NO_x emission rates to the TEC of a typical emission condition, respectively.

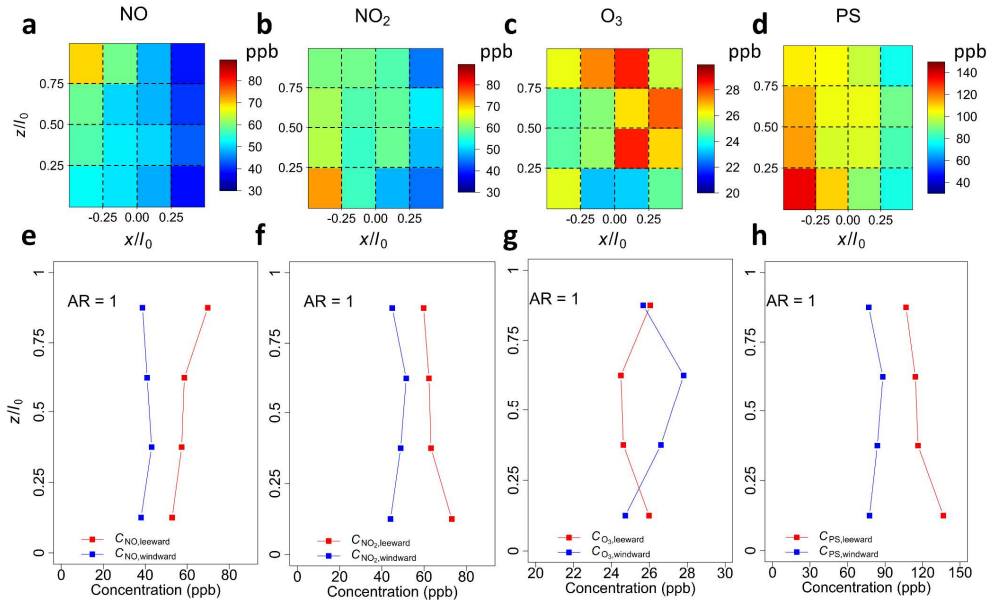


Figure 4.16. The spatial distribution of air pollution in the regular canyon. The spatial distribution of NO, NO_2, O_3, and PS (ppb) in the regular street canyon (**a-d**). Line graph panels **e-h** present the vertical distribution of pollutants along the leeward and windward facets. Subscripts "leeward" and "windward" represent the magnitude of differences along with the leeward wall ($-0.5 < x/l_0 < -0.25$) and the windward wall ($0.25 < x/l_0 < 0.5$), respectively. See text for details.

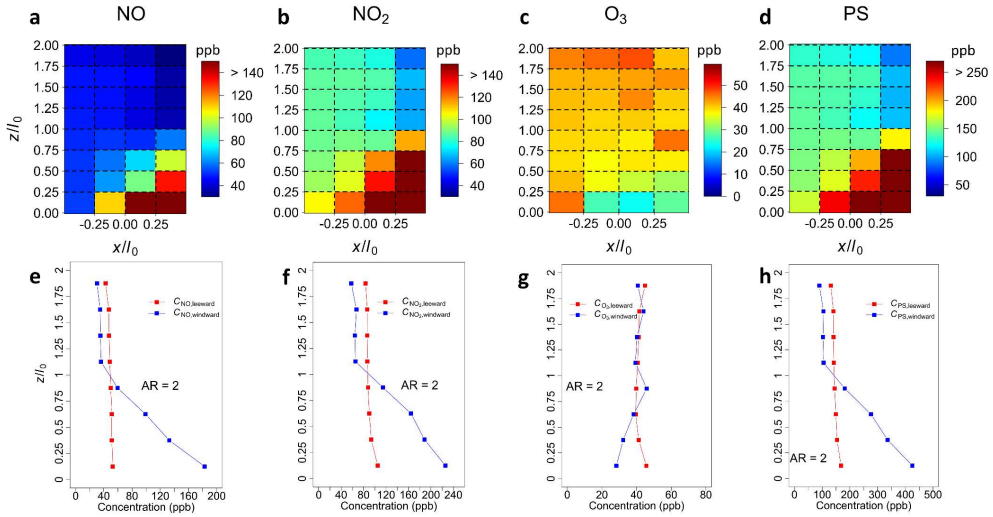


Figure 4.17. The spatial distribution of air pollution in the deep canyon. The spatial distribution of NO, NO_2, O_3, and PS (ppb) in the deep street canyon (**a-d**). Line graph panels **e-h** present the vertical distribution of pollutants along the leeward and windward facets. Subscripts "leeward" and "windward" represent the magnitude of differences along with the leeward wall ($-0.5 < x/l_0 < -0.25$) and the windward wall ($0.25 < x/l_0 < 0.5$), respectively. See text for details.

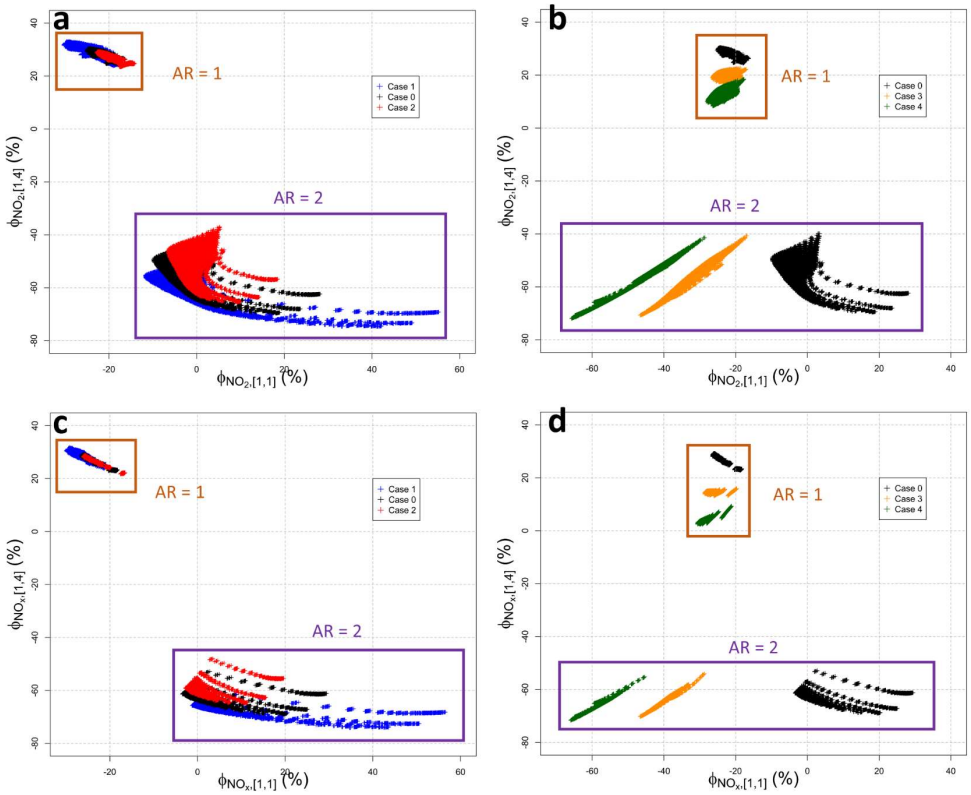


Figure 4.18. The overestimation and underestimation of air pollution by the one-box model. **a-d.** The overestimation and underestimation of NO_x and NO_2 mixing-ratios by the typical one-box model compared to the 16-box model (AR = 1) and 32-box models (AR = 2) at the pedestrian level under different external wind velocities (U_0 = 2 m s^{-1} for Case 0; U_0 = 1.2 m s^{-1} for Case 1; U_0 = 2.8 m s^{-1} for Case 2) (see, Figures 4.18a and 4.18c); and from the 16-box model and 32-box models at the pedestrian level under different emission heterogeneities (Figures 4.18b and 4.18d). The rectangular frame provides the range of over- and underestimation.

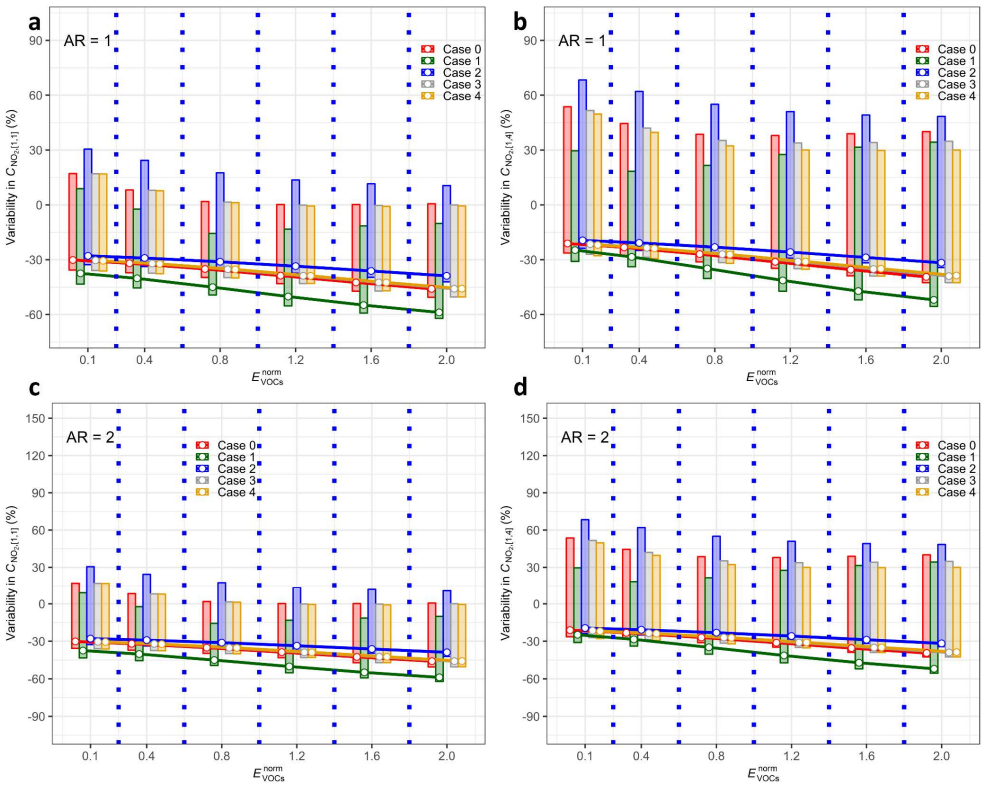


Figure 4.19. The variability in NO_2 mixing-ratios under different emissions. **a-d.** The variability in the mixing-ratio of NO_2 (%) by using the empirical equation under different normalised NO_x emissions ($E^{norm}_{NO_x}$), VOC emissions (E^{norm}_{VOCs}), and primary NO_2 fractions (f_{NO_2}) in regular and deep street canyons, respectively. Each area that divided by vertical blue dotted lines represent one VOC emission scenario as labelled. The points and solid lines represent the variability in modelled NO_2 for the intense emission condition (IEC) on Marylebone Road ($E^{norm}_{NO_x}$ = 2, f_{NO_2} = 0.26).

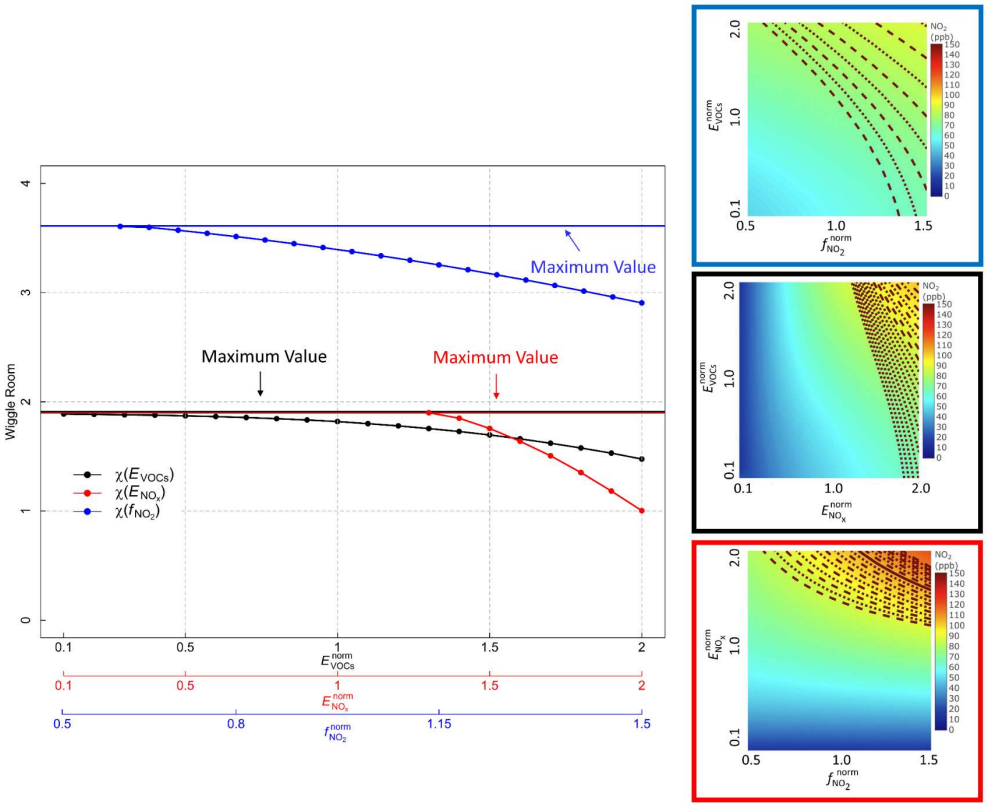


Figure 4.20. The variation of wiggle room under different emission scenarios. The variation of wiggle room for different normalised NO_x emissions ($E^{norm}_{NO_x}$), VOC emissions (E^{norm}_{VOCs}), and primary NO_2 ($f^{norm}_{NO_2}$) in Case 0 (U_0 = 2 m s^{-1}). The solid lines represent the maximum values of the wiggle room through the two-dimensional emission phase space in the present study. The frame on the right represents the visual wiggle room, the colours of the frame indicate the various parameters, and the curves in each figure reflect the parameter values. See text for more details.

Table 4.3. Fleet-averaged traffic emission factors from UK National Atmospheric Emissions Inventory (NAEI) for the model evaluation.

Year	NO_x (g/km)	CO (g/km)	f_{NO_2}
2010	0.460	3.709	0.193
2011	0.423	2.867	0.198
2012	0.444	2.461	0.203
2013	0.445	2.068	0.208
2014	0.409	1.373	0.213
2015	0.393	1.117	0.226
2016	0.383	0.870	0.232
2017	0.373	0.796	0.250
2018	0.356	0.703	0.256
2019	0.357	0.688	0.262

Note: These fleet-averaged emission factors combined hot exhaust and cold start for cars and LGVs, by road type (for VOCs, urban factors also include evaporative emissions) in central London.

Table 4.4. Empirical advective and turbulent velocities in the 16-box model for Marylebone Road.

	Advection				Turbulence			
Model	Vertical	Value ($m\ s^{-1}$)	Horizontal	Value ($m\ s^{-1}$)	Vertical	Value ($m\ s^{-1}$)	Horizontal	Value ($m\ s^{-1}$)
16-box	$W_{a,[2,1]}$	0.1659	$U_{a,[1,1]}$	0	$w_{e,[2,1]}$	0.0121	$u_{e,[1,1]}$	0
	$W_{a,[2,2]}$	0.1128	$U_{a,[1,2]}$	-0.2260	$w_{e,[2,2]}$	0.0139	$u_{e,[1,2]}$	0.0152
	$W_{a,[2,3]}$	-0.1038	$U_{a,[1,3]}$	-0.4269	$w_{e,[2,3]}$	0.0001	$u_{e,[1,3]}$	0.0101
	$W_{a,[2,4]}$	-0.4038	$U_{a,[1,4]}$	-0.4503	$w_{e,[2,4]}$	0.0001	$u_{e,[1,4]}$	0.0129
	$W_{a,[3,1]}$	0.2884	$U_{a,[2,1]}$	0	$w_{e,[3,1]}$	0.0001	$u_{e,[2,1]}$	0
	$W_{a,[3,2]}$	0.2258	$U_{a,[2,2]}$	-0.1161	$w_{e,[3,2]}$	0.0001	$u_{e,[2,2]}$	0.0130
	$W_{a,[3,3]}$	-0.1808	$U_{a,[2,3]}$	-0.2465	$w_{e,[3,3]}$	0.0001	$u_{e,[2,3]}$	0.0001
	$W_{a,[3,4]}$	-0.6923	$U_{a,[2,4]}$	-0.3316	$w_{e,[3,4]}$	0.0001	$u_{e,[2,4]}$	0.0072
	$W_{a,[4,1]}$	0.2062	$U_{a,[3,1]}$	0	$w_{e,[4,1]}$	0.0001	$u_{e,[3,1]}$	0
	$W_{a,[4,2]}$	0.1632	$U_{a,[3,2]}$	0.0872	$w_{e,[4,2]}$	0.0345	$u_{e,[3,2]}$	0.0022
	$W_{a,[4,3]}$	-0.0919	$U_{a,[3,3]}$	0.1605	$w_{e,[4,3]}$	0.0001	$u_{e,[3,3]}$	0.0007
	$W_{a,[4,4]}$	-0.6021	$U_{a,[3,4]}$	0.0974	$w_{e,[4,4]}$	0.1567	$u_{e,[3,4]}$	0.0001
	$W_{a,[5,1]}$	0.0017	$U_{a,[4,1]}$	0	$w_{e,[5,1]}$	0.0146	$u_{e,[4,1]}$	0
	$W_{a,[5,2]}$	0.0084	$U_{a,[4,2]}$	0.2075	$w_{e,[5,2]}$	0.0375	$u_{e,[4,2]}$	0.0346
	$W_{a,[5,3]}$	0	$U_{a,[4,3]}$	0.3560	$w_{e,[5,3]}$	0.0443	$u_{e,[4,3]}$	0.0303
	$W_{a,[5,4]}$	0	$U_{a,[4,4]}$	0.3004	$w_{e,[5,4]}$	0.0414	$u_{e,[4,4]}$	0.0282

Table 4.5. Model evaluation statistics for chemical species for urban street canyons, N is the data count. Statistics for ADMS-urban with advanced canyon module were taken from Hood et al. (2021). The best model performance statistics are underlined. Values in red represent modelling results with new, place-specific, physical parameters for the 16-box model (Table 4.4) derived from a combination of observed concentrations and LES fluxes (16-box-ps).

Site	Species	Model	FAC2	RMSD	$RMSD_u$	$RMSD_s$	R	IOA
Schildhornstrasse (N = 289)	NO_x	one-box	0.77	154.86	66.29	139.95	0.46	0.48
		16-box	0.91	99.65	56.59	82.02	0.81	0.68
		ADMS-urban	0.92				0.86	0.77
Goettingerstrasse (N = 302)	NO_x	one-box	0.63	219.80	85.55	202.47	0.53	0.43
		16-box	0.82	155.43	93.20	124.39	0.69	0.61
		ADMS-urban	0.95				0.86	0.74
Jagtvej (N = 883)	NO_x	one-box	0.78	54.16	28.21	46.23	0.81	0.66
		16-box	0.92	47.41	37.33	29.23	0.77	0.68
		ADMS-urban	0.93				0.90	0.82
Marylebone Road (N = 1850)	NO_x	one-box	1.02	124.71	54.55	112.15	-0.07	0.41
		16-box	1.06	93.82	55.58	75.59	0.54	0.61
		16-box-ps	0.86	65.79	42.55	50.18	0.83	0.75
		ADMS-urban	0.61				0.62	0.62
	NO_2	one-box	1.17	29.80	14.76	25.89	0.12	0.41
		16-box	1.20	22.29	15.05	16.57	0.65	0.61
		16-box-ps	1.08	16.59	16.10	3.99	0.86	0.73
		ADMS-urban	0.82				0.62	0.59

4.5 Acknowledgements

The authors would like to thank the University of Birmingham's BlueBEAR HPC service (http://www.bear.bham.ac.uk) for offering the computational resource. A.R.MK thanks funding support of the Natural Environment Research Council (grants NE/S013814/1, NE/S003487/1).

CHAPTER 5 MODELLING OF DEEP CANYON AIR POLLUTION CHEMISTRY AND TRANSPORT: A WINTERTIME NAPLES CASE STUDY

Author Statement

This chapter encompasses work that has been previously published. The details of the publication are as follows:

Dai, Y., Mazzeo, A., Zhong, J., Cai, X., Mele, B., Toscano, D., Murena, F. and MacKenzie, A.R., 2023. Modelling of Deep Street Canyon Air Pollution Chemistry and Transport: A Wintertime Naples Case Study. Atmosphere, 14(9), p.1385.

The contributions of the authors are as follows:

Conceptualization, **A. Mazzeo** and **Y. Dai** (**author of the thesis**); methodology, software, **Y. Dai**; formal analysis, writing—original draft preparation, **Yuqing Dai**; writing—review and editing, **A. Mazzeo**, **J. Zhong.**, **Xiaoming Cai**, **D. Toscano**, **F. Murena**, **A.R. MacKenzie**; supervision, **A.R. MacKenzie**.

Abstract

The impact of urban morphology on air quality, particularly within deep canyons with longer residence times for complex chemical processes, remains insufficiently addressed. A flexible multi-box framework was used to simulate air quality at different canyon heights (3 m and 12 m). This approach incorporated essential parameters, including ventilation rates, background concentrations, photochemical schemes, and reaction coefficients. A field

campaign within a deep canyon with an aspect ratio of 3.7, in Naples, Italy was conducted and used for the model evaluation. Model performance demonstrated good agreement, especially at the street level, when employing a realistic light intensity profile and incorporating VOC chemistry. Our findings indicate that peroxyl radical production affects NO_2 and O_3 levels by up to 9.5% in deep canyons and underscore the significance of vertical distribution (approximately 5% variance) in health assessments and urban air quality strategy development. The model response was sensitive to changes in emissions as expected, but also, somewhat more surprisingly, to background conditions, emphasizing that policies to remove pollution hotspots must include local and broader citywide action. This work advances the understanding of air quality dynamics in deep urban canyons and presents a valuable tool for effective air quality management in intricate urban environments.

5.1 Introduction

Street canyons are streets that are bounded by buildings on both sides, and can be divided into three types based on the ratio of building height (h) to street width (w) (aspect ratio, AR): i.e., wide canyons (AR < 1), regular canyons (AR = 1), and deep canyons (AR > 1) (BaikKang and Kim, 2007, Oke et al., 2017, Vardoulakis et al., 2003, ZhongCai and Bloss, 2016a). Urban canyons are basic morphological units in densely populated cities. Urban canyons exhibit a unique microclimate and the canyon walls form a physical barrier that restricts the dispersion of air pollutants (Demuzere et al., 2019). Deep urban

canyons with high ARs are particularly challenging as they create environments with limited vertical mixing and reduced atmospheric pollution dispersion. The interaction between these factors creates pollution "hotspots", leading to a situation where high concentrations of contaminants can accumulate even in areas with relatively low emissions (BrightBloss and Cai, 2013, Han et al., 2018, ZhongCai and Bloss, 2015). This poses a significant risk to public health (Turner et al., 2020, Shah et al., 2015, Landrigan et al., 2018), necessitating a thorough understanding of the physical and chemical processes governing air pollutant dispersion and the development of effective mitigation strategies (Dai et al., 2022a).

Few studies have addressed air pollution dispersion in deep urban canyons, even though deep canyons are common in many subtropical and tropical urban areas (BarlowHarman and Belcher, 2004b, Cui et al., 2019, Gu et al., 2011). Ng and Chau (2014) assessed the effective permeability of the built landscape, and setback configurations, in mitigating air pollutant exposure in isolated deep canyons (AR = 2, 4, 6). Their results indicated that building separation and setbacks were effective in reducing personal air exposures, particularly in the case of perpendicular wind. YuanNg and Norford (2014) employed a computational fluid dynamics (CFD) parametric approach to investigate the effects of urban permeability and building geometries on air pollutant dispersion in high-density urban areas. Their results highlighted the necessity for mitigation strategies in planning and designing activities to address air pollution in deep street canyons. By implementing strategies promoting convection effects, such as building separation, porosity, and

stepped podium voids, air pollutant dispersion in high-density cities can be improved. Rakowska et al. (2014) conducted a study examining the impact of traffic volume and fleet composition on air pollutant concentrations in a busy Hong Kong business district. Their work focused on typical urban street canyons and open roadways, discovering that despite a nearly tenfold increase in traffic volume in wide and open roadways, on-road and roadside pollutant concentrations were significantly lower than in street canyons. This finding highlights the importance of considering not only total traffic volume but also urban planning strategies and traffic composition when addressing air quality. The strong contrast observed in their study underscores the need for comprehensive urban air quality management, integrating urban planning strategies with their impact on traffic-related air pollution and pedestrian exposure to pollutants.

Hood et al. (2021) applied an air quality dispersion model (i.e., ADMS-Urban) to cater for various canyon geometries, especially deep and/or asymmetric canyons, in air quality simulations. Unlike the widely used Operational Street Pollution Model (OSPM), which overlooks features such as high ARs, pavements, and building porosity, this new model provides a comprehensive representation by considering up to six component sources to illustrate the various effects of street canyons on the dispersion of road traffic emissions. Their work evaluates the model effectiveness against data from the "Optimisation of modelling methods for traffic pollution in streets" (TRAPOS) project and 42 monitoring sites in London. Murena et al. (2009) modelled carbon oxide (a passive tracer) within a deep canyon (AR = 5.7) in Naples using

CFD and OSPM (Windows version). While CFD simulations matched well actual CO measurements, the OSPM model showed discrepancies. Fu et al. (2017) investigated the effects of street canyon geometry on air pollutant distributions in downtown Beijing using a CFD model and an urban-scale traffic pollutant dispersion model. The study revealed that taller buildings, particularly those exceeding 40 meters in height, obstruct ventilation in street canyons, resulting in elevated pollutant concentrations. Results also suggested that meticulous planning of the asymmetry ratio in street canyons can contribute to an increase in ventilation and thus, a reduction in overall human exposure to air pollutants. He et al. (2017) investigated the impact of street aspect ratios, viaducts, and road barriers on vehicular CO exposure in high-rise deep street canyons using CFD under neutral atmospheric conditions. Higher carbon monoxide (CO) exposure was observed in street canyons with two main vortexes (AR between 5 and 6). Viaduct settings and road barriers were found to affect CO exposure in street canyons differently depending on the aspect ratio.

Despite the valuable insights provided by these studies, none of them explicitly consider the role of atmospheric chemistry. Limited research has been conducted on the role of volatile organic compounds (VOCs) in air pollution chemistry in deep canyons. For instance, the complex interactions between VOCs and other atmospheric species can lead to the formation of secondary pollutants, such as ozone (O_3) and secondary organic aerosols (SOAs) (Sun et al., 2016, ZhongCai and Bloss, 2016a, Li et al., 2020). Studies showed that increased aspect ratios of urban canyons can result in poorer air quality due

to limited ventilation (Dai et al., 2022a, Zhang et al., 2020). In a deep canyon, several critical atmospheric phenomena directly affect the dispersion and concentration of air pollutants. First, restricted ventilation leads to longer residence time of air parcels within deep canyons. Emissions (typically from vehicles) disperse less efficiently in the vertical, culminating in a stratification and increased concentration of pollutants at the street level; secondly, the inherent geometric characteristics of deep canyons attenuate the amount of direct solar irradiance received at ground level. This diminished solar input may induce cooler street surface temperatures, potentially impacting buoyancy-driven ventilation processes within the canyon; in addition, the towering structures flanking these urban canyons facilitate multiple reflection pathways for pollutants. This dynamic can prolong the residence time of these pollutants within the canyon, further amplifying ground-level concentrations. Lastly, longer residence times within deep canyons are conducive to the progression of slower atmospheric chemical reactions. For example, peroxyl radicals are primarily produced during the oxidation of VOCs in the presence of ozone or NO_x (NO + NO_2). Once formed, these radicals can undergo various reactions that further impact the concentrations of NO_2 and O_3. One of the main fates of peroxyl radicals in urban environments is to react with NO to form NO_2:

$$RO_2 + NO \rightarrow NO_2 + RO \tag{5.1}$$

This reaction reduces the concentration of NO, increasing NO_2 levels in the atmosphere. Higher NO_2 concentrations contribute to O_3 production during

daylight hours, creating “hotspots” with intensified pollutant concentrations. While the influence of such reactions is typically marginal in regular canyons due to effective ventilation (BrightBloss and Cai, 2013), it becomes more important in areas where air residence time is extended (ZhongCai and Bloss, 2016a). Therefore, there remains a need for further research that integrates the effects of chemical reactions and interactions within the context of air pollution dispersion in deep urban canyons.

Although CFD-based models can provide a detailed and accurate representation of the atmospheric flow and other physical phenomena in street canyon simulations, generally these models require a significant amount of computational power and are time-consuming to operate, especially for large and complex simulations involved with atmospheric chemistry (e.g., hundreds of thousands of chemical reactions) (BrightBloss and Cai, 2013). Deep canyons necessitate a larger number of CFD cells, which means that incorporating VOC chemistry intensifies computational time, limiting the feasibility of high-resolution simulations (ZhongCai and Bloss, 2016a). The effects of meteorological factors on air pollution chemistry in deep urban canyons have received limited attention. The interaction of meteorological variables, such as solar radiation, temperature, and humidity, with air pollutants in street canyons can significantly impact the formation and dispersion of secondary pollutants (GraweCai and Harrison, 2007, Huang et al., 2021, Zhang et al., 2020). While the importance of these factors is recognized, there remains a notable dearth of relevant literature and monitoring data in relation to vertical levels within a deep canyon.

Our recent study (Dai et al., 2021a) has shown that the flexible multi-box model (MBM-FleX) is one of the most effective models for simulating air quality in urban canyons with high aspect ratios. It is a two-dimensional (2D) model that divides the canyon into multiple boxes, each representing a different layer of the atmosphere. The model considers the effect of building height, ventilation, VOC radical reactions, and street level emissions on the dispersion of pollutants in the canyon. The multi-box model also allows for customized emission inventory, which is necessary for accurately modelling air quality in complex urban environments.

Below, the performance of the multi-box model was assessed under the specific conditions of a deep street canyon (AR = 3.7) in Naples, Italy, the capital of the Campania region and the country's third-largest city. The urban area boasts a population of about a million but considering the metropolitan region extending approximately 20 miles beyond city limits, the population reaches around 3 million. The historical centre of Naples underwent remodelling during the Spanish occupation in the 16th century to accommodate the Spanish army. This area, known as the "Spanish neighbourhood", features narrow streets approximately 5 m wide, forming a grid pattern lined with densely packed residential buildings approximately 20 m high. These deep urban street canyons are often associated with compromised air quality. Major contributors to nitrogen oxide air pollution in Naples include road and maritime transport, with NO_x levels often exceeding the European threshold limit of 40 μg m^{-3} as annual average or 200 μg m^{-3} as hourly average. High levels of NO_2 are not the city's only air pollution concern:

high levels of VOCs and active photochemistry during the warm season contribute to elevated O_3 levels, posing an additional environmental challenge.

In this Chapter, a field monitoring campaign was conducted within a deep street canyon in the "Spanish neighbourhood" of Naples, Italy, having an aspect ratio (AR) of 3.7. A flexible multi-box framework was employed to simulate air quality at different elevations within the canyon, integrating essential parameters like ventilation rates, background concentrations, photochemical reaction mechanisms, and reaction coefficients. The study further investigated vertical dispersion of pollutants and conducted sensitivity tests to explore the interaction times between VOCs and NO_x in the production of O_3. The paper is organized as follows. Section 5.2 outlines the sampling site conditions, the multi-box frameworks (including the typical MBM-FleX and a revised version termed MBM-FleX_r), model configurations and model scenarios, and data analysis methods. Section 5.3 presents a comparison of box-model simulations with CFD, describes concentration fields, analyses MBM-FleX results, evaluates model sensitivity, and assesses the performance of MBM-FleX_r. Section 5.4 provides the conclusions.

5.2 Methodology

5.2.1 Field data

Time series of nitric oxide (NO), nitrogen dioxide (NO_2), and ozone (O_3) were collected from Via Santa Teresella (40°50'14.5"N, 14°14'41.6"E) in Naples, Italy. Via Santa Teresella exhibits a distinct topography and urban surface characteristics that significantly influence its local microclimate and air

quality. This narrow street, with a height of 20 m and a width of 5.4 m (see Figure 5.1a), displays a canyon-like geometry (AR ≈ 3.7) and is lined with closely spaced, tall residential buildings (Murena and Prati, 2020). The canyon orientation extends from west-southwest (70°) to east-northeast (250°), with a street length (i.e., the unmodelled y-direction) of approximately 105 m between two crossroads. The confined layout of Via Santa Teresella limits traffic speed, affecting the dispersion of air pollutants. In addition, inconsistent and intermittent balconies on the both lee- and windward sides of the canyon hinder ventilation between the canyon and the surrounding environment (Murena and Mele, 2016). The urban surface in this region predominantly consists of paved surfaces and near-flat building rooftops, further shaping the local microclimate and air quality conditions.

NO, NO_2, and O_3 concentrations were collected in successive 15-minute intervals from two distinct heights during January 11th to 15th, 2021. Each collection cycle commenced with a 15-minute interval at 3 m, immediately followed by another 15-minute interval at 12 m. This routine was consistently implemented between the hours of 8:00 and 20:00. The potential under-resolution challenges due to the 15-minute sampling interval might miss rapid fluctuations in pollutant levels caused by transient emission sources or quick meteorological shifts. The interval may inadequately represent short-lived turbulent motions and fast-reacting chemical pathways. It may compromise the precision and reliability of model predictions, potentially obscuring transient yet significant pollutant dynamics, but the longer sampling interval offers broader insights and a more averaged perspective. It can be more

representative of sustained pollution sources, like constant vehicular traffic, as opposed to fleeting sources.

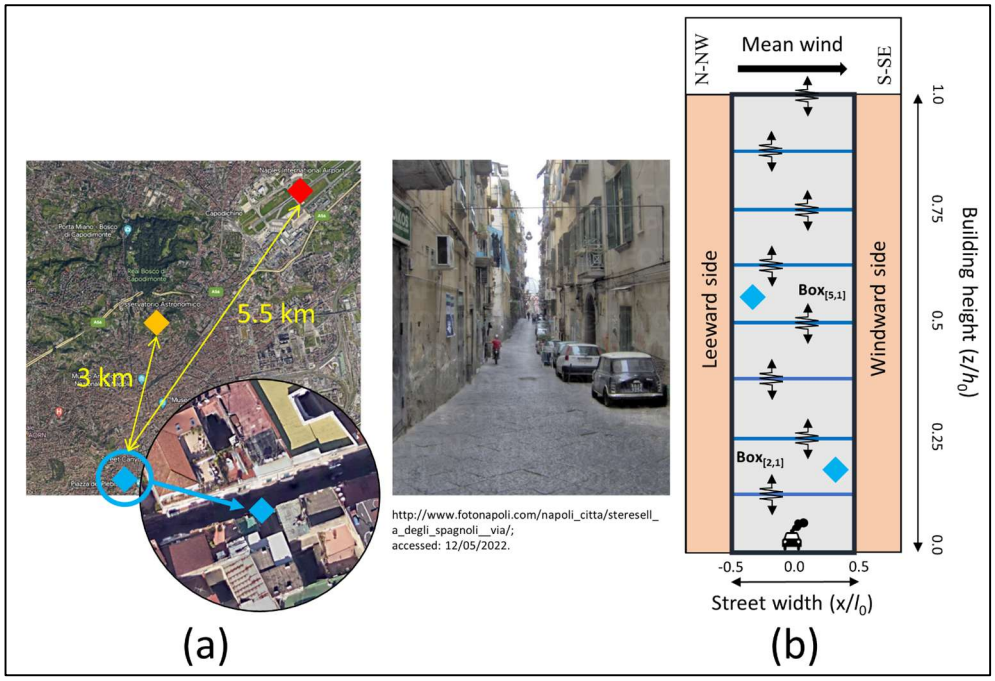


Figure 5.1. Map view of the monitoring site and locations (blue points), the urban background site (orange point), and the meteorological site (red point) in Via Santa Teresella (a); and a conceptual framework of MBM FleX/MBM-FleX_r for the deep canyon (b). Blue frames represent compartments that resolve a large vortex, and the black frame represents the entire volume of street canyon. Well-mix assumption has been made and pollutants are homogeneously distributed in each finer box.

The monitoring sites were located at the heights of h_1 = 3 m and h_2 = 12 m on the southside of the street (blue diamond in Figure 5.1a). Equipment and measurement methods followed the standard established by European Community (2008/50/CE). The observations were subsequently converted

into mixing ratios for each model grid based on in-situ temperature and atmospheric pressure measurements. Simultaneously, a pre-installed camera recorded vehicle counts, grouped into passenger cars, two-wheel motor vehicles, and light-duty vehicles, throughout the monitoring campaign. In the data collection process, there were inevitably some gaps; however, these gaps did not exceed a duration of 30 minutes, ensuring no consecutive missing data points. To address these gaps, a linear interpolation method was employed, which allowed for the estimation of missing values based on the known data points surrounding each gap. As a result, 129 (64.5%) data points were available for model evaluation. For this evaluation, only measured data were utilized for comparison, while any imputed data resulting from the gap-filling procedure were excluded. This approach ensured that the model evaluation was based solely on observed data, providing a more reliable assessment of the model capability to represent actual conditions, and maintaining the robustness of the evaluation process.

Hourly measured NO_2, O_3, and CO data from the Osservatorio Astronomico (NA01, yellow diamond in Figure 5.1a) were employed to represent urban background conditions above the deep urban canyon. The NA01 site is situated at the Capodimonte Observatory at a latitude of 40°51'46.8" N and longitude of 14°15'18" E. Its location, distanced from direct pollution sources such as traffic and industrial emissions, ensures that it captures the broader air quality characteristics of the urban environment, rather than being influenced by localized pollution hotspots. The data can be accessed through the European Air Quality Portal (https://discomap.eea.europa.eu/map/fme/). Hourly

meteorological conditions, such as temperature, wind direction, and wind speed in the ambient background, were obtained from Naples International Airport (NIA, red square in Figure 5.1a), which is located approximately 5.5 km northeast of the canyon at a similar altitude (with latitude 40°53'06" N and longitude 14°17'20.4" E, respectively). Meteorological data can be acquired using the "openair" R package (Carslaw and Ropkins, 2012).

5.2.2. The multi-box framework and some new developments

In a previous study (Dai et al., 2021a), a multi-box model was employed to simulate a passive scalar (PS) and reactive species including NO_2, O_3, and VOC free radicals in regular and deep street canyons. The simulation employed an Eulerian process-based model called MBM-FleX, which combines physical and chemical processes to estimate air pollutant concentrations in the urban canyon environment. The algorithm for MBM-FleX can be expressed as:

$$\frac{dC_{q,[k,i]}}{dt} = E_{q,[k,i]} - \frac{G_{a,[k,i+1]}+G_{e,[k,i+1]}}{l_i} + \frac{G_{a,[k,i]}+G_{e,[k,i]}}{l_i} - \frac{F_{a,[k+1,i]}+F_{e,[k+1,i]}}{h_k} + \frac{F_{a,[k,i]}+F_{e,[k,i]}}{h_k} + \Delta S_{q,[k,i]} + \Delta V_{q,[k,i]} \quad (5.2)$$

where $C_{q,[k,i]}$ (ppb) is the mixing-ratio of the q^{th} species in $Box_{[k,i]}$, $E_{q,[k,i]}$ (ppb s^{-1}) represents the emission rate of the q^{th} species into $Box_{[k,i]}$, h_k (m) and l_i (m) are the box height and box width, $\Delta S_{q,[k,i]}$ (ppb s^{-1}) is the net production rate of the q^{th} species due to chemistry, and $\Delta V_{q,[k,i]}$ (ppb s^{-1}) is the net deposition term of the q^{th} species in $Box_{[k,i]}$. $F_{a,[k,i]}$ (ppb m s^{-1}) and $G_{a,[k,i]}$ (ppb s^{-1}) represent the mixing-ratio fractional fluxes due to advection. $F_{e,[k,i]}$ (ppb m s-1) and $G_{e,[k,i]}$ (ppb s^{-1}) represent the mixing-ratio fluxes due to turbulent diffusion formulated by the Fick's law. Here, the dynamical components (i.e., advection and turbulence) were numerically calculated with 4^{th}-order precision using

the Runge-Kutta algorithm. Chemical species were treated at different time intervals based on their respective chemical lifetimes, as described in ZhongCai and Bloss (2017). Using predefined LES results corresponding to each canyon geometry as the driving factors for the model dynamics, MBM-FleX accurately identifies the main airflow characteristics within an idealised regular (AR = 1) and a deep (AR = 2) urban canyon (e.g., counter rotating vortices in deep canyons, respectively) (Dai et al., 2021a). The modelled gaseous species, such as NO, NO_2, and O_3, closely match those predicted from LES, while reducing the computational resources required for processing. For example, the computing time decreases from two weeks to less than six minutes for a deep canyon (AR = 2) simulation with VOC radical chemistry.

The mass transfer between street canyons and the overlying background is vital in determining the degree of segregation of urban canyons. A number, m, of exchange velocities are used to describe the flux-escaping processes for a m×n box model at the nth layer, such as $w_{e,[k,4]}$ and $w_{e,[k,8]}$ at the rooftop of regular and deep canyons in Figures 5.1a and 5.1c. Here k represents the k^{th} grid along the x-axis (i.e., horizontal direction) and the escaping mass flux ($f_{ex,q}$) can be expressed as:

$$f_{ex,q} = \sum_{k=1}^{m} w_{e,[k,n]} \times (\mathrm{C}_{q,[k,n]} - \mathrm{C}_{q,b}) \quad (5.3)$$

where $C_{q,[\mathrm{k,n}]}$ represents the concentration of q^{th} species within the k^{th} box at the n^{th} layer, and $C_{q,b}$ is the concentration in the overlying background. Multi-exchange rates can provide a more precise depiction of physical processes, such as the determination of mass flux entering and escaping the canyon but,

in the Naples case study, the application of such a set of exchange rates was deemed impractical for several reasons: (1) the intricate derivation of dynamical parameters based on the flux balance theory from the CFD; (2) the substantial requirement for background and initial concentrations during model "spin-up" periods; and (3) the implementation of a coupled modelling system that can effectively link local and regional scales (e.g., Kim et al. (2018c)). For this case study, both the original version of the MBM-FleX and a modified variant of the MBM-FleX (hereafter referred to as MBM-FleX_r *v*1.0, a 2D model as illustrated in Figure 5.1b, d and Figure 5.1b) were deployed for simulating urban canyon air quality. In this variant, MBM-FleX_r, the exchange velocity between the street canyon and the background was represented using a single parameter, $w_{t,0}$, while preserving the other dynamic components within the canyon. This approach allows for the proper preservation of airflow characteristics within the canyon. The exchange mass flux can be described as follows:

$$f_{ex,q} = w_{e,0} \times (\mathrm{C}_{q,0} - \mathrm{C}_{q,b}) \quad (5.4)$$

$C_{q,0}$ is the concentration of q^{th} species in the entire canyon (i.e., Box_0) for each iteration (i.e., 0.03 s for long-lived species and 0.003 s for short-lived species):

$$\mathrm{C}_{q,0} = \sum_{i=1,j=1}^{m,n} \mathrm{C}_{q,[i,j]}/(m \times n) \quad (5.5)$$

The performance of MBM-FleX_r has been evaluated in comparison to both MBM-FleX and LES models in estimating the dispersion of a passive scalar (PS) as well as reactive species, including NO_2 and O_3, within idealized regular (AR = 1) and deep (AR = 2) urban canyons. Detailed information on this assessment

can be found in the Supporting Information. It is also worth noting that the multi-box framework is based on the steady-state assumption, juxtaposed with the inherent unsteady characteristics' nature of field measurements. Techniques like CFD-based models offer closer real-world approximations, and online instruments provide granular observations, they demand higher computational and financial resources. Quantitative metrics like root-mean-square deviation (RMSD) or temporal correlation coefficients provide clearer insights into the alignment between model predictions and field data (Section 5.4).

5.2.3. Model configuration and data pre-processing

A key step of this study is to evaluate the dynamical parameters by conducting a comparative analysis of the one-dimensional (1D) MBM-FleX (1 × 8), MBM-FleX_r (1 × 8), and CFD outputs for an idealised deep canyon with an AR of 3. The derived dynamical parameters were then applied to the real deep canyon. If MBM-FleX and MBM-FleX_r produce estimates that are sufficiently close to those of the CFD modelling, the multi-box models, with the derived exchange velocities, can replace further CFD simulations due to its ability to quickly handle complex chemical reactions and more modeling scenarios. To achieve this, the multi-box model configurations replicated those of the CFD approach. A concise summary of the parameters is provided below, with specifics available in Murena and Mele (2016). The canyon geometry was defined by a building height of 18 m and a street width of 6 m (i.e., AR = 3). The initial concentration of CO is 372 μmol m^{-3} (~10 mg m^{-3}, 8700 ppb) under steady-stage conditions, and the inlet flow rate (i.e., prevailing wind speed) is 2.0 m s^{-}

[1]. CO is regarded as a PS, determined solely by physical processes, and its concentration within the street canyon diminished over time in wash-out simulations depending on the exchange velocity between the canyon and the background, since there were no emission sources within the canyon. Predicted CO in the deep canyon were compared between multi-box models and CFD results at t = 17 min (~1013 s, 50% wash-out time, see Section 5.4 for details). The CFD simulations used to parameterize the multi-box model represent a canyon with lower aspect ratio than the actual canyon under study. Given our present knowledge constraints, these parameters serve as the best option to configure the model.

Advective velocities and turbulent velocities in the MBM-FleX and MBM-FleX_r models are important in determining the dynamical components inside street canyons. These values could be derived based on advective flux, turbulent flux, and concentration gradients between adjacent boxes, which could be obtained from LES and CFD simulations (Dai et al., 2021a). Under a 2D framework, eddies within street canyons can be properly parameterized. Here CFD was used for simulating an idealised canyon with AR of 3 (Murena and Mele, 2016) to present the real canyon characterized by an AR of 3.7. This approach has several uncertainties, including: (1) variation in the number of vortices with different ARs (Yang et al., 2020); (2) the presence of building balconies that can strongly modify the wind flow pattern within street canyons (Karkoulias et al., 2020, Murena and Mele, 2016); (3) the Reynolds number (Re) within the canyon influences the number of vortices (a higher Re may result in a reduced number of vortices, even in a deep canyon) (ChewAliabadi and Norford,

2018a); and (4) other factors such as short-time varying wind speeds (Murena and Mele, 2014), heating effects (influencing atmospheric stability) (Cai, 2012b), roof shapes (Huang et al., 2021), and mechanical turbulence (SolazzoCai and Vardoulakis, 2009, Vachon et al., 2002). Including vortices could further increase modelling uncertainties. Therefore, the multi-box models were simplified from 2D to 1D consisting of eight boxes (Figure 5.1b), which captures the combined effect of vertical mixing of scalars, resulting from both large vortices and small turbulent eddies within the street canyon through parameterization. Each box of the MBM-FleX and MBM-FleX_r has a grid spacing of 2.7 m × 2.5 m × 1 m = 6.75 m^3. This streamlined representation allowed for the disregard of horizontal advection and turbulence (i.e., $u_{a,[k,i]}$ and $u_{e,[k,i]}$), focusing primarily on the vertical mixing velocities (i.e., $w_{e,[k,0]}$). The rationale behind choosing eight boxes lies in maintaining a balance between computational efficiency and an acceptable degree of accuracy in capturing concentration gradients. The $w_{e,[k,0]}$ parameter serves as the primary focus of our investigation and encapsulates the most significant aspects of the mass transfer process. This term is derived from the concentration gradient during a brief time interval in the CFD simulation. The derived dynamical parameters allow the same atmospheric conditions between the multi-box model and the CFD simulations, with a neutral atmosphere being presumed. The details are presented in the Section 5.1 and the Supporting Information (Table 5.3).

In this study, traffic emissions were released at the bottom level of boxes, and emission factors were calculated using the Computer Program to Calculate Emission from Road Transport (COPERT) procedure (Ntziachristos et al.,

2000) with a unit of [g km^{-1} h^{-1}], representing the relationship between the amount of pollutants emitted from tail pipes into the atmosphere and the corresponding traffic activities. The hot exhaust emissions of NO_x (= NO + NO_2), CO, and VOCs at 20 km h^{-1} from each class of vehicles were obtained and then used to calculate the equivalent mixing-ratio rates into the model mesh volume of $Box_{[1,1]}$ and $Box_{[1,2]}$ at standard temperature and pressure conditions (293 K and 1 atm) (Table 5.4). It is noted that these emission rates are based on available data and may not perfectly represent the actual measured temperature in January. The relative contributions of ethene (C_2H_4), propene (C_3H_6), formaldehyde (HCHO), and acetaldehyde (CH_3CHO) to the total VOC emissions were 42%, 27%, 13%, and 18% (BrightBloss and Cai, 2013), respectively. Unless otherwise noted, all percentages discussed below (i.e., "%") denote volume percent changes or proportions in pollutant abundances. The primary fraction of NO_2 for each vehicle type was obtained, along with the calculation of hourly traffic emissions based on emission factors, traffic composition and counts.

In modelling air quality within street canyons, it is crucial to obtain accurate background values for model inputs. The NA01 monitoring site (Section 5.1, Figure 5.1a), located approximately 3 km away from the deep street canyon, could potentially underestimate NO_2 and overestimate O_3 levels for the overlying background at the canyon location. Therefore, a scaling factor of 1.5 was applied to modify the background NO_2 levels (i.e., scaled urban background, SUB). This adjustment ensures that the background NO_2 for the canyon is higher than those at the NA01 site but lower than the observations

at 12 m within the deep canyon, maintaining a proper gradient as depicted in Figure 5.2c. Consequently, O_3 levels will also increase slightly due to the associated chemical processes. The impact of volatile organic compounds (VOC) radical chemistry on NO_2 and O_3 concentrations in the canyons was investigated. Simulations were conducted using both a simple NO_x-O_3 cycle and the reduced chemical scheme (RCS) to compare the respective impacts on pollution levels. The RCS comprises 51 species and 136 reactions, incorporating methane and eight parent non-methane hydrocarbons (NMHCs): isoprene, ethene, propene, formaldehyde, acetaldehyde, methanol, ethanol, and peroxyacetyl nitrate, providing a comprehensive representation of the major reactive components in urban canyon air chemistry (BrightBloss and Cai, 2013). In the RCS, the photolysis rates were initially calculated using the Tropospheric Ultraviolet and Visible (TUV) Radiation Model *v*4.1 (Madronich et al., 2002) for simulations during midsummer daytime at the mid-latitude regions (Birmingham, UK). These rates were found to be significantly higher than those observed in Naples in winter (Hersbach et al., 2020). Also, in this extreme deep urban canyon, shading effects could have an important impact on the concentrations of reactive species (Bourbia and Awbi, 2004, GraweCai and Harrison, 2007, Dai et al., 2022c, Paolini et al., 2014). Therefore, the photochemical rates (Table 5.5) were scaled through a comparison of daytime surface solar radiation, which was obtained from the ERA5 global atmospheric reanalysis dataset, between the 1st of August in Birmingham and the monitoring period in January in Naples. The diurnal profile of net surface solar radiation was calculated as well.

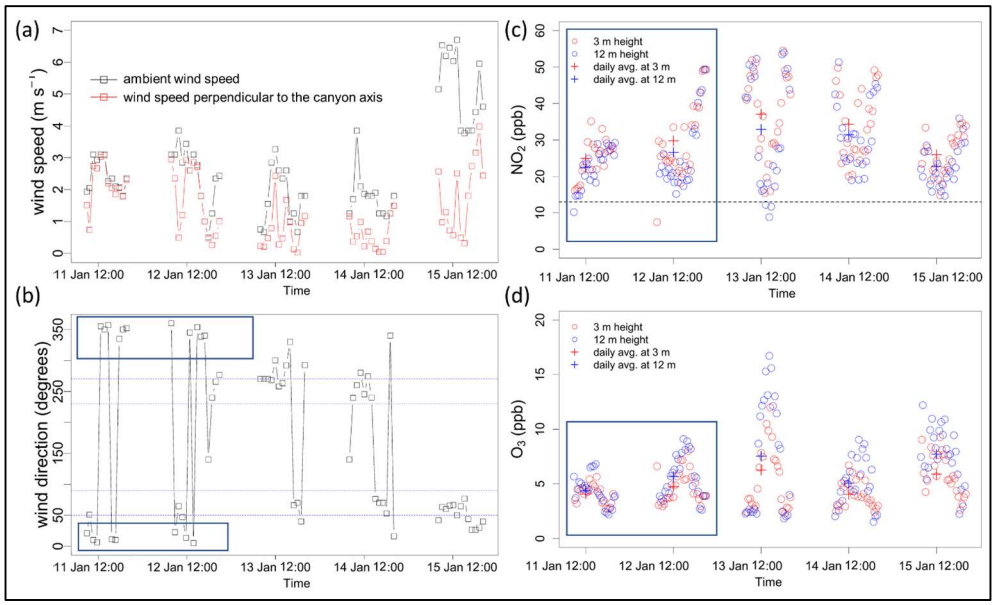


Figure 5.2. Diurnal variations (8:00-20:00) of ambient wind speed and the wind speed perpendicular to the canyon axis (a) and wind direction (b), and of NO_2 (a) and O_3 (b) concentrations at various heights within the deep street canyon, Naples. The time period is from the 11th to the 15th in January, with a 15-min interval. Wind directions between the dashed blue lines represent conditions of wind mainly parallel to the street axis (i.e., 50° 90° and 230°-270°). Crosses indicate daily concentration averages, and dashed black line denotes WHO Air Quality Guidelines.

In the present study, the angle of wind incidence (α) is delineated as the angle formed between the prevailing wind direction and the canyon axis, which enabled the decomposition of wind vectors into perpendicular to street (α = 90°) and along-street (α = 0° or 180°) directions. The dynamical parameters for MBM-FleX, derived from CFD simulations, inherently integrate the assumptions embedded within the CFD models, encompassing initial conditions, background conditions, canyon geometry, and other relevant factors. The boundary conditions for MBM-FleX are established based on these

CFD assumptions, specifically accounting for the effects of perpendicular wind on canyon ventilation. Parallel wind has been posited to exert a larger influence on street canyon ventilation (Sin et al., 2023) but the focus here was on scenarios where the ambient wind blows perpendicular to the canyon-axis, as detailed in Section 5.2. Drawing from prior research (Kwak et al., 2011, NiachouLivada and Santamouris, 2008), it was assumed that a linear relationship exists between vertical mixing velocities and the perpendicular velocity of the wind above the roof level.

5.2.4. Model simulation and data post-process

The earliest available air pollutant observations each day throughout the study period were used to generate essential chemical intermediates for the model simulations. A 30-minute "spin-up" of the MBM-FleX/MBM-FleX_r models was conducted, without sources and dynamics. The resulting mixing ratios of all species at t = 30 minutes were considered to be the background conditions for subsequent simulations through the day. Physical, chemical, and emission modules were activated after spin-up.

To evaluate the model performance, final simulation results were chosen according to the monitoring height. For example, if the monitor was situated at 3 m above the ground, concentrations at the second box (i.e., $Box_{[2,0]}$) were employed for evaluation, whereas if the monitor was positioned at 12 m, concentrations at the fifth box (i.e., $Box_{[5,0]}$) were used. Vehicular emissions, exchange rates, and urban background levels for key pollutants (i.e., NO_2, O_3, and CO) were dynamically changed on an hourly basis. To assess model

sensitivity, and to investigate the potential influence of various control strategies on air quality within the deep canyon, different model scenarios were designed (Table 5.1). Cases RCS_UK and SIM_UK use MBM-FleX with either the RCS or a simple NO_x-O_3 cycle, employing photochemical kinetics representative of midsummer daytime in West Midlands, UK. Cases RCS_IT and SIM_IT use MBM-FleX with either the RCS or a simple NO_x-O_3 cycle, employing photochemical kinetics characteristic of conditions in Naples, Italy. Cases RCS_IT_E1 and RCS_IT_E2 correspond to scenarios with 50% reductions in NO_x and VOC emissions. RCS_IT_B1 to RCS_IT_B3 demonstrate varying background conditions with low, medium, and high NO_x levels, to understand the influence of different background pollutant concentrations. Lastly, cases with the suffix "R" (e.g., RCS_UK_R) are dedicated to evaluating the performance of the MBM-FleX_r model, an alternative version of MBM-FleX, under various conditions.

Six widely-employed statistical metrics were utilized to assess the performance of the models (WillmottRobeson and Matsuura, 2012, Chang and Hanna, 2004), encompassing Pearson's correlation coefficient (r), proportion of model results within a factor of two of observations (FAC2), root-mean-square deviation (RMSD), systematic RMSD (RMSDs), unsystematic RMSD (RMSDu), and index of agreement (IOA) (Cai and Steyn, 2000, Willmott, 1981, Willmott et al., 1985, WillmottRobeson and Matsuura, 2012). The r quantifies the linear correlation between two data sets, with values ranging from -1 to 1; FAC2 is defined as the proportion of predicted data situated within a factor of two of the observations; RMSD calculates the average distance between corresponding pairs of estimates and observations, while systematic and

unsystematic RMSD offer valuable insights into the origins of model uncertainty; IOA signifies the degree of congruence between model simulations and measurements, with a value of 1 indicating an impeccable alignment between the two data sets. The mathematical descriptions are provided below:

$$0.5 \leq \frac{P_r}{O_r}(\text{FAC2}) \leq 2.0 \tag{5.6}$$

$$\text{RMSD} = \sqrt{\frac{\sum_{r=1}^{N}(P_r - O_r)^2}{N}} \tag{5.7}$$

$$\text{RMSD}_u = \sqrt{\frac{\sum_{r=1}^{N}(P_r - \hat{P}_r)^2}{N}} \tag{5.8}$$

$$\text{RMSD}_s = \sqrt{\frac{\sum_{r=1}^{N}(\hat{P}_r - O_r)^2}{N}} \tag{5.9}$$

$$\text{R} = \frac{1}{N-1}\sum_{r=1}^{N}\left(\frac{P_r - \overline{P}}{\delta_P}\right)\left(\frac{O_r - \overline{O}}{\delta_O}\right) \tag{5.10}$$

$$\text{IOA} = \begin{cases} 1 - \frac{\sum_{r=1}^{N}|P_r - O_r|}{2\sum_{r=1}^{N}|O_r - \overline{O}|}, \sum_{r=1}^{N}|P_r - O_r| \leq 2\sum_{r=1}^{N}\left|O_r - \overline{O}\right| \\ \frac{2\sum_{r=1}^{N}|O_r - \overline{O}|}{\sum_{r=1}^{N}|P_r - O_r|} - 1, \sum_{r=1}^{N}|P_r - O_r| > 2\sum_{r=1}^{N}\left|O_r - \overline{O}\right| \end{cases} \tag{5.11}$$

here O_r and P_r are the r^{th} rank of values from continuous observations and modelling, respectively; N represents the total number of datasets; the bar sign represents the mean concentration (e.g., P denotes the mean value of simulations); $\hat{P}_r$ can be estimated from the equation:

$$\hat{P}_r = a + b \times O_r \tag{5.12}$$

a and b are intercept and slope, respectively. Therefore, the following relationship can be derived:

$$\mathrm{RMSD}^2 = \mathrm{RMSD}_u{}^2 + \mathrm{RMSD}_s{}^2 \quad (5.13)$$

The values of R, FAC2 and IOA that converge to one and RMSD that converges to zero indicate that the model estimates are closer to the observations and, therefore, a better model performance.

Table 5.1. Overview of the model scenarios

Case	Model	Chemical scheme	Photolysis rates	Scaling factor for background NO_2*	Emissions
RCS_UK	MBM-FleX	RCS	Constant rates	1.5	On-road emissions
SIM_UK	MBM-FleX	Simple chemistry	Constant rates	1.5	On-road emissions
RCS_IT	MBM-FleX	RCS	Diurnal profile	1.5	On-road emissions
SIM_IT	MBM-FleX	Simple chemistry	Diurnal profile	1.5	On-road emissions
RCS_IT_E1	MBM-FleX	RCS	Diurnal profile	1.5	Reduced NO_x emissions
RCS_IT_E2	MBM-FleX	RCS	Diurnal profile	1.5	Reduced VOC emissions
RCS_IT_B1	MBM-FleX	RCS	Diurnal profile	0.5	On-road emissions
RCS_IT_B2	MBM-FleX	RCS	Diurnal profile	1.0	On-road emissions
RCS_IT_B3	MBM-FleX	RCS	Diurnal profile	3.0	On-road emissions
RCS_UK_R	MBM-FleX_r	RCS	Constant rates	1.5	On-road emissions
SIM_UK_R	MBM-FleX_r	Simple chemistry	Constant rates	1.5	On-road emissions
RCS_IT_R	MBM-FleX_r	RCS	Diurnal profile	1.5	On-road emissions
SIM_IT_R	MBM-FleX_r	Simple chemistry	Diurnal profile	1.5	On-road emissions

***** Here, a scaling factor refers to a value by which the background NO_2 was multiplied.

5.3. Results and Discussion

5.3.1. Comparing box-model simulations with CFD

The first investigation analysed the vertical distribution of air pollutants within an idealized deep canyon. This preliminary analysis employed three distinct models: MBM-FleX (1 × 8), MBM-FleX_r (1 × 8), and CFD simulations. MBM-FleX and MBM-FleX_r were adapted from 2D to 1D models for simulating the real canyon scenarios, and Figure 5.2 presents the vertical profiles of CO mixing ratios obtained from these models, with results truncated at around 12 minutes, corresponding to a 50% flushing time. The MBM-FleX and MBM-FleX_r grids integrate multiple CFD meshes that have been averaged to a coarser resolution, enabling a more straightforward comparative evaluation of model performance. The MBM-FleX and MBM-FleX_r (1D mode) were used to track vertical mixing ratio gradients within the canyon; that is, our analysis focused exclusively on the vertical distribution of air pollutants. The vertical profiles of CO mixing ratios modelled by MBM-FleX (green solid line) and MBM-FleX_r (black solid line) exhibited good agreement, with an index of agreement (IOA) of 0.97. The canyon-averaged CO mixing ratios for MBM-FleX, MBM FleX_r, and CFD models were 5008.0 ppb, 4921.8 ppb, and 4973.8 ppb, respectively, with minimal differences of approximately 0.7% and -1.0%. Figure 5.2b illustrates the dissipation rates of CO mixing ratios at different heights within the multi-box models. The results reveal that the locations at the bottom of the canyon exhibit slow dissipation rates, characterized by a gradual and continuous decrease in high pollution levels. In contrast, the boxes

located higher up display a rapid and steep downward trend, followed by a more gradual decline until stabilization is reached.

The results indicate that the multi-box models effectively captured the primary features of CO within the deep canyon, including: (1) a decreasing trend of CO mixing ratios with increasing building heights, and (2) the dissipation rates of CO mixing ratios from the canyon to the background atmosphere. As a result, assuming that the values of dynamical parameters alter proportionally with perpendicular cross-canyon wind speeds (Section 5.3), pre-defined dynamical sets (Table 5.3) were used to simulate air quality with MBM-FleX and MBM-FleX_r serving as proxies for RANS modeling results. The model accuracy was evaluated by comparing the model results with observations at heights of 3 m and 12 m within the street canyon.

5.3.2. Concentration fields

Meteorological conditions play a critical role in shaping air quality within urban canyons and, also, influencing the model performance. To contextualize the analysis of the modelling results, it is essential to provide an overview of the meteorological conditions during the monitoring campaign. Figure 5.2a and 5.2b display quarter-hourly measurements of ambient wind velocity and directional data, offering crucial insights for interpreting the findings. In Figure 5.2a, wind speeds perpendicular to the canyon axis (represented by black points) were compared. Between 11th and 13th January, wind velocity exhibited a notable increase around 10:00 a.m. in the morning, stabilizing at approximately 3.0 m s^{-1}, before decreasing during the afternoon. This pattern

is strikingly similar to the wind features previously observed in Naples' airport Capodichino (Murena, 2012). The orientation of the street canyon is 70°-250°. Throughout the monitoring campaign, the wind direction, as illustrated by the grey lines in Figure 5.2b, reveals that the wind predominantly flowed parallel to the street canyon, primarily occurring from 13th to 15th January 2021. During the first two days of the study period (11th and 12th January, blue frame in Figure 5.2), the ambient wind direction was predominantly perpendicular to the canyon axis, which is the primary focus of our investigation.

Figure 5.2c and Figure 5.2d depict the temporal variations (from 8:00 a.m. to 20:00 p.m.) in NO_2 and O_3 mixing ratios at distinct vertical heights within the deep urban canyon during the monitoring campaign. The observations reveal that NO_2 mixing ratios at 3 meters height were consistently higher than those at 12-m height, with the difference in daily averaged levels ranging between 9.8% (2.4 ppb) and 12.2% (3.2 ppb). This suggests that ground-level NO_2 mixing ratios were predominantly affected by local emission sources (e.g., vehicular traffic), diluting from the canyon bottom to the top. Such concentration gradients expose pedestrians, especially those at lower elevations, to elevated levels of NO_2. Note that NO_2 at both height levels substantially exceeded the World Health Organization's (WHO) Air Quality Guideline (AQG) of 13 ppb (25 μg m^{-3}) for daily NO_2 levels, with exceedances ranging from 91.9% to 185.2%. In contrast, O_3 levels consistently adhered to the WHO AQG (50 ppb for an 8-hour maximum average). O_3 mixing ratios at 12-m height were slightly higher (by about 1 ppb) compared to those at 3-m height, especially at around 12:00 pm. This difference can potentially be

attributed to a result of a combination of factors including thermal dynamics, chemical reactions, deposition processes, and atmospheric mixing. For example, the concentration of background ozone tends to increase in the afternoon. This rise, in tandem with the vertical mixing, results in a heterogeneous distribution of ozone. Specifically, the ozone concentration at 12-m height is more affected by the elevated background level compared to the 3-m height. Additionally, during midday, the photolysis of NO_2 at the surface swiftly generates NO, which then reacts with O_3 through the titration effect, leading to reduced O_3 levels at the 3-m height. It would be worthwhile to investigate this further with detailed observations and modelling techniques to understand the underlying processes better.

5.3.3. MBM-FleX results

Figure 5.3 presents modeled mixing ratios for NO_2, NO_x, and O_3 as simulated by the MBM-FleX in relation to observed values at distinct building heights (i.e., 3 m and 12 m) within the urban street canyon. Table 5.2 offers a statistical evaluation of modeled air pollutants compared to observations at both sampling locations, while Table 5.6 and Table 5.7 supplied a thorough assessment of model performance at 3 m and 12 m within the canyon. The MBM-FleX model consistently underestimates NO_x mixing ratios, which can be effectively treated as passive scalars in all cases. This underestimation may be attributed to uncertainties in background conditions and emission inventories. When photochemical reaction rates, representative of summer midday conditions in the West Midlands, UK, were adopted, O_3 formation accelerated markedly, leading to overestimated mixing ratios in both RCS_UK

and SIM_UK cases. Additionally, volatile organic compound (VOC) radical chemistry contributes significantly to NO_2 and O_3 formation within the canyon due to limited ventilation, extended residence time, and increased reaction time. Implementation of a simple NO_x-O_3 cycle can suppress such overestimation.

Table 5.2. Statistical evaluation of the MBM-FleX for NO_2, NO_x, and O_3 within the deep canyon (AR = 3.7) in Naples, Italy.

Case	Species	n	FAC2	r	RMSEs (ppb)	RMSEu (ppb)	RMSE (ppb)	IOA
RCS_UK	NO_2	48	0.92	0.62	1.3	8.6	8.7	0.18
	NO_x		0.73	0.48	18.73	15.48	24.3	0.45
	O_3		0	0.26	55.39	38.38	67.39	-0.95
SIM_UK	NO_2	48	0.5	0.62	11.06	3.98	11.76	-0.18
	NO_x		0.92	0.59	13.19	13.68	19	0.59
	O_3		0.42	0.56	5.48	0.93	5.56	-0.53
RCS_IT	NO_2	48	0.99	0.65	2.12	6.03	6.39	0.42
	NO_x		0.92	0.54	12.79	15.43	20.04	0.55
	O_3		0.75	0.67	0.57	2.34	2.41	0.28
SIM_IT	NO_2	48	1	0.61	2.75	4.34	5.14	0.51
	NO_x		0.92	0.59	13.19	13.68	19	0.59
	O_3		0.02	0.67	4.33	0.68	4.38	-0.4

The averaged O_3 mixing ratios were overestimated by 49.1 ppb (1185.1%) in RCS_UK and by 6.7 ppb (163.8%) in SIM_UK. Without VOC chemistry, a considerable fraction of NO_2 is neglected, with the time averaged NO_2 being underestimated by approximately 6.4 ppb (20.4%) in RCS_UK and by 14.3 ppb

(48.3%) in SIM_UK. RCS_IT showed the most favorable performance when compared to observations, exhibiting a difference of 1.8 ppb (6.2%) for NO_2 and 0.7 ppb (13.0%) for O_3. The model results from RCS_IT were taken as the baseline for subsequent comparisons with RCS_IT_E and RCS_IT_B in the next section. As expected, SIM_IT displayed similar results for NO_2 when compared to RCS_IT, but the O_3 mixing ratios were slightly lower due to the absence of VOC radical chemistry.

In the deep urban canyon, a high photolysis rate can intensify O_3 formation, as exemplified by RCS_UK, even when VOC radical reactions become less significant (SIM_UK). Consequently, O_3 mixing ratios in such environments may pose a considerable concern during summer periods when solar radiation is intense. Our simulations indicate that O_3 mixing ratios display a vertical distribution, potentially exposing individuals at O_3 higher building heights to increased O_3 levels. This trend can also be found from the observed values. Moreover, peroxyacetyl nitrate (PAN) is a crucial photochemical pollutant generated through reactions between NO_2 and the peroxyacetyl radical (PA), typically considered as a photochemical product of VOCs. Although both PAN and O_3 are photochemical pollutants, their responses to precursors and temperature differ (Wang et al., 2017, Li et al., 2019). In RCS_IT, the spatiotemporal averaged PAN level within the canyon throughout the simulation period is 0.6 ppb, with a maximum value of 2.4 ppb at the street level on January 12th, 2021. Exposure to PAN at the street level could significantly increase when solar radiation is high (e.g., RCS_UK). In light of these findings, future research is recommended to focus on refining model

parameters and incorporating additional photochemical species, such as PAN, to enhance the accuracy of air quality predictions in deep canyon environments. Investigating the influence of seasonal fluctuations in solar radiation and meteorological conditions on photochemical pollutant concentrations will facilitate a more comprehensive understanding of the underlying processes and potential health hazards associated with elevated pollutant exposure at varying building heights.

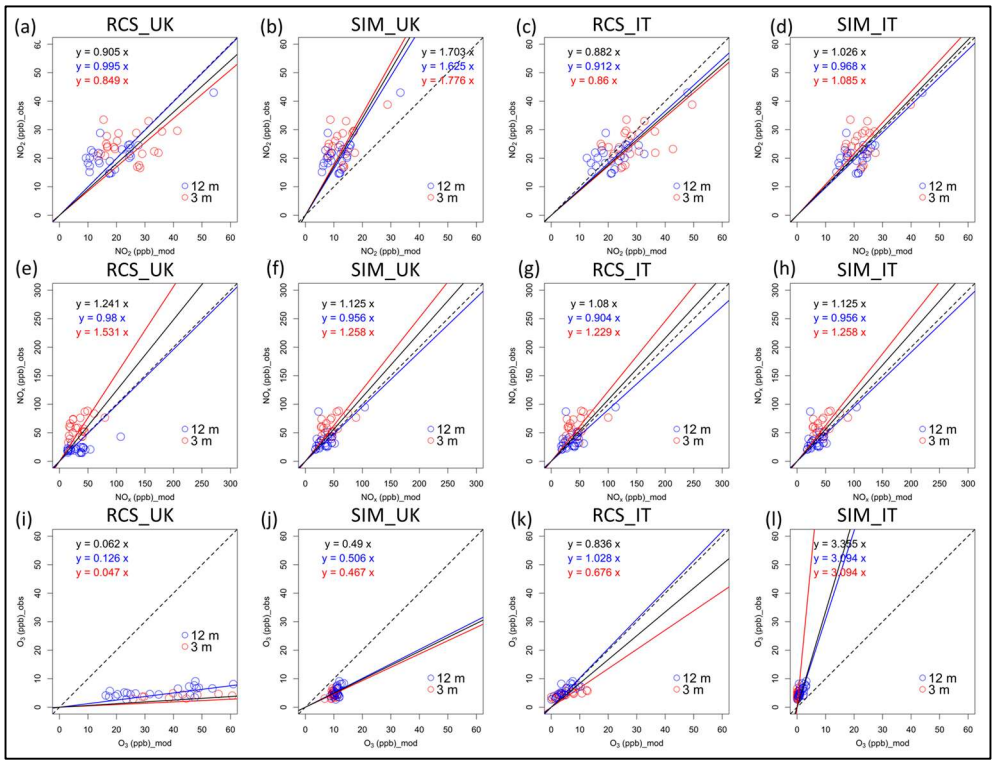


Figure 5.3. Scatter plot illustrating the correlation between modelled (MBM-FleX) and observed NO_2, NO_x, and O_3 concentrations at various heights within the deep street canyon. The red line delineates the relationship between modelled and observed values at 3 m height, the blue line represents the relationship at 12 m height, and the black line signifies model evaluations using data from all heights.

5.3.4. Model simulation sensitivity

Various modelling scenarios (RCS_IT_E1-E2, RCS_IT_B1-B3) were explored to understand the model response to changes in emissions and background conditions. The impact of emission rates and background conditions on air quality within the deep canyon can be expressed as the differences between RCS_IT_E/B and RCS_IT (See Figure 5.4). The red line in Figure 5.4 illustrates the percentage differences in air pollutant mixing ratios between the various modeling cases and their corresponding RCS_IT, attributable to reductions in NO_x emissions (by 50%, RCS_IT_E1), VOC emissions (by 50%, RCS_IT_E2), and background conditions (RCS_IT_B1-B3).

RCS_IT_E1 reveals that lowering NO_x emissions leads to reduced NO_2 and NO_x mixing ratios at both heights and increased ground-level O_3 mixing ratios. The reductions in NO_2 and NO_x at the street level are 3.4 ppb (10.4%) and 8.3 ppb (16.9%), respectively, which are substantially greater than those at the 12 m building height (1.0 ppb, 3.7% at the 3 m level, and 2.3 ppb, 5.7% at the 12 m level). The increases in O_3 mixing ratios are 1.9 ppb (40.3%) and 0.6 ppb (11.7%) at the 3 m and 12 m levels of the canyon, respectively. Case RCS_IT_E2 indicates that reduced VOC emissions result in similar decreases in NO_2 mixing ratios through chemical processes at both 3 m and 12 m levels. However, changes in NO_x levels in the street canyon did not vary substantially. This suggests that the urban atmosphere is sensitive to both NO_x and VOC emissions. Reducing VOCs offers additional benefits, as O_3 concentrations slightly decreased (1.6 ppb and 0.7 ppb) rather than increasing as in case

RCS_IT_E1. This reduction may become more significant during summer daytime when photochemical processes intensify.

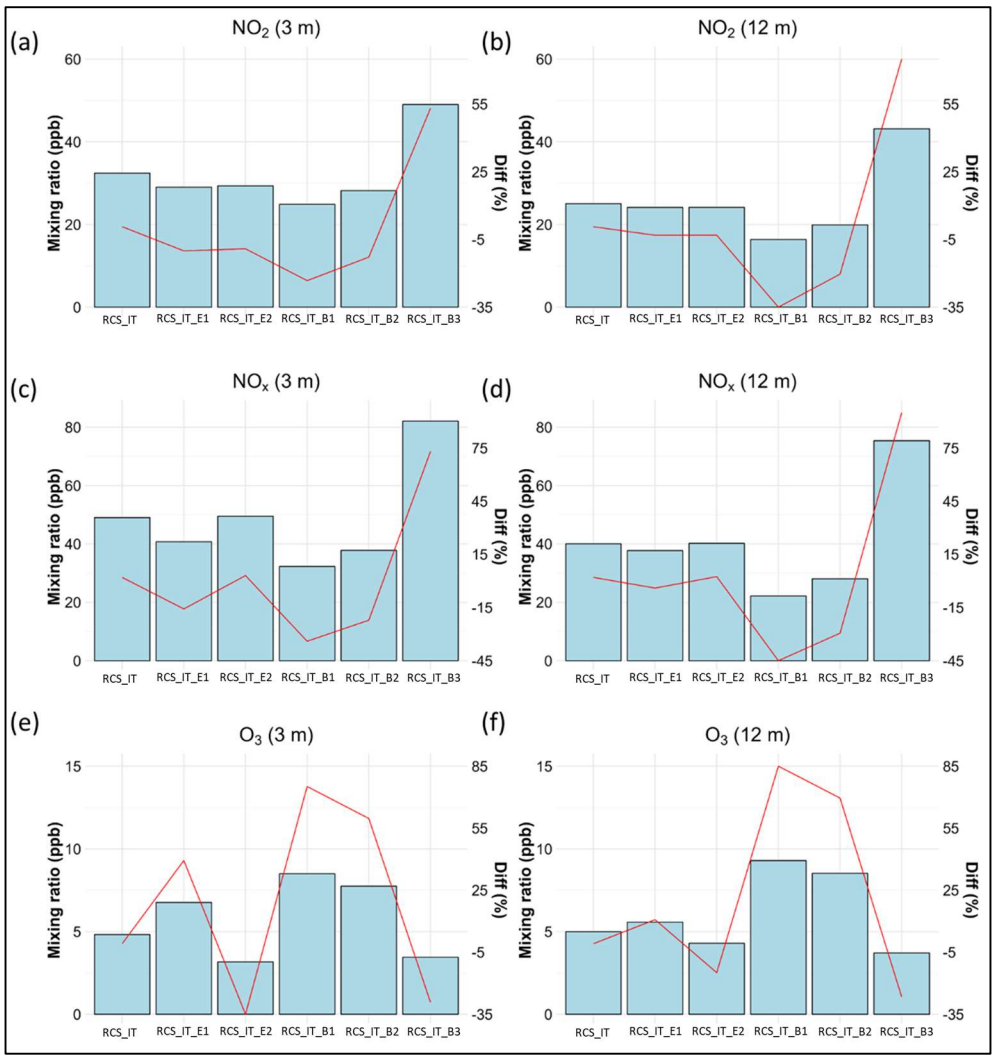


Figure 5.4. The time-averaged concentrations of pollutants (represented by bar plots) at various heights under different modelling scenarios within the deep canyon throughout the entire simulation period. The red line shows the percentage differences in air pollutant mixing ratios between the various modelling cases and their corresponding baseline condition (RCS_IT), attributable to changes in NO_x emissions, VOC emissions, and background conditions.

The model results also indicate that background NO_x conditions significantly impact air pollution within the canyon. Lower background NO_x levels were associated with decreased NO_2 (e.g., 7.5 ppb, 23.3% at the 3 m level and 8.7 ppb, 34.7% at the 12 m level in RCS_IT_B1) and NO_x (16.8 ppb, 34.2% and 17.9 ppb, 44.6%, respectively) mixing ratios and increased O_3 levels, while high background NO_x conditions exhibited the opposite trend. In line with changes in traffic emissions (i.e., RCS_IT_E1 and RCS_IT_E2), these results indicate that the street level is more affected by traffic emissions, while the upper level of the canyon is more influenced by overlying background conditions. Strategies must be carefully designed to propose targeted approaches for mitigating air pollution at different heights within the canyon. The susceptibility of the canyon to background conditions highlights the need to consider background conditions when designing air quality management strategies for urban canyons. Policymakers and urban planners should implement integrated strategies to control local and citywide concentrations in order to reduce the exposure risk of pollutants for populations within street canyons. Localized actions could include: (1) the integration of vertical greenery systems or green walls on building facades and (2) the establishment of low-emission zones coupled with restrictions on vehicle assess during high pollution periods. On a citywide scale, strategies should involve thoughtful urban planning with attention to building orientations, heights, and spacing. Additionally, augmenting urban green spaces, such as parks and gardens, and enforcing stringent emission standards for both industries and vehicles are

pivotal. Incentives to accelerate the adoption of electric or hybrid vehicles would also be effective, for gas-phase pollutants at least.

5.3.5. The performance of MBM-FleX_r

In the current study, the performance of MBM-FleX_r — an advanced and flexible methodology developed for future integration with regional-scale air quality models, similar to Kim et al. (2018c) — was evaluated. Figure 5.11 presents scatter plots comparing MBM-FleX_r simulations with observations, while Table 5.7 provides a statistical evaluation of MBM FleX_r at various heights within the deep canyon. Consistent with its predecessor MBM-FleX, RCS_IT_R, which incorporates VOC radical chemistry and a photochemical reaction intensity profile, exhibits the highest performance for NO_2, NO_x, and O_3 simulations in MBM-FleX_r, with IOA values of 0.6, 0.63, and 0.55, respectively. The model shows enhanced performance at 12 m compared to 3 m; it should also be noted that optimizing overall model performance for the canyon air quality simulation may yield varying model performance at different heights. The differences between modelled and observed values are mainly attributed to systematic errors (Table 5.7).

The findings support the viability of using simplified exchange rates between the urban canyon and the ambient background while preserving pollution concentration gradients at the street level. However, a more in-depth evaluation of MBM-FleX_r performance in the horizontal direction is warranted by using 2D box models in future research. This will enable a more comprehensive understanding of the model capabilities and limitations,

contributing to the improvement and refinement of air quality estimations in intricate urban environment.

5.4. Conclusions

Multi-box frameworks, incorporating both dynamics and chemistry, were employed to simulate reactive pollutants within deep urban canyon environments. The model results were assessed against measured NO_2, NO_x, and O_3 at different building heights for a real deep canyon located in Naples, Italy. Firstly, using the dynamical parameters derived from the computational fluid dynamics (CFD) results, the vertical distribution of CO within an idealised deep canyon with an AR of 3, as modelled by one-dimensional MBM-FleX, exhibited a strong agreement with the results obtained from the CFD simulations. The dynamical parameters were applied to the real canyon with an AR of 3.7, which closely approximated the idealized canyon. Model results show that increasing photolysis rates (e.g., during summer months with strong solar radiation) may lead to an intensification of O_3 formation within the deep canyon from less than 10 ppb to 50 ppb and even higher (e.g., Figure 5.3). This finding suggests that factors such as the shading effects (influencing photochemical kinetics) should be considered in future simulations for more accurate prediction (Zhang et al., 2020). The research emphasizes the importance of accounting for vertical distribution when assessing the health impacts of air pollutants and developing effective air quality control strategies in deep urban canyons.

The study employed various modelling scenarios (Cases RCS_IT_E/B) to provide the understanding of model response to changes in emissions and background conditions in the context of air quality within deep urban canyons. RCS_IT showed the best model performance in the evaluation against the observations and was used as the baseline for further scenarios in which reducing NO_x and VOC emissions and varying background conditions were discussed. Strong reductions in emissions are needed for even modest returns in air quality; reducing 50% emissions can lead to improvements in air quality by 10.4% to 16.9% at the street level. The deep street canyon atmosphere is sensitive to both NO_x and VOC emissions. Somewhat more surprisingly, since the background pollutant field can change the top-of-street flux appreciably, the model response was sensitive to changes in background conditions. This emphasizes the need for targeted approaches and consideration of regional and local background conditions in the design of air quality management strategies. Additionally, the performance of the newly developed MBM-FleX_r was assessed. The model exhibits some overestimation at rooftop heights, particularly on the windward side, but it effectively captures pollution concentration gradients at the ground level. This approach has potential to integrate seamlessly with regional-scale air quality models, and so improve our understanding of air quality dynamics within complex urban environments over a range of scales.

To future improve the multi-box model accuracy, several important factors must be considered: Firstly, the distinctive geometry of urban canyons impacts ventilation rates, often leading to trapped pollutants; thus, gauging these rates

is essential for predicting how pollutants might behave in these environments. Secondly, as urban canyons are embedded within the broader urban framework, their interaction with the ambient air quality becomes paramount; accurate integration of background concentrations at the rooftop level ensures a holistic portrayal of pollutants, encompassing both pre-existing and canyon-specific emissions. Lastly, given that primary pollutants in urban settings transform into secondary pollutants under sunlight, models must incorporate these photochemical processes, enabling predictions about both the dispersion and evolution of these pollutants.

Future research efforts should focus on incorporating additional photochemical species, such as peroxyacetyl nitrate (PAN), to improve the accuracy of air quality predictions within deep urban canyon environments. Examining the impact of seasonal variations in solar radiation and meteorological conditions on photochemical pollutant concentrations will provide a more comprehensive understanding of the underlying processes and potential health hazards related to elevated pollutant exposure at different building heights. A thorough evaluation of MBM-FleX_r performance using 2D multi-layer box models is recommended to facilitate a more in-depth understanding of the model's capabilities and limitations.

5.5. Supporting Information

This study involved conducting model evaluations for MBM-FleX_r by comparing it to its origin version, MBM-FleX, and LES results. The model initial and background conditions, emissions, other configurations, along with

operational procedures, have been kept consistent with our prior work (c.f., Dai et al. (2022a)). Here, some briefings were summarized: the box-dimensions for MBM-FleX/MBM-FleX_r are 4 × 4 for the regular canyon (AR = 1) and 4 × 8 for the deep canyon (AR = 2), respectively; the prevailing wind speed is 2 m s^{-1}; exchange velocities we,0 are 0.021 m s^{-1} and 0.012 m s^{-1} for regular and deep canyons, respectively (BrightBloss and Cai, 2013, ZhongCai and Bloss, 2015); a simple NO_x-O_3 chemistry with a *J*-value of 9.20×10-3 s^{-1} for NO_2 photodegradation, and a reduced chemical scheme (RCS) with 51 species and 136 reactions including hydroperoxyl radical chemistry are adopted (BrightBloss and Cai, 2013). The RCS explicitly incorporated inorganic chemistry from a more comprehensive chemical scheme Master Chemical Mechanism (MCM) and maintained OH levels within 10% of those predicted by the full MCM.

Figure 5.7 and Figure 5.8 show results of different air quality models for an idealized regular canyon (AR = 1) using the simple NO_x-O_3 chemistry and reduced chemical scheme (RCS) chemistry. Meanwhile, Figure 5.9 and Figure 5.10 show the result of two chemical schemes for a deep canyon (AR = 2), respectively. In the regular canyon, the spatial distribution of a chemically inert passive tracer (PS) exhibited good agreements between MBM-FleX and LES models, and our prior work (Dai et al., 2021a) provides detailed discussions on the results. The modified version of MBM-FleX (MBM-FleX_r) presented comparable performance to the original MBM FleX and LES on the leeward side. The model exhibited a tendency to overestimate passive tracer (PS) concentrations along the windward side of the canyon; for

instance, the overestimation amounted to approximately 17% in the case of a standard canyon, and 12% for a deep canyon configuration. This discrepancy can be attributed to the significant influence of urban background factors on the location at the windward crest of buildings, that is, employing an averaging-flux approach for the entire street canyon may consequently result in an underestimation of the impact of fresh air influx into the canyon. For reactive species, MBM-FleX_r with the simple NO_x-O_3 chemistry overestimated NO_2 concentrations, with the largest differences occurring on the windward side of the canyon (i.e., 14 ppb and 35 ppb for regular and deep canyons, respectively). O_3 was overestimated on the leeward side (~1 ppb) but was underestimated on the windward side (~3 ppb) due to the complex dynamics and segregation effects in chemistry (ZhongCai and Bloss, 2014, Li et al., 2021). VOC chemistry, to some extent, amplified these differences as showed in Figure 5.8. Moreover, MBM-FleX_r tended to underestimate PS concentrations at the pedestrian level in the deep canyon, with the degree of underestimation reducing with increasing building height. Eventually, MBM-FleX_r-modelled PS surpassed those of LES on the windward roof. NO_2 and O_3 showed a tendency of overestimate. The differences between MBM-FleX_r and MBM-FleX/LES become more significant on the leeward side for O_3 and on the windward side for NO_2, possibly due to uncertainties in representing tightly coupled physical and chemical processes. MBM-FleX_r can also reproduce the spatial distribution of air pollution within urban canyons and agreed well with LES, though it lost some accuracy compared to its original version MBM-FleX. Both the MBM-FleX and MBM-FleX_r for simulations in the real canyon

following parameter evaluations were employed to further assess model applicability.

There are some challenges in dynamic parameters derivation processes. These parameters employed by the multi-box models are derived from CFD simulations. For every new modelling scenario, there is an imperative to initiate CFD in order to furnish the necessary data for multi-box model parameter estimations. Moreover, the measured data often displays pronounced variability, shaped by oscillating meteorological conditions, emission origins, and additional external variables. Assimilating this multifaceted data into an integrated model introduces its own array of complexities.

Supporting Figures

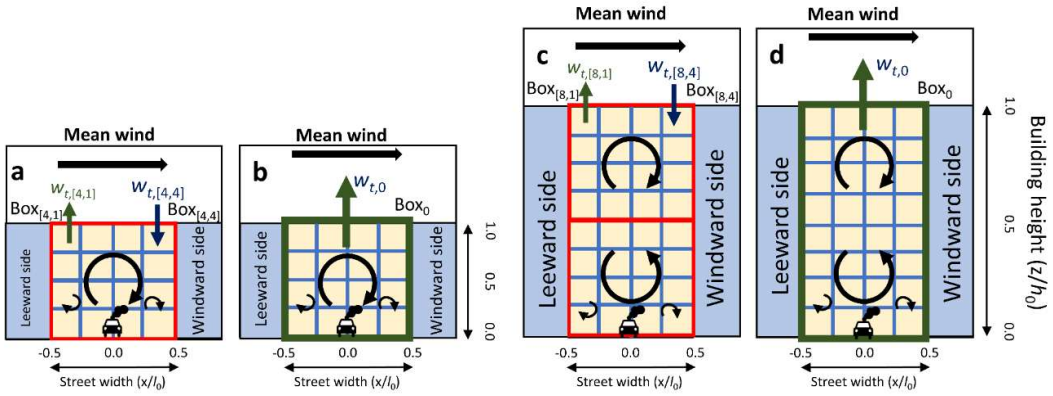


Figure 5.5. Diagram of the multi-box model (MBM-FleX) for air quality simulation within (a, b) regular and (c, d) deep street canyons. Red frames represent compartments that resolve a large vortex, blue lines further split the canyon volume into finer boxes, indicating the spatial resolution of the model within canyons, and green frame represents the entire volume of street canyons.

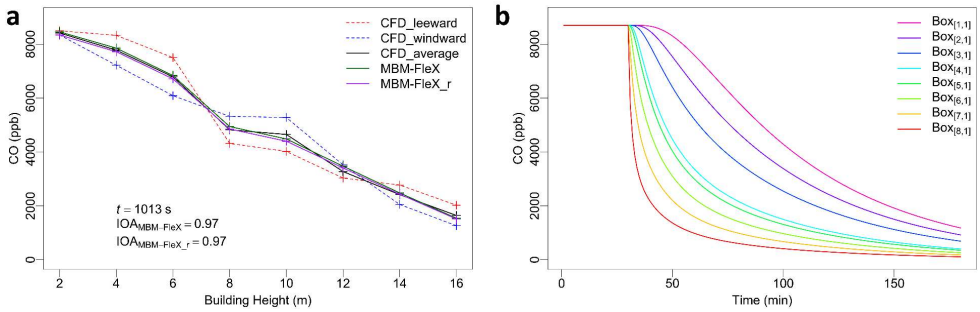


Figure 5.6. Model results of CO concentrations from MBM-FleX, MBM-FleX_r, and CFD (i.e., RANS) for a deep canyon (AR = 4.5), where (a) shows the vertical distributions of CO concentrations within the canyon, and (b) illustrates the dissipation rates of CO with time.

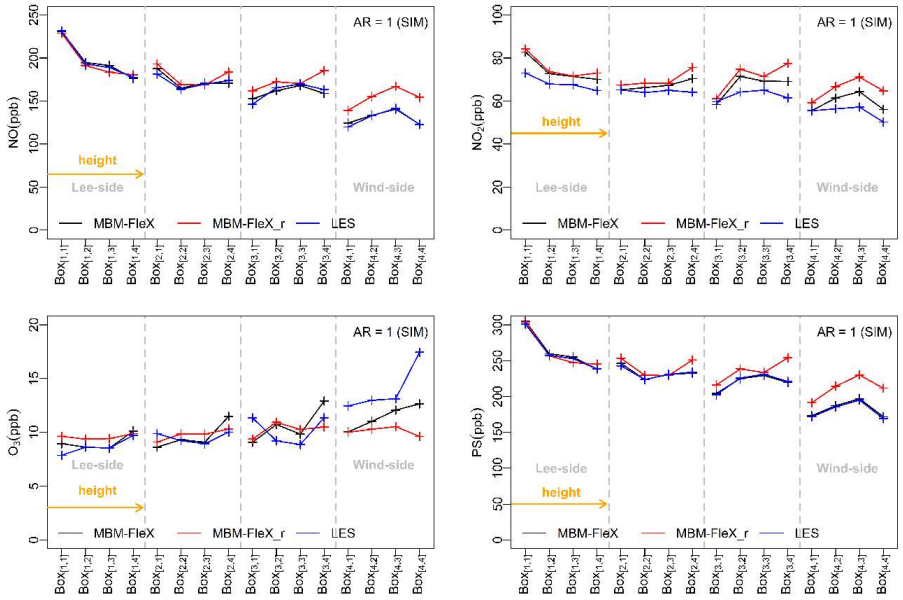


Figure 5.7. Model results of NO, NO_2, O_3, and PS from the original (i.e., MBM-FleX), revised (e.g., MBM-FleX_r) multi-box models, and large-eddy simulations (LES) with the simple NO_x-O_3 chemistry for the regular canyon (AR = 1). Black line represents results from MBM-FleX, red line represents results from MBM-FleX_r, and blue line represents results from LES, respectively. The grey dashed lines represent the division of the canyon horizontally, from the lee-side to the wind-side; in each panel the height increases as indicated by the orange arrow.

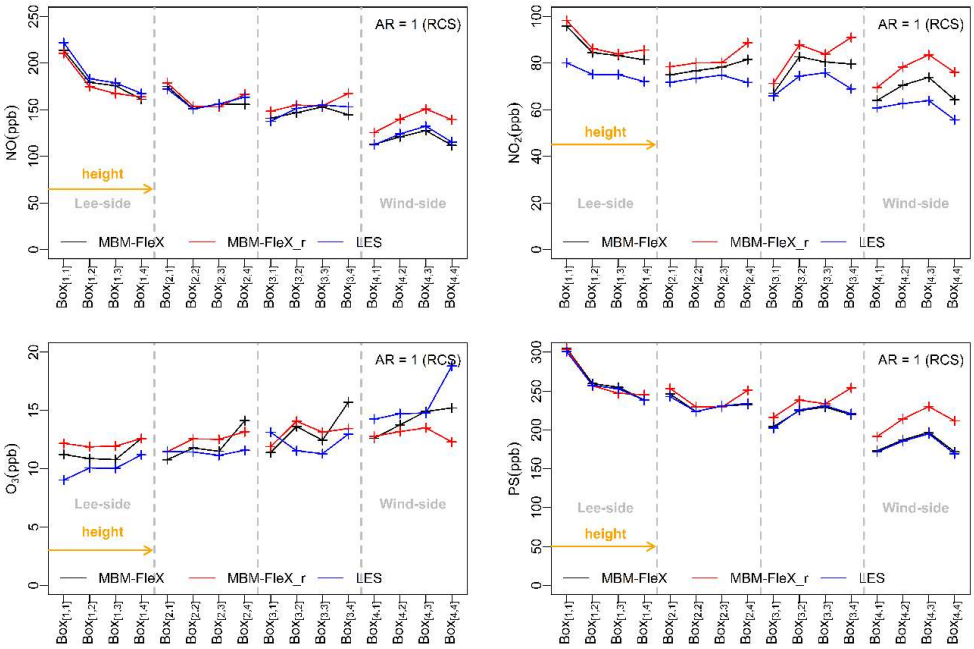


Figure 5.8. Model results of NO, NO_2, O_3, and PS from the original (i.e., MBM-FleX), revised (e.g., MBM-FleX_r) multi-box models, and large-eddy simulations (LES) with the reduced chemical scheme (RCS) for the regular canyon (AR = 1). Black line represents results from MBM-FleX, red line represents results from MBM-FleX_r, and blue line represents results from LES, respectively. The grey dashed lines represent the division of the canyon horizontally, from the lee-side to the wind-side; in each panel the height increases as indicated by the orange arrow.

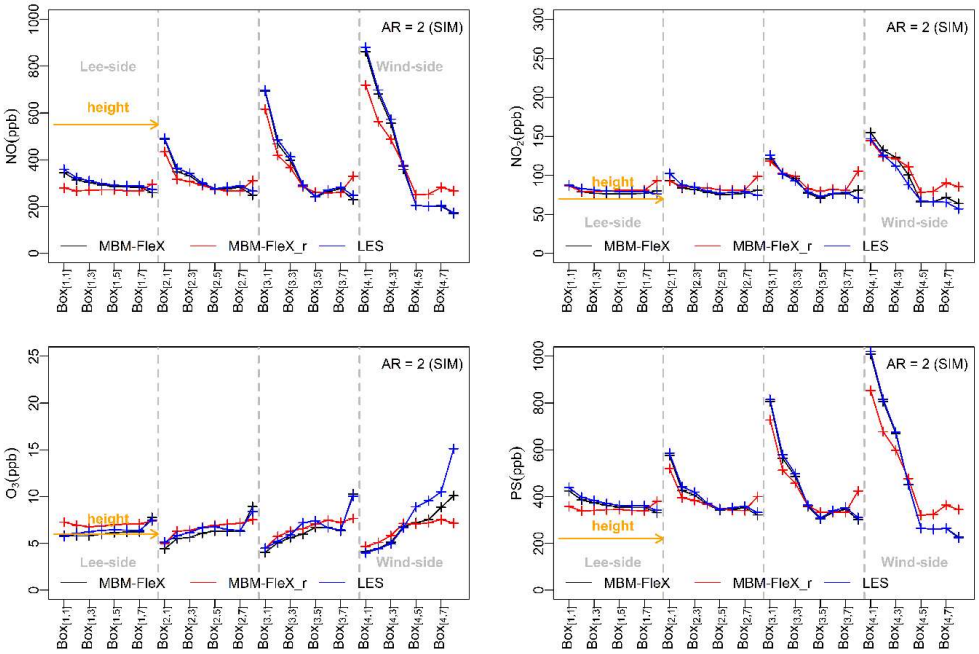


Figure 5.9. Model results of NO, NO_2, O_3, and PS from the original (i.e., MBM-FleX), revised (e.g., MBM-FleX_r) multi-box models, and large-eddy simulations (LES) with the simple NO_x-O_3 chemistry for the deep canyon (AR = 2). Black line represents results from MBM-FleX, red line represents results from MBM-FleX_r, and blue line represents results from LES, respectively. The grey dashed lines represent the division of the canyon horizontally, from the lee-side to the wind-side; in each panel the height increases as indicated by the orange arrow.

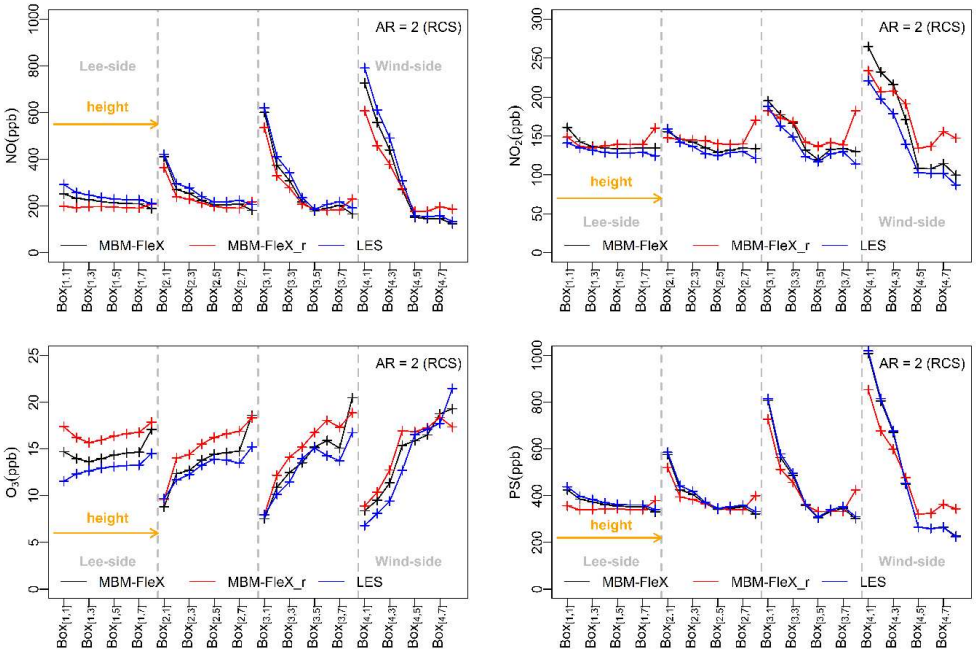


Figure 5.10. Model results of NO, NO_2, O_3, and PS from the original (i.e., MBM-FleX), revised (e.g., MBM-FleX_r) multi-box models, and large-eddy simulations (LES) with reduced chemical scheme (RCS) for the deep canyon (AR = 2). Black line represents results from MBM-FleX, red line represents results from MBM-FleX_r, and blue line represents results from LES, respectively. The grey dashed lines represent the division of the canyon horizontally, from the lee-side to the wind-side; in each panel the height increases as indicated by the orange arrow.

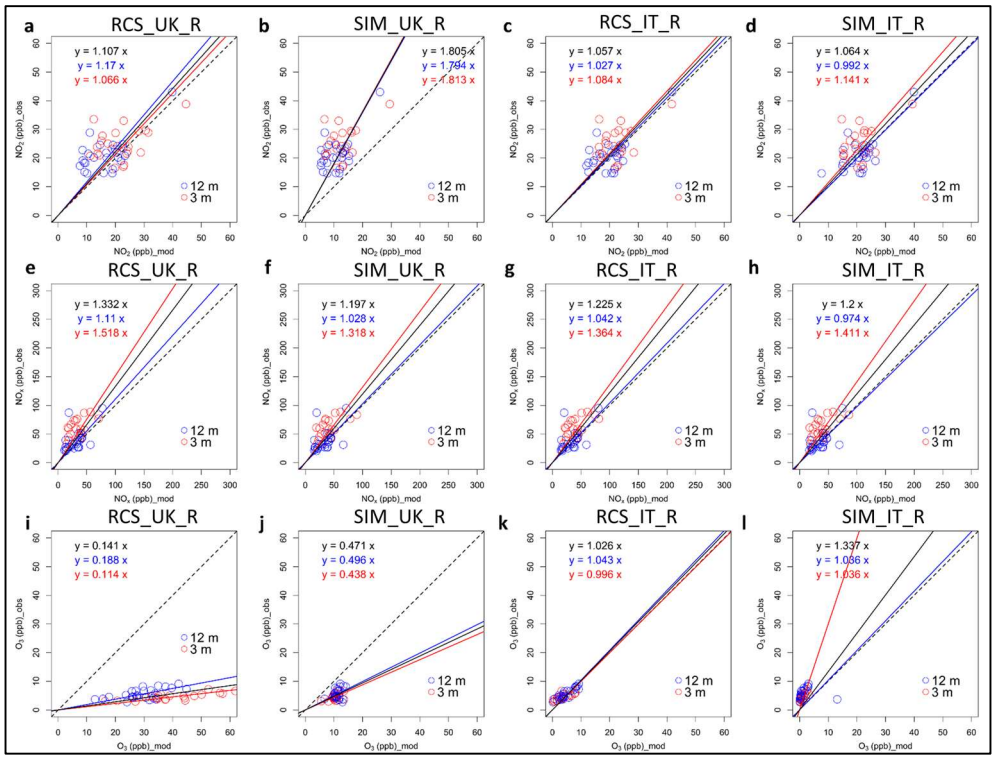


Figure 5.11. Scatter plot illustrating the correlation between modelled (MBM-FleX_r) and observed NO_2, NO_x, and O_3 concentrations at various heights within the deep street canyon. The red line delineates the relationship between modelled and observed values at 3 m height, the blue line represents the relationship at 12 m height, and the black line signifies model evaluations using data from all heights.

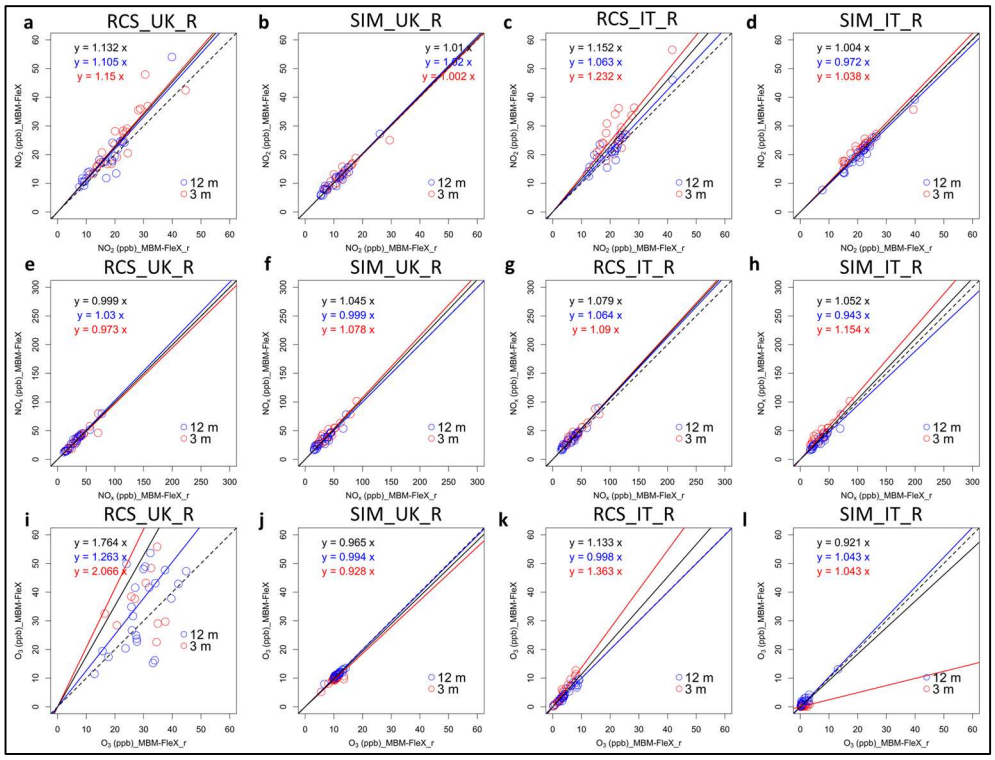


Figure 5.12. Scatter plot illustrating the correlation between MBM-FleX_r and MBM-FleX simulations at various heights within the deep street canyon. The red line delineates the relationship between modelled and observed values at 3 m height, the blue line represents the relationship at 12 m height, and the black line signifies model evaluations using data from all heights.

Supporting Tables

Table 5.3. Turbulent mixing velocities used in the MBM-FleX/MBM-FleX_r model, these dynamical parameters are derived from wash-out CFD simulations for a deep canyon (AR = 3) under a prevailing wind speed of 2 m s^{-1} in the neutral atmosphere.

Vertical turbulence (m s^{-1})	
w_t = 3.2e-04	w_t = 3.2e-04
$w_{e[2,1]}$ = 3.92e-03	$w_{e[2,1]}$ = 3.92e-03
$w_{e[3,1]}$ = 2.4e-04	$w_{e[3,1]}$ = 2.4e-04
$w_{e[4,1]}$ = 1.99e-02	$w_{e[4,1]}$ = 1.99e-02
$w_{e[5,1]}$ = 2.76e-02	$w_{e[5,1]}$ = 2.76e-02

Table 5.4. Emission factors of main vehicle categories calculated using COPERT procedure at 20 km h^{-1}, the unit has been transformed from g km^{-1} h^{-1} into ppb according to the volume of model mesh under a standard pressure and 293 K.

Category	**CO**		**NO_x**		**VOCs**		**Primary NO_2**
	g km^{-1} h^{-1}	ppb s^{-1}	g km^{-1} h^{-1}	ppb^{-1}	g km^{-1} h^{-1}	ppb^{-1}	NO_2/NO_x
Buses	2.93	0.104	10.05	0.217	0.65	0.054	0.115
Heavy Duty Trucks	2.68	0.095	7.95	0.171	1.20	0.100	0.113
L-Category	8.82	0.313	0.12	0.003	2.39	0.198	0.040
Light Commercial Vehicles	2.08	0.074	1.54	0.033	0.22	0.019	0.245
Passenger Cars	6.97	0.247	0.62	0.013	0.66	0.054	0.160

Table 5.5. Photochemical reactions and their reaction rate coefficients (J-values) at 293 K included in the Reduced Chemical Scheme (RCS).

Order	Reactions	*J*-values	Type
1	$O_3 \rightarrow OH + OH$	3.40×10^{-6}	Inorganic
2	$H_2O_2 \rightarrow OH + OH$	7.11×10^{-6}	Inorganic
3	$NO_2 \rightarrow NO + O_3$	9.20×10^{-3}	Inorganic
4	$NO_3 \rightarrow NO$	2.34×10^{-2}	Inorganic
5	$NO_3 \rightarrow NO_2 + O_3$	1.83×10^{-1}	Inorganic
6	$HONO \rightarrow OH + NO$	2.02×10^{-3}	Inorganic
7	$HNO_3 \rightarrow OH + NO_2$	6.30×10^{-7}	Inorganic
8	$HCHO \rightarrow CO + HO_2 + HO_2$	3.05×10^{-5}	Organic
9	$HCHO \rightarrow H_2 + CO$	4.61×10^{-5}	Organic
10	$CH_3CHO \rightarrow CH_3O_2 + HO_2 + CO$	5.07×10^{-6}	Organic
11	$CARB_7 = CH_3CO_3 + HCHO + HO_2$	3.36×10^{-6}	Organic
12	$HOCH_2CHO = HCHO + CO + HO_2 + HO_2$	1.77×10^{-5}	Organic
13	$UCARB10 = CH_3CO_3 + HCHO + HO_2$	1.62×10^{-5}	Organic
14	$CARB6 = CH_3CO_3 + CO + HO_2$	1.26×10^{-4}	Organic
15	$UCARB12 = CH_3CO_3 + HOCH_2CHO + CO + HO_2$	1.62×10^{-5}	Organic
16	$CH_3NO_3 = HCHO + HO_2 + NO_2$	8.96×10^{-7}	Organic
17	$CH_3OOH = HCHO + HO_2 + OH$	5.44×10^{-6}	Organic
18	$CH_3CO_3H = CH_3O_2 + OH$	5.44×10^{-6}	Organic
19	$HOCH_2CO_3H = HCHO + HO_2 + OH$	5.44×10^{-6}	Organic
20	$RU14OOH = UCARB12 + HO_2 + OH$	1.37×10^{-6}	Organic
21	$RU14OOH = UCARB10 + HCHO + HO_2 + OH$	4.07×10^{-6}	Organic
22	$RU12OOH = CARB6 + HOCH_2CHO + OH$	5.44×10^{-6}	Organic
23	$RU10OOH = CH_3CO_3 + HOCH_2CHO + OH$	5.44×10^{-6}	Organic
24	$HOC2H4OOH = HCHO + HCHO + HO_2 + OH$	5.44×10^{-6}	Organic
25	$RN9OOH = CH_3CHO + HCHO + HO_2 + OH$	5.44×10^{-6}	Organic

Table 5.6. Statistical evaluation of the MBM-FleX for NO_2, NO_x, and O_3 at different building heights within the deep street canyon (AR = 3.7).

Case	Species	Location	n	FAC2	r	RMSEs	RMSEu	RMSE	IOA
RCS_UK	NO_2	3 m	23	0.96	0.44	0.56	10.4	10.42	-0.03
		12 m	25	0.88	0.74	2.55	6.24	6.74	0.28
	NO_x	3 m	23	0.52	0.5	26.72	13.6	29.98	0.04
		12 m	25	0.92	0.58	7.94	15.61	17.51	0.48
	O_3	3 m	23	0.01	0.61	81.32	35.03	88.54	-0.98
		12 m	25	0.01	0.71	36.22	13.98	38.82	-0.91
SIM_UK	NO_2	3 m	23	0.48	0.47	12.48	4.01	13.1	-0.27
		12 m	25	0.52	0.72	9.66	3.77	10.37	-0.19
	NO_x	3 m	23	0.87	0.5	17.42	13.26	21.89	0.33
		12 m	25	0.96	0.59	7.74	13.86	15.88	0.57
	O_3	3 m	23	0.39	0.3	5.29	0.77	5.34	-0.67
		12 m	25	0.44	0.57	5.69	0.8	5.74	-0.44
RCS_IT	NO_2	3 m	23	0.99	0.48	3.44	6.54	7.39	0.35
		12 m	25	0.99	0.71	1.24	5.16	5.3	0.4
	NO_x	3 m	23	0.87	0.44	17.55	14.95	23.06	0.29
		12 m	25	0.96	0.59	6.62	15.43	16.79	0.5
	O_3	3 m	23	0.65	0.76	1.73	2.33	2.91	-0.2
		12 m	25	0.84	0.8	0.93	1.59	1.84	0.51
SIM_IT	NO_2	3 m	23	0.99	0.48	3.99	4.23	5.81	0.43
		12 m	25	0.99	0.72	1.43	4.19	4.43	0.52
	NO_x	3 m	23	0.87	0.5	17.42	13.26	21.89	0.33
		12 m	25	0.96	0.59	7.74	13.86	15.88	0.57
	O_3	3 m	23	0.01	0.57	4.43	0.21	4.44	-0.6
		12 m	25	0.04	0.68	4.28	0.67	4.33	-0.25

Table 5.7. Statistical evaluation of the MBM-FleX_r for NO_2, NO_x, and O_3 within the deep street canyon (AR = 3.7).

Case	Species	location	n	FAC2	r	RMSEs	RMSEu	RMSE	IOA
		total	0.98	0.55	3.56	4.51	5.75	0.5	0.98
	NO_2	3 m	0.96	0.43	5.03	4.61	6.82	0.37	0.96
		12 m	0.99	0.68	1.88	4.14	4.54	0.56	1
		total	0.79	0.49	16.88	13.64	21.7	0.54	0.79
RCS_UK_R	NO_x	3 m	0.7	0.62	22.16	12.97	25.68	0.19	0.7
		12 m	0.88	0.46	11.31	13.04	17.26	0.57	0.88
		total	0.04	0.22	3.96	1.9	4.4	-0.4	0.04
	O_3	3 m	0.04	0.74	3.6	0.58	3.65	-0.51	0.04
		12 m	0.04	0.08	4.3	2.52	4.99	-0.35	0.04
		total	0.98	0.55	3.56	4.51	5.75	0.5	0.98
	NO_2	3 m	0.96	0.43	5.03	4.61	6.82	0.37	0.96
		12 m	0.99	0.68	1.88	4.14	4.54	0.56	0.99
		total	0.79	0.49	16.88	13.64	21.7	0.54	0.79
SIM_UK_R	NO_x	3 m	0.7	0.62	22.16	12.97	25.68	0.19	0.7
		12 m	0.88	0.46	11.31	13.04	17.26	0.57	0.88
		total	0.04	0.22	3.96	1.9	4.4	-0.4	0.04
	O_3	3 m	0.04	0.74	3.6	0.58	3.65	-0.51	0.04
		12 m	0.04	0.08	4.3	2.52	4.99	-0.35	0.04
		total	0.98	0.59	3.14	4.75	5.7	0.48	0.98
	NO_2	3 m	0.96	0.44	4.11	4.86	6.36	0.4	0.96
		12 m	0.99	0.66	2.11	4.53	5	0.49	0.99
		total	0.85	0.58	16.11	12.95	20.67	0.57	0.85
RCS_IT_R	NO_x	3 m	0.78	0.58	20.59	12.89	24.29	0.26	0.78
		12 m	0.92	0.53	10.72	12.74	16.65	0.59	0.92
		total	0.77	0.86	1.04	1.31	1.67	0.45	0.77
	O_3	3 m	0.7	0.79	1.16	1.41	1.83	0.08	0.7
		12 m	0.84	0.9	1.01	1.14	1.52	0.61	0.84
		total	0.98	0.55	3.56	4.51	5.75	0.5	0.98
	NO_2	3 m	0.96	0.43	5.03	4.61	6.82	0.37	0.96
		12 m	0.99	0.68	1.88	4.14	4.54	0.56	0.99
		total	0.79	0.49	16.88	13.64	21.7	0.54	0.79
SIM_IT_R	NO_x	3 m	0.7	0.62	22.16	12.97	25.68	0.19	0.7
		12 m	0.88	0.46	11.31	13.04	17.26	0.57	0.88
		total	0.04	0.22	3.96	1.9	4.4	-0.4	0.04
	O_3	3 m	0.04	0.74	3.6	0.58	3.65	-0.51	0.04
		12 m	0.04	0.08	4.3	2.52	4.99	-0.35	0.04

CHAPTER 6 GENERAL DISCUSSION

6.1 Thesis Overview and Major Results

The thesis fundamentally transforms the understanding of air quality within urban street canyons through the development and application of the innovative multi-box photochemical model, MBM-FleX. It demonstrates that considering the interplay of chemical processes, urban geometries, and environmental conditions is paramount for accurate air quality assessments and effective pollution mitigation strategies. The thesis highlights the limitations of simpler models and emphasizes the significance of including nuanced factors such as shading effects and VOC chemistry. Furthermore, it extends the scope of its applicability through real-world validations and the integration with regional-scale models, ultimately establishing MBM-FleX as a vital tool for nuanced, reliable urban air quality management. The work not only enhances our comprehension of pollutant dynamics within complex urban microenvironments but also lays a robust foundation for future advancements in air quality modelling and policy formulation.

In **Chapter 2**, this thesis develops the process-based multi-box photochemical model (i.e., MBM-FleX) for street canyon air quality simulations, featuring a flexible number of boxes and based on dynamical parameters calculated from large-eddy simulation (LES) outputs. The model performance, when coupled with a simplified NO_x-O_3 cycle (or even a more complex NO_x-O_3-VOC chemistry), has been evaluated for both regular (with an aspect ratio of 1,

AR = 1) and deep (AR = 2) urban canyons, comparing it to the published LES data and one- and two-box simulations.

The results present that while the single-box model captures the average state of air pollutants in street canyons, aligning with previous studies (Bright et al., 2013, Zhong et al., 2016b), the MBM-FleX model accurately reproduces the spatial concentration gradients of air pollutants within street canyons, capturing spatial and temporal evolution patterns for air pollutants within both regular and deep street canyons. The multi-box model is less computationally efficient than one-box models and two-box models, but it can provide additional spatial information (i.e., horizontal distribution) on reactive species within street canyons based on coupled chemical-transport processes in a relatively short computational time (e.g., < 1 min for each simulation with VOC free-radical chemistry).

In this chapter, we found that segregation effects have a substantial impact on reactive species, particularly on short-lived species. For example, the multi-box model overestimates hydroxy (OH) and hydroperoxyl (HO_2) mixing ratios, with their vertical variations being less significant compared to the LES results due to their short chemical timescales. In the regular canyon, the NO and O_3 titration reaction becomes more effective due to less segregation along the windward facet, underestimating O_3 and overestimating NO_2 levels, respectively. On the leeward side, the overestimated NO_2 results in overestimated O_3 through photochemical reactions, and further overestimation of NO_2 is attributed to OH/HO_2 chemistry. In an idealised deep

canyon with poor ventilation, the relationship of reactive species in the upper compartment between the multi-box (i.e., with 32 boxes within the canyon) and LES models is consistent with that in the regular canyon. However, in the lower compartments, O_3 concentrations are always overestimated, and there are noticeable variations of OH and HO_2 concentrations vertically. Under the simple NO_x-O_3 cycle, the differences between the multi-box model and the LES become smaller, especially for the deep canyon. While the impact of VOC free-radical chemistry on reactive species like NO_2 might be underestimated in comparison to the LES, the MBM-FleX captures the vertical contribution of VOCs on these pollutants within street canyons, which represents a marked improvement over the traditional one- and two-box models. This presents a more nuanced understanding of the chemical dynamics of air pollution in urban microenvironments.

In summary (i.e., **Chapter 2**), the multi-box framework allows for insightful investigations into multiple processes and their complex interactions, making it a practical and operational tool for air quality assessment or pollution mitigation management in street canyons. The model effectively simulates reactive species in street canyons with different geometrics, capturing spatial concentration patterns and vertical contributions of VOCs to pollutants, with a performance superior to simpler zero- and one-dimensional models. The study shows the importance of considering segregation effects, especially for short-lived species, and highlights the potential of the multi-box model in air quality management applications.

In **Chapter 3**, we applied the multi-box model MBM-FleX coupled with chemical schemes to investigate shading effects on NO_2, O_3, and O_x within urban street canyons. The results underscore notable discrepancies between shaded and unshaded scenarios, signifying that shading effects, in combination with chemical processes, emissions, and tracer transport, can significantly modify the magnitude and spatial distribution of air pollution within street canyons. The shading effects on pollution distribution are particularly prominent under certain conditions, such as when the solar zenith angle is such that a regular canyon (AR = 1) is half-shaded, or when wind blows through shaded areas, thereby enhancing photochemistry.

The study demonstrates that the inclusion of VOC chemistry is critical in modelling the shading effects, especially regarding its impact on O_x concentrations in street canyons. The results also show that prevailing wind speeds and shading intensity have a significant, yet complex, impact on pollutant concentrations. This complexity suggests that a simple proxy approach to simulate shading effects on street-canyon air quality is insufficient, underscoring the need to include shading effects and VOC free-radical chemistry in future air quality simulations. Furthermore, we propose that the substantial effect of shading on street canyon O_3 could have implications to produce Highly Oxidized Molecules (HOMs) and possibly new particle formation, necessitating further investigation. In conclusion, this study offers initial quantification of shading effects on reactive air pollutants under varying conditions and introduces a fast computational technique for scenario analysis. This technique, which maintains adequate spatial resolution and represents

transport, mixing, and chemical processes, can be expanded into a toolkit for street network air quality simulations.

In **Chapter 4**, the study investigates the challenges faced by policymakers aiming to develop effective mitigation strategies, particularly focusing on the impact of emissions and primary NO_2 in the presence of VOC free-radical chemistry. This chapter reveals that compliance with air quality standards depends on assumptions about chemistry, which are often absent from regulatory modelling. The introduction of VOC free-radical chemistry to the model decreases the air quality management "wiggle room," particularly when ambient wind speeds are low. In deep canyons, the effect of VOC free-radical chemistry on air quality is more significant, between 60% and 70% for all ambient wind speeds.

The compliance lines in the two-dimensional E_{NOx}—f_{NO2} space indicate that multi-variate synergistic controls offer a more effective way of reducing NO_2 in street canyons. However, the optimum path for air quality improvements varies significantly based on the canyon geometry and should be evaluated carefully in each case. The distance between the current emission scenario and the three-dimensional compliance surface can help stakeholders design more effective strategies for improving air quality in urban areas.

The study also highlights the importance of considering the effects of prevailing wind velocity (U_0) on NO_2 mixing-ratios, which can improve or deteriorate air quality within the modelled urban canyons by up to ~25% and ~60%, respectively. The airflow inside street canyons is assumed to be

linearly scaled to U_0, but the effects on NO_2 are highly non-linear due to the tight coupling of chemistry-transport processes. In the regular canyon, the wiggle room drops rapidly when U_0 is low, making VOC free-radical chemistry more important.

Emission heterogeneity and its potential implications for coordinated urban planning of transport and the built environment are also discussed. The results show that emission heterogeneity can alter the mass fluxes escaping the canyons, affecting the overall mixing-ratio of pollutants within canyons. This aspect becomes even more critical when considering the blocking effect of central barriers and the segregation impact, which warrants future investigation.

Overall, **Chapter 4** underscores the need to account for free-radical chemistry and other factors such as canyon geometry, wind velocity, and emission heterogeneity when modelling air quality in urban canyons. By considering these factors, policymakers and stakeholders can develop more effective strategies for improving air quality in urban areas and better understand the complex relationship between emission factors and free-radical chemistry.

In **Chapter 5**, the multi-box framework integrated with dynamics and chemistry to simulate reactive pollutants within a deep urban canyon in Naples, Italy. The work underscores the important role of photochemical reactions on NO_2 and O_3 concentrations in such environments, highlighting the need to account for factors such as shading effects impacting photochemical kinetics in future studies. The model correlates well with observed data.

Moreover, the study evaluates the performance of MBM-FleX_r, a newly developed, flexible framework designed for compatibility with regional-scale air quality models. Results suggest that simplified exchange rates between the urban canyon and the ambient background can be adopted while maintaining accurate street-level pollution concentration gradients. This synergistic approach could enhance urban air quality forecasts, providing policymakers with robust data to make informed decisions.

6.2 Limitations and suggestions for future research

As with any research endeavor, there are limitations and areas for future work that warrant attention. These limitations and future research directions provide ample opportunities for further exploration and refinement. Pursuing these research avenues will contribute to the development of more effective air quality management strategies and the improvement of public health in urban environments.

(1) Aerosol microphysics: Aerosol microphysics is known to introduce non-linear processes within street canyons similar to gaseous chemistry (Gelbard and Seinfeld, 1980, JacobsonTabazadeh and Turco, 1996, Jacobson and Seinfeld, 2004, Zhong et al., 2020a, Zhong et al., 2020b). Previously, a two-box model was developed in conjunction with ultrafine particle (UFP) microphysics to simulate the number concentration size distribution of UFP at ground-level. Rapid adjustments in UFPs at the street-canyon scale were identified, strongly influenced by emission, exchange, and the

evaporation/condensation processes of semi-volatile substances (Zhong et al., 2018). Future studies could extend the multi-box framework to include detailed size-dependent aerosol microphysics, which could have implications for understanding the sources and sinks of aerosols in street canyons and their effects on human health.

(2) Vegetation and street canyon configurations: The present thesis does not delve into the effects of spatially segregated emissions resulting from vegetation within urban canyons. The influence of green infrastructure in canyons is highly context-dependent (HewittAshworth and MacKenzie, 2020, ElliottEon and Breadsell, 2020, Tomson et al., 2021). Subsequent research endeavors could employ the multi-box model to simulate air pollution in street canyons with a diverse range of green infrastructures, enabling a more comprehensive understanding of air quality impacts under various urban planning scenarios. However, accurate physical parameters for in-canyon dynamics are currently challenging to obtain, which poses a limitation for this line of investigation.

(3) Advanced chemical schemes: Further investigations could incorporate more detailed chemical schemes (e.g., Master Chemical Mechanism) into the multi-box model, enhancing the accuracy of pollutant predictions and potentially capturing the formation of Highly Oxidized Molecules (HOMs) and new particle formation.

(4) Model evaluation and integration: Future research should include the evaluation of modeling results using more field measurements for different cities as an intercomparison. The implementation of vertical profiling is essential, especially for deep canyons, as it provides critical insights into the vertical distribution of pollutants and the intricate dispersion mechanisms influenced by the surrounding built environment. The strategic placement of monitoring instruments on both the windward and leeward sides of the street canyons is crucial. The windward side captures the ingress air quality, establishing a baseline for comparison, while the leeward side elucidates the modifications in pollutant levels induced by the street canyon's microenvironment, shedding light on the effects of local emissions and building configurations. Additionally, a more challenging task would be to merge the effects of airflow parallel to the street axis on the diffusion and transformation of chemical species, which would enable a wider range of model applications. Integrating the multi-box model with regional-scale air quality models could also be considered to study the combined impact of local and regional air pollution sources.

(5) Seasonal and meteorological influences: Investigating the impact of seasonal variations in solar radiation and meteorological conditions on photochemical pollutant concentrations will contribute to a more comprehensive understanding of the underlying processes and potential health hazards related to elevated pollutant exposure.

(6) Health impact assessments: To better understand the health implications of air pollution within urban street canyons, future studies should consider incorporating the air quality model with vertical distribution of pollutants in exposure assessments and estimate the associated health risks for different population groups.

(7) Indoor air quality issues: The multi-box framework can be adapted to simulate indoor air quality and assess pollutant concentrations and dispersion in various indoor environments. This approach helps identify pollutant sources, evaluate mitigation strategies, and inform guidelines for healthier living and working spaces, contributing to a better understanding of indoor and outdoor air quality relationships.

(8) Street network: Particularly in cities similar to Munich or those employing the ADMS-Urban model, future research can explore the application and adaptation of the multi-box framework to model complex street network systems. This approach could potentially highlight hotspots of air pollution at a more granular level and guide more effective urban planning and traffic management strategies.

APPENDICES

Appendix A: Multi-box model parameters

Table S1 Advective and turbulent velocities in the 16-box model for the regular canyon.

Model	Advection				Turbulence			
	Vertical	Value ($m\ s^{-1}$)	Horizontal	Value ($m\ s^{-1}$)	Vertical	Value ($m\ s^{-1}$)	Horizontal	Value ($m\ s^{-1}$)
16-box	$W_{a,[2,1]}$	0.1468	$U_{a,[1,1]}$	0	$w_{e,[2,1]}$	0.0111	$u_{e,[1,1]}$	0
	$W_{a,[2,2]}$	0.0938	$U_{a,[1,2]}$	-0.1879	$w_{e,[2,2]}$	0.0136	$u_{e,[1,2]}$	0.0169
	$W_{a,[2,3]}$	-0.0723	$U_{a,[1,3]}$	-0.2903	$w_{e,[2,3]}$	0.0001	$u_{e,[1,3]}$	0.0160
	$W_{a,[2,4]}$	-0.1731	$U_{a,[1,4]}$	-0.1920	$w_{e,[2,4]}$	0.0001	$u_{e,[1,4]}$	0.0270
	$W_{a,[3,1]}$	0.2539	$U_{a,[2,1]}$	0	$w_{e,[3,1]}$	0.0001	$u_{e,[2,1]}$	0
	$W_{a,[3,2]}$	0.1849	$U_{a,[2,2]}$	-0.0950	$w_{e,[3,2]}$	0.0001	$u_{e,[2,2]}$	0.0167
	$W_{a,[3,3]}$	-0.1255	$U_{a,[2,3]}$	-0.1716	$w_{e,[3,3]}$	0.0001	$u_{e,[2,3]}$	0.0071
	$W_{a,[3,4]}$	-0.2971	$U_{a,[2,4]}$	-0.1422	$w_{e,[3,4]}$	0.0001	$u_{e,[2,4]}$	0.0138
	$W_{a,[4,1]}$	0.1815	$U_{a,[3,1]}$	0	$w_{e,[4,1]}$	0.0001	$u_{e,[3,1]}$	0
	$W_{a,[4,2]}$	0.1335	$U_{a,[3,2]}$	0.0767	$w_{e,[4,2]}$	0.0194	$u_{e,[3,2]}$	0.0034
	$W_{a,[4,3]}$	-0.0639	$U_{a,[3,3]}$	0.1313	$w_{e,[4,3]}$	0.0001	$u_{e,[3,3]}$	0.0001
	$W_{a,[4,4]}$	-0.2597	$U_{a,[3,4]}$	0.0676	$w_{e,[4,4]}$	0.0649	$u_{e,[3,4]}$	0.0001
	$W_{a,[5,1]}$	0.0015	$U_{a,[4,1]}$	0	$w_{e,[5,1]}$	0.0101	$u_{e,[4,1]}$	0
	$W_{a,[5,2]}$	0.0069	$U_{a,[4,2]}$	0.1809	$w_{e,[5,2]}$	0.0258	$u_{e,[4,2]}$	0.1389
	$W_{a,[5,3]}$	0	$U_{a,[4,3]}$	0.2898	$w_{e,[5,3]}$	0.0305	$u_{e,[4,3]}$	0.0852
	$W_{a,[5,4]}$	0	$U_{a,[4,4]}$	0.2087	$w_{e,[5,4]}$	0.0285	$u_{e,[4,4]}$	0.0438

Table S2 Advective and turbulent velocities in the 32-box model for the deep canyon.

	Advection				Turbulence			
Model	Vertical	Value ($m\ s^{-1}$)	Horizontal	Value ($m\ s^{-1}$)	Vertical	Value ($m\ s^{-1}$)	Horiz-ontal	Value ($m\ s^{-1}$)
32-box	$W_{a,[2,1]}$	-0.0199	$U_{a,[1,1]}$	0.00	$w_{e,[2,1]}$	0.015	$u_{e,[1,1]}$	0.00
	$W_{a,[2,2]}$	-0.0106	$U_{a,[1,2]}$	0.0167	$w_{e,[2,2]}$	0.0102	$u_{e,[1,2]}$	0.0001
	$W_{a,[2,3]}$	0.0049	$U_{a,[1,3]}$	0.0348	$w_{e,[2,3]}$	0.0123	$u_{e,[1,3]}$	0.0001
	$W_{a,[2,4]}$	0.0216	$U_{a,[1,4]}$	0.0286	$w_{e,[2,4]}$	0.0062	$u_{e,[1,4]}$	0.0001
	$W_{a,[3,1]}$	-0.0134	$U_{a,[2,1]}$	0.0000	$w_{e,[3,1]}$	0.0366	$u_{e,[2,1]}$	0.0000
	$W_{a,[3,2]}$	-0.0145	$U_{a,[2,2]}$	-0.0060	$w_{e,[3,2]}$	0.0913	$u_{e,[2,2]}$	0.0001
	$W_{a,[3,3]}$	-0.0028	$U_{a,[2,3]}$	-0.0025	$w_{e,[3,3]}$	0.0565	$u_{e,[2,3]}$	0.0001
	$W_{a,[3,4]}$	0.0286	$U_{a,[2,4]}$	0.0045	$w_{e,[3,4]}$	0.0184	$u_{e,[2,4]}$	0.0001
	$W_{a,[4,1]}$	0.0217	$U_{a,[3,1]}$	0.0000	$w_{e,[4,1]}$	0.0435	$u_{e,[3,1]}$	0.0000
	$W_{a,[4,2]}$	0.0046	$U_{a,[3,2]}$	-0.0323	$w_{e,[4,2]}$	0.0669	$u_{e,[3,2]}$	0.0001
	$W_{a,[4,3]}$	-0.0343	$U_{a,[3,3]}$	-0.0448	$w_{e,[4,3]}$	0.0656	$u_{e,[3,3]}$	0.0001
	$W_{a,[4,4]}$	0.0033	$U_{a,[3,4]}$	-0.0222	$w_{e,[4,4]}$	0.0383	$u_{e,[3,4]}$	0.0001
	$W_{a,[5,1]}$	0.0763	$U_{a,[4,1]}$	0.0000	$w_{e,[5,1]}$	0.0524	$u_{e,[4,1]}$	0.0000
	$W_{a,[5,2]}$	0.0444	$U_{a,[4,2]}$	-0.0531	$w_{e,[5,2]}$	0.0834	$u_{e,[4,2]}$	0.0001
	$W_{a,[5,3]}$	-0.0381	$U_{a,[4,3]}$	-0.1048	$w_{e,[5,3]}$	0.0639	$u_{e,[4,3]}$	0.5207
	$W_{a,[5,4]}$	-0.0956	$U_{a,[4,4]}$	-0.0641	$w_{e,[5,4]}$	0.0381	$u_{e,[4,4]}$	0.0001
	$W_{a,[6,1]}$	0.1167	$U_{a,[5,1]}$	0.0000	$w_{e,[6,1]}$	0.0656	$u_{e,[5,1]}$	0.0000
	$W_{a,[6,2]}$	0.0772	$U_{a,[5,2]}$	-0.0422	$w_{e,[6,2]}$	0.0001	$u_{e,[5,2]}$	0.0513
	$W_{a,[6,3]}$	-0.0334	$U_{a,[5,3]}$	-0.0747	$w_{e,[6,3]}$	0.0001	$u_{e,[5,3]}$	0.0308
	$W_{a,[6,4]}$	-0.1492	$U_{a,[5,4]}$	-0.0782	$w_{e,[6,4]}$	0.3252	$u_{e,[5,4]}$	0.0457
	$W_{a,[7,1]}$	0.1148	$U_{a,[6,1]}$	0.0000	$w_{e,[7,1]}$	0.2363	$u_{e,[6,1]}$	0.0000
	$W_{a,[7,2]}$	0.0772	$U_{a,[6,2]}$	0.0019	$w_{e,[7,2]}$	0.0001	$u_{e,[6,2]}$	0.0439
	$W_{a,[7,3]}$	-0.0272	$U_{a,[6,3]}$	0.0018	$w_{e,[7,3]}$	0.0111	$u_{e,[6,3]}$	0.0001
	$W_{a,[7,4]}$	-0.1437	$U_{a,[6,4]}$	-0.0063	$w_{e,[7,4]}$	0.0001	$u_{e,[6,4]}$	0.0097
	$W_{a,[8,1]}$	0.0698	$U_{a,[7,1]}$	0.0000	$w_{e,[8,1]}$	0.0001	$u_{e,[7,1]}$	0.0000
	$W_{a,[8,2]}$	0.0567	$U_{a,[7,2]}$	0.0447	$w_{e,[8,2]}$	0.0818	$u_{e,[7,2]}$	0.1643
	$W_{a,[8,3]}$	0.0010	$U_{a,[7,3]}$	0.0640	$w_{e,[8,3]}$	0.0823	$u_{e,[7,3]}$	0.0110
	$W_{a,[8,4]}$	-0.1210	$U_{a,[7,4]}$	0.0364	$w_{e,[8,4]}$	0.0380	$u_{e,[7,4]}$	0.0009
	$W_{a,[9,1]}$	0.0000	$U_{a,[8,1]}$	0	$w_{e,[9,1]}$	0.0067	$u_{e,[8,1]}$	0
	$W_{a,[9,2]}$	0.0000	$U_{a,[8,2]}$	0.0654	$w_{e,[9,2]}$	0.0180	$u_{e,[8,2]}$	0.0818
	$W_{a,[9,3]}$	0.0000	$U_{a,[8,3]}$	0.1089	$w_{e,[9,3]}$	0.0234	$u_{e,[8,3]}$	0.0823
	$W_{a,[9,4]}$	0.0023	$U_{a,[8,4]}$	0.0901	$w_{e,[9,}$	0.0200	$u_{e,[8,4]}$	0.0380

Appendix B: RCS mechanism

Table S3 All chemical reactions consisted in the Reduced Chemical Scheme (RCS). The reactions and coefficients are derived from the Master Chemical Mechanism (MCM) v3.1 by (REF) with the standard sea-level pressure of 1013.25 hPa and the temperature of 293 K (20 °C). The units of rate constants are s^{-1} for first order reactions and ppb s^{-1} for second order reactions.

Order	Reactions	Rate Constant, k		Type
1	$O_3 \longrightarrow OH + OH$	3.40×10^{-6}	JFAC	photolysis
2	$NO + O_3 \longrightarrow NO_2$	1.40×10^{-12}	exp(-1310/T)	bimolecular
3	$NO + NO \longrightarrow NO_2 + NO_2$	3.30×10^{-39}	exp(530/T)*O_2	termolecular
4	$NO + NO_3 \longrightarrow NO_2 + NO_2$	1.80×10^{-11}	exp(110/T)	bimolecular
5	$OH + O_3 \longrightarrow HO_2$	1.70×10^{-12}	exp(-940/T)	bimolecular
6	$OH + H_2 \longrightarrow HO_2$	7.70×10^{-12}	exp(-2100/T)	bimolecular
7	$OH + CO \longrightarrow HO_2$	1.30×10^{-13}	**KMT05**	bimolecular
8	$OH + H_2O_2 \longrightarrow HO_2$	2.90×10^{-12}	exp(-160/T)	bimolecular
9	$HO_2 + O_3 \longrightarrow OH$	2.03×10^{-16}	$(T/300)^{4.57}$exp(693/T)	bimolecular
10	$OH + HO_2 \longrightarrow$	4.80×10^{-11}	exp(250/T)	bimolecular
11	$HO_2 + HO_2 \longrightarrow H_2O_2$	2.20×10^{-13}	**KMT06*** exp(600/T)	bimolecular
12	$HO_2 + HO_2 \longrightarrow H_2O_2$	1.90×10^{-33}	M***KMT06***exp (980/T)	termolecular
13	$OH + NO \longrightarrow HONO$		**KMT07**	termolecular
14	$OH + NO_2 \longrightarrow HNO_3$		**KMT08**	termolecular
15	$OH + NO_3 \longrightarrow HO_2 + NO_2$		2.00×10^{-11}	bimolecular
16	$HO_2 + NO \longrightarrow OH + NO_2$	3.60×10^{-12}	exp(270/T)	bimolecular
17	$HO_2 + NO_2 \longrightarrow HO_2NO_2$		**KMT09**	termolecular
18	$HO_2NO_2 \longrightarrow HO_2 + NO_2$		**KMT10**	bimolecular
19	$OH + HO_2NO_2 \longrightarrow NO_2$	1.90×10^{-12}	exp(270/T)	bimolecular
20	$OH + HONO \longrightarrow NO_2$	2.50×10^{-12}	exp(-260/T)	bimolecular
21	$NO_2 + O_3 \longrightarrow NO_3$	1.40×10^{-13}	exp(-2470/T)	bimolecular

Order	Reactions	Rate Constant, k		Type
22	$OH + HNO_3 \longrightarrow NO_3$		**KMT11**	bimolecular
23	$H_2O_2 + h\nu \longrightarrow OH + OH$	7.11×10^{-6}	JFAC	photolysis
24	$NO_3 + h\nu \longrightarrow NO + O_3$	9.20×10^{-3}	JFAC	photolysis
25	$NO_3 + h\nu \longrightarrow NO$	2.34×10^{-2}	JFAC	photolysis
26	$NO_3 + h\nu \longrightarrow NO_2 + O_3$	1.83×10^{-1}	JFAC	photolysis
27	$HONO + h\nu \longrightarrow OH + NO$	2.02×10^{-3}	JFAC	photolysis
28	$HNO_3 + h\nu \longrightarrow OH + NO_2$	6.30×10^{-7}	JFAC	photolysis
29	$OH + CH_4 = CH_3O_2$	9.65×10^{-20}	$T^{2.58}\exp(-1082/T)$	bimolecular
30	$OH + C_2H_4 = HOCH_2CH_2O_2$		**KMT15**	termolecular
31	$OH + C_3H_6 = RN9O2$		**KMT16**	termolecular
32	$O_3 + C_2H_4 = HCHO + CO + HO_2 + OH$	9.14×10^{-15}	exp(-2580/T)*0.13	bimolecular
33	$O_3 + C_2H_4 = HCHO + HCOOH$	9.14×10^{-15}	exp(-2580/T)*0.87	bimolecular
34	$O_3 + C_3H_6 = HCHO + CO + CH_3O_2 + OH$	5.51×10^{-15}	exp(-1878/T)*0.36	bimolecular
35	$O_3 + C_3H_6 = HCHO + CH_3CO_2H$	5.51×10^{-15}	exp(-1878/T)*0.64	bimolecular
36	$OH + C_5H_8 = RU14O2$	2.54×10^{-11}	exp(410/T)	bimolecular
37	$O_3 + C_5H_8 = UCARB10 + CO + HO_2 + OH$	7.86×10^{-15}	exp(-1913/T)*0.27	bimolecular
38	$O_3 + C_5H_8 = UCARB10 + HCOOH$	7.86×10^{-15}	exp(-1913/T)*0.73	bimolecular
39	$HCHO = CO + HO_2 + HO_2$	3.05×10^{-5}	JFAC	photolysis
40	$HCHO = H_2 + CO$	4.61×10^{-5}	JFAC	photolysis
41	$CH_3CHO = CH_3O_2 + HO_2 + CO$	5.07×10^{-6}	JFAC	photolysis
42	$OH + HCHO = HO_2 + CO$	1.20×10^{-14}	T*exp(287/T)	bimolecular
43	$OH + CH_3CHO = CH_3CO_3$	5.55×10^{-12}	exp(311/T)	bimolecular
44	$OH + CH_3OH = HO_2 + HCHO$	6.01×10^{-18}	T2* exp(170/T)	bimolecular
45	$OH + C_2H_5OH = CH_3CHO + HO_2$	6.18×10^{-18}	T2*exp(532/T)*0.887	bimolecular
46	$OH + C_2H_5OH = HOCH_2CH_2O_2$	6.18×10^{-18}	T2*exp(532/T)*0.113	bimolecular
47	$HCOOH + OH = HO_2$	4.50×10^{-13}		bimolecular
48	$CH_3CO_2H + OH = CH_3O_2$	8.00×10^{-13}		bimolecular
49	$CH_3O_2 + NO = HCHO + HO_2 + NO_2$	3.00×10^{-12}	exp(280/T)*0.999	bimolecular

Order	Reactions	Rate Constant, k		Type
50	$HOCH_2CH_2O_2 + NO = HCHO + HCHO + HO_2 + NO_2$		$KR_{O2}NO$*0.995*0.776	bimolecular
51	$HOCH_2CH_2O_2 + NO = HOCH_2CHO + HO_2 + NO_2$		$KR_{O2}NO$*0.995*0.224	bimolecular
52	$RN9O2 + NO = CH_3CHO + HCHO + HO_2 + NO_2$		$KR_{O2}NO$*0.979	bimolecular
53	$CH_3CO_3 + NO = CH_3O_2 + NO_2$		*KAPNO*	bimolecular
54	$HOCH_2CO_3 + NO = HO_2 + HCHO + NO_2$		*KAPNO*	bimolecular
55	$RU14O2 + NO = UCARB12 + HO_2 + NO_2$		*KRO2NO**0.900*0.252	bimolecular
56	$RU14O2 + NO = UCARB10 + HCHO + HO_2 + NO_2$		*KRO2NO**0.900*0.748	bimolecular
57	$RU12O2 + NO = CH_3CO_3 + HOCH_2CHO + NO_2$		*KRO2NO**0.7	bimolecular
58	$RU12O2 + NO = CARB7 + CO + HO_2 + NO_2$		*KRO2NO**0.3	bimolecular
59	$RU10O2 + NO = CH_3CO_3 + HOCH_2CHO + NO_2$		*KRO2NO**0.5	bimolecular
60	$RU10O2 + NO = CARB6 + HCHO + HO_2 + NO_2$		*KRO2NO**0.3	bimolecular
61	$RU10O2 + NO = CARB7 + HCHO + HO_2 + NO_2$		*KRO2NO**0.2	bimolecular
62	$CH_3O_2 + NO = CH_3NO_3$	3.00×10^{-12}	exp(280/T)*0.001	bimolecular
63	$HOCH_2CH_2O_2 + NO = HOC_2H_4N_{O3}$		*KRO2NO**0.005	bimolecular
64	RN9O2 + NO = RN9NO3		*KRO2NO**0.021	bimolecular
65	RU14O2 + NO = RU14NO3		*KRO2NO**0.100	bimolecular
66	$CH_3O_2 + HO_2 = CH_3OOH$	4.10×10^{-13}	exp(790/T)	bimolecular
67	$HOCH_2CH_2O_2 + HO_2 = HOC_2H_4OOH$	2.03×10^{-13}	exp(1250/T)	bimolecular
68	$RN9O2 + HO_2 = RN9OOH$		*KRO2HO2**0.520	bimolecular
69	$CH_3CO_3 + HO_2 = CH_3CO_3H$		*KAPHO2*	bimolecular
70	$HOCH_2CO_3 + HO_2 = HOCH_2CO_3H$		*KAPHO2*	bimolecular

Order	Reactions	Rate Constant, k		Type
71	RU14O2 + HO_2 = RU14OOH		*KRO2HO2**0.770	bimolecular
72	RU12O2 + HO_2 = RU12OOH		*KRO2HO2**0.706	bimolecular
73	RU10O2 + HO_2 = RU10OOH		*KRO2HO2**0.625	bimolecular
74	CH_3O_2 = HCHO + HO_2	1.82×10^{-12}	exp(416/T)*0.33*RO_2	R
75	CH_3O_2 = HCHO	1.82×10^{-13}	exp(416/T)*0.335*RO_2	R
76	CH_3O_2 = CH_3OH	1.82×10^{-13}	exp(416/T)*0.335*RO_2	R
77	$HOCH_2CH_2O_2$ = $HOCH_2CHO$ + HO_2	2.00×10^{-12}	RO_2*0.224	R
78	RN9O2 = CH_3CHO + HCHO + HO_2	8.80×10^{-13}	RO_2	R
79	CH_3CO_3 = CH_3O_2	1.00×10^{-11}	RO_2	R
80	$HOCH_2CO_3$ = HCHO + HO_2	1.00×10^{-11}	RO_2	R
81	RU14O2 = UCARB12 + HO_2	1.71×10^{-12}	RO_2*0.252	R
82	RU14O2 = UCARB10 + HCHO + HO_2	1.71×10^{-12}	RO_2*0.748	R
83	RU12O2 = CH3CO_3 + $HOCH_2CHO$	2.00×10^{-12}	RO_2*0.7	R
84	RU12O2 = CARB7 + $HOCH_2CHO$ + HO_2	2.00×10^{-12}	RO_2*0.3	R
85	RU10O2 = CH_3CO_3 + $HOCH_2CHO$	2.00×10^{-12}	RO_2*0.5	R
86	RU10O2 = CARB6 + HCHO + HO_2	2.00×10^{-12}	RO_2*0.3	R
87	RU10O2 = CARB7 + HCHO + HO_2	2.00×10^{-12}	RO_2*0.2	R
88	CARB7 = CH_3CO_3 + HCHO + HO_2	3.36×10^{-6}	JFAC	photolysis
89	$HOCH_2CHO$ = HCHO + CO + HO_2 + HO_2	1.77×10^{-5}	JFAC	photolysis
90	UCARB10 = CH_3CO_3 + HCHO + HO_2	1.62×10^{-5}	JFAC	photolysis
91	CARB6 = CH_3CO_3 + CO + HO_2	1.26×10^{-4}	JFAC	photolysis
92	UCARB12 = CH_3CO_3 + $HOCH_2CHO$ + CO + HO_2	1.62×10^{-5}	JFAC	photolysis
93	OH + CARB7 = CARB6 + HO_2	3.00×10^{-12}		bimolecular
94	OH + UCARB10 = RU10O2	2.50×10^{-11}		bimolecular
95	O_3 + UCARB10 = HCHO + CH_3CO_3 + CO + OH	2.85×10^{-18}	0.59	bimolecular
96	O_3 + UCARB10 = HCHO + CARB6 + H_2O_2	2.85×10^{-18}	0.41	bimolecular

Order	Reactions	Rate Constant, k		Type
97	OH + $HOCH_2CHO$ = $HOCH_2CO_3$	1.00×10^{-11}		bimolecular
98	OH + CARB6 = CH_3CO_3 + CO	1.72×10^{-11}		bimolecular
99	OH + UCARB12 = RU12O2	4.52×10^{-11}		bimolecular
100	O_3 + UCARB12 = $HOCH_2CHO$ + CH_3CO_3 + CO + OH	2.40×10^{-17}	0.89	bimolecular
101	O_3 + UCARB12 = $HOCH_2CHO$ + CARB6 + H_2O_2	2.40×10^{-17}	0.11	bimolecular
102	CH_3NO_3 = HCHO + HO_2 + NO_2	8.96×10^{-7}	JFAC	photolysis
103	OH + CH_3NO_3 = HCHO + NO_2	1.00×10^{-14}	exp(1060/T)	bimolecular
104	OH + $HOC_2H_4NO_3$ = $HOCH_2CHO$ + NO_2	1.09×10^{-12}		bimolecular
105	OH + RN9NO3 = CARB7 + NO_2	1.31×10^{-12}		bimolecular
106	OH + RU14NO3 = UCARB12 + NO_2	5.55×10^{-11}		bimolecular
107	CH_3OOH = HCHO + HO_2 + OH	5.44×10^{-6}	JFAC	photolysis
108	CH_3CO_3H = CH_3O_2 + OH	5.44×10^{-6}	JFAC	photolysis
109	$HOCH_2CO_3H$ = HCHO + HO_2 + OH	5.44×10^{-6}	JFAC	photolysis
110	RU14OOH = UCARB12 + HO_2 + OH	1.37×10^{-6}	JFAC	photolysis
111	RU14OOH = UCARB10 + HCHO + HO_2 + OH	4.07×10^{-6}	JFAC	photolysis
112	RU12OOH = CARB6 + $HOCH_2CHO$ + HO_2 + OH	5.44×10^{-6}	JFA	photolysis
113	RU10OOH = CH_3CO_3 + $HOCH_2CHO$ + OH	5.44×10^{-6}	JFAC	photolysis
114	HOC2H4OOH = HCHO + HCHO + HO_2 + OH	5.44×10^{-6}	JFAC	photolysis
115	RN9OOH = CH3CHO + HCHO + HO_2 + OH	5.44×10^{-6}	JFAC	photolysis
116	OH + CH_3OOH = CH_3O_2	1.90×10^{-11}	exp(190/T)	bimolecular
117	OH + CH_3OOH = HCHO + OH	1.00×10^{-11}	exp(190/T)	bimolecular
118	OH + CH_3CO_3H = CH_3CO_3	3.70×10^{-12}		bimolecular
119	OH + $HOCH_2CO_3H$ = $HOCH_2CO_3$	6.19×10^{-12}		bimolecular

Order	Reactions	Rate Constant, k		Type
120	OH + RU14OOH = UCARB12 + OH	7.51×10^{-11}		bimolecular
121	OH + RU12OOH = RU12O2	3.00×10^{-11}		bimolecular
122	OH + RU10OOH = RU10O2	3.00×10^{-11}		bimolecular
123	OH + HOC2H4OOH = $HOCH_2CHO$ + OH	2.13×10^{-11}		bimolecular
124	OH + RN9OOH = CARB7 + OH	2.50×10^{-11}		bimolecular
125	$CH_3CO_3 + NO_2 = PAN$		**KFPAN**	termolecular
126	$PAN = CH_3CO_3 + NO_2$		**KBPAN**	termolecular
127	$HOCH_2CO_3 + NO_2 = PHAN$		**KFPAN**	termolecular
128	$PHAN = HOCH_2CO_3 + NO_2$		**KBPAN**	termolecular
129	$OH + PAN = HCHO + CO + NO_2$	9.50×10^{-13}	exp(-650/T)	bimolecular
130	$OH + PHAN = HCHO + CO + NO_2$	1.12×10^{-12}		bimolecular
131	$RU12O2 + NO_2 = RU12PAN$		**KFPAN***0.061	termolecular
132	$RU12PAN = RU12O_2 + NO_2$		**KBPAN**	termolecular
133	$RU10O2 + NO_2 = MPAN$		**KFPAN***0.041	termolecular
134	$MPAN = RU10O2 + NO_2$		**KBPAN**	termolecular
135	$OH + MPAN = CARB7 + CO + NO_2$	3.60×10^{-12}		bimolecular
136	$OH + RU12PAN = UCARB10 + NO_2$	2.52×10^{-11}		bimolecular

Note: JFAC is a scaling factor that can be applied to the photolysis rate constant to account for variations in cloudiness, JFAC is equal to 1.0, i.e., under clear sky conditions under the unshaded condition in this work.

Appendix C: Fortran90 code for MBM-FleX

As aforementioned in main chapters, the multi-box model was coded using Fortran 90. The model code includes three submodules: main project, dynamical driver, and chemical script. The extracts from each module implementation are listed below.

```
!#*****************************************************************************#
Chemistry module
!#*****************************************************************************#
subroutine chemi(Carr, deltaTime, beta, dtchem)
use globalValue
implicit none
integer::counter,nshort
    real::deltaTime, beta, dtchem,idtlong
    real::Carr(nbv,nbh,Numspe),iNO(nbv,nbh),iNO2(nbv,nbh),iNO3(nbv,nbh),iO3(nbv,n
    bh),iH2(nbv,nbh),iPoHO2NO2(nbv,nbh)
    real::iCO(nbv,nbh),iH2O2(nbv,nbh),iHONO(nbv,nbh),iHNO3(nbv,nbh),iHO2NO2(nb
    v,nbh),iLoMPAN(nbv,nbh),iLoRN9OOH(nbv,nbh)
    real::iCH4(nbv,nbh),iC2H4(nbv,nbh),iC3H6(nbv,nbh),iC5H8(nbv,nbh),iC2H5OH(nb
    v,nbh),iPoNO2(nbv,nbh),iPoNO(nbv,nbh)
    real::iCH3NO3(nbv,nbh),iOH(nbv,nbh),iHO2(nbv,nbh),iCH3O2(nbv,nbh),iCH3OH(n
    bv,nbh),iLoPAN(nbv,nbh),iPoO3(nbv,nbh)
    real::iHOCH2CH2O2(nbv,nbh),iCH3CO2H(nbv,nbh),iCH3CHO(nbv,nbh),iRU14O2(n
    bv,nbh),iUCARB10(nbv,nbh),iPoC2H5OH(nbv,nbh)
    real::iHCHO(nbv,nbh),iCH3CO3(nbv,nbh),iHOCH2CHO(nbv,nbh),iRN9O2(nbv,nbh),i
    HCOOH(nbv,nbh),iLoPHAN(nbv,nbh)
    real::iCARB6(nbv,nbh),iUCARB12(nbv,nbh),iRU12O2(nbv,nbh),iCARB7(nbv,nbh),iR
    U10O2(nbv,nbh),iLoRN9NO3(nbv,nbh)
    real::iHOC2H4NO3(nbv,nbh),iRN9NO3(nbv,nbh),iRU14NO3(nbv,nbh),iCH3OOH(nb
    v,nbh),iHOC2H4OOH(nbv,nbh),iPoCH3NO3(nbv,nbh)
    real::iRN9OOH(nbv,nbh),iCH3CO3H(nbv,nbh),iHOCH2CO3H(nbv,nbh),iRU14OOH(n
    bv,nbh),iRU12OOH(nbv,nbh),iPoC5H8(nbv,nbh)
    real::iRU10OOH(nbv,nbh),iHOCH2CO3(nbv,nbh),iPAN(nbv,nbh),iPHAN(nbv,nbh),iR
    U12PAN(nbv,nbh),iMPAN(nbv,nbh),iPoHNO3(nbv,nbh)
    real::ick(nbv,nbh,136),irk(nbv,nbh,14),iRO2(nbv,nbh),iLoO3(nbv,nbh),iLoNO2(nbv,
    nbh),iLoNO(nbv,nbh),iLoHONO(nbv,nbh)
    real::iLoHO2NO2(nbv,nbh),iLoHNO3(nbv,nbh),iLoH2O2(nbv,nbh),iLoH2(nbv,nbh),i
    LoCO(nbv,nbh),iLoCH4(nbv,nbh),iLoC5H8(nbv,nbh)
    real::iLoC3H6(nbv,nbh),iLoC2H4(nbv,nbh),iLoUCARB12(nbv,nbh),iLoUCARB10(nb
    v,nbh),iLoHOCH2CHO(nbv,nbh),iLoHOC2H4NO3(nbv,nbh)
    real::iLoHCOOH(nbv,nbh),iLoHCHO(nbv,nbh),iLoCH3OH(nbv,nbh),iLoCH3NO3(nbv,
    nbh),iLoCH3CO2H(nbv,nbh),iLoRU12OOH(nbv,nbh)
```

```
      real::iLoCARB7(nbv,nbh),iLoCARB6(nbv,nbh),iLoC2H5OH(nbv,nbh),iLoHOCH2CO3
      H(nbv,nbh),iLoRU14OOH(nbv,nbh),iLoRU10OOH(nbv,nbh)
      real::iLoHOC2H4OOH(nbv,nbh),iLoCH3OOH(nbv,nbh),iLoCH3CO3H(nbv,nbh),iLoC
      H3CHO(nbv,nbh),iLoRU14NO3(nbv,nbh),iLoRU12PAN(nbv,nbh)
      real::iPoHONO(nbv,nbh),iPoH2O2(nbv,nbh),iPoH2(nbv,nbh),iPoCO(nbv,nbh),iPoCH
      4(nbv,nbh),iPoC2H4(nbv,nbh),iPoC3H6(nbv,nbh)
      real::iPoCH3OH(nbv,nbh),iPoCH3CO2H(nbv,nbh),iPoCH3CHO(nbv,nbh),iPoUCARB1
      0(nbv,nbh),iPoHCHO(nbv,nbh),iPoHOCH2CHO(nbv,nbh)
      real::iPoHCOOH(nbv,nbh),iPoCARB6(nbv,nbh),iPoUCARB12(nbv,nbh),iPoCARB7(n
      bv,nbh),iPoMPAN(nbv,nbh),iPoRU12PAN(nbv,nbh)
      real::iPoHOC2H4NO3(nbv,nbh),iPoPHAN(nbv,nbh),iPoPAN(nbv,nbh),iPoRU10OOH(
      nbv,nbh),iPoRU12OOH(nbv,nbh),iPoRU14OOH(nbv,nbh)
      real::iPoRU14NO3(nbv,nbh),iPoRN9OOH(nbv,nbh),iPoRN9NO3(nbv,nbh),iPoHOCH
      2CO3H(nbv,nbh),iPoHOC2H4OOH(nbv,nbh),iPoCH3OOH(nbv,nbh)
      real::iPoCH3CO3H(nbv,nbh),iPoOH(nbv,nbh),iPoNO3(nbv,nbh),iPoHO2(nbv,nbh),iL
      oRU14O2(nbv,nbh),iLoRU12O2(nbv,nbh),iLoRU10O2(nbv,nbh)
      real::iLoRN9O2(nbv,nbh),iLoOH(nbv,nbh),iLoNO3(nbv,nbh),iLoHOCH2CO3(nbv,nb
      h),iLoHOCH2CH2O2(nbv,nbh),iLoHO2(nbv,nbh),iLoCH3O2(nbv,nbh)
      real::iLoCH3CO3(nbv,nbh),iPoCH3O2(nbv,nbh),iPoHOCH2CH2O2(nbv,nbh),iPoRN9
      O2(nbv,nbh),iPoRU10O2(nbv,nbh),iPoCH3CO3(nbv,nbh)
      real::iPoRU12O2(nbv,nbh),iPoRU14O2(nbv,nbh),iPoHOCH2CO3(nbv,nbh)!,(nbv,nb
      h),(nbv,nbh),(nbv,nbh),(nbv,nbh),

idtlong = deltaTime;
      counter = 0;
nshort = idtlong/dtchem;
!#*****************************************************************************#
!#************ Declaration initial concentration for chemistry *****************#
!#*****************************************************************************#
      iNO = Carr(:,:,1)
      iNO2 = Carr(:,:,2)
      iNO3 = Carr(:,:,3)
      iO3 = Carr(:,:,4)
      iH2 = Carr(:,:,5)

      iCO = Carr(:,:,6)
      iH2O2 = Carr(:,:,7)
      iHONO = Carr(:,:,8)
      iHNO3 = Carr(:,:,9)
      iHO2NO2 = Carr(:,:,10)

      iCH4 = Carr(:,:,11)
      iC2H4 = Carr(:,:,12)
```

```
iC3H6 = Carr(:,:,13)
iC5H8 = Carr(:,:,14)
iC2H5OH = Carr(:,:,15)

iCH3NO3 = Carr(:,:,16)
iOH =     Carr(:,:,17)
iHO2 = Carr(:,:,18)
iCH3O2 = Carr(:,:,19)
iCH3OH = Carr(:,:,20)

iHOCH2CH2O2 =  Carr(:,:,21)
iCH3CO2H = Carr(:,:,22)
iCH3CHO = Carr(:,:,23)
iRU14O2 = Carr(:,:,24)
iUCARB10 = Carr(:,:,25)

iHCHO = Carr(:,:,26)
iCH3CO3 = Carr(:,:,27)
iHOCH2CHO = Carr(:,:,28)
iRN9O2 = Carr(:,:,29)
iHCOOH = Carr(:,:,30)

iCARB6 = Carr(:,:,31)
iUCARB12 = Carr(:,:,32)
iRU12O2 = Carr(:,:,33)
iCARB7 = Carr(:,:,34)
iRU10O2 = Carr(:,:,35)

iHOC2H4NO3 = Carr(:,:,36)
iRN9NO3 = Carr(:,:,37)
iRU14NO3 = Carr(:,:,38)
iCH3OOH = Carr(:,:,39)
iHOC2H4OOH = Carr(:,:,40)

iRN9OOH =      Carr(:,:,41)
iCH3CO3H = Carr(:,:,42)
iHOCH2CO3H = Carr(:,:,43)
iRU14OOH = Carr(:,:,44)
iRU12OOH = Carr(:,:,45)

iRU10OOH = Carr(:,:,46)
iHOCH2CO3 = Carr(:,:,47)
iPAN = Carr(:,:,48)
```

```
      iPHAN = Carr(:,:,49)
      iRU12PAN = Carr(:,:,50)

      iMPAN = Carr(:,:,51)
!#*****************************************************************************#
!#****************** Declaration for reaction constants *********************#
!#*****************************************************************************#
      ick(:,:,1)=3.40e-6     ! ick1
      ick(:,:,2)=4.01e-4;      ! ick2
      ick(:,:,3)=2.63e-9;      ! ick3
      ick(:,:,4)=6.56e-1;      ! ick4
      ick(:,:,5)=1.72e-3;      ! ick5
      ick(:,:,6)=1.49e-4;      ! ick6
      ick(:,:,7)=5.06e-3;      ! ick7
      ick(:,:,8)=4.21e-2;      ! ick8
      ick(:,:,9)=4.86e-5;      ! ick9
      ick(:,:,10)=2.82e+0;           ! ick10
      ick(:,:,11)=8.74e-2; ! ick11
      ick(:,:,12)=6.92e-2; ! ick12
      ick(:,:,13)=2.54e-1; ! ick13
      ick(:,:,14)=3.08e-1; ! ick14
      ick(:,:,15)=5.01e-1; ! ick15
      ick(:,:,16)=2.27e-1; ! ick16
      ick(:,:,17)=3.59e-2; ! ick17
      ick(:,:,18)=3.74e-2; ! ick18
      ick(:,:,19)=1.20e-1; ! ick19
      ick(:,:,20)=2.58e-2; ! ick20
      ick(:,:,21)=4.08e-3; ! ick21
      ick(:,:,22)=7.11e-6; ! ick22
      ick(:,:,23)=9.20e-3; ! ick23
      ick(:,:,24)=2.34e-2; ! ick24
      ick(:,:,25)=1.83e-1; ! ick25
      ick(:,:,26)=2.02e-3; ! ick26
      ick(:,:,27)=6.30e-7; ! ick27
      ick(:,:,28)=1.39e-4; ! ick28
      ick(:,:,29)=2.00e-1; ! ick29
      ick(:,:,30)=7.19e-1; ! ick30
      ick(:,:,31)=4.46e-9; ! ick31
      ick(:,:,32)=2.99e-8;           ! ick32
      ick(:,:,33)=8.18e-8; ! ick33
      ick(:,:,34)=1.45e-7; ! ick34
      ick(:,:,35)=2.58e+0;           ! ick35
      ick(:,:,36)=7.76e-8; ! ick36
```

```
ick(:,:,37)=2.10e-7; ! ick37
ick(:,:,38)=3.05e-5; ! ick38
ick(:,:,39)=4.61e-5; ! ick39
ick(:,:,40)=5.07e-6;          ! ick40
ick(:,:,41)=2.35e-1; ! ick41
ick(:,:,42)=4.02e-1; ! ick42
ick(:,:,43)=2.31e-2; ! ick43
ick(:,:,44)=7.24e-2; ! ick44
ick(:,:,45)=9.23e-3; ! ick45
ick(:,:,46)=1.13e-2; ! ick46
ick(:,:,47)=2.00e-2; ! ick47
ick(:,:,48)=1.95e-1;          ! ick48
ick(:,:,49)=1.68e-1; ! ick49
ick(:,:,50)=4.84e-2; ! ick50
ick(:,:,51)=2.13e-1; ! ick51
ick(:,:,52)=5.10e-1; ! ick52
ick(:,:,53)=5.10e-1; ! ick53
ick(:,:,54)=4.93e-2; ! ick54
ick(:,:,55)=1.46e-1; ! ick55
ick(:,:,56)=1.52e-1; ! ick56
ick(:,:,57)=6.52e-2; ! ick57
ick(:,:,58)=1.09e-1; ! ick58
ick(:,:,59)=6.52e-2; ! ick59
ick(:,:,60)=4.35e-2; ! ick60
ick(:,:,61)=1.95e-4; ! ick61
ick(:,:,62)=1.09e-3; ! ick62
ick(:,:,63)=4.56e-3; ! ick63
ick(:,:,64)=2.17e-2;          ! ick64
ick(:,:,65)=1.52e-1; ! ick65
ick(:,:,66)=3.62e-1; ! ick66
ick(:,:,67)=3.20e-1; ! ick67
ick(:,:,68)=3.75e-1; ! ick68
ick(:,:,69)=3.75e-1; ! ick69
ick(:,:,70)=4.74e-1; ! ick70
ick(:,:,71)=4.35e-1; ! ick71
ick(:,:,72)=3.85e-1;          ! ick72
ick(:,:,73)=6.22e-3; ! ick73
ick(:,:,74)=6.32e-3; ! ick74
ick(:,:,75)=6.32e-3; ! ick75
ick(:,:,76)=1.12e-2; ! ick76
ick(:,:,77)=2.20e-2; ! ick77
ick(:,:,78)=2.50e-1; ! ick78
ick(:,:,79)=2.50e-1; ! ick79
```

```
ick(:,:,80)=1.08e-2; ! ick80
ick(:,:,81)=3.20e-2; ! ick81
ick(:,:,82)=3.51e-2; ! ick82
ick(:,:,83)=1.50e-2; ! ick83
ick(:,:,84)=2.50e-2; ! ick84
ick(:,:,85)=1.50e-2; ! ick85
ick(:,:,86)=1.00e-2; ! ick86
ick(:,:,87)=3.36e-6; ! ick87
ick(:,:,88)=1.77e-5; ! ick88
ick(:,:,89)=1.62e-5; ! ick89
ick(:,:,90)=1.26e-4; ! ick90
ick(:,:,91)=1.62e-5; ! ick91
ick(:,:,92)=7.51e-2; ! ick92
ick(:,:,93)=6.26e-1; ! ick93
ick(:,:,94)=4.21e-8; ! ick94
ick(:,:,95)=2.93e-8; ! ick95
ick(:,:,96)=2.50e-1; ! ick96
ick(:,:,97)=4.31e-1; ! ick97
ick(:,:,98)=1.13e+0;          ! ick98
ick(:,:,99)=5.35e-7; ! ick99
ick(:,:,100)=6.61e-8;         ! ick100
ick(:,:,101)=8.96e-7;         ! ick101
ick(:,:,102)=9.33e-3;         ! ick102
ick(:,:,103)=2.73e-2;         ! ick103
ick(:,:,104)=3.28e-2;         ! ick104
ick(:,:,105)=1.39e+0;         ! ick105
ick(:,:,106)=5.44e-6;         ! ick106
ick(:,:,107)=5.44e-6;         ! ick107
ick(:,:,108)=5.44e-6;         ! ick108
ick(:,:,109)=1.37e-6;         ! ick109
ick(:,:,110)=4.07e-6;         ! ick110
ick(:,:,111)=5.44e-6;         ! ick111
ick(:,:,112)=5.44e-6;         ! ick112
ick(:,:,113)=5.44e-6;         ! ick113
ick(:,:,114)=5.44e-6;         ! ick114
ick(:,:,115)=9.10e-1;         ! ick115
ick(:,:,116)=4.79e-1;         ! ick116
ick(:,:,117)=9.27e-2;         ! ick117
ick(:,:,118)=1.55e-1;         ! ick118
ick(:,:,119)=1.88e+0;         ! ick119
ick(:,:,120)=7.51e-1;         ! ick120
ick(:,:,121)=7.51e-1;         ! ick121
ick(:,:,122)=5.34e-1;         ! ick122
```

```
      ick(:,:,123)=6.26e-1;          ! ick123
      ick(:,:,124)=2.68e-1;          ! ick124
      ick(:,:,125)=1.51e-4;          ! ick125
      ick(:,:,126)=2.68e-1;          ! ick126
      ick(:,:,127)=1.51e-4;          ! ick127
      ick(:,:,128)=2.59e-3;          ! ick128
      ick(:,:,129)=2.81e-2;          ! ick129
      ick(:,:,130)=1.63e-2;          ! ick130
      ick(:,:,131)=1.51e-4;          ! ick131
      ick(:,:,132)=1.10e-2;          ! ick132
      ick(:,:,133)=1.51e-4;          ! ick133
      ick(:,:,134)=9.02e-2;          ! ick134
      ick(:,:,135)=6.31e-1;          ! ick135
      ick(:,:,136)=7.65E-07          ! ick136

      irk(:,:,1)=6.22e-3     ! irk73
      irk(:,:,2)=6.32e-3     ! irk74
      irk(:,:,3)=6.32e-3     ! irk75
      irk(:,:,4)=1.12e-2     ! irk76
      irk(:,:,5)=2.20e-2     ! irk77
      irk(:,:,6)=2.50e-1     ! irk78
      irk(:,:,7)=2.50e-1     ! irk79
      irk(:,:,8)=1.08e-2     ! irk80
      irk(:,:,9)=3.20e-2     ! irk81
      irk(:,:,10)=3.51e-2    ! irk82
      irk(:,:,11)=1.50e-2    ! irk83
      irk(:,:,12)=2.50e-2    ! irk84
      irk(:,:,13)=1.50e-2    ! irk85
      irk(:,:,14)=1.00e-2    ! irk86

      iRO2                                                                    =
      iCH3O2+iHOCH2CH2O2+iRN9O2+iCH3CO3+iHOCH2CO3+iRU14O2+iRU12O2+iRU
      10 O2
!#*****************************************************************************#
!#          ****************** RO2 permutation reactions *********************#
!#*****************************************************************************#
      ick(:,:,73)  = irk(:,:,1)*iRO2; ick(:,:,74)  = irk(:,:,2)*iRO2; ick(:,:,75)  = irk(:,:,3)*iRO2;
      ick(:,:,76)  = irk(:,:,4)*iRO2;
      ick(:,:,77)  = irk(:,:,5)*iRO2; ick(:,:,78)  = irk(:,:,6)*iRO2; ick(:,:,79)  = irk(:,:,7)*iRO2;
      ick(:,:,80)  = irk(:,:,8)*iRO2;
      ick(:,:,81)  = irk(:,:,9)*iRO2; ick(:,:,82)  = irk(:,:,10)*iRO2; ick(:,:,83)  = irk(:,:,11)*iRO2;
      ick(:,:,84)  = irk(:,:,12)*iRO2;
      ick(:,:,85)  = irk(:,:,13)*iRO2; ick(:,:,86)  = irk(:,:,14)*iRO2;
```

```
!#*****************************************************************************#
!#****************** Calculation of photolysis rates ********************#
!#*****************************************************************************#
!# 0 photolysis reaction 0-0
      ick(:,:,1) = beta*ick(:,:,1);
!# 1 photolysis reaction 1-6
      ick(:,:,22) = beta*ick(:,:,22);ick(:,:,23)=beta*ick(:,:,23);ick(:,:,24)=beta*ick(:,:,24);
      ick(:,:,25) = beta*ick(:,:,25);ick(:,:,26)=beta*ick(:,:,26);ick(:,:,27)=beta*ick(:,:,27);
!# 2 photolysis reaction 7-9
      ick(:,:,38) = beta*ick(:,:,38);ick(:,:,39)=beta*ick(:,:,39);ick(:,:,40)=beta*ick(:,:,40);
!# 3 photolysis reaction 10-14
      ick(:,:,87) = beta*ick(:,:,87);ick(:,:,88)=beta*ick(:,:,88);ick(:,:,89)=beta*ick(:,:,89);
      ick(:,:,90) = beta*ick(:,:,90);ick(:,:,91)=beta*ick(:,:,91);
!# 4 photolysis reaction 15-15
      ick(:,:,101) = beta*ick(:,:,101);
!# 5 photolysis reaction 16-24
      ick(:,:,106)=beta*ick(:,:,106);ick(:,:,107)=beta*ick(:,:,107);ick(:,:,108)=beta*ick(:,:,10
8);
      ick(:,:,109)=beta*ick(:,:,109);ick(:,:,110)=beta*ick(:,:,110);ick(:,:,111)=beta*ick(:,:,11
1);
      ick(:,:,112)=beta*ick(:,:,112);ick(:,:,113)=beta*ick(:,:,113);ick(:,:,114)=beta*ick(:,:,11
4);
!#*****************************************************************************#
!#****************** Calculation of loss & prod terms ********************#
!#*****************************************************************************#
!#         ****************** Calculation of loss terms ********************#
!#*****************************************************************************#
! Solver Species no.1: NO
      iLoNO = ick(:,:,2)*iO3 + 2*ick(:,:,3)*iNO + ick(:,:,4)*iNO3 +
      ick(:,:,13)*iOH+ick(:,:,16)*iHO2 + ick(:,:,48)*iCH3O2 + ick(:,:,49)*iHOCH2CH2O2 +
      ick(:,:,50)*iHOCH2CH2O2 + ick(:,:,51)*iRN9O2 + ick(:,:,52)*iCH3CO3 +
      ick(:,:,53)*iHOCH2CO3 + ick(:,:,54)*iRU14O2 + ick(:,:,55)*iRU14O2 +
      ick(:,:,56)*iRU12O2 + ick(:,:,57)*iRU12O2 + ick(:,:,58)*iRU10O2 +
      ick(:,:,59)*iRU10O2 + ick(:,:,60)*iRU10O2 + ick(:,:,61)*iCH3O2 +
      ick(:,:,62)*iHOCH2CH2O2 + ick(:,:,63)*iRN9O2+ ick(:,:,64)*iRU14O2;
! Solver Species no.2: NO2
      iLoNO2 = ick(:,:,14)*iOH + ick(:,:,17)*iHO2 + ick(:,:,136)*iO3 + ick(:,:,23) +
      ick(:,:,124)*iCH3CO3 + ick(:,:,126)*iHOCH2CO3 + ick(:,:,130)*iRU12O2 +
      ick(:,:,132)*iRU10O2;
! Solver Species no.4: O3
      iLoO3 = ick(:,:,1) + ick(:,:,2)*iNO + ick(:,:,5)*iOH + ick(:,:,9)*iHO2 + ick(:,:,31)*iC2H4
      + ick(:,:,32)*iC2H4 + ick(:,:,33)*iC3H6 + ick(:,:,34)*iC3H6 + ick(:,:,36)*iC5H8 +
      ick(:,:,100)*iUCARB12 + ick(:,:,136)*iNO2;
```

```
! Solver Species no.5: H2
      iLoH2 = ick(:,:,6)*iOH;
! Solver Species no.6: CO
      iLoCO = ick(:,:,7)*iOH;
! Solver Species no.7: H2O2
      iLoH2O2 = ick(:,:,8)*iOH + ick(:,:,22);
! Solver Species no.8: HONO
      iLoHONO = ick(:,:,20)*iOH + ick(:,:,26);
! Solver Species no.9: HNO3
      iLoHNO3 = ick(:,:,21)*iOH + ick(:,:,27);
! Solver Species no.10: HO2NO2
      iLoHO2NO2 = ick(:,:,18) + ick(:,:,19)*iOH;
! Solver Species no.11: CH4
      iLoCH4 = ick(:,:,28)*iOH;
! Solver Species no.12: C2H4
      iLoC2H4 = ick(:,:,29)*iOH + ick(:,:,31)*iO3 + ick(:,:,32)*iO3;
! Solver Species no.13: C3H6
      iLoC3H6 = ick(:,:,30)*iOH + ick(:,:,33)*iO3 + ick(:,:,34)*iO3;
! Solver Species no.14: C5H8
      iLoC5H8 = ick(:,:,35)*iOH + ick(:,:,36)*iO3 + ick(:,:,37)*iO3;
! Solver Species no.15: C2H5OH
      iLoC2H5OH = ick(:,:,44)*iOH + ick(:,:,45)*iOH;
! Solver Species no.16: CH3NO3
      iLoCH3NO3 = ick(:,:,101) + ick(:,:,102)*iOH;
! Solver Species no.20: CH3OH
      iLoCH3OH = ick(:,:,43)*iOH;
! Solver Species no.22: CH3CO2H
      iLoCH3CO2H = ick(:,:,47)*iOH;
! Solver Species no.23: CH3CHO
      iLoCH3CHO = ick(:,:,40) + ick(:,:,42)*iOH;
! Solver Species no.25: UCARB10
      iLoUCARB10 = ick(:,:,89) + ick(:,:,93)*iOH + ick(:,:,94)*iO3 + ick(:,:,95)*iO3;
! Solver Species no.26: HCHO
      iLoHCHO = ick(:,:,38) + ick(:,:,39) + ick(:,:,41)*iOH;
! Solver Species no.28: HOCH2CHO
      iLoHOCH2CHO = ick(:,:,88) + ick(:,:,96)*iOH;
! Solver Species no.30: HCOOH
      iLoHCOOH = ick(:,:,46)*iOH;
! Solver Species no.31: CARB6
      iLoCARB6 = ick(:,:,90) + ick(:,:,97)*iOH;
! Solver Species no.32: UCARB12
      iLoUCARB12 = ick(:,:,91) + ick(:,:,98)*iOH + ick(:,:,99)*iO3 + ick(:,:,100)*iO3;
! Solver Species no.34: CARB7
```

```
      iLoCARB7 = ick(:,:,87) + ick(:,:,92)*iOH;
! Solver Species no.35: RU10O2
!  corrected on 20/07
      iLoRU10O2 = ick(:,:,58)*iNO + ick(:,:,59)*iNO + ick(:,:,60)*iNO + ick(:,:,72)*iHO2 +
      ick(:,:,84) + ick(:,:,85) + ick(:,:,86) + ick(:,:,132)*iNO2;
! Solver Species no.36: HOC2H4NO3
      iLoHOC2H4NO3 = ick(:,:,103)*iOH;
! Solver Species no.37: RN9NO3
      iLoRN9NO3 = ick(:,:,104)*iOH;
! Solver Species no.38: RU14NO3
      iLoRU14NO3 = ick(:,:,105)*iOH;
! Solver Species no.39: CH3OOH
      iLoCH3OOH = ick(:,:,106) + ick(:,:,115)*iOH + ick(:,:,116)*iOH;
! Solver Species no.40: HOC2H4OOH
      iLoHOC2H4OOH = ick(:,:,113) + ick(:,:,122)*iOH;
! Solver Species no.41: RN9OOH
      iLoRN9OOH = ick(:,:,114) + ick(:,:,123)*iOH;
! Solver Species no.42: CH3CO3H
      iLoCH3CO3H = ick(:,:,107) + ick(:,:,117)*iOH;
! Solver Species no.43: HOCH2CO3H
      iLoHOCH2CO3H = ick(:,:,108) + ick(:,:,118)*iOH;
! Solver Species no.44: RU14OOH
      iLoRU14OOH = ick(:,:,109) + ick(:,:,110) + ick(:,:,119)*iOH;
! Solver Species no.45: RU12OOH
      iLoRU12OOH = ick(:,:,111) + ick(:,:,120)*iOH;
! Solver Species no.46: RU10OOH
      iLoRU10OOH = ick(:,:,112) + ick(:,:,121)*iOH;
! Solver Species no.48: PAN
      iLoPAN = ick(:,:,125) + ick(:,:,128)*iOH;
! Solver Species no.49: PHAN
      iLoPHAN = ick(:,:,127) + ick(:,:,129)*iOH;
! Solver Species no.50: RU12PAN
      iLoRU12PAN = ick(:,:,131) + ick(:,:,135)*iOH;
! Solver Species no.51: MPAN
      iLoMPAN = ick(:,:,133) + ick(:,:,134)*iOH;
!#*****************************************************************************#
!#          ****************** Calculation of prod terms *********************#
!#*****************************************************************************#
! solver species no.1: NO
      iPoNO = ick(:,:,23)*iNO2 + ick(:,:,24)*iNO3 + ick(:,:,26)*iHONO;
! solver species no.2: NO2
      iPoNO2 = ick(:,:,2)*iNO*iO3 + 2*ick(:,:,3)*iNO*iNO + 2*ick(:,:,4)*iNO*iNO3 +
      ick(:,:,15)*iOH*iNO3 + ick(:,:,16)*iHO2*iNO + ick(:,:,18)*iHO2NO2 +
```

```
      ick(:,:,19)*iOH*iHO2NO2 + ick(:,:,20)*iOH*iHONO + ick(:,:,25)*iNO3 +
      ick(:,:,27)*iHNO3 + ick(:,:,48)*iCH3O2*iNO + ick(:,:,49)*iHOCH2CH2O2*iNO +
      ick(:,:,50)*iHOCH2CH2O2*iNO + ick(:,:,51)*iRN9O2*iNO + ick(:,:,52)*iCH3CO3*iNO +
      ick(:,:,53)*iHOCH2CO3*iNO + ick(:,:,54)*iRU14O2*iNO + ick(:,:,55)*iRU14O2*iNO +
      ick(:,:,56)*iRU12O2*iNO + ick(:,:,57)*iRU12O2*iNO + ick(:,:,58)*iRU10O2*iNO +
      ick(:,:,59)*iRU10O2*iNO + ick(:,:,60)*iRU10O2*iNO + ick(:,:,101)*iCH3NO3 +
      ick(:,:,102)*iOH*iCH3NO3 + ick(:,:,103)*iOH*iHOC2H4NO3 +
      ick(:,:,104)*iOH*iRN9NO3 + ick(:,:,105)*iOH*iRU14NO3 + ick(:,:,125)*iPAN +
      ick(:,:,127)*iPHAN + ick(:,:,128)*iOH*iPAN + ick(:,:,129)*iOH*iPHAN +
      ick(:,:,131)*iRU12PAN + ick(:,:,133)*iMPAN + ick(:,:,134)*iOH*iMPAN +
      ick(:,:,135)*iOH*iRU12PAN;
! solver species no.4: O3
      iPoO3 = ick(:,:,23)*iNO2 + ick(:,:,25)*iNO3;
! solver species no.5: H2
      iPoH2 = ick(:,:,39)*iHCHO;
! solver species no.6: CO
      iPoCO = ick(:,:,31)*iO3*iC2H4 + ick(:,:,33)*iO3*iC3H6 + ick(:,:,36)*iO3*iC5H8 +
      ick(:,:,38)*iHCHO + ick(:,:,39)*iHCHO + ick(:,:,40)*iCH3CHO + ick(:,:,41)*iOH*iHCHO
      + ick(:,:,57)*iRU12O2*iNO + ick(:,:,88)*iHOCH2CHO + ick(:,:,90)*iCARB6 +
      ick(:,:,91)*iUCARB12 + ick(:,:,94)*iO3*iUCARB10 + ick(:,:,97)*iOH*iCARB6 +
      ick(:,:,99)*iO3*iUCARB12 + ick(:,:,128)*iOH*iPAN + ick(:,:,129)*iOH*iPHAN +
      ick(:,:,134)*iOH*iMPAN;
! solver species no.7: H2O2
      iPoH2O2 = ick(:,:,11)*iHO2*iHO2 + ick(:,:,12)*iHO2*iHO2 +
      ick(:,:,95)*iO3*iUCARB10 + ick(:,:,100)*iO3*iUCARB12;
! solver species no.8: HONO
      iPoHONO = ick(:,:,13)*iOH*iNO;
! solver species no.9: HNO3
      iPoHNO3 = ick(:,:,14)*iOH*iNO2;
! solver species no.10: HO2NO2
      iPoHO2NO2 = ick(:,:,17)*iHO2*iNO2;
! set these units and zero value for the species with no production terms
! solver species no.11: CH4
      iPoCH4 = 0.0
! solver species no.12: C2H4
      iPoC2H4 = 0.0
! solver species no.13: C3H6
      iPoC3H6 =0.0
! solver species no.14: C5H8
      iPoC5H8 = 0.0
! solver species no.15: C2H5OH
      iPoC2H5OH = 0.0
! The end
```

```
! solver species no.16: CH3NO3
    iPoCH3NO3 = ick(:,:,61)*iCH3O2*iNO;
! solver species no.20: CH3OH
    iPoCH3OH = ick(:,:,75)*iCH3O2
! solver species no.22: CH3CO2H
    iPoCH3CO2H = ick(:,:,34)*iO3*iC3H6;
! solver species no.23: CH3CHO
    iPoCH3CHO = ick(:,:,44)*iOH*iC2H5OH + ick(:,:,51)*iRN9O2*iNO +
    ick(:,:,77)*iRN9O2 + ick(:,:,114)*iRN9OOH;
! solver species no.25: UCARB10
    iPoUCARB10 = ick(:,:,36)*iO3*iC5H8 + ick(:,:,37)*iO3*iC5H8 +
    ick(:,:,55)*iRU14O2*iNO + ick(:,:,81)*iRU14O2 + ick(:,:,110)*iRU14OOH +
    ick(:,:,135)*iOH*iRU12PAN;
! solver species no.26: HCHO
    iPoHCHO = ick(:,:,31)*iO3*iC2H4 + ick(:,:,32)*iO3*iC2H4 + ick(:,:,33)*iO3*iC3H6 +
    ick(:,:,34)*iO3*iC3H6 + ick(:,:,43)*iOH*iCH3OH + ick(:,:,48)*iCH3O2*iNO +
    2*ick(:,:,49)*iHOCH2CH2O2*iNO + ick(:,:,51)*iRN9O2*iNO +
    ick(:,:,53)*iHOCH2CO3*iNO + ick(:,:,55)*iRU14O2*iNO + ick(:,:,59)*iRU10O2*iNO +
    ick(:,:,60)*iRU10O2*iNO + ick(:,:,73)*iCH3O2 + ick(:,:,74)*iCH3O2 +
    ick(:,:,77)*iRN9O2 + ick(:,:,79)*iHOCH2CO3 + ick(:,:,81)*iRU14O2 +
    ick(:,:,85)*iRU10O2 + ick(:,:,86)*iRU10O2 + ick(:,:,87)*iCARB7 +
    ick(:,:,88)*iHOCH2CHO + ick(:,:,89)*iUCARB10 + ick(:,:,94)*iO3*iUCARB10 +
    ick(:,:,95)*iO3*iUCARB10 + ick(:,:,101)*iCH3NO3 + ick(:,:,102)*iOH*iCH3NO3 +
    ick(:,:,106)*iCH3OOH + ick(:,:,108)*iHOCH2CO3H + ick(:,:,110)*iRU14OOH +
    2*ick(:,:,113)*iHOC2H4OOH + ick(:,:,114)*iRN9OOH + ick(:,:,116)*iOH*iCH3OOH +
    ick(:,:,128)*iOH*iPAN + ick(:,:,129)*iOH*iPHAN;
! solver species no.28: HOCH2CHO
    iPoHOCH2CHO = ick(:,:,50)*iHOCH2CH2O2*iNO + ick(:,:,56)*iRU12O2*iNO +
    ick(:,:,58)*iRU10O2*iNO + ick(:,:,76)*iHOCH2CH2O2 + ick(:,:,82)*iRU12O2 +
    ick(:,:,83)*iRU12O2 + ick(:,:,84)*iRU10O2 + ick(:,:,91)*iUCARB12 +
    ick(:,:,99)*iO3*iUCARB12 + ick(:,:,100)*iO3*iUCARB12 +
    ick(:,:,103)*iOH*iHOC2H4NO3 + ick(:,:,111)*iRU12OOH + ick(:,:,112)*iRU10OOH +
    ick(:,:,122)*iOH*iHOC2H4OOH;
! solver species no.30: HCOOH
    iPoHCOOH = ick(:,:,32)*iO3*iC2H4 + ick(:,:,37)*iO3*iC5H8;
! solver species no.31: CARB6
    iPoCARB6 = ick(:,:,59)*iRU10O2*iNO + ick(:,:,85)*iRU10O2 + ick(:,:,92)*iOH*iCARB7
    + ick(:,:,95)*iO3*iUCARB10 + ick(:,:,100)*iO3*iUCARB12 + ick(:,:,111)*iRU12OOH;
! solver species no.32: UCARB12
    iPoUCARB12 = ick(:,:,54)*iRU14O2*iNO + ick(:,:,80)*iRU14O2 +
    ick(:,:,105)*iOH*iRU14NO3 + ick(:,:,109)*iRU14OOH + ick(:,:,119)*iOH*iRU14OOH;
! solver species no.34: CARB7
```

```
      iPoCARB7 = ick(:,:,57)*iRU12O2*iNO + ick(:,:,60)*iRU10O2*iNO +
      ick(:,:,83)*iRU12O2 + ick(:,:,86)*iRU10O2 + ick(:,:,104)*iOH*iRN9NO3 +
      ick(:,:,123)*iOH*iRN9OOH + ick(:,:,134)*iOH*iMPAN;
! solver species no.36: HOC2H4NO3
      iPoHOC2H4NO3 = ick(:,:,62)*iHOCH2CH2O2*iNO;
! solver species no.37: RN9NO3
      iPoRN9NO3 = ick(:,:,63)*iRN9O2*iNO;
! solver species no.38: RU14NO3
      iPoRU14NO3 = ick(:,:,64)*iRU14O2*iNO;
! solver species no.39: CH3OOH
      iPoCH3OOH = ick(:,:,65)*iCH3O2*iHO2;
! solver species no.40: HOC2H4OOH
      iPoHOC2H4OOH = ick(:,:,66)*iHOCH2CH2O2*iHO2;
! solver species no.41: RN9OOH
      iPoRN9OOH = ick(:,:,67)*iRN9O2*iHO2;
! solver species no.42: CH3CO3H
      iPoCH3CO3H = ick(:,:,68)*iCH3CO3*iHO2;
! solver species no.43: HOCH2CO3H
      iPoHOCH2CO3H = ick(:,:,69)*iHOCH2CO3*iHO2;
! solver species no.44: RU14OOH
      iPoRU14OOH = ick(:,:,70)*iRU14O2*iHO2;
! solver species no.45: RU12OOH
      iPoRU12OOH = ick(:,:,71)*iRU12O2*iHO2;
! solver species no.46: RU10OOH
      iPoRU10OOH = ick(:,:,72)*iRU10O2*iHO2;
! solver species no.48: PAN
      iPoPAN = ick(:,:,124)*iCH3CO3*iNO2;
! solver species no.49: PHAN
      iPoPHAN = ick(:,:,126)*iHOCH2CO3*iNO2;
! solver species no.50: RU12PAN
      iPoRU12PAN = ick(:,:,130)*iRU12O2*iNO2;
! solver species no.51: MPAN
      iPoMPAN = ick(:,:,132)*iRU10O2*iNO2;
!#*****************************************************************************#
!#****************** Slow reactions ********************#
!#*****************************************************************************#
!# Calculation of the chemical production and loss terms
! Solver Species no.1: NO
      iNO = iNO + (iPoNO - iLoNO*iNO)*idtlong;
! Solver Species no.2: NO2
      iNO2 = iNO2 + (iPoNO2 - iLoNO2*iNO2)*idtlong;
! Solver Species no.4: O3
      iO3 = iO3 + (iPoO3 - iLoO3*iO3)*idtlong;
```

```
! Solver Species no.5: H2
      iH2 = iH2 + (iPoH2 - iLoH2*iH2)*idtlong;
! Solver Species no.6: CO
      iCO = iCO + (iPoCO - iLoCO*iCO)*idtlong;
! Solver Species no.7: H2O2
      iH2O2 = iH2O2 + (iPoH2O2 - iLoH2O2*iH2O2)*idtlong;
! Solver Species no.8: HONO
      iHONO = iHONO + (iPoHONO - iLoHONO*iHONO)*idtlong;
! Solver Species no.9: HNO3
      iHNO3 = iHNO3 + (iPoHNO3 - iLoHNO3*iHNO3)*idtlong;
! Solver Species no.10: HO2NO2
      iHO2NO2 = iHO2NO2 + (iPoHO2NO2 - iLoHO2NO2*iHO2NO2)*idtlong;
! Solver Species no.11: CH4
      iCH4 = iCH4 + (iPoCH4 - iLoCH4*iCH4)*idtlong;
! Solver Species no.12: C2H4
      iC2H4 = iC2H4 + (iPoC2H4 - iLoC2H4*iC2H4)*idtlong;
! Solver Species no.13: C3H6
      iC3H6 = iC3H6 + (iPoC3H6 - iLoC3H6*iC3H6)*idtlong;
! Solver Species no.14: C5H8
      iC5H8 = iC5H8 + (iPoC5H8 - iLoC5H8*iC5H8)*idtlong;
! Solver Species no.15: C2H5OH
      iC2H5OH = iC2H5OH + (iPoC2H5OH - iLoC2H5OH*iC2H5OH)*idtlong;
! Solver Species no.16: CH3NO3
      iCH3NO3 = iCH3NO3 + (iPoCH3NO3 - iLoCH3NO3*iCH3NO3)*idtlong;
! Solver Species no.20: CH3OH
      iCH3OH = iCH3OH + (iPoCH3OH - iLoCH3OH*iCH3OH)*idtlong;
! Solver Species no.22: CH3CO2H
      iCH3CO2H = iCH3CO2H + (iPoCH3CO2H - iLoCH3CO2H*iCH3CO2H)*idtlong;
! Solver Species no.23: CH3CHO
      iCH3CHO = iCH3CHO + (iPoCH3CHO - iLoCH3CHO*iCH3CHO)*idtlong;
! Solver Species no.25: UCARB10
      iUCARB10 = iUCARB10 + (iPoUCARB10 - iLoUCARB10*iUCARB10)*idtlong;
! Solver Species no.26: HCHO
      iHCHO = iHCHO + (iPoHCHO - iLoHCHO*iHCHO)*idtlong;
! Solver Species no.28: HOCH2CHO
      iHOCH2CHO = iHOCH2CHO + (iPoHOCH2CHO -
iLoHOCH2CHO*iHOCH2CHO)*idtlong;
! Solver Species no.30: HCOOH
      iHCOOH = iHCOOH + (iPoHCOOH - iLoHCOOH*iHCOOH)*idtlong;
! Solver Species no.31: CARB6
      iCARB6 = iCARB6 + (iPoCARB6 - iLoCARB6*iCARB6)*idtlong;
! Solver Species no.32: UCARB12
      iUCARB12 = iUCARB12 + (iPoUCARB12 - iLoUCARB12*iUCARB12)*idtlong;
```

```
! Solver Species no.34: CARB7
      iCARB7 = iCARB7 + (iPoCARB7 - iLoCARB7*iCARB7)*idtlong;
! Solver Species no.36: HOC2H4NO3
      iHOC2H4NO3 = iHOC2H4NO3+(iPoHOC2H4NO3-
iLoHOC2H4NO3*iHOC2H4NO3)*idtlong;
! Solver Species no.37: RN9NO3
      iRN9NO3 = iRN9NO3+(iPoRN9NO3-iLoRN9NO3*iRN9NO3)*idtlong;
! Solver Species no.38: RU14NO3
      iRU14NO3 = iRU14NO3+(iPoRU14NO3-iLoRU14NO3*iRU14NO3)*idtlong;
! Solver Species no.39: CH3OOH
      iCH3OOH = iCH3OOH+(iPoCH3OOH-iLoCH3OOH*iCH3OOH)*idtlong;
! Solver Species no.40: HOC2H4OOH
      iHOC2H4OOH = iHOC2H4OOH+(iPoHOC2H4OOH-
iLoHOC2H4OOH*iHOC2H4OOH)*idtlong;
! Solver Species no.41: RN9OOH
      iRN9OOH = iRN9OOH+(iPoRN9OOH-iLoRN9OOH*iRN9OOH)*idtlong;
! Solver Species no.42: CH3CO3H
      iCH3CO3H = iCH3CO3H+(iPoCH3CO3H-iLoCH3CO3H*iCH3CO3H)*idtlong;
! Solver Species no.43: HOCH2CO3H
      iHOCH2CO3H = iHOCH2CO3H+(iPoHOCH2CO3H-
iLoHOCH2CO3H*iHOCH2CO3H)*idtlong;
! Solver Species no.44: RU14OOH
      iRU14OOH = iRU14OOH+(iPoRU14OOH-iLoRU14OOH*iRU14OOH)*idtlong;
! Solver Species no.45: RU12OOH
      iRU12OOH = iRU12OOH+(iPoRU12OOH-iLoRU12OOH*iRU12OOH)*idtlong;
! Solver Species no.46: RU10OOH
      iRU10OOH = iRU10OOH+(iPoRU10OOH-iLoRU10OOH*iRU10OOH)*idtlong;
! Solver Species no.48: PAN
      iPAN = iPAN+(iPoPAN-iLoPAN*iPAN)*idtlong;
! Solver Species no.49: PHAN
      iPHAN = iPHAN+(iPoPHAN-iLoPHAN*iPHAN)*idtlong;
! Solver Species no.50: RU12PAN
      iRU12PAN = iRU12PAN+(iPoRU12PAN-iLoRU12PAN*iRU12PAN)*idtlong;
! Solver Species no.51: MPAN
      iMPAN = iMPAN+(iPoMPAN-iLoMPAN*iMPAN)*idtlong
!#*************************************************************************************
*******#
!#          ****************** Fast reactions ********************#
!#*************************************************************************************
*******#
do while (counter < nshort)
  !#  ****************** calculation of loss term ******************* ##
  ! Solver Species no.3: NO3
```

```
  iLoNO3 = ick(:,:,4)*iNO+ick(:,:,15)*iOH+ick(:,:,24)+ick(:,:,25);
  ! Solver Species no.17: OH
  iLoOH                                                
```

```
  iLoRU12O2                                                                    =
ick(:,:,56)*iNO+ick(:,:,57)*iNO+ick(:,:,71)*iHO2+ick(:,:,82)+ick(:,:,83)+ick(:,:,130)*iNO2;
  ! Solver Species no.35: RU10O2
  iLoRU10O2                                                                    =
ick(:,:,58)*iNO+ick(:,:,59)*iNO+ick(:,:,60)*iNO+ick(:,:,72)*iHO2+ick(:,:,84)+ick(:,:,85)+ick
(:,:,86)+ick(:,:,132)*iNO2;
  ! Solver Species no.47: HOCH2CO3
  iLoHOCH2CO3 = ick(:,:,53)*iNO+ick(:,:,69)*iHO2+ick(:,:,79)+ick(:,:,126)*iNO2;

  !#  ****************** calculation of production term ******************* ##
  ! solver species no.3: NO3
  iPoNO3=ick(:,:,21)*iOH*iHNO3+ick(:,:,136)*iNO2*iO3
  ! solver species no.17: OH
  iPoOH = 2*ick(:,:,1)*iO3+ick(:,:,9)*iHO2*iO3+ick(:,:,16)*iHO2*iNO+2* &

ick(:,:,22)*iH2O2+ick(:,:,26)*iHONO+ick(:,:,27)*iHNO3+ick(:,:,31)*iO3*iC2H4+ick(:,:,33)*
iO3*iC3H6+ &
  ick(:,:,36)*iO3*iC5H8+ick(:,:,94)*iO3*iUCARB10+ &
  ick(:,:,99)*iO3*iUCARB12+ick(:,:,106)*iCH3OOH+ick(:,:,107)*iCH3CO3H+ &

ick(:,:,108)*iHOCH2CO3H+ick(:,:,109)*iRU14OOH+ick(:,:,110)*iRU14OOH+ick(:,:,111)*i
RU12OOH+ick(:,:,112)*iRU10OOH+ick(:,:,113)*iHOC2H4OOH+ick(:,:,114)*iRN9OOH+ick
(:,:,116)*iOH*iCH3OOH+ &

ick(:,:,119)*iOH*iRU14OOH+ick(:,:,122)*iOH*iHOC2H4OOH+ick(:,:,123)*iOH*iRN9OOH;

! solver species no.18: HO2
    iPoHO2 = ick(:,:,5)*iOH*iO3 + ick(:,:,6)*iOH*iH2 + ick(:,:,7)*iOH*iCO +
    ick(:,:,8)*iOH*iH2O2 + ick(:,:,15)*iOH*iNO3 + ick(:,:,18)*iHO2NO2 +
    ick(:,:,31)*iO3*iC2H4 + ick(:,:,36)*iO3*iC5H8 + 2*ick(:,:,38)*iHCHO +
    ick(:,:,40)*iCH3CHO + ick(:,:,41)*iOH*iHCHO + ick(:,:,43)*iOH*iCH3OH +
    ick(:,:,44)*iOH*iC2H5OH + ick(:,:,46)*iHCOOH*iOH + ick(:,:,48)*iCH3O2*iNO +
    ick(:,:,49)*iHOCH2CH2O2*iNO + ick(:,:,50)*iHOCH2CH2O2*iNO +
    ick(:,:,51)*iRN9O2*iNO + ick(:,:,53)*iHOCH2CO3*iNO + ick(:,:,54)*iRU14O2*iNO +
    ick(:,:,55)*iRU14O2*iNO + ick(:,:,57)*iRU12O2*iNO + ick(:,:,59)*iRU10O2*iNO +
    ick(:,:,60)*iRU10O2*iNO + ick(:,:,73)*iCH3O2 + ick(:,:,76)*iHOCH2CH2O2 +
    ick(:,:,77)*iRN9O2 + ick(:,:,79)*iHOCH2CO3 + ick(:,:,80)*iRU14O2 +
    ick(:,:,81)*iRU14O2 + ick(:,:,83)*iRU12O2 + ick(:,:,85)*iRU10O2 +
    ick(:,:,86)*iRU10O2 + ick(:,:,87)*iCARB7 + 2*ick(:,:,88)*iHOCH2CHO +
    ick(:,:,89)*iUCARB10 + ick(:,:,90)*iCARB6 + ick(:,:,91)*iUCARB12 +
    ick(:,:,92)*iOH*iCARB7 + ick(:,:,101)*iCH3NO3 + ick(:,:,106)*iCH3OOH +
    ick(:,:,108)*iHOCH2CO3H + ick(:,:,109)*iRU14OOH + ick(:,:,110)*iRU14OOH +
    ick(:,:,111)*iRU12OOH+ick(:,:,113)*iHOC2H4OOH+ick(:,:,114)*iRN9OOH;
```

```
! solver species no.19: CH3O2
    iPoCH3O2 = ick(:,:,28)*iOH*iCH4 + ick(:,:,33)*iO3*iC3H6 + ick(:,:,40)*iCH3CHO +
    ick(:,:,47)*iCH3CO2H*iOH + ick(:,:,52)*iCH3CO3*iNO + ick(:,:,78)*iCH3CO3 +
    ick(:,:,107)*iCH3CO3H + ick(:,:,115)*iOH*iCH3OOH;
!solver species no.21: HOCH2CH2O2
    iPoHOCH2CH2O2 = ick(:,:,29)*iOH*iC2H4 + ick(:,:,45)*iOH*iC2H5OH;
! solver species no.24: RU14O2
    iPoRU14O2 = ick(:,:,35)*iOH*iC5H8;
! solver species no.27: CH3CO3
    iPoCH3CO3 = ick(:,:,42)*iOH*iCH3CHO + ick(:,:,56)*iRU12O2*iNO +
    ick(:,:,58)*iRU10O2*iNO + ick(:,:,82)*iRU12O2 + ick(:,:,84)*iRU10O2 +
    ick(:,:,87)*iCARB7 + ick(:,:,89)*iUCARB10 + ick(:,:,90)*iCARB6 +
    ick(:,:,91)*iUCARB12 + ick(:,:,94)*iO3*iUCARB10 + ick(:,:,97)*iOH*iCARB6 +
    ick(:,:,99)*iO3*iUCARB12 + ick(:,:,112)*iRU10OOH + ick(:,:,117)*iOH*iCH3CO3H +
    ick(:,:,125)*iPAN;
! solver species no.29: RN9O2
    iPoRN9O2 = ick(:,:,30)*iOH*iC3H6;
! solver species no.33: RU12O2
    iPoRU12O2 = ick(:,:,98)*iOH*iUCARB12 + ick(:,:,120)*iOH*iRU12OOH +
    ick(:,:,131)*iRU12PAN;
! solver species no.35: RU10O2
    iPoRU10O2 = ick(:,:,93)*iOH*iUCARB10 + ick(:,:,121)*iOH*iRU10OOH +
ick(:,:,133)*iMPAN;
! solver species no.47: HOCH2CO3
    iPoHOCH2CO3 = ick(:,:,96)*iOH*iHOCH2CHO + ick(:,:,118)*iOH*iHOCH2CO3H +
    ick(:,:,127)*iPHAN;
!#*****************************************************************************
*******#
!#          ****************** Calculation of fast chemistry *********************#
!#*****************************************************************************
*******#
! Solver Species no.3: NO3
    iNO3 = iPoNO3/iLoNO3 + (iNO3-iPoNO3/iLoNO3)/(1 + dtchem*iLoNO3 +
    0.5*dtchem*dtchem*iLoNO3*iLoNO3);
! Solver Species no.17: OH
    iOH = iPoOH/iLoOH + (iOH-iPoOH/iLoOH)/(1 + dtchem*iLoOH +
    0.5*dtchem*dtchem*iLoOH*iLoOH);
! Solver Species no.18: HO2
    iHO2 = iPoHO2/iLoHO2 + (iHO2-iPoHO2/iLoHO2)/(1 + dtchem*iLoHO2 +
    0.5*dtchem*dtchem*iLoHO2*iLoHO2);
! Solver Species no.19: CH3O2
```

```
      iCH3O2 = iPoCH3O2/iLoCH3O2 + (iCH3O2-iPoCH3O2/iLoCH3O2)/(1 +
      dtchem*iLoCH3O2 + 0.5*dtchem*dtchem*iLoCH3O2*iLoCH3O2);
! Solver Species no.21: HOCH2CH2O2
      iHOCH2CH2O2 = iPoHOCH2CH2O2/iLoHOCH2CH2O2 + (iHOCH2CH2O2-
      iPoHOCH2CH2O2/iLoHOCH2CH2O2)/(1 + dtchem*iLoHOCH2CH2O2 +
      0.5*dtchem*dtchem*iLoHOCH2CH2O2*iLoHOCH2CH2O2);
! Solver Species no.24: RU14O2
      iRU14O2 = iPoRU14O2/iLoRU14O2 + (iRU14O2-iPoRU14O2/iLoRU14O2)/(1 +
      dtchem*iLoRU14O2 + 0.5*dtchem*dtchem*iLoRU14O2*iLoRU14O2);
! Solver Species no.27: CH3CO3
      iCH3CO3 = iPoCH3CO3/iLoCH3CO3 + (iCH3CO3-iPoCH3CO3/iLoCH3CO3)/(1 +
      dtchem*iLoCH3CO3 + 0.5*dtchem*dtchem*iLoCH3CO3*iLoCH3CO3);
! Solver Species no.29: RN9O2
      iRN9O2 = iPoRN9O2/iLoRN9O2 + (iRN9O2-iPoRN9O2/iLoRN9O2)/(1 +
      dtchem*iLoRN9O2 + 0.5*dtchem*dtchem*iLoRN9O2*iLoRN9O2);
! Solver Species no.33: RU12O2
      iRU12O2 = iPoRU12O2/iLoRU12O2 + (iRU12O2-iPoRU12O2/iLoRU12O2)/(1 +
      dtchem*iLoRU12O2 + 0.5*dtchem*dtchem*iLoRU12O2*iLoRU12O2);
! Solver Species no.35: RU10O2
      iRU10O2 = iPoRU10O2/iLoRU10O2 + (iRU10O2-iPoRU10O2/iLoRU10O2)/(1 +
      dtchem*iLoRU10O2 + 0.5*dtchem*dtchem*iLoRU10O2*iLoRU10O2);
! Solver Species no.47: HOCH2CO3
      iHOCH2CO3 = iPoHOCH2CO3/iLoHOCH2CO3 + (iHOCH2CO3-
      iPoHOCH2CO3/iLoHOCH2CO3)/(1 + dtchem*iLoHOCH2CO3 +
      0.5*dtchem*dtchem*iLoHOCH2CO3*iLoHOCH2CO3);
  counter = counter + 1
enddo
!#**************************************************************************************
*******#
!#          ****************** Chemical outputs *********************#
!#**************************************************************************************
*******#
! Initial species NO 01-10
      Carr(:,:,1) = iNO;
      Carr(:,:,2) = iNO2;
      Carr(:,:,3) = iNO3;
      Carr(:,:,4) = iO3;
      Carr(:,:,5) = iH2;

      Carr(:,:,6) = iCO;
      Carr(:,:,7) = iH2O2;
      Carr(:,:,8) = iHONO;
      Carr(:,:,9) = iHNO3;
```

```
Carr(:,:,10) = iHO2NO2;
! Initial species NO 11-20
Carr(:,:,11) = iCH4;
Carr(:,:,12) = iC2H4;
Carr(:,:,13) = iC3H6;
Carr(:,:,14) = iC5H8;
Carr(:,:,15) = iC2H5OH;

Carr(:,:,16) = iCH3NO3;
Carr(:,:,17) = iOH;
Carr(:,:,18) = iHO2;
Carr(:,:,19) = iCH3O2;
Carr(:,:,20) = iCH3OH;
! Initial species NO 21-30
Carr(:,:,21) = iHOCH2CH2O2;
Carr(:,:,22) = iCH3CO2H;
Carr(:,:,23) = iCH3CHO;
Carr(:,:,24) = iRU14O2;
Carr(:,:,25) = iUCARB10;

Carr(:,:,26) = iHCHO;
Carr(:,:,27) = iCH3CO3;
Carr(:,:,28) = iHOCH2CHO;
Carr(:,:,29) = iRN9O2;
Carr(:,:,30) = iHCOOH;
! Initial species NO 31-40
Carr(:,:,31) = iCARB6;
Carr(:,:,32) = iUCARB12;
Carr(:,:,33) = iRU12O2;
Carr(:,:,34) = iCARB7;
Carr(:,:,35) = iRU10O2;

Carr(:,:,36) = iHOC2H4NO3;
Carr(:,:,37) = iRN9NO3;
Carr(:,:,38) = iRU14NO3;
Carr(:,:,39) = iCH3OOH;
Carr(:,:,40) = iHOC2H4OOH;
! Initial species NO 41-51
Carr(:,:,41) = iRN9OOH;
Carr(:,:,42) = iCH3CO3H;
Carr(:,:,43) = iHOCH2CO3H;
Carr(:,:,44) = iRU14OOH;
Carr(:,:,45) = iRU12OOH;
```

```
      Carr(:,:,46) = iRU10OOH;
      Carr(:,:,47) = iHOCH2CO3;
      Carr(:,:,48) = iPAN;
      Carr(:,:,49) = iPHAN;
      Carr(:,:,50) = iRU12PAN;

      Carr(:,:,51) = iMPAN
return
end subroutine
!#*****************************************************************************************
*******#
!#         ****************** Dynamical module ********************#
!#*****************************************************************************************
*******#
subroutine exclock(u,w,UU,WW,Carr,cBgarr,h,l,deltaTime, NoS)
use globalValue
implicit none
      real::u(nbv+1,nbh),w(nbv+1,nbh),UU(nbv+1,nbh),WW(nbv+1,nbh),Carr(nbv,nbh,N
      umspe),cBgarr(Numspe),h(nbv),l(nbh)
      real::k1(nbv,nbh),k2(nbv,nbh),k3(nbv,nbh),k4(nbv,nbh)
      real::deltaTime
      integer::NoS,i,k
!# this programme uses Rugge-Kutta solve the matrix ODEs
!# Carr: solution in matrix
!# output: Carr(kbox,ibox,Species)
!# e.g. Carr(1,1,1) refers to concentrations of 1st species(NO) in Box(1,1)
!# fw: vertical fluxes
!# fu: horizontal fluxes
!# residual: should be 0 for a correct solution
!# solve ODEs via runge-kutta forth-order equations
      k = 1; i = 1;NoS = 1
      k1 = 0.0; k2 = 0.0;
      k3 = 0.0; k4 = 0.0;
do NoS=1,Numspe
!#*****************************************************************************************
*******#
!#         ****************** Runge-Kutta ********************#
!#*****************************************************************************************
*******#
!# 1st order EQ
!# Equation for corner position
```

```
k1(1,1) = -(0.5*(sign(1.0,WW(2,1)) + 1)*WW(2,1)*Carr(1,1,NoS) + 0.5*(1-
sign(1.0,WW(2,1)))*WW(2,1)*Carr(2,1,NoS))/h(1) - (w(2,1)*(Carr(1,1,NoS) -
Carr(2,1,NoS)))/h(1) - (0.5*(sign(1.0,UU(1,2)) + 1)*UU(1,2)*Carr(1,1,NoS) + 0.5*(1 -
sign(1.0,UU(1,2)))*UU(1,2)*Carr(1,2,NoS))/l(1) - (u(1,2)*(Carr(1,1,NoS) -
Carr(1,2,NoS)))/l(1)

k1(nbv,1) = (0.5*(sign(1.0,WW(nbv,1)) + 1)*WW(nbv,1)*Carr(nbv - 1,1,NoS) +
0.5*(1 - sign(1.0,WW(nbv,1)))*WW(nbv,1)*Carr(nbv,1,NoS))/h(nbv) +
(w(nbv,1)*(Carr(nbv - 1,1,NoS) - Carr(nbv,1,NoS)))/h(nbv) - (w(nbv +
1,1)*(Carr(nbv,1,NoS) - cBgarr(NoS)))/h(nbv) - (0.5*(sign(1.0,UU(nbv,2)) +
1)*UU(nbv,2)*Carr(nbv,1,NoS) + 0.5*(1 -
sign(1.0,UU(nbv,2)))*UU(nbv,2)*Carr(nbv,2,NoS))/l(1) -
(u(nbv,2)*(Carr(nbv,1,NoS) - Carr(nbv,2,NoS)))/l(1)

k1(1,nbh) = - (0.5*(sign(1.0,WW(2,nbh)) + 1)*WW(2,nbh)*Carr(1,nbh,NoS) + 0.5*(1
- sign(1.0,WW(2,nbh)))*WW(2,nbh)*Carr(2,nbh,NoS))/h(1) -
(w(2,nbh)*(Carr(1,nbh,NoS) - Carr(2,nbh,NoS)))/h(1) + (0.5*(sign(1.0,UU(1,nbh)) +
1)*UU(1,nbh)*Carr(1,nbh - 1,NoS) + 0.5*(1 -
sign(1.0,UU(1,nbh)))*UU(1,nbh)*Carr(1,nbh,NoS))/l(nbh) + (u(1,nbh)*(Carr(1,nbh -
1,NoS) - Carr(1,nbh,NoS)))/l(nbh)

k1(nbv,nbh) = (0.5*(sign(1.0,WW(nbv,nbh)) + 1)*WW(nbv,nbh)*Carr(nbv -
1,nbh,NoS) + 0.5*(1 -
sign(1.0,WW(nbv,nbh)))*WW(nbv,nbh)*Carr(nbv,nbh,NoS))/h(nbv) +
(w(nbv,nbh)*(Carr(nbv - 1,nbh,NoS) - Carr(nbv,nbh,NoS)))/h(nbv) - (w(nbv +
1,nbh)*(Carr(nbv,nbh,NoS) - cBgarr(NoS)))/h(nbv) + (0.5*(sign(1.0,UU(nbv,nbh)) +
1)*UU(nbv,nbh)*Carr(nbv,nbh - 1,NoS) + 0.5*(1 - sign(1.0,UU(nbv,nbh)))*
UU(nbv,nbh)*Carr(nbv,nbh,NoS))/l(nbh) + (u(nbv,nbh)*(Carr(nbv,nbh - 1,NoS) -
Carr(nbv,nbh,NoS)))/l(nbh)
!# Equation for edge i.e. ground or walls...
if (nbv>2)Then
!# for wall
    do k=2,nbv – 1
    k1(k,1) = (0.5*(sign(1.0,WW(k,1)) + 1)*WW(k,1)*Carr(k - 1,1,NoS) + 0.5*(1 -
    sign(1.0,WW(k,1)))*WW(k,1)*Carr(k,1,NoS))/h(k) + (w(k,1)*(Carr(k - 1,1,NoS) -
    Carr(k,1,NoS)))/h(k) - (0.5*(sign(1.0,WW(k + 1,1)) + 1)*WW(k + 1,1)*Carr(k,1,NoS)
    + 0.5*(1 - sign(1.0,WW(k + 1,1)))*WW(k + 1,1)*Carr(k + 1,1,NoS))/h(k) - (w(k +
    1,1)*(Carr(k,1,NoS) - Carr(k + 1,1,NoS)))/h(k) - (0.5*(sign(1.0,UU(k,2)) +
    1)*UU(k,2)*Carr(k,1,NoS) + 0.5*(1 - sign(1.0,UU(k,2)))*UU(k,2)*Carr(k,2,NoS))/l(1)
    - (u(k,2)*(Carr(k,1,NoS) - Carr(k,2,NoS)))/l(1)

    k1(k,nbh) = (0.5*(sign(1.0,WW(k,nbh)) + 1)*WW(k,nbh)*Carr(k - 1,nbh,NoS) +
    0.5*(1 - sign(1.0,WW(k,nbh)))*WW(k,nbh)*Carr(k,nbh,NoS))/h(2) +
```

```
      (w(k,nbh)*(Carr(k - 1,nbh,NoS) - Carr(k,nbh,NoS)))/h(k) - (0.5*(sign(1.0,WW(k +
      1,nbh)) + 1)*WW(k + 1,nbh)*Carr(k,nbh,NoS) + 0.5*(1 - sign(1.0,WW(k +
      1,nbh)))*WW(k + 1,nbh)*Carr(k + 1,nbh,NoS))/h(k) - (w(k + 1,nbh)*
      (Carr(k,nbh,NoS) - Carr(k + 1,nbh,NoS)))/h(k) + (0.5*(sign(1.0,UU(k,nbh)) +
      1)*UU(k,nbh)*Carr(k,nbh - 1,NoS) + 0.5*(1 -
      sign(1.0,UU(k,nbh)))*UU(k,nbh)*Carr(k,nbh,NoS))/l(nbh) + (u(k,nbh)*(Carr(k,nbh -
      1,NoS) - Carr(k,nbh,NoS)))/l(nbh)
    enddo
  endif
if (nbh>2)Then
!# for ground and rooftop
do i=2,nbh - 1
      k1(1,i) = - (0.5*(sign(1.0,WW(2,i)) + 1)*WW(2,i)*Carr(1,i,NoS) + 0.5*(1 -
      sign(1.0,WW(2,i)))*WW(2,i)*Carr(2,i,NoS))/h(1) - (w(2,i)*(Carr(1,i,NoS) -
      Carr(2,i,NoS)))/h(1) + (0.5* (sign(1.0,UU(1,i)) + 1)*UU(1,i)*Carr(1,i - 1,NoS) + 0.5*(1
      - sign(1.0,UU(1,i)))*UU(1,i)*Carr(1,i,NoS))/l(i) + (u(1,i)*(Carr(1,i - 1,NoS) -
      Carr(1,i,NoS)))/l(i) - (0.5*(sign(1.0,UU(1,i + 1)) + 1)*UU(1,i + 1)*Carr(1,i,NoS) +
      0.5*(1 - sign(1.0,UU(1,i + 1)))*UU(1,i + 1)*Carr(1,i + 1,NoS))/l(i) - (u(1,i +
      1)*(Carr(1,i,NoS) - Carr(1,i + 1,NoS)))/l(i)

      k1(nbv,i) = (0.5*(sign(1.0,WW(nbv,i)) + 1)*WW(nbv,i)*Carr(nbv - 1,i,NoS) + 0.5*(1 -
      sign(1.0,WW(nbv,i)))*WW(nbv,i)*Carr(nbv,i,NoS))/h(nbv) + (w(nbv,i)*(Carr(nbv -
      1,i,NoS) - Carr(nbv,i,NoS)))/ h(nbv) - (w(nbv + 1,i)*(Carr(nbv,i,NoS) -
      cBgarr(NoS)))/h(nbv) + (0.5*(sign(1.0,UU(nbv,i)) + 1)*UU(nbv,i)*Carr(nbv,i - 1,NoS)
      + 0.5*(1 - sign(1.0,UU(nbv,i)))*UU(nbv,i)*Carr(nbv,i,NoS))/l(i) +
      (u(nbv,i)*(Carr(nbv,i - 1,NoS) - Carr(nbv,i,NoS)))/l(i) - (0.5*(sign(1.0,UU(nbv,i + 1))
      + 1)*UU(nbv,i + 1)*Carr(nbv,i,NoS) + 0.5*(1 - sign(1.0,UU(nbv,i + 1)))*UU(nbv,i +
      1)*Carr(nbv,i + 1,NoS))/ l(i) - (u(nbv,i + 1)*(Carr(nbv,i,NoS) - Carr(nbv,i +
      1,NoS)))/l(i)
      enddo
endif
if(nbv>2 .and. nbh>2)Then
!## Equation for in - canyon box
      do k=2,nbv - 1
            do i=2,nbh - 1
k1(k,i) = (0.5*(sign(1.0,WW(k,i)) + 1)*WW(k,i)*Carr(k - 1,i,NoS) + 0.5*(1 -
sign(1.0,WW(k,i)))*WW(k,i)*Carr(k,i,NoS))/h(k) + (w(k,i)*(Carr(k - 1,i,NoS) -
Carr(k,i,NoS)))/h(k) - (0.5*(sign(1.0,WW(k + 1,i)) + 1)*WW(k + 1,i)*Carr(k,i,NoS) + 0.5*(1
- sign(1.0,WW(k + 1,i)))*WW(k + 1,i)*Carr(k + 1,i,NoS))/h(k) - (w(k + 1,i)*(Carr(k,i,NoS)
- Carr(k + 1,i,NoS)))/h(k) + (0.5*(sign(1.0,UU(k,i)) + 1)*UU(k,i)*Carr(k,i - 1,NoS) + 0.5*(1
- sign(1.0,UU(k,i)))*UU(k,i)*Carr(k,i,NoS))/l(i) + (u(k,i)*(Carr(k,i - 1,NoS) -
Carr(k,i,NoS)))/l(i) - (0.5*(sign(1.0,UU(k,i + 1)) + 1)*UU(k,i + 1)*Carr(k,i,NoS) + 0.5* (1 -
```

```
sign(1.0,UU(k,i + 1)))*UU(k,i + 1)*Carr(k,i + 1,NoS))/l(i) - (u(k,i + 1)*(Carr(k,i,NoS) -
Carr(k,i + 1,NoS)))/l(i)
enddo
    enddo
        endif
!# 2nd order EQ
!# Equation for corner position
    k2(1,1) = - (0.5*(sign(1.0,WW(2,1)) + 1)*WW(2,1)*(Carr(1,1,NoS) +
    deltaTime*k1(1,1)/2) + 0.5*(1 - sign(1.0,WW(2,1)))*WW(2,1)*Carr(2,1,NoS))/h(1)
    - (w(2,1)*((Carr(1,1,NoS) + deltaTime*k1(1,1)/2) - Carr(2,1,NoS)))/h(1) -
    (0.5*(sign(1.0,UU(1,2)) + 1)*UU(1,2)*(Carr(1,1,NoS) + deltaTime*k1(1,1)/2) +
    0.5*(1 - sign(1.0,UU(1,2)))*UU(1,2)*Carr(1,2,NoS))/l(1) - (u(1,2)*((Carr(1,1,NoS) +
    deltaTime*k1(1,1)/2) - Carr(1,2,NoS)))/l(1)

    k2(nbv,1) = (0.5*(sign(1.0,WW(nbv,1)) + 1)*WW(nbv,1)*Carr(nbv - 1,1,NoS) +
    0.5*(1 - sign(1.0,WW(nbv,1)))*WW(nbv,1)*(Carr(nbv,1,NoS) +
    deltaTime*k1(nbv,1)/2))/h(nbv) + (w(nbv,1)*(Carr(nbv - 1,1,NoS) -
    (Carr(nbv,1,NoS) + deltaTime*k1(nbv,1)/2)))/h(nbv) - (w(nbv +
    1,1)*((Carr(nbv,1,NoS) + deltaTime*k1(nbv,1)/2) - cBgarr(NoS)))/h(nbv) -
    (0.5*(sign(1.0,UU(nbv,2)) + 1)*UU(nbv,2)*(Carr(nbv,1,NoS) +
    deltaTime*k1(nbv,1)/2) + 0.5*(1 -
    sign(1.0,UU(nbv,2)))*UU(nbv,2)*Carr(nbv,2,NoS))/l(1) -
    (u(nbv,2)*((Carr(nbv,1,NoS) + deltaTime*k1(nbv,1)/2) - Carr(nbv,2,NoS)))/l(1)

    k2(1,nbh) = - (0.5*(sign(1.0,WW(2,nbh)) + 1)*WW(2,nbh)*(Carr(1,nbh,NoS) +
    deltaTime*k1(1,nbh)/2) + 0.5*(1 -
    sign(1.0,WW(2,nbh)))*WW(2,nbh)*Carr(2,nbh,NoS))/h(1) -
    (w(2,nbh)*((Carr(1,nbh,NoS) + deltaTime*k1(1,nbh)/2) - Carr(2,nbh,NoS)))/h(1) +
    (0.5*(sign(1.0,UU(1,nbh)) + 1)*UU(1,nbh)*Carr(1,nbh - 1,NoS) + 0.5*(1 -
    sign(1.0,UU(1,nbh)))*UU(1,nbh)*(Carr(1,nbh,NoS) + deltaTime*k1(1,nbh)/2))/
    l(nbh) + (u(1,nbh)*(Carr(1,nbh - 1,NoS) - (Carr(1,nbh,NoS) +
    deltaTime*k1(1,nbh)/2)))/l(nbh)

    k2(nbv,nbh) = (0.5*(sign(1.0,WW(nbv,nbh)) + 1)*WW(nbv,nbh)*Carr(nbv -
    1,nbh,NoS) + 0.5*(1 - sign(1.0,WW(nbv,nbh)))*WW(nbv,nbh)*(Carr(nbv,nbh,NoS) +
    deltaTime*k1(nbv,nbh)/2))/h(nbv) + (w(nbv,nbh)* (Carr(nbv - 1,nbh,NoS) -
    (Carr(nbv,nbh,NoS) + deltaTime*k1(nbv,nbh)/2)))/h(nbv) - (w(nbv +
    1,nbh)*((Carr(nbv,nbh,NoS) + deltaTime*k1(nbv,nbh)/2) - cBgarr(NoS)))/h(nbv) +
    (0.5*(sign(1.0,UU(nbv,nbh)) + 1)*UU(nbv,nbh)*Carr(nbv,nbh - 1,NoS) + 0.5*(1 -
    sign(1.0,UU(nbv,nbh)))*UU(nbv,nbh)*(Carr(nbv,nbh,NoS) +
    deltaTime*k1(nbv,nbh)/2))/l(nbh) + (u(nbv,nbh)*(Carr(nbv,nbh - 1,NoS) -
    (Carr(nbv,nbh,NoS) + deltaTime*k1(nbv,nbh)/2)))/l(nbh)
!# Equation for edge i.e. ground or walls...
```

```
if (nbv>2)Then
!# for wall
do k=2,nbv - 1
    k2(k,1) = (0.5*(sign(1.0,WW(k,1)) + 1)*WW(k,1)*Carr(k - 1,1,NoS) + 0.5*(1 -
    sign(1.0,WW(k,1)))*WW(k,1)*(Carr(k,1,NoS) + deltaTime*k1(k,1)/2))/h(k) +
    (w(k,1)*(Carr(k - 1,1,NoS) - (Carr(k,1,NoS) + deltaTime*k1(k,1)/2)))/h(k) -
    (0.5*(sign(1.0,WW(k + 1,1)) + 1)*WW(k + 1,1)*(Carr(k,1,NoS) +
    deltaTime*k1(k,1)/2) + 0.5*(1 - sign(1.0,WW(k + 1,1)))*WW(k + 1,1)*Carr(k +
    1,1,NoS))/h(k) - (w(k + 1,1)*((Carr(k,1,NoS) + deltaTime*k1(k,1)/2) - Carr(k +
    1,1,NoS)))/h(k) - (0.5*(sign(1.0,UU(k,2)) + 1)*UU(k,2)*(Carr(k,1,NoS) +
    deltaTime*k1(k,1)/2) + 0.5*(1 - sign(1.0,UU(k,2)))*UU(k,2)*Carr(k,2,NoS))/l(1) -
    (u(k,2)*((Carr(k,1,NoS) + deltaTime*k1(k,1)/2) - Carr(k,2,NoS)))/l(1)

    k2(k,nbh) = (0.5*(sign(1.0,WW(k,nbh)) + 1)*WW(k,nbh)*Carr(k - 1,nbh,NoS) +
    0.5*(1 - sign(1.0,WW(k,nbh)))*WW(k,nbh)*(Carr(k,nbh,NoS) +
    deltaTime*k1(k,nbh)/2))/h(2) + (w(k,nbh)*(Carr(k - 1,nbh,NoS) - (Carr(k,nbh,NoS)
    + deltaTime*k1(k,nbh)/2)))/h(k) - (0.5*(sign(1.0,WW(k + 1,nbh)) + 1)*WW(k +
    1,nbh)*(Carr(k,nbh,NoS) + deltaTime*k1(k,nbh)/2) + 0.5*(1 - sign(1.0,WW(k +
    1,nbh)))*WW(k + 1,nbh)*Carr(k + 1,nbh,NoS))/h(k) - (w(k +
    1,nbh)*((Carr(k,nbh,NoS) + deltaTime*k1(k,nbh)/2) - Carr(k + 1,nbh,NoS)))/h(k) +
    (0.5*(sign(1.0,UU(k,nbh)) + 1)*UU(k,nbh)*Carr(k,nbh - 1,NoS) + 0.5*(1 -
    sign(1.0,UU(k,nbh)))*UU(k,nbh)*(Carr(k,nbh,NoS) +
    deltaTime*k1(k,nbh)/2))/l(nbh) + (u(k,nbh)*(Carr(k,nbh - 1,NoS) -
    (Carr(k,nbh,NoS) + deltaTime*k1(k,nbh)/2)))/l(nbh)
    enddo
endif
if(nbh>2)Then
!# for ground and rooftop
    do i=2,nbh - 1
    k2(1,i) = - (0.5*(sign(1.0,WW(2,i)) + 1)*WW(2,i)*(Carr(1,i,NoS) +
    deltaTime*k1(1,i)/2) + 0.5*(1 - sign(1.0,WW(2,i)))*WW(2,i)*Carr(2,i,NoS))/h(1) -
    (w(2,i)*((Carr(1,i,NoS) + deltaTime*k1(1,i)/2) - Carr(2,i,NoS)))/h(1) +
    (0.5*(sign(1.0,UU(1,i)) + 1)*UU(1,i)*Carr(1,i - 1,NoS) + 0.5*(1 -
    sign(1.0,UU(1,i)))*UU(1,i)*(Carr(1,i,NoS) + deltaTime*k1(1,i)/2))/l(i) +
    (u(1,i)*(Carr(1,i - 1,NoS) - (Carr(1,i,NoS) + deltaTime*k1(1,i)/2)))/l(i) -
    (0.5*(sign(1.0,UU(1,i + 1)) + 1)*UU(1,i + 1)*(Carr(1,i,NoS) + deltaTime*k1(1,i)/2) +
    0.5*(1 - sign(1.0,UU(1,i + 1)))*UU(1,i + 1)*Carr(1,i + 1,NoS))/l(i) - (u(1,i +
    1)*((Carr(1,i,NoS) + deltaTime*k1(1,i)/2) - Carr(1,i + 1,NoS)))/l(i)

    k2(nbv,i) = (0.5*(sign(1.0,WW(nbv,i)) + 1)*WW(nbv,i)*Carr(nbv - 1,i,NoS) + 0.5*(1 -
    sign(1.0,WW(nbv,i)))*WW(nbv,i)*(Carr(nbv,i,NoS) +
    deltaTime*k1(nbv,i)/2))/h(nbv) + (w(nbv,i)*(Carr(nbv - 1,i,NoS) - (Carr(nbv,i,NoS)
    + deltaTime*k1(nbv,i)/2)))/h(nbv) - (w(nbv + 1,i)*((Carr(nbv,i,NoS) +
```

```
    deltaTime*k1(nbv,i)/2) - cBgarr(NoS)))/h(nbv) + (0.5*(sign(1.0,UU(nbv,i)) +
    1)*UU(nbv,i)*Carr(nbv,i - 1,NoS) + 0.5*(1 - sign(1.0,UU(nbv,i)))*UU(nbv,i)*
    (Carr(nbv,i,NoS) + deltaTime*k1(nbv,i)/2))/l(i) + (u(nbv,i)*(Carr(nbv,i - 1,NoS) -
    (Carr(nbv,i,NoS) + deltaTime*k1(nbv,i)/2)))/l(i) - (0.5*(sign(1.0,UU(nbv,i + 1)) +
    1)*UU(nbv,i + 1)*(Carr(nbv,i,NoS) + deltaTime*k1(nbv,i)/2) + 0.5*(1 -
    sign(1.0,UU(nbv,i + 1)))*UU(nbv,i + 1)*Carr(nbv,i + 1,NoS))/l(i) - (u(nbv,i +
    1)*((Carr(nbv,i,NoS) + deltaTime*k1(nbv,i)/2) - Carr(nbv,i + 1,NoS)))/l(i)
    enddo
endif
if(nbv>2 .and. nbh>2)Then
!## Equation for in - canyon box
    do k=2,nbv - 1
        do i=2,nbh - 1
    k2(k,i) = (0.5*(sign(1.0,WW(k,i)) + 1)*WW(k,i)*Carr(k - 1,i,NoS) + 0.5*(1 -
    sign(1.0,WW(k,i)))*WW(k,i)*(Carr(k,i,NoS) + deltaTime*k1(k,i)/2))/h(k) +
    (w(k,i)*(Carr(k - 1,i,NoS) - (Carr(k,i,NoS) + deltaTime*k1(k,i)/2)))/h(k) -
    (0.5*(sign(1.0,WW(k + 1,i)) + 1)*WW(k + 1,i)*(Carr(k,i,NoS) + deltaTime*k1(k,i)/2)
    + 0.5*(1 - sign(1.0,WW(k + 1,i)))*WW(k + 1,i)*Carr(k + 1,i,NoS))/h(k) - (w(k +
    1,i)*((Carr(k,i,NoS) + deltaTime*k1(k,i)/2) - Carr(k + 1,i,NoS)))/h(k) +
    (0.5*(sign(1.0,UU(k,i)) + 1)*UU(k,i)*Carr(k,i - 1,NoS) + 0.5*(1 -
    sign(1.0,UU(k,i)))*UU(k,i)*(Carr(k,i,NoS) + deltaTime*k1(k,i)/2))/l(i) +
    (u(k,i)*(Carr(k,i - 1,NoS) - (Carr(k,i,NoS) + deltaTime*k1(k,i)/2)))/l(i) - (0.5*
    (sign(1.0,UU(k,i + 1)) + 1)*UU(k,i + 1)*(Carr(k,i,NoS) + deltaTime*k1(k,i)/2) + 0.5*(1
    - sign(1.0,UU(k,i + 1)))*UU(k,i + 1)*Carr(k,i + 1,NoS))/l(i) - (u(k,i + 1)*((Carr(k,i,NoS)
    + deltaTime*k1(k,i)/2) - Carr(k,i + 1,NoS)))/l(i)
        enddo
    enddo
endif
!# 3rd order EQ
!# Equation for corner position
    k3(1,1) = - (0.5*(sign(1.0,WW(2,1)) + 1)*WW(2,1)*(Carr(1,1,NoS) +
    deltaTime*k2(1,1)/2) + 0.5*(1 - sign(1.0,WW(2,1)))*WW(2,1)*Carr(2,1,NoS))/h(1)
    - (w(2,1)*((Carr(1,1,NoS) + deltaTime*k2(1,1)/2) - Carr(2,1,NoS)))/h(1) -
    (0.5*(sign(1.0,UU(1,2)) + 1)*UU(1,2)*(Carr(1,1,NoS) + deltaTime*k2(1,1)/2) +
    0.5*(1 - sign(1.0,UU(1,2)))*UU(1,2)*Carr(1,2,NoS))/l(1) - (u(1,2)*((Carr(1,1,NoS) +
    deltaTime*k2(1,1)/2) - Carr(1,2,NoS)))/l(1)

    k3(nbv,1) = (0.5*(sign(1.0,WW(nbv,1)) + 1)*WW(nbv,1)*Carr(nbv - 1,1,NoS) +
    0.5*(1 - sign(1.0,WW(nbv,1)))*WW(nbv,1)*(Carr(nbv,1,NoS) +
    deltaTime*k2(nbv,1)/2))/h(nbv) + (w(nbv,1)*(Carr(nbv - 1,1,NoS) -
    (Carr(nbv,1,NoS) + deltaTime* k2(nbv,1)/2)))/h(nbv) - (w(nbv +
    1,1)*((Carr(nbv,1,NoS) + deltaTime*k2(nbv,1)/2) - cBgarr(NoS)))/h(nbv) -
    (0.5*(sign(1.0,UU(nbv,2)) + 1)*UU(nbv,2)*(Carr(nbv,1,NoS) +
```

```
    deltaTime*k2(nbv,1)/2) + 0.5*(1 -
    sign(1.0,UU(nbv,2)))*UU(nbv,2)*Carr(nbv,2,NoS))/l(1) -
    (u(nbv,2)*((Carr(nbv,1,NoS) + deltaTime*k2(nbv,1)/2) - Carr(nbv,2,NoS)))/l(1)

    k3(1,nbh) = - (0.5*(sign(1.0,WW(2,nbh)) + 1)*WW(2,nbh)*(Carr(1,nbh,NoS) +
    deltaTime*k2(1,nbh)/2) + 0.5*(1 -
    sign(1.0,WW(2,nbh)))*WW(2,nbh)*Carr(2,nbh,NoS))/h(1) -
    (w(2,nbh)*((Carr(1,nbh,NoS) + deltaTime*k2(1,nbh)/2) - Carr(2,nbh,NoS)))/h(1) +
    (0.5*(sign(1.0,UU(1,nbh)) + 1)*UU(1,nbh)*Carr(1,nbh - 1,NoS) + 0.5*(1 -
    sign(1.0,UU(1,nbh)))*UU(1,nbh)*(Carr(1,nbh,NoS) +
    deltaTime*k2(1,nbh)/2))/l(nbh) + (u(1,nbh)*(Carr(1,nbh - 1,NoS) -
    (Carr(1,nbh,NoS) + deltaTime*k2(1,nbh)/2)))/l(nbh)

    k3(nbv,nbh) = (0.5*(sign(1.0,WW(nbv,nbh)) + 1)*WW(nbv,nbh)*Carr(nbv -
    1,nbh,NoS) + 0.5*(1 - sign(1.0,WW(nbv,nbh)))*WW(nbv,nbh)*(Carr(nbv,nbh,NoS) +
    deltaTime*k2(nbv,nbh)/2))/h(nbv) + (w(nbv,nbh)*(Carr(nbv - 1,nbh,NoS) -
    (Carr(nbv,nbh,NoS) + deltaTime*k2(nbv,nbh)/2)))/h(nbv) - (w(nbv +
    1,nbh)*((Carr(nbv,nbh,NoS) + deltaTime*k2(nbv,nbh)/2) - cBgarr(NoS)))/h(nbv) +
    (0.5*(sign(1.0,UU(nbv,nbh)) + 1)*UU(nbv,nbh)*Carr(nbv,nbh - 1,NoS) + 0.5*(1 -
    sign(1.0,UU(nbv,nbh)))*UU(nbv,nbh)* (Carr(nbv,nbh,NoS) +
    deltaTime*k2(nbv,nbh)/2))/l(nbh) + (u(nbv,nbh)*(Carr(nbv,nbh - 1,NoS) -
    (Carr(nbv,nbh,NoS) + deltaTime*k2(nbv,nbh)/2)))/l(nbh)
!# Equation for edge i.e. ground or walls...
if (nbv>2)Then
!# for wall
do k=2,nbv - 1
    k3(k,nbh) = (0.5*(sign(1.0,WW(k,nbh)) + 1)*WW(k,nbh)*Carr(k - 1,nbh,NoS) +
    0.5*(1 - sign(1.0,WW(k,nbh)))*WW(k,nbh)*(Carr(k,nbh,NoS) +
    deltaTime*k2(k,nbh)/2))/h(2) + (w(k,nbh)*(Carr(k - 1,nbh,NoS) - (Carr(k,nbh,NoS)
    + deltaTime*k2(k,nbh)/2)))/h(k) - (0.5*(sign(1.0,WW(k + 1,nbh)) + 1)*WW(k +
    1,nbh)*(Carr(k,nbh,NoS) + deltaTime*k2(k,nbh)/2) + 0.5*(1 - sign(1.0,WW(k +
    1,nbh)))*WW(k + 1,nbh)*Carr(k + 1,nbh,NoS))/h(k) - (w(k +
    1,nbh)*((Carr(k,nbh,NoS) + deltaTime*k2(k,nbh)/2) - Carr(k + 1,nbh,NoS)))/h(k) +
    (0.5*(sign(1.0,UU(k,nbh)) + 1)*UU(k,nbh)*Carr(k,nbh - 1,NoS) + 0.5*(1 -
    sign(1.0,UU(k,nbh)))*UU(k,nbh)*(Carr(k,nbh,NoS) +
    deltaTime*k2(k,nbh)/2))/l(nbh) + (u(k,nbh)*(Carr(k,nbh - 1,NoS) -
    (Carr(k,nbh,NoS) + deltaTime*k2(k,nbh)/2)))/l(nbh)
    enddo
endif
if (nbh>2)Then
!# for ground and rooftop
    do i=2,nbh - 1
```

```
    k3(1,i) = - (0.5*(sign(1.0,WW(2,i)) + 1)*WW(2,i)*(Carr(1,i,NoS) +
    deltaTime*k2(1,i)/2) + 0.5*(1 - sign(1.0,WW(2,i)))*WW(2,i)*Carr(2,i,NoS))/h(1) -
    (w(2,i)*((Carr(1,i,NoS) + deltaTime*k2(1,i)/2) - Carr(2,i,NoS)))/h(1) + (0.5*
    (sign(1.0,UU(1,i)) + 1)*UU(1,i)*Carr(1,i - 1,NoS) + 0.5*(1 -
    sign(1.0,UU(1,i)))*UU(1,i)*(Carr(1,i,NoS) + deltaTime*k2(1,i)/2))/l(i) +
    (u(1,i)*(Carr(1,i - 1,NoS) - (Carr(1,i,NoS) + deltaTime*k2(1,i)/2)))/l(i) -
    (0.5*(sign(1.0,UU(1,i + 1)) + 1)*UU(1,i + 1)*(Carr(1,i,NoS) + deltaTime*k2(1,i)/2) +
    0.5*(1 - sign(1.0,UU(1,i + 1)))*UU(1,i + 1)*Carr(1,i + 1,NoS))/l(i) - (u(1,i +
    1)*((Carr(1,i,NoS) + deltaTime*k2(1,i)/2) - Carr(1,i + 1,NoS)))/l(i)

k3(nbv,i) = (0.5*(sign(1.0,WW(nbv,i)) + 1)*WW(nbv,i)*Carr(nbv - 1,i,NoS) + 0.5*(1 -
sign(1.0,WW(nbv,i)))*WW(nbv,i)*(Carr(nbv,i,NoS) + deltaTime*k2(nbv,i)/2))/h(nbv) +
(w(nbv,i)*(Carr(nbv - 1,i,NoS) - (Carr(nbv,i,NoS) + deltaTime*k2(nbv,i)/2)))/h(nbv) -
(w(nbv + 1,i)*((Carr(nbv,i,NoS) + deltaTime*k2(nbv,i)/2) - cBgarr(NoS)))/h(nbv) +
(0.5*(sign(1.0,UU(nbv,i)) + 1)*UU(nbv,i)*Carr(nbv,i - 1,NoS) + 0.5*(1 -
sign(1.0,UU(nbv,i)))*UU(nbv,i)*(Carr(nbv,i,NoS) + deltaTime*k2(nbv,i)/2))/l(i) +
(u(nbv,i)*(Carr(nbv,i - 1,NoS) - (Carr(nbv,i,NoS) + deltaTime*k2(nbv,i)/2)))/l(i) -
(0.5*(sign(1.0,UU(nbv,i + 1)) + 1)*UU(nbv,i + 1)*(Carr(nbv,i,NoS) +
deltaTime*k2(nbv,i)/2) + 0.5*(1 - sign(1.0,UU(nbv,i + 1)))*UU(nbv,i + 1)*Carr(nbv,i +
1,NoS))/l(i) - (u(nbv,i + 1)*((Carr(nbv,i,NoS) + deltaTime*k2(nbv,i)/2) - Carr(nbv,i +
1,NoS)))/l(i)
    enddo
endif
if(nbv>2 .and. nbh>2)Then
!## Equation for in - canyon box
    do k=2,nbv - 1
do i=2,nbh - 1
    k3(k,i) = (0.5*(sign(1.0,WW(k,i)) + 1)*WW(k,i)*Carr(k - 1,i,NoS) + 0.5*(1 -
    sign(1.0,WW(k,i)))*WW(k,i)*(Carr(k,i,NoS) + deltaTime*k2(k,i)/2))/h(k) +
    (w(k,i)*(Carr(k - 1,i,NoS) - (Carr(k,i,NoS) + deltaTime*k2(k,i)/2)))/h(k) - (0.5*
    (sign(1.0,WW(k + 1,i)) + 1)*WW(k + 1,i)*(Carr(k,i,NoS) + deltaTime*k2(k,i)/2) +
    0.5*(1 - sign(1.0,WW(k + 1,i)))*WW(k + 1,i)*Carr(k + 1,i,NoS))/h(k) - (w(k +
    1,i)*((Carr(k,i,NoS) + deltaTime*k2(k,i)/2) - Carr(k + 1,i,NoS)))/h(k) +
    (0.5*(sign(1.0,UU(k,i)) + 1)*UU(k,i)*Carr(k,i - 1,NoS) + 0.5*(1 -
    sign(1.0,UU(k,i)))*UU(k,i)*(Carr(k,i,NoS) + deltaTime*k2(k,i)/2))/l(i) +
    (u(k,i)*(Carr(k,i - 1,NoS) - (Carr(k,i,NoS) + deltaTime*k2(k,i)/2)))/l(i) -
    (0.5*(sign(1.0,UU(k,i + 1)) + 1)*UU(k,i + 1)*(Carr(k,i,NoS) + deltaTime*k2(k,i)/2) +
    0.5*(1 - sign(1.0,UU(k,i + 1)))*UU(k,i + 1)*Carr(k,i + 1,NoS))/l(i) - (u(k,i +
    1)*((Carr(k,i,NoS) + deltaTime*k2(k,i)/2) - Carr(k,i + 1,NoS)))/l(i)
        enddo
    enddo
endif
!# 4th order EQ
```

```
!# Equation for corner position
    k4(1,1) = - (0.5*(sign(1.0,WW(2,1)) + 1)*WW(2,1)*(Carr(1,1,NoS) +
    deltaTime*k3(1,1)) + 0.5*(1 - sign(1.0,WW(2,1)))*WW(2,1)*Carr(2,1,NoS))/h(1) -
    (w(2,1)*((Carr(1,1,NoS) + deltaTime*k3(1,1)) - Carr(2,1,NoS)))/h(1) -
    (0.5*(sign(1.0,UU(1,2)) + 1)*UU(1,2)* (Carr(1,1,NoS) + deltaTime*k3(1,1)) + 0.5*(1
    - sign(1.0,UU(1,2)))*UU(1,2)*Carr(1,2,NoS))/l(1) - (u(1,2)*((Carr(1,1,NoS) +
    deltaTime*k3(1,1)) - Carr(1,2,NoS)))/l(1)

    k4(nbv,1) = (0.5*(sign(1.0,WW(nbv,1)) + 1)*WW(nbv,1)*Carr(nbv - 1,1,NoS) +
    0.5*(1 - sign(1.0,WW(nbv,1)))*WW(nbv,1)*(Carr(nbv,1,NoS) +
    deltaTime*k3(nbv,1)))/h(nbv) + (w(nbv,1)*(Carr(nbv - 1,1,NoS) - (Carr(nbv,1,NoS)
    + deltaTime*k3(nbv,1))))/h(nbv) - (w(nbv + 1,1)*((Carr(nbv,1,NoS) +
    deltaTime*k3(nbv,1)) - cBgarr(NoS)))/h(nbv) - (0.5*(sign(1.0,UU(nbv,2)) +
    1)*UU(nbv,2)*(Carr(nbv,1,NoS) + deltaTime*k3(nbv,1)) + 0.5*(1 -
    sign(1.0,UU(nbv,2)))*UU(nbv,2)*Carr(nbv,2,NoS))/l(1) - (u(nbv,2)*
    ((Carr(nbv,1,NoS) + deltaTime*k3(nbv,1)) - Carr(nbv,2,NoS)))/l(1)

    k4(1,nbh) = - (0.5*(sign(1.0,WW(2,nbh)) + 1)*WW(2,nbh)*(Carr(1,nbh,NoS) +
    deltaTime*k3(1,nbh)) + 0.5*(1 -
    sign(1.0,WW(2,nbh)))*WW(2,nbh)*Carr(2,nbh,NoS))/h(1) -
    (w(2,nbh)*((Carr(1,nbh,NoS) + deltaTime*k3(1,nbh)) - Carr(2,nbh,NoS)))/h(1) +
    (0.5* (sign(1.0,UU(1,nbh)) + 1)*UU(1,nbh)*Carr(1,nbh - 1,NoS) + 0.5*(1 -
    sign(1.0,UU(1,nbh)))*UU(1,nbh)*(Carr(1,nbh,NoS) + deltaTime*k3(1,nbh)))/l(nbh)
    + (u(1,nbh)*(Carr(1,nbh - 1,NoS) - (Carr(1,nbh,NoS) +
    deltaTime*k3(1,nbh))))/l(nbh)

    k4(nbv,nbh) = (0.5*(sign(1.0,WW(nbv,nbh)) + 1)*WW(nbv,nbh)*Carr(nbv -
    1,nbh,NoS) + 0.5*(1 - sign(1.0,WW(nbv,nbh)))*WW(nbv,nbh)*(Carr(nbv,nbh,NoS) +
    deltaTime*k3(nbv,nbh)))/h(nbv) + (w(nbv,nbh)*(Carr(nbv - 1,nbh,NoS) -
    (Carr(nbv,nbh,NoS) + deltaTime*k3(nbv,nbh))))/h(nbv) - (w(nbv +
    1,nbh)*((Carr(nbv,nbh,NoS) + deltaTime*k3(nbv,nbh)) - cBgarr(NoS)))/h(nbv) +
    (0.5*(sign(1.0,UU(nbv,nbh)) + 1)*UU(nbv,nbh)*Carr(nbv,nbh - 1,NoS) + 0.5*(1 -
    sign(1.0,UU(nbv,nbh)))*UU(nbv,nbh)*(Carr(nbv,nbh,NoS) +
    deltaTime*k3(nbv,nbh)))/l(nbh) + (u(nbv,nbh)*(Carr(nbv,nbh - 1,NoS) -
    (Carr(nbv,nbh,NoS) + deltaTime*k3(nbv,nbh))))/l(nbh)
    !# Equation for edge i.e. ground or walls...
  if (nbv>2)Then
    !# for wall
    do k=2,nbv - 1
    k4(k,1) = (0.5*(sign(1.0,WW(k,1)) + 1)*WW(k,1)*Carr(k - 1,1,NoS) + 0.5*(1 -
    sign(1.0,WW(k,1)))*WW(k,1)*(Carr(k,1,NoS) + deltaTime*k3(k,1)))/h(k) +
    (w(k,1)*(Carr(k - 1,1,NoS) - (Carr(k,1,NoS) + deltaTime*k3(k,1))))/h(k) -
    (0.5*(sign(1.0,WW(k + 1,1)) + 1)* WW(k + 1,1)*(Carr(k,1,NoS) + deltaTime*k3(k,1))
```

```
        + 0.5*(1 - sign(1.0,WW(k + 1,1)))*WW(k + 1,1)*Carr(k + 1,1,NoS))/h(k) - (w(k +
        1,1)*((Carr(k,1,NoS) + deltaTime*k3(k,1)) - Carr(k + 1,1,NoS)))/h(k) -
        (0.5*(sign(1.0,UU(k,2)) + 1)*UU(k,2)*(Carr(k,1,NoS) + deltaTime*k3(k,1)) + 0.5*(1 -
        sign(1.0,UU(k,2)))*UU(k,2)*Carr(k,2,NoS))/l(1) - (u(k,2)*((Carr(k,1,NoS) +
        deltaTime*k3(k,1)) - Carr(k,2,NoS)))/l(1)

        k4(k,nbh) = (0.5*(sign(1.0,WW(k,nbh)) + 1)*WW(k,nbh)*Carr(k - 1,nbh,NoS) +
        0.5*(1 - sign(1.0,WW(k,nbh)))*WW(k,nbh)*(Carr(k,nbh,NoS) +
        deltaTime*k3(k,nbh)))/h(2) + (w(k,nbh)*(Carr(k - 1,nbh,NoS) - (Carr(k,nbh,NoS) +
        deltaTime*k3(k,nbh))))/h(k) - (0.5*(sign(1.0,WW(k + 1,nbh)) + 1)*WW(k +
        1,nbh)*(Carr(k,nbh,NoS) + deltaTime*k3(k,nbh)) + 0.5*(1 - sign(1.0,WW(k +
        1,nbh)))*WW(k + 1,nbh)*Carr(k + 1,nbh,NoS))/h(k) - (w(k +
        1,nbh)*((Carr(k,nbh,NoS) + deltaTime*k3(k,nbh)) - Carr(k + 1,nbh,NoS)))/h(k) +
        (0.5*(sign(1.0,UU(k,nbh)) + 1)*UU(k,nbh)*Carr(k,nbh - 1,NoS) + 0.5*(1 -
        sign(1.0,UU(k,nbh)))*UU(k,nbh)*(Carr(k,nbh,NoS) + deltaTime*k3(k,nbh)))/l(nbh)
        + (u(k,nbh)*(Carr(k,nbh - 1,NoS) - (Carr(k,nbh,NoS) +
        deltaTime*k3(k,nbh))))/l(nbh)
            enddo
        endif
    if (nbh>2)then
    ! for ground and rooftop
        do i=2,nbh - 1
        k4(1,i) = - (0.5*(sign(1.0,WW(2,i)) + 1)*WW(2,i)*(Carr(1,i,NoS) +
        deltaTime*k3(1,i)) + 0.5*(1 - sign(1.0,WW(2,i)))*WW(2,i)*Carr(2,i,NoS))/h(1) -
        (w(2,i)*((Carr(1,i,NoS) + deltaTime*k3(1,i)) - Carr(2,i,NoS)))/h(1) +
        (0.5*(sign(1.0,UU(1,i)) + 1)*UU(1,i)*Carr(1,i - 1,NoS) + 0.5*(1 -
        sign(1.0,UU(1,i)))*UU(1,i)*(Carr(1,i,NoS) + deltaTime*k3(1,i)))/l(i) +
        (u(1,i)*(Carr(1,i - 1,NoS) - (Carr(1,i,NoS) + deltaTime*k3(1,i))))/l(i) -
        (0.5*(sign(1.0,UU(1,i + 1)) + 1)*UU(1,i + 1)*(Carr(1,i,NoS) + deltaTime*k3(1,i)) +
        0.5*(1 - sign(1.0,UU(1,i + 1)))*UU(1,i + 1)*Carr(1,i + 1,NoS))/l(i) - (u(1,i +
        1)*((Carr(1,i,NoS) + deltaTime*k3(1,i)) - Carr(1,i + 1,NoS)))/l(i)

        k4(nbv,i) = (0.5*(sign(1.0,WW(nbv,i)) + 1)*WW(nbv,i)*Carr(nbv - 1,i,NoS) + 0.5*(1 -
        sign(1.0,WW(nbv,i)))*WW(nbv,i)*(Carr(nbv,i,NoS) + deltaTime*k3(nbv,i)))/h(nbv)
        + (w(nbv,i)*(Carr(nbv - 1,i,NoS) - (Carr(nbv,i,NoS) + deltaTime*k3(nbv,i))))/h(nbv)
        - (w(nbv + 1,i)*((Carr(nbv,i,NoS) + deltaTime*k3(nbv,i)) - cBgarr(NoS)))/h(nbv) +
        (0.5*(sign(1.0,UU(nbv,i)) + 1)*UU(nbv,i)*Carr(nbv,i - 1,NoS) + 0.5*(1 -
        sign(1.0,UU(nbv,i)))*UU(nbv,i)*(Carr(nbv,i,NoS) + deltaTime*k3(nbv,i)))/l(i) +
        (u(nbv,i)*(Carr(nbv,i - 1,NoS) - (Carr(nbv,i,NoS) + deltaTime*k3(nbv,i))))/l(i) -
        (0.5*(sign(1.0,UU(nbv,i + 1)) + 1)*UU(nbv,i + 1)*(Carr(nbv,i,NoS) +
        deltaTime*k3(nbv,i)) + 0.5*(1 - sign(1.0,UU(nbv,i + 1)))*UU(nbv,i + 1)*Carr(nbv,i +
        1,NoS))/l(i) - (u(nbv,i + 1)*((Carr(nbv,i,NoS) + deltaTime*k3(nbv,i)) - Carr(nbv,i +
        1,NoS)))/l(i)
```

```
            enddo
        endif
if (nbv>2 .and. nbh>2)then
!# Equation for in - canyon box
do k=2,nbv - 1
        do i=2,nbh - 1
        k4(k,i) = (0.5*(sign(1.0,WW(k,i)) + 1)*WW(k,i)*Carr(k - 1,i,NoS) + 0.5*(1 -
        sign(1.0,WW(k,i)))*WW(k,i)*(Carr(k,i,NoS) + deltaTime*k3(k,i)))/h(k) +
        (w(k,i)*(Carr(k - 1,i,NoS) - (Carr(k,i,NoS) + deltaTime*k3(k,i))))/h(k) -
        (0.5*(sign(1.0,WW(k + 1,i)) + 1)*WW(k + 1,i)*(Carr(k,i,NoS) + deltaTime*k3(k,i))
        + 0.5*(1 - sign(1.0,WW(k + 1,i)))*WW(k + 1,i)*Carr(k + 1,i,NoS))/h(k) - (w(k +
        1,i)*((Carr(k,i,NoS) + deltaTime*k3(k,i)) - Carr(k + 1,i,NoS)))/h(k) +
        (0.5*(sign(1.0,UU(k,i)) + 1)*UU(k,i)*Carr(k,i - 1,NoS) + 0.5* (1 -
        sign(1.0,UU(k,i)))*UU(k,i)*(Carr(k,i,NoS) + deltaTime*k3(k,i)))/l(i) +
        (u(k,i)*(Carr(k,i - 1,NoS) - (Carr(k,i,NoS) + deltaTime*k3(k,i))))/l(i) -
        (0.5*(sign(1.0,UU(k,i + 1)) + 1)*UU(k,i + 1)*(Carr(k,i,NoS) + deltaTime*k3(k,i))
        + 0.5*(1 - sign(1.0,UU(k,i + 1)))*UU(k,i + 1)*Carr(k,i + 1,NoS))/l(i) - (u(k,i +
        1)*((Carr(k,i,NoS) + deltaTime*k3(k,i)) - Carr(k,i + 1,NoS)))/l(i)
        enddo
    enddo
  endif

        do k=1,nbv
            do i=1,nbh
        Carr(k,i,NoS) = Carr(k,i,NoS) + deltaTime*(k1(k,i)+2*k2(k,i)+2*k3(k,i)+k4(k,i))/6.0
            enddo
        enddo
enddo

return
end subroutine
#*******************************************************************************#
#*******************************************************************************#
```

REFERENCES

ABHIJITH, K., KUMAR, P., GALLAGHER, J., MCNABOLA, A., BALDAUF, R., PILLA, F., BRODERICK, B., DI SABATINO, S. & PULVIRENTI, B. 2017. Air pollution abatement performances of green infrastructure in open road and built-up street canyon environments–A review. *Atmospheric Environment,* 162**,** 71-86.

AHMAD, K., KHARE, M. & CHAUDHRY, K. 2005. Wind tunnel simulation studies on dispersion at urban street canyons and intersections—a review. *Journal of Wind Engineering and Industrial Aerodynamics,* 93**,** 697-717.

ALEXANDROV, V., SAMEH, A., SIDDIQUE, Y. & ZLATEV, Z. 1997. Numerical integration of chemical ODE problems arising in air pollution models. *Environmental Modeling & Assessment,* 2**,** 365-377.

ALLEN, E. B., RAO, L. E., STEERS, R. J., BYTNEROWICZ, A. & FENN, M. E. 2009. Impacts of atmospheric nitrogen deposition on vegetation and soils in Joshua Tree National Park. *The Mojave Desert: ecosystem processes and sustainability. University of Nevada Press, Las Vegas, Nevada, USA***,** 78-100.

ANENBERG, S. C., HENZE, D. K., TINNEY, V., KINNEY, P. L., RAICH, W., FANN, N., MALLEY, C. S., ROMAN, H., LAMSAL, L. & DUNCAN, B. 2018. Estimates of the global burden of ambient PM 2.5, ozone, and NO 2 on asthma incidence and emergency room visits. *Environmental health perspectives,* 126**,** 107004.

ARYA, S. P. 1999. *Air pollution meteorology and dispersion*, Oxford University Press New York.

AUMONT, B., SZOPA, S. & MADRONICH, S. 2005. Modelling the evolution of organic carbon during its gas-phase tropospheric oxidation: development of an explicit model based on a self generating approach. *Atmospheric Chemistry and Physics,* 5**,** 2497-2517.

BAIK, J.-J., KANG, Y.-S. & KIM, J.-J. 2007. Modeling reactive pollutant dispersion in an urban street canyon. *Atmospheric Environment,* 41**,** 934-949.

BAKER, J., WALKER, H. L. & CAI, X. 2004. A study of the dispersion and transport of reactive pollutants in and above street canyons—a large eddy simulation. *Atmospheric Environment,* 38**,** 6883-6892.

BARLOW, J. F., HARMAN, I. N. & BELCHER, S. E. 2004a. Scalar fluxes from urban street canyons. Part I: Laboratory simulation. *Boundary-Layer Meteorology,* 113**,** 369-385.

BARLOW, J. F., HARMAN, I. N. & BELCHER, S. E. 2004b. Scalar fluxes from urban street canyons. Part I: Laboratory simulation. *Boundary-Layer Meteorology,* 113**,** 369-385.

BERKOWICZ, R. 2000. OSPM-A parameterised street pollution model. *Environmental monitoring and assessment,* 65**,** 323-331.

BISHOP, G. A. & STEDMAN, D. H. 2015. Reactive nitrogen species emission trends in three light-/medium-duty United States fleets. *Environmental science & technology,* 49**,** 11234-11240.

BLOSS, W. 2009. Atmospheric chemical processes of importance in cities. *Issues in Environmental Science and Technology,* 28**,** 42.

BORTIER, K., DE TEMMERMAN, L. & CEULEMANS, R. 2000. Effects of ozone exposure in open-top chambers on poplar (Populus nigra) and beech (Fagus sylvatica): a comparison. *Environmental Pollution,* 109**,** 509-516.

BOULTER, P., BARLOW, T., LATHAM, S. & MCCRAE, I. 2009. Emission factors 2009: Report 1-a review of methods for determining hotexhaust emission factors for road vehicles. *TRL Published Project Report*.

BOURBIA, F. & AWBI, H. 2004. Building cluster and shading in urban canyon for hot dry climate: Part 2: Shading simulations. *Renewable Energy,* 29**,** 291-301.

BRIGHT, V. B., BLOSS, W. J. & CAI, X. 2013. Urban street canyons: Coupling dynamics, chemistry and within-canyon chemical processing of emissions. *Atmospheric Environment,* 68**,** 127-142.

BRITTER, R. & HANNA, S. 2003. Flow and dispersion in urban areas. *Annual review of fluid mechanics,* 35**,** 469-496.

BROWN, S. S. & STUTZ, J. 2012. Nighttime radical observations and chemistry. *Chemical Society Reviews,* 41**,** 6405-6447.

BUCCOLIERI, R., JEANJEAN, A. P., GATTO, E. & LEIGH, R. J. 2018. The impact of trees on street ventilation, NOx and PM2. 5 concentrations across heights in Marylebone Rd street canyon, central London. *Sustainable Cities and Society,* 41**,** 227-241.

BUCKLAND, A. & MIDDLETON, D. 1999. Nomograms for calculating pollution within street canyons. *Atmospheric Environment,* 33**,** 1017-1036.

BUSH, T., TSAGATAKIS, I., PASSANT, N., GRIFFIN, A. & PEARSON, B. 2010. UK emission mapping methodology 2007. *Didcot, Oxfordshire, ED48954*.

CAI, X.-M. 2012a. Effects of wall heating on flow characteristics in a street canyon. *Boundary-layer meteorology,* 142**,** 443-467.

CAI, X.-M., BARLOW, J. & BELCHER, S. 2008. Dispersion and transfer of passive scalars in and above street canyons—large-eddy simulations. *Atmospheric Environment,* 42**,** 5885-5895.

CAI, X.-M. & STEYN, D. 2000. Modelling study of sea breezes in a complex coastal environment. *Atmospheric Environment,* 34**,** 2873-2885.

CAI, X. 2012b. Effects of differential wall heating in street canyons on dispersion and ventilation characteristics of a passive scalar. *Atmospheric environment,* 51**,** 268-277.

CALFAPIETRA, C., FARES, S., MANES, F., MORANI, A., SGRIGNA, G. & LORETO, F. 2013. Role of Biogenic Volatile Organic Compounds (BVOC) emitted by urban trees on ozone concentration in cities: A review. *Environmental pollution,* 183**,** 71-80.

CARPENTER, L., CLEMITSHAW, K., BURGESS, R., PENKETT, S., CAPE, J. & MCFADYEN, G. 1998. Investigation and evaluation of the NOx/O3 photochemical steady state. *Atmospheric Environment,* 32**,** 3353-3365.

CARRASSI, A., BOCQUET, M., BERTINO, L. & EVENSEN, G. 2018. Data assimilation in the geosciences: An overview of methods, issues, and perspectives. *Wiley Interdisciplinary Reviews: Climate Change,* 9**,** e535.

CARSLAW, D. C., BEEVERS, S. D., TATE, J. E., WESTMORELAND, E. J. & WILLIAMS, M. L. 2011. Recent evidence concerning higher NOx emissions from passenger cars and light duty vehicles. *Atmospheric Environment,* 45**,** 7053-7063.

CARSLAW, D. C., MURRELLS, T. P., ANDERSSON, J. & KEENAN, M. 2016. Have vehicle emissions of primary NO2 peaked? *Faraday discussions,* 189**,** 439-454.

CARSLAW, D. C. & ROPKINS, K. 2012. Openair—an R package for air quality data analysis. *Environmental Modelling & Software,* 27**,** 52-61.

CHAMEIDES, W., LINDSAY, R., RICHARDSON, J. & KIANG, C. 1988. The role of biogenic hydrocarbons in urban photochemical smog: Atlanta as a case study. *Science,* 241**,** 1473-1475.

CHANG, J. C. & HANNA, S. R. 2004. Air quality model performance evaluation. *Meteorology and Atmospheric Physics,* 87**,** 167-196.

CHATZIDIMITRIOU, A. & YANNAS, S. 2017. Street canyon design and improvement potential for urban open spaces; the influence of canyon aspect ratio and orientation on microclimate and outdoor comfort. *Sustainable cities and society,* 33**,** 85-101.

CHENG, Y., LIEN, F., YEE, E. & SINCLAIR, R. 2003. A comparison of large eddy simulations with a standard k–ε Reynolds-averaged Navier–Stokes model for the prediction of a fully developed turbulent flow over a matrix of cubes. *Journal of Wind Engineering and Industrial Aerodynamics,* 91**,** 1301-1328.

CHEW, L. W., ALIABADI, A. A. & NORFORD, L. K. 2018a. Flows across high aspect ratio street canyons: Reynolds number independence revisited. *Environmental Fluid Mechanics,* 18**,** 1275-1291.

CHEW, L. W., ALIABADI, A. A. & NORFORD, L. K. 2018b. Flows across high aspect ratio street canyons: Reynolds number independence revisited. *Environmental Fluid Mechanics,* 18**,** 1275-1291.

CHOWDHURY, B., KARAMCHANDANI, P., SYKES, R., HENN, D. & KNIPPING, E. 2015. Reactive puff model SCICHEM: Model enhancements and performance studies. *Atmospheric Environment,* 117**,** 242-258.

CIMORELLI, A. J., PERRY, S. G., VENKATRAM, A., WEIL, J. C., PAINE, R. J., WILSON, R. B., LEE, R. F., PETERS, W. D. & BRODE, R. W. 2005. AERMOD: A dispersion model for industrial source applications. Part I: General model formulation and boundary layer characterization. *Journal of applied meteorology,* 44**,** 682-693.

CLAPP, L. J. & JENKIN, M. E. 2001. Analysis of the relationship between ambient levels of O3, NO2 and NO as a function of NOx in the UK. *Atmospheric Environment,* 35**,** 6391-6405.

COHEN, B. 2006. Urbanization in developing countries: Current trends, future projections, and key challenges for sustainability. *Technology in society,* 28**,** 63-80.

COLBECK, I. & MACKENZIE, A. R. 1994. Air pollution by photochemical oxidants.

COLE, H. S. & SUMMERHAYS, J. E. 1979. A review of techniques available for estimating short-term NO2 concentrations. *Journal of the Air Pollution Control Association,* 29**,** 812-817.

COLLETT, R. S. & ODUYEMI, K. 1997. Air quality modelling: a technical review of mathematical approaches. *Meteorological Applications: A journal of forecasting, practical applications, training techniques and modelling,* 4**,** 235-246.

COMEAP 2018. Available online: https://www.gov.uk/government/publications/nitrogen-dioxide-effects-on-mortality/associations-of-long-term-average-concentrations-of-nitrogen-dioxide-with-mortality-2018-comeap-summary (accessed on 24 August 2021).

CUI, D., HU, G., AI, Z., DU, Y., MAK, C. M. & KWOK, K. 2019. Particle image velocimetry measurement and CFD simulation of pedestrian level wind environment around U-type street canyon. *Building and Environment,* 154**,** 239-251.

CUI, Z., CAI, X. & J. BAKER, C. 2004. Large‐eddy simulation of turbulent flow in a street canyon. *Quarterly Journal of the Royal Meteorological Society,* 130**,** 1373-1394.

DABBERDT, W. F., LUDWIG, F. & JOHNSON JR, W. B. 1973. Validation and applications of an urban diffusion model for vehicular pollutants. *Atmospheric Environment (1967),* 7**,** 603-618.

DAI, Y., CAI, X., ZHONG, J. & MACKENZIE, A. R. 2021a. Modelling chemistry and transport in urban street canyons: Comparing offline multi-box models with large-eddy simulation. *Atmospheric Environment,* 264**,** 118709.

DAI, Y., CAI, X., ZHONG, J. & MACKENZIE, A. R. 2021b. Modelling chemistry and transport in urban street canyons: Comparing offline multi-box models with large-eddy simulation. *Atmospheric Environment*, 118709.

DAI, Y., CAI, X., ZHONG, J. & MACKENZIE, A. R. 2022a. Chemistry, street canyon geometry, and emissions effects on NO2 "hotspots" and regulatory "wiggle room". *npj Climate and Atmospheric Science,* 5, 102.

DAI, Y., CAI, X., ZHONG, J. & MACKENZIE, A. R. 2022b. Street canyon NO2 "hotspots" and regulatory "wiggle room": the interacting effects of free-radical chemistry, canyon geometry, primary NO2, and emissions. *npj Climate and Atmospheric Science,* Under-Review.

DAI, Y., CAI, X., ZHONG, J., MAZZEO, A. & MACKENZIE, A. R. 2022c. Chemistry, transport, emission, and shading effects on NO2 and Ox distributions within urban canyons. *Environmental Pollution,* 315, 120347.

DAVISON, J., ROSE, R. A., FARREN, N. J., WAGNER, R. L., MURRELLS, T. P. & CARSLAW, D. C. 2021. Verification of a National Emission Inventory and Influence of On-road Vehicle Manufacturer-Level Emissions. *Environmental Science & Technology*.

DE VISSCHER, A. 2013. *Air dispersion modeling: foundations and applications*, John Wiley & Sons.

DEFRA 2005. Department of Environment, Food and Rural Affairs. Available online: https://uk-air.defra.gov.uk/assets/documents/reports/cat05/0703151041_primno2v3.pdf (accessed on 24 August 2021).

DEFRA 2011. The Air Quality Strategy for England, Scotland, Wales and Northern Ireland - Volume 1. Department of the Environment, transport and the regions.

DEFRA 2017a. UK Plan for tackling roadside nitrogen dioxide concentrations. Technical report. Department for Environment, Food and Rural Affairs London.

DEFRA 2017b. UK plan for tackling roadside nitrogen dioxide concentrations: An overview. Department of the Environment, transport and the regions.

DEFRA 2019a. Air Pollution in the UK 2018: Compliance Assessment Summary. Department of the Environment, transport and the regions.

DEFRA 2019b. Clean air strategy 2019. DEFR.

DEFRA 2023. Draft air quality strategy. Department for Environment, Food and Rural Affairs London.

DEMUZERE, M., BECHTEL, B., MIDDEL, A. & MILLS, G. 2019. Mapping Europe into local climate zones. *PloS one,* 14, e0214474.

DENBY, B., GEORGIEVA, E. & LÜKEWILLE, A. 2011. The application of models under the European Union's Air Quality Directive: a technical reference guide. Technical Report 10/2011, European Environmental Agency, Copenhagen.

DEPAUL, F. & SHEIH, C. 1986. Measurements of wind velocities in a street canyon. *Atmospheric Environment (1967),* 20, 455-459.

DI SABATINO, S., BUCCOLIERI, R., PULVIRENTI, B. & BRITTER, R. 2008. Flow and pollutant dispersion in street canyons using FLUENT and ADMS-Urban. *Environmental Modeling & Assessment,* 13, 369-381.

DING, D., XING, J., WANG, S., DONG, Z., ZHANG, F., LIU, S. & HAO, J. 2021. Optimization of a NO x and VOC Cooperative Control Strategy Based on Clean Air Benefits. *Environmental Science & Technology*.

DOMINGO, J. L. & ROVIRA, J. 2020. Effects of air pollutants on the transmission and severity of respiratory viral infections. *Environmental research,* 187, 109650.

DONOVAN, R. G., STEWART, H. E., OWEN, S. M., MACKENZIE, A. R. & HEWITT, C. N. 2005. Development and application of an urban tree air quality score for photochemical

pollution episodes using the Birmingham, United Kingdom, area as a case study. *Environmental Science & Technology,* 39**,** 6730-6738.

DRAGANI, R., REDAELLI, G., VISCONTI, G., MARIOTTI, A., RUDAKOV, V., MACKENZIE, A. R. & STEFANUTTI, L. 2002. High-resolution stratospheric tracer fields reconstructed with Lagrangian techniques: A comparative analysis of predictive skill. *Journal of the atmospheric sciences,* 59**,** 1943-1958.

DRAXLER, R. R. 1992. *Hybrid single-particle Lagrangian integrated trajectories (HY-SPLIT), Version 3.0: User's guide and model description*, US Department of Commerce, National Oceanic and Atmospheric Administration ….

DRISCOLL, J. F., CHEN, R.-H. & YOON, Y. 1992. Nitric oxide levels of turbulent jet diffusion flames: effects of residence time and Damkohler number. *Combustion and Flame,* 88**,** 37-49.

ELIASSON, I., OFFERLE, B., GRIMMOND, C. & LINDQVIST, S. 2006. Wind fields and turbulence statistics in an urban street canyon. *Atmospheric environment,* 40**,** 1-16.

ELLIOTT, H., EON, C. & BREADSELL, J. K. 2020. Improving City vitality through urban heat reduction with green infrastructure and design solutions: A systematic literature review. *Buildings,* 10**,** 219.

EMMANUEL, R. & KRÜGER, E. 2012. Urban heat island and its impact on climate change resilience in a shrinking city: The case of Glasgow, UK. *Building and Environment,* 53**,** 137-149.

EMMERSON, K. M., MACKENZIE, A. R., OWEN, S. M., EVANS, M. J. & SHALLCROSS, D. E. 2004. A Lagrangian model with simple primary and secondary aerosol scheme 1: comparison with UK PM_{10} data. *Atmos. Chem. Phys.,* 4**,** 2161-2170.

EVANS, M., SHALLCROSS, D., LAW, K., WILD, J., SIMMONDS, P., SPAIN, T., BERRISFORD, P., METHVEN, J., LEWIS, A. & MCQUAID, J. 2000. Evaluation of a Lagrangian box model using field measurements from EASE (Eastern Atlantic Summer Experiment) 1996. *Atmospheric Environment,* 34**,** 3843-3863.

FELLINI, S., RIDOLFI, L. & SALIZZONI, P. 2020. Street canyon ventilation: Combined effect of cross‐section geometry and wall heating. *Quarterly Journal of the Royal Meteorological Society,* 146**,** 2347-2367.

FINLAYSON-PITTS, B. J. & PITTS JR, J. N. 1999. *Chemistry of the upper and lower atmosphere: theory, experiments, and applications*, Elsevier.

FIRDAUS, G. & AHMAD, A. 2011. Changing air quality in Delhi, India: determinants, trends, and policy implications. *Regional Environmental Change,* 11**,** 743-752.

FU, X., LIU, J., BAN-WEISS, G. A., ZHANG, J., HUANG, X., OUYANG, B., POPOOLA, O. & TAO, S. 2017. Effects of canyon geometry on the distribution of traffic-related air pollution in a large urban area: Implications of a multi-canyon air pollution dispersion model. *Atmospheric Environment,* 165**,** 111-121.

FU, X., XIANG, S., LIU, Y., LIU, J., YU, J., MAUZERALL, D. L. & TAO, S. 2020. High-resolution simulation of local traffic-related NOx dispersion and distribution in a complex urban terrain. *Environmental Pollution,* 263**,** 114390.

GARMORY, A., KIM, I., BRITTER, R. & MASTORAKOS, E. 2009. Simulations of the dispersion of reactive pollutants in a street canyon, considering different chemical mechanisms and micromixing. *Atmospheric Environment,* 43**,** 4670-4680.

GARMORY, A., RICHARDSON, E. & MASTORAKOS, E. 2006. Micromixing effects in a reacting plume by the stochastic fields method. *Atmospheric Environment,* 40**,** 1078-1091.

GELBARD, F. & SEINFELD, J. H. 1980. Simulation of multicomponent aerosol dynamics. *Journal of colloid and Interface Science,* 78**,** 485-501.

GENG, F., CAI, C., TIE, X., YU, Q., AN, J., PENG, L., ZHOU, G. & XU, J. 2009. Analysis of VOC emissions using PCA/APCS receptor model at city of Shanghai, China. *Journal of atmospheric chemistry,* 62**,** 229-247.

GEORGE, I. J., HAYS, M. D., HERRINGTON, J. S., PRESTON, W., SNOW, R., FAIRCLOTH, J., GEORGE, B. J., LONG, T. & BALDAUF, R. W. 2015. Effects of cold temperature and ethanol content on VOC emissions from light-duty gasoline vehicles. *Environmental science & technology,* 49**,** 13067-13074.

GIDHAGEN, L., JOHANSSON, C., LANGNER, J. & OLIVARES, G. 2004. Simulation of NOx and ultrafine particles in a street canyon in Stockholm, Sweden. *Atmospheric Environment,* 38**,** 2029-2044.

GOOD, N., MÖLTER, A., ACKERSON, C., BACHAND, A., CARPENTER, T., CLARK, M. L., FEDAK, K. M., KAYNE, A., KOEHLER, K. & MOORE, B. 2016. The Fort Collins Commuter Study: Impact of route type and transport mode on personal exposure to multiple air pollutants. *Journal of exposure science & environmental epidemiology,* 26**,** 397-404.

GRAWE, D., CAI, X.-M. & HARRISON, R. M. 2007. Large eddy simulation of shading effects on NO2 and O3 concentrations within an idealised street canyon. *Atmospheric Environment,* 41**,** 7304-7314.

GROMKE, C., BUCCOLIERI, R., DI SABATINO, S. & RUCK, B. 2008. Dispersion study in a street canyon with tree planting by means of wind tunnel and numerical investigations–evaluation of CFD data with experimental data. *Atmospheric Environment,* 42**,** 8640-8650.

GROMKE, C. & RUCK, B. 2007. Influence of trees on the dispersion of pollutants in an urban street canyon—experimental investigation of the flow and concentration field. *Atmospheric Environment,* 41**,** 3287-3302.

GRYLLS, T., SUTER, I. & VAN REEUWIJK, M. 2020. Steady-state large-eddy simulations of convective and stable urban boundary layers. *Boundary-Layer Meteorology,* 175**,** 309-341.

GU, Z.-L., ZHANG, Y.-W., CHENG, Y. & LEE, S.-C. 2011. Effect of uneven building layout on air flow and pollutant dispersion in non-uniform street canyons. *Building and Environment,* 46**,** 2657-2665.

HAN, B.-S., BAIK, J.-J., KWAK, K.-H. & PARK, S.-B. 2018. Large-eddy simulation of reactive pollutant exchange at the top of a street canyon. *Atmospheric Environment,* 187**,** 381-389.

HANG, J., CHEN, X., CHEN, G., CHEN, T., LIN, Y., LUO, Z., ZHANG, X. & WANG, Q. 2020. The influence of aspect ratios and wall heating conditions on flow and passive pollutant exposure in 2D typical street canyons. *Building and Environment,* 168**,** 106536.

HARRISON, R. M. 2018. Urban atmospheric chemistry: A very special case for study. *npj Climate and Atmospheric Science,* 1**,** 1-5.

HE, L., HANG, J., WANG, X., LIN, B., LI, X. & LAN, G. 2017. Numerical investigations of flow and passive pollutant exposure in high-rise deep street canyons with various street aspect ratios and viaduct settings. *Science of the Total Environment,* 584**,** 189-206.

HEARD, D. E. & PILLING, M. J. 2003. Measurement of OH and HO_2 in the troposphere. *Chemical Reviews,* 103**,** 5163-5198.

HERSBACH, H., BELL, B., BERRISFORD, P., HIRAHARA, S., HORÁNYI, A., MUÑOZ‐SABATER, J., NICOLAS, J., PEUBEY, C., RADU, R. & SCHEPERS, D. 2020. The ERA5 global reanalysis. *Quarterly Journal of the Royal Meteorological Society,* 146**,** 1999-2049.

HESTER, R. E. & HARRISON, R. M. 2009. *Air quality in urban environments*, Royal Society of Chemistry.

HEWITT, C. N., ASHWORTH, K. & MACKENZIE, A. R. 2020. Using green infrastructure to improve urban air quality (GI4AQ). *Ambio,* 49**,** 62-73.

HEWITT, C. N. & JACKSON, A. V. 2008. *Handbook of atmospheric science: Principles and applications*, John Wiley & Sons.

HOFFMANN, B., BOOGAARD, H., DE NAZELLE, A., ANDERSEN, Z. J., ABRAMSON, M., BRAUER, M., BRUNEKREEF, B., FORASTIERE, F., HUANG, W. & KAN, H. 2021. WHO air quality guidelines 2021–aiming for healthier air for all: a joint statement by medical, public health, scientific societies and patient representative organisations. *International journal of public health***,** 88.

HOLMAN, C., HARRISON, R. & QUEROL, X. 2015. Review of the efficacy of low emission zones to improve urban air quality in European cities. *Atmospheric Environment,* 111**,** 161-169.

HOOD, C., STOCKER, J., SEATON, M., JOHNSON, K., O'NEILL, J., THORNE, L. & CARRUTHERS, D. 2021. Comprehensive evaluation of an advanced street canyon air pollution model. *Journal of the Air & Waste Management Association,* 71**,** 247-267.

HUANG, Y., LEI, C., LIU, C.-H., PEREZ, P., FOREHEAD, H., KONG, S. & ZHOU, J. L. 2021. A review of strategies for mitigating roadside air pollution in urban street canyons. *Environmental Pollution,* 280**,** 116971.

JACOBSON, M. Z. & JACOBSON, M. Z. 2005. *Fundamentals of atmospheric modeling*, Cambridge university press.

JACOBSON, M. Z. & SEINFELD, J. H. 2004. Evolution of nanoparticle size and mixing state near the point of emission. *Atmospheric Environment,* 38**,** 1839-1850.

JACOBSON, M. Z., TABAZADEH, A. & TURCO, R. P. 1996. Simulating equilibrium within aerosols and nonequilibrium between gases and aerosols. *Journal of Geophysical Research: Atmospheres,* 101**,** 9079-9091.

JANSSEN, N. A., HOEK, G., SIMIC-LAWSON, M., FISCHER, P., VAN BREE, L., TEN BRINK, H., KEUKEN, M., ATKINSON, R. W., ANDERSON, H. R. & BRUNEKREEF, B. 2011. Black carbon as an additional indicator of the adverse health effects of airborne particles compared with PM10 and PM2. 5. *Environmental health perspectives,* 119**,** 1691-1699.

JASAK, H., JEMCOV, A. & TUKOVIC, Z. OpenFOAM: A C++ library for complex physics simulations. International workshop on coupled methods in numerical dynamics, 2007. IUC Dubrovnik Croatia, 1-20.

JEANJEAN, A. P., HINCHLIFFE, G., MCMULLAN, W., MONKS, P. S. & LEIGH, R. J. 2015. A CFD study on the effectiveness of trees to disperse road traffic emissions at a city scale. *Atmospheric Environment,* 120**,** 1-14.

JOHNSON, W., LUDWIG, F., DABBERDT, W. & ALLEN, R. 1973. An urban diffusion simulation model for carbon monoxide. *Journal of the Air Pollution Control Association,* 23**,** 490-498.

JOINT AIR QUALITY UNIT 2017. Improving Air Quality in the UK: Tackling Nitrogen Dioxide in Our Towns and Cities. *Department for Environment Food & Rural Affairs and Department for Transport: London, UK*.

KAKOSIMOS, K. E., HERTEL, O., KETZEL, M. & BERKOWICZ, R. 2010. Operational Street Pollution Model (OSPM)–a review of performed application and validation studies, and future prospects. *Environmental Chemistry,* 7**,** 485-503.

KARKOULIAS, V., MARAZIOTI, P., GEORGIOU, D. & MARAZIOTIS, E. 2020. Computational Fluid Dynamics modeling of the trace elements dispersion and comparison with measurements in a street canyon with balconies in the city of Patras, Greece. *Atmospheric Environment,* 223**,** 117210.

KIM, D., CHEN, Z., ZHOU, L.-F. & HUANG, S.-X. 2018a. Air pollutants and early origins of respiratory diseases. *Chronic diseases and translational medicine,* 4**,** 75-94.

KIM, M. J., PARK, R. J. & KIM, J.-J. 2012. Urban air quality modeling with full O3–NOx–VOC chemistry: Implications for O3 and PM air quality in a street canyon. *Atmospheric Environment,* 47**,** 330-340.

KIM, Y., WU, Y., SEIGNEUR, C. & ROUSTAN, Y. 2018b. Multi-scale modeling of urban air pollution: development and application of a Street-in-Grid model (v1.0) by coupling MUNICH (v1.0) and Polair3D (v1.8.1).

KIM, Y., WU, Y., SEIGNEUR, C. & ROUSTAN, Y. 2018c. Multi-scale modeling of urban air pollution: Development and application of a Street-in-Grid model (v1. 0) by coupling MUNICH (v1. 0) and Polair3D (v1. 8.1). *Geoscientific Model Development,* 11**,** 611-629.

KNIGHT, F. 1921. Risk, uncertainty and profit Houghton Mifflin Company. *Boston and New York*.

KORSAKISSOK, I. & MALLET, V. 2010. Development and application of a reactive plume-in-grid model: evaluation over Greater Paris. *Atmospheric Chemistry and Physics,* 10**,** 8917-8931.

KOVAR-PANSKUS, A., LOUKA, P., SINI, J.-F., SAVORY, E., CZECH, M., ABDELQARI, A., MESTAYER, P. & TOY, N. 2002. Influence of geometry on the mean flow within urban street canyons–a comparison of wind tunnel experiments and numerical simulations. *Water, air and soil pollution: focus,* 2**,** 365-380.

KROL, M. C., MOLEMAKER, M. J. & DE ARELLANO, J. V. G. 2000. Effects of turbulence and heterogeneous emissions on photochemically active species in the convective boundary layer. *Journal of Geophysical Research: Atmospheres,* 105**,** 6871-6884.

KUKKONEN, J., OLSSON, T., SCHULTZ, D., BAKLANOV, A., KLEIN, T., MIRANDA, A., MONTEIRO, A., HIRTL, M., TARVAINEN, V. & BOY, M. 2012. A review of operational, regional-scale, chemical weather forecasting models in Europe. *Atmospheric Chemistry and Physics,* 12**,** 1-87.

KUMAR, P., KETZEL, M., VARDOULAKIS, S., PIRJOLA, L. & BRITTER, R. 2011. Dynamics and dispersion modelling of nanoparticles from road traffic in the urban atmospheric environment—a review. *Journal of Aerosol Science,* 42**,** 580-603.

KWAK, K.-H. & BAIK, J.-J. 2012. A CFD modeling study of the impacts of NOx and VOC emissions on reactive pollutant dispersion in and above a street canyon. *Atmospheric environment,* 46**,** 71-80.

KWAK, K.-H., BAIK, J.-J. & LEE, K.-Y. 2013. Dispersion and photochemical evolution of reactive pollutants in street canyons. *Atmospheric Environment,* 70**,** 98-107.

KWAK, K.-H., BAIK, J.-J., LEE, S.-H. & RYU, Y.-H. 2011. Computational fluid dynamics modelling of the diurnal variation of flow in a street canyon. *Boundary-layer meteorology,* 141**,** 77-92.

LAFRANCHI, B., WOLFE, G., THORNTON, J., HARROLD, S., BROWNE, E., MIN, K., WOOLDRIDGE, P., GILMAN, J., KUSTER, W. & GOLDAN, P. 2009. Closing the peroxy acetyl nitrate budget: observations of acyl peroxy nitrates (PAN, PPN, and MPAN) during BEARPEX 2007. *Atmospheric Chemistry and Physics,* 9**,** 7623-7641.

LANDRIGAN, P. J., FULLER, R., ACOSTA, N. J., ADEYI, O., ARNOLD, R., BALDÉ, A. B., BERTOLLINI, R., BOSE-O'REILLY, S., BOUFFORD, J. I. & BREYSSE, P. N. 2018. The Lancet Commission on pollution and health. *The lancet,* 391**,** 462-512.

LASHGARI, A. 2005. Long Term Measurements of Peroxy Acetyl Nitrate (PAN) in Southern California.

LATEB, M., MERONEY, R. N., YATAGHENE, M., FELLOUAH, H., SALEH, F. & BOUFADEL, M. 2016. On the use of numerical modelling for near-field pollutant dispersion in urban environments− A review. *Environmental Pollution,* 208**,** 271-283.

LEE, J. D., LEWIS, A. C., MONKS, P. S., JACOB, M., HAMILTON, J. F., HOPKINS, J. R., WATSON, N. M., SAXTON, J. E., ENNIS, C. & CARPENTER, L. J. 2006. Ozone photochemistry and elevated isoprene during the UK heatwave of August 2003. *Atmospheric Environment,* 40**,** 7598-7613.

LEELŐSSY, Á., MOLNÁR, F., IZSÁK, F., HAVASI, Á., LAGZI, I. & MÉSZÁROS, R. 2014. Dispersion modeling of air pollutants in the atmosphere: a review. *Central European Journal of Geosciences,* 6**,** 257-278.

LI, C. W., BRASSEUR, G. P., SCHMIDT, H. & MELLADO, J. P. 2021. Error induced by neglecting subgrid chemical segregation due to inefficient turbulent mixing in regional chemical-transport models in urban environments. *Atmospheric Chemistry and Physics,* 21**,** 483-503.

LI, K., JACOB, D. J., LIAO, H., ZHU, J., SHAH, V., SHEN, L., BATES, K. H., ZHANG, Q. & ZHAI, S. 2019. A two-pollutant strategy for improving ozone and particulate air quality in China. *Nature Geoscience,* 12**,** 906-910.

LI, N., HE, Q., GREENBERG, J., GUENTHER, A., LI, J., CAO, J., WANG, J., LIAO, H., WANG, Q. & ZHANG, Q. 2018. Impacts of biogenic and anthropogenic emissions on summertime ozone formation in the Guanzhong Basin, China. *Atmospheric Chemistry and Physics,* 18**,** 7489-7507.

LI, Q., SU, G., LI, C., LIU, P., ZHAO, X., ZHANG, C., SUN, X., MU, Y., WU, M. & WANG, Q. 2020. An investigation into the role of VOCs in SOA and ozone production in Beijing, China. *Science of the Total Environment,* 720**,** 137536.

LI, X.-X., LEUNG, D. Y., LIU, C.-H. & LAM, K. M. 2008. Physical modeling of flow field inside urban street canyons. *Journal of Applied Meteorology and Climatology,* 47**,** 2058-2067.

LIETZKE, B. & VOGT, R. 2013. Variability of CO_2 concentrations and fluxes in and above an urban street canyon. *Atmospheric environment,* 74**,** 60-72.

LIU, C.-H. & LEUNG, D. Y. 2008. Numerical study on the ozone formation inside street canyons using a chemistry box model. *Journal of Environmental Sciences,* 20**,** 832-837.

LIU, C.-H., LEUNG, D. Y. & BARTH, M. C. 2005. On the prediction of air and pollutant exchange rates in street canyons of different aspect ratios using large-eddy simulation. *Atmospheric Environment,* 39**,** 1567-1574.

LIU, J., CUI, S., CHEN, G., ZHANG, Y., WANG, X., WANG, Q., GAO, P. & HANG, J. 2021. The influence of solar natural heating and NOx-O3 photochemistry on flow and reactive pollutant exposure in 2D street canyons. *Science of The Total Environment,* 759**,** 143527.

LIU, Y., WANG, H., JING, S., GAO, Y., PENG, Y., LOU, S., CHENG, T., TAO, S., LI, L. & LI, Y. 2019. Characteristics and sources of volatile organic compounds (VOCs) in Shanghai during summer: Implications of regional transport. *Atmospheric Environment,* 215**,** 116902.

LU, F., XU, D., CHENG, Y., DONG, S., GUO, C., JIANG, X. & ZHENG, X. 2015. Systematic review and meta-analysis of the adverse health effects of ambient PM2. 5 and PM10 pollution in the Chinese population. *Environmental research,* 136**,** 196-204.

LYU, X., WANG, N., GUO, H., XUE, L., JIANG, F., ZEREN, Y., CHENG, H., CAI, Z., HAN, L. & ZHOU, Y. 2019. Causes of a continuous summertime O 3 pollution event in Jinan, a central city in the North China Plain. *Atmospheric Chemistry and Physics,* 19**,** 3025-3042.

MADRONICH, S. & FLOCKE, S. 1999. The role of solar radiation in atmospheric chemistry. *Environmental photochemistry.* Springer.

MADRONICH, S., FLOCKE, S., ZENG, J., PETROPAVLOVSKIKH, I. & LEE-TAYLOR, J. 2002. Tropospheric ultraviolet and visible (TUV) radiation model. *National Center for Atmospheric Research (NCAR), Boulder, CO. Home page at: http://www. acd. ucar. edu/TUV*.

MASEY, N., HAMILTON, S. & BEVERLAND, I. J. 2018. Development and evaluation of the RapidAir® dispersion model, including the use of geospatial surrogates to represent street canyon effects. *Environmental Modelling & Software,* 108**,** 253-263.

MCVICAR, T. R., RODERICK, M. L., DONOHUE, R. J. & VAN NIEL, T. G. 2012. Less bluster ahead? Ecohydrological implications of global trends of terrestrial near‐surface wind speeds. *Ecohydrology,* 5**,** 381-388.

MELLOR, A. M., MELLO, J., DUFFY, K. P., EASLEY, W. & FAULKNER, J. 1998. Skeletal Mechanism for NO x Chemistry in Diesel Engines. *SAE transactions***,** 786-801.

MILLS, G. 1997. An urban canopy-layer climate model. *Theoretical and applied climatology,* 57**,** 229-244.

MONKS, P. S., ARCHIBALD, A., COLETTE, A., COOPER, O., COYLE, M., DERWENT, R., FOWLER, D., GRANIER, C., LAW, K. S. & MILLS, G. 2015. Tropospheric ozone and its precursors from the urban to the global scale from air quality to short-lived climate forcer. *Atmospheric Chemistry and Physics,* 15**,** 8889-8973.

MORADPOUR, M., AFSHIN, H. & FARHANIEH, B. 2017. A numerical investigation of reactive air pollutant dispersion in urban street canyons with tree planting. *Atmospheric Pollution Research,* 8**,** 253-266.

MORRIS, C., SIMMONDS, I. & PLUMMER, N. 2001. Quantification of the influences of wind and cloud on the nocturnal urban heat island of a large city. *Journal of Applied Meteorology and Climatology,* 40**,** 169-182.

MOZAFFAR, A., ZHANG, Y.-L., FAN, M., CAO, F. & LIN, Y.-C. 2020. Characteristics of summertime ambient VOCs and their contributions to O3 and SOA formation in a suburban area of Nanjing, China. *Atmospheric Research,* 240**,** 104923.

MUILWIJK, C., SCHRIJVERS, P., WUERZ, S. & KENJEREŠ, S. 2016. Simulations of photochemical smog formation in complex urban areas. *Atmospheric Environment,* 147**,** 470-484.

MURENA, F. 2012. Monitoring and modelling carbon monoxide concentrations in a deep street canyon: application of a two-box model. *Atmospheric pollution research,* 3**,** 311-316.

MURENA, F., DI BENEDETTO, A., D'ONOFRIO, M. & VITIELLO, G. 2011. Mass transfer velocity and momentum vertical exchange in simulated deep street canyons. *Boundary-layer meteorology,* 140**,** 125-142.

MURENA, F., FAVALE, G., VARDOULAKIS, S. & SOLAZZO, E. 2009. Modelling dispersion of traffic pollution in a deep street canyon: Application of CFD and operational models. *Atmospheric Environment,* 43**,** 2303-2311.

MURENA, F. & MELE, B. 2014. Effect of short–time variations of wind velocity on mass transfer rate between street canyons and the atmospheric boundary layer. *Atmospheric Pollution Research,* 5**,** 484-490.

MURENA, F. & MELE, B. 2016. Effect of balconies on air quality in deep street canyons. *Atmospheric Pollution Research,* 7**,** 1004-1012.

MURENA, F. & PRATI, M. 2020. The contribution of high emitters vehicles to FPS number concentration in the historical centre of Naples. *Air Quality***,** 22.

MURRAY, C. J., ARAVKIN, A. Y., ZHENG, P., ABBAFATI, C., ABBAS, K. M., ABBASI-KANGEVARI, M., ABD-ALLAH, F., ABDELALIM, A., ABDOLLAHI, M. & ABDOLLAHPOUR, I. 2020. Global burden of 87 risk factors in 204 countries and territories, 1990–2019: a systematic analysis for the Global Burden of Disease Study 2019. *The Lancet,* 396**,** 1223-1249.

NÆSS, P., SAGLIE, I.-L. & RICHARDSON, T. 2020. Urban sustainability: is densification sufficient? *European Planning Studies,* 28**,** 146-165.

NG, W.-Y. & CHAU, C.-K. 2014. A modeling investigation of the impact of street and building configurations on personal air pollutant exposure in isolated deep urban canyons. *Science of the Total Environment,* 468**,** 429-448.

NIACHOU, K., LIVADA, I. & SANTAMOURIS, M. 2008. Experimental study of temperature and airflow distribution inside an urban street canyon during hot summer weather conditions. Part II: Airflow analysis. *Building and environment,* 43**,** 1393-1403.

NIKOLOVA, I., JANSSEN, S., VOS, P., VRANCKEN, K., MISHRA, V. & BERGHMANS, P. 2011. Dispersion modelling of traffic induced ultrafine particles in a street canyon in Antwerp, Belgium and comparison with observations. *Science of the total environment,* 412**,** 336-343.

NIKOLOVA, I., MACKENZIE, A. R., CAI, X., ALAM, M. S. & HARRISON, R. M. 2016. Modelling component evaporation and composition change of traffic-induced ultrafine particles during travel from street canyon to urban background. *Faraday discussions,* 189**,** 529-546.

NILSSON, T. M. & NIKLASSON, G. A. 1995. Radiative cooling during the day: simulations and experiments on pigmented polyethylene cover foils. *Solar energy materials and solar cells,* 37**,** 93-118.

NTZIACHRISTOS, L., SAMARAS, Z., EGGLESTON, S., GORISSEN, N., HASSEL, D. & HICKMAN, A. 2000. Copert iii. *Computer Programme to calculate emissions from road transport, methodology and emission factors (version 2.1), European Energy Agency (EEA), Copenhagen*.

OKE, T. R. 1988. Street design and urban canopy layer climate. *Energy and buildings,* 11**,** 103-113.

OKE, T. R., MILLS, G., CHRISTEN, A. & VOOGT, J. A. 2017. *Urban climates*, Cambridge University Press.

OKE, T. R., MILLS, G. & VOOGT, J. 2017. *Urban climates*, Cambridge University Press.

OWEN, S., MACKENZIE, A., STEWART, H., DONOVAN, R. & HEWITT, C. 2003. Biogenic volatile organic compound (VOC) emission estimates from an urban tree canopy. *Ecological Applications,* 13**,** 927-938.

PAOLINI, R., MAININI, A. G., POLI, T. & VERCESI, L. 2014. Assessment of thermal stress in a street canyon in pedestrian area with or without canopy shading. *Energy Procedia,* 48**,** 1570-1575.

PARK, S.-J., KIM, J.-J., KIM, M. J., PARK, R. J. & CHEONG, H.-B. 2015. Characteristics of flow and reactive pollutant dispersion in urban street canyons. *Atmospheric Environment,* 108**,** 20-31.

PEARCE, H., LEVINE, J. G., CAI, X. & MACKENZIE, A. R. 2021. Introducing the Green Infrastructure for Roadside Air Quality (GI4RAQ) Platform: Estimating Site-Specific Changes in the Dispersion of Vehicular Pollution Close to Source. *Forests,* 12**,** 769.

PUGH, T., MACKENZIE, A., LANGFORD, B., NEMITZ, E., MISZTAL, P. & HEWITT, C. 2011. The influence of small-scale variations in isoprene concentrations on atmospheric chemistry over a tropical rainforest. *Atmospheric Chemistry and Physics,* 11**,** 4121-4134.

PUGH, T. A., MACKENZIE, A. R., WHYATT, J. D. & HEWITT, C. N. 2012. Effectiveness of green infrastructure for improvement of air quality in urban street canyons. *Environmental science & technology,* 46**,** 7692-7699.

QIU, Y., MA, Z. & LI, K. 2019. A modeling study of the peroxyacetyl nitrate (PAN) during a wintertime haze event in Beijing, China. *Science of the Total Environment,* 650**,** 1944-1953.

QIU, Y., MA, Z., LI, K., LIN, W., TANG, Y., DONG, F. & LIAO, H. 2020. Markedly enhanced levels of peroxyacetyl nitrate (PAN) during COVID‐19 in Beijing. *Geophysical Research Letters,* 47**,** e2020GL089623.

R CORE TEAM, T. 2019. R: A language and environment for statistical computing. Vienna, Austria.

RAKOWSKA, A., WONG, K. C., TOWNSEND, T., CHAN, K. L., WESTERDAHL, D., NG, S., MOČNIK, G., DRINOVEC, L. & NING, Z. 2014. Impact of traffic volume and composition on the air quality and pedestrian exposure in urban street canyon. *Atmospheric Environment,* 98**,** 260-270.

RISSANEN, M. P., KURTEN, T., SIPILÄ, M., THORNTON, J. A., KANGASLUOMA, J., SARNELA, N., JUNNINEN, H., JØRGENSEN, S., SCHALLHART, S. & KAJOS, M. K. 2014. The formation of highly oxidized multifunctional products in the ozonolysis of cyclohexene. *Journal of the American Chemical Society,* 136**,** 15596-15606.

SAHU, L., TRIPATHI, N. & YADAV, R. 2017. Contribution of biogenic and photochemical sources to ambient VOCs during winter to summer transition at a semi-arid urban site in India. *Environmental Pollution,* 229**,** 595-606.

SALIM, S. M., BUCCOLIERI, R., CHAN, A. & DI SABATINO, S. 2011. Numerical simulation of atmospheric pollutant dispersion in an urban street canyon: Comparison between RANS and LES. *Journal of Wind Engineering and Industrial Aerodynamics,* 99**,** 103-113.

SALIZZONI, P., SOULHAC, L. & MEJEAN, P. 2009. Street canyon ventilation and atmospheric turbulence. *Atmospheric Environment,* 43**,** 5056-5067.

SALMOND, J., WILLIAMS, D., LAING, G., KINGHAM, S., DIRKS, K., LONGLEY, I. & HENSHAW, G. 2013. The influence of vegetation on the horizontal and vertical distribution of pollutants in a street canyon. *Science of the Total Environment,* 443**,** 287-298.

SATSANGI, G. S., LAKHANI, A., KULSHRESTHA, P. & TANEJA, A. 2004. Seasonal and diurnal variation of surface ozone and a preliminary analysis of exceedance of its critical levels at a semi-arid site in India. *Journal of Atmospheric Chemistry,* 47**,** 271-286.

SAUNDERS, S. M., JENKIN, M. E., DERWENT, R. & PILLING, M. 2003. Protocol for the development of the Master Chemical Mechanism, MCM v3 (Part A): tropospheric degradation of non-aromatic volatile organic compounds. *Atmospheric Chemistry and Physics,* 3**,** 161-180.

SCHLICHTING, H. & GERSTEN, K. 2016. *Boundary-layer theory*, Springer.

SCHLICHTING, H. & KESTIN, J. 1961. *Boundary layer theory*, Springer.

SECO, R., PEÑUELAS, J., FILELLA, I., LLUSIÀ, J., MOLOWNY-HORAS, R., SCHALLHART, S., METZGER, A., MÜLLER, M. & HANSEL, A. 2011. Contrasting winter and summer

VOC mixing ratios at a forest site in the Western Mediterranean Basin: the effect of local biogenic emissions. *Atmospheric Chemistry and Physics,* 11**,** 13161-13179.

SEINFELD, J. & PANDIS, S. 2008. Atmospheric Chemistry and Physics. 1997. *New York*.

SEINFELD, J. H. & PANDIS, S. N. 2016. *Atmospheric chemistry and physics: from air pollution to climate change*, John Wiley & Sons.

SHAH, A. S., LEE, K. K., MCALLISTER, D. A., HUNTER, A., NAIR, H., WHITELEY, W., LANGRISH, J. P., NEWBY, D. E. & MILLS, N. L. 2015. Short term exposure to air pollution and stroke: systematic review and meta-analysis. *bmj,* 350.

SHEN, H., SUN, Z., CHEN, Y., RUSSELL, A. G., HU, Y., ODMAN, M. T., QIAN, Y., ARCHIBALD, A. T. & TAO, S. 2021. Novel method for ozone isopleth construction and diagnosis for the ozone control strategy of Chinese cities. *Environmental science & technology,* 55**,** 15625-15636.

SILLMAN, S. 1999. The relation between ozone, NOx and hydrocarbons in urban and polluted rural environments. *Atmospheric Environment,* 33**,** 1821-1845.

SIN, C. H., JON, K. S., UN, G. H., THAE, Y. I., KIM, H., TOKGO, J. & RI, H. M. 2023. Evaluation of the ventilation and pollutant exposure risk level inside 3D street canyon with void deck under different wind directions. *Environmental Science and Pollution Research,* 30**,** 61808-61828.

SINGH, H. B. & HANST, P. L. 1981. Peroxyacetyl nitrate (PAN) in the unpolluted atmosphere: An important reservoir for nitrogen oxides. *Geophysical Research Letters,* 8**,** 941-944.

SOLAZZO, E., CAI, X. & VARDOULAKIS, S. 2009. Improved parameterisation for the numerical modelling of air pollution within an urban street canyon. *Environmental Modelling & Software,* 24**,** 381-388.

SOLAZZO, E., VARDOULAKIS, S. & CAI, X. 2011. A novel methodology for interpreting air quality measurements from urban streets using CFD modelling. *Atmospheric environment,* 45**,** 5230-5239.

SOULHAC, L., SALIZZONI, P., CIERCO, F.-X. & PERKINS, R. 2011. The model SIRANE for atmospheric urban pollutant dispersion; part I, presentation of the model. *Atmospheric environment,* 45**,** 7379-7395.

STOCKER, J., HOOD, C., CARRUTHERS, D. & MCHUGH, C. 2012. ADMS-Urban: developments in modelling dispersion from the city scale to the local scale. *International Journal of Environment and Pollution,* 50**,** 308-316.

STONE JR, B., MEDNICK, A. C., HOLLOWAY, T. & SPAK, S. N. 2007. Is compact growth good for air quality? *Journal of the American Planning Association,* 73**,** 404-418.

STULL, R. B. 2012. *An introduction to boundary layer meteorology*, Springer Science & Business Media.

SUN, J., WU, F., HU, B., TANG, G., ZHANG, J. & WANG, Y. 2016. VOC characteristics, emissions and contributions to SOA formation during hazy episodes. *Atmospheric Environment,* 141**,** 560-570.

SUTTON, R. T., MACLEAN, H., SWINBANK, R., O'NEILL, A. & TAYLOR, F. 1994. High-resolution stratospheric tracer fields estimated from satellite observations using Lagrangian trajectory calculations. *Journal of the atmospheric sciences,* 51**,** 2995-3005.

SYKES, R., PARKER, S., HENN, D. & LEWELLEN, W. 1994. Turbulent mixing with chemical reaction in the planetary boundary layer. *Journal of Applied Meteorology and Climatology,* 33**,** 825-834.

TAKANO, Y. & MOONEN, P. 2013. On the influence of roof shape on flow and dispersion in an urban street canyon. *Journal of Wind Engineering and Industrial Aerodynamics,* 123**,** 107-120.

TIAN, Q., HUANG, G., HU, K. & NIYOGI, D. 2019. Observed and global climate model based changes in wind power potential over the Northern Hemisphere during 1979–2016. *Energy,* 167**,** 1224-1235.

TIWARY, A. & WILLIAMS, I. 2018. *Air pollution: measurement, modelling and mitigation*, CRC Press.

TOMINAGA, Y. & STATHOPOULOS, T. 2011. CFD modeling of pollution dispersion in a street canyon: Comparison between LES and RANS. *Journal of Wind Engineering and Industrial Aerodynamics,* 99**,** 340-348.

TOMSON, M., KUMAR, P., BARWISE, Y., PEREZ, P., FOREHEAD, H., FRENCH, K., MORAWSKA, L. & WATTS, J. F. 2021. Green infrastructure for air quality improvement in street canyons. *Environment international,* 146**,** 106288.

TURNER, M. C., ANDERSEN, Z. J., BACCARELLI, A., DIVER, W. R., GAPSTUR, S. M., POPE III, C. A., PRADA, D., SAMET, J., THURSTON, G. & COHEN, A. 2020. Outdoor air pollution and cancer: An overview of the current evidence and public health recommendations. *CA: a cancer journal for clinicians,* 70**,** 460-479.

UNITED NATIONS 2018. Revision of world urbanization prospects. *United Nations: New York, NY, USA,* 799.

VACHON, G., LOUKA, P., ROSANT, J., MESTAYER, P. & SINI, J. 2002. Measurements of traffic-induced turbulence within a street canyon during the Nantes' 99 experiment. *WATER AIR AND SOIL POLLUTION FOCUS,* 2**,** 127-140.

VALACH, A., LANGFORD, B., NEMITZ, E., MACKENZIE, A. & HEWITT, C. 2014. Concentrations of selected volatile organic compounds at kerbside and background sites in central London. *Atmospheric Environment,* 95**,** 456-467.

VALACH, A., LANGFORD, B., NEMITZ, E., MACKENZIE, A. R. & HEWITT, C. 2015. Seasonal and diurnal trends in concentrations and fluxes of volatile organic compounds in central London. *Atmospheric Chemistry and Physics,* 15**,** 7777-7796.

VARDOULAKIS, S., FISHER, B. E., PERICLEOUS, K. & GONZALEZ-FLESCA, N. 2003. Modelling air quality in street canyons: a review. *Atmospheric environment,* 37**,** 155-182.

VARDOULAKIS, S., VALIANTIS, M., MILNER, J. & APSIMON, H. 2007. Operational air pollution modelling in the UK—Street canyon applications and challenges. *Atmospheric Environment,* 41**,** 4622-4637.

VAUTARD, R., CATTIAUX, J., YIOU, P., THÉPAUT, J.-N. & CIAIS, P. 2010. Northern Hemisphere atmospheric stilling partly attributed to an increase in surface roughness. *Nature geoscience,* 3**,** 756-761.

VAUTARD, R., SCHAAP, M., BERGSTRÖM, R., BESSAGNET, B., BRANDT, J., BUILTJES, P., CHRISTENSEN, J., CUVELIER, C., FOLTESCU, V. & GRAFF, A. 2009. Skill and uncertainty of a regional air quality model ensemble. *Atmospheric Environment,* 43**,** 4822-4832.

VERATTI, G., FABBI, S., BIGI, A., LUPASCU, A., TINARELLI, G., TEGGI, S., BRUSASCA, G., BUTLER, T. M. & GHERMANDI, G. 2020. Towards the coupling of a chemical transport model with a micro-scale Lagrangian modelling system for evaluation of urban NOx levels in a European hotspot. *Atmospheric Environment***,** 117285.

VERSTEEG, H. & MALALASEKERA, W. 1995. An introduction to CFD. *The Finite Volume Method*.

VINUESA, J.-F. & DE ARELLANO, J. V.-G. 2005. Introducing effective reaction rates to account for the inefficient mixing of the convective boundary layer. *Atmospheric Environment,* 39**,** 445-461.

WANG, L., SU, J., GU, Z. & TANG, L. 2020. Numerical study on flow field and pollutant dispersion in an ideal street canyon within a real tree model at different wind velocities. *Computers & Mathematics with Applications*.

WANG, N., LYU, X., DENG, X., HUANG, X., JIANG, F. & DING, A. 2019. Aggravating O3 pollution due to NOx emission control in eastern China. *Science of the Total Environment,* 677**,** 732-744.

WANG, P., CHEN, Y., HU, J., ZHANG, H. & YING, Q. 2018. Attribution of tropospheric ozone to NO x and VOC emissions: considering ozone formation in the transition regime. *Environmental science & technology,* 53**,** 1404-1412.

WANG, T., XUE, L., BRIMBLECOMBE, P., LAM, Y. F., LI, L. & ZHANG, L. 2017. Ozone pollution in China: A review of concentrations, meteorological influences, chemical precursors, and effects. *Science of the Total Environment,* 575**,** 1582-1596.

WATSON, L., SHALLCROSS, D., UTEMBE, S. & JENKIN, M. 2008. A Common Representative Intermediates (CRI) mechanism for VOC degradation. Part 2: Gas phase mechanism reduction. *Atmospheric Environment,* 42**,** 7196-7204.

WENG, Q. & FU, P. 2014. Modeling annual parameters of clear-sky land surface temperature variations and evaluating the impact of cloud cover using time series of Landsat TIR data. *Remote Sensing of Environment,* 140**,** 267-278.

WESTMORELAND, E. J., CARSLAW, N., CARSLAW, D. C., GILLAH, A. & BATES, E. 2007. Analysis of air quality within a street canyon using statistical and dispersion modelling techniques. *Atmospheric Environment,* 41**,** 9195-9205.

WILLIAMSON, J. 1980. Low-storage runge-kutta schemes. *Journal of Computational Physics,* 35**,** 48-56.

WILLMOTT, C. J. 1981. On the validation of models. *Physical geography,* 2**,** 184-194.

WILLMOTT, C. J., ACKLESON, S. G., DAVIS, R. E., FEDDEMA, J. J., KLINK, K. M., LEGATES, D. R., O'DONNELL, J. & ROWE, C. M. 1985. Statistics for the evaluation and comparison of models. *Journal of Geophysical Research: Oceans,* 90**,** 8995-9005.

WILLMOTT, C. J., ROBESON, S. M. & MATSUURA, K. 2012. A refined index of model performance. *International Journal of climatology,* 32**,** 2088-2094.

WORLD HEALTH, O. 2018. Air pollution and child health: prescribing clean air: summary. World Health Organization.

WORLD HEALTH, O. 2021. *WHO global air quality guidelines: particulate matter (PM2.5 and PM10), ozone, nitrogen dioxide, sulfur dioxide and carbon monoxide,* Geneva, World Health Organization.

WU, L., HANG, J., WANG, X., SHAO, M. & GONG, C. 2021. APFoam 1.0: integrated computational fluid dynamics simulation of O 3–NO x–volatile organic compound chemistry and pollutant dispersion in a typical street canyon. *Geoscientific Model Development,* 14**,** 4655-4681.

WU, R. & XIE, S. 2017. Spatial distribution of ozone formation in China derived from emissions of speciated volatile organic compounds. *Environmental science & technology,* 51**,** 2574-2583.

XIA, B. & SUN, D.-W. 2002. Applications of computational fluid dynamics (CFD) in the food industry: a review. *Computers and electronics in agriculture,* 34**,** 5-24.

XIE, X., HUANG, Z. & WANG, J.-S. 2005. Impact of building configuration on air quality in street canyon. *Atmospheric Environment,* 39**,** 4519-4530.

XU, W., ZHANG, G., WANG, Y., TONG, S., ZHANG, W., MA, Z., LIN, W., KUANG, Y., YIN, L. & XU, X. 2021. Aerosol Promotes Peroxyacetyl Nitrate Formation During Winter in the North China Plain. *Environmental Science & Technology,* 55**,** 3568-3581.

YANG, G., LIU, Y. & LI, X. 2020. Spatiotemporal distribution of ground-level ozone in China at a city level. *Scientific reports,* 10**,** 1-12.

YANG, H., CHEN, G., WANG, D., HANG, J., LI, Q. & WANG, Q. 2021a. Influences of street aspect ratios and realistic solar heating on convective heat transfer and

ventilation in full-scale 2D street canyons. *Building and Environment,* 204**,** 108125.

YANG, H., CHEN, T., LIN, Y., BUCCOLIERI, R., MATTSSON, M., ZHANG, M., HANG, J. & WANG, Q. 2020. Integrated impacts of tree planting and street aspect ratios on CO dispersion and personal exposure in full-scale street canyons. *Building and environment,* 169**,** 106529.

YANG, H., LAM, C. K. C., LIN, Y., CHEN, L., MATTSSON, M., SANDBERG, M., HAYATI, A., CLAESSON, L. & HANG, J. 2021b. Numerical investigations of Re-independence and influence of wall heating on flow characteristics and ventilation in full-scale 2D street canyons. *Building and Environment,* 189**,** 107510.

YAZID, A. W. M., SIDIK, N. A. C., SALIM, S. M. & SAQR, K. M. 2014. A review on the flow structure and pollutant dispersion in urban street canyons for urban planning strategies. *Simulation,* 90**,** 892-916.

YUAN, C., NG, E. & NORFORD, L. K. 2014. Improving air quality in high-density cities by understanding the relationship between air pollutant dispersion and urban morphologies. *Building and Environment,* 71**,** 245-258.

ZENG, W., ZHAO, H., LIU, R., YAN, W., QIU, Y., YANG, F., SHU, C. & ZHAN, Y. 2020. Association between NO2 cumulative exposure and influenza prevalence in mountainous regions: a case study from southwest China. *Environmental research,* 189**,** 109926.

ZENG, Z., ZIEGLER, A. D., SEARCHINGER, T., YANG, L., CHEN, A., JU, K., PIAO, S., LI, L. Z., CIAIS, P. & CHEN, D. 2019. A reversal in global terrestrial stilling and its implications for wind energy production. *Nature Climate Change,* 9**,** 979-985.

ZHANG, K., CHEN, G., WANG, X., LIU, S., MAK, C. M., FAN, Y. & HANG, J. 2019. Numerical evaluations of urban design technique to reduce vehicular personal intake fraction in deep street canyons. *Science of the Total Environment,* 653**,** 968-994.

ZHANG, K., CHEN, G., ZHANG, Y., LIU, S., WANG, X., WANG, B. & HANG, J. 2020. Integrated impacts of turbulent mixing and NOX-O3 photochemistry on reactive pollutant dispersion and intake fraction in shallow and deep street canyons. *Science of the Total Environment,* 712**,** 135553.

ZHANG, Q., HE, K. & HUO, H. 2012. Cleaning China's air. *Nature,* 484**,** 161-162.

ZHANG, X., CHEN, X. & ZHANG, X. 2018. The impact of exposure to air pollution on cognitive performance. *Proceedings of the National Academy of Sciences,* 115**,** 9193-9197.

ZHONG, J., CAI, X.-M. & BLOSS, W. J. 2014. Modelling segregation effects of heterogeneous emissions on ozone levels in idealised urban street canyons: Using photochemical box models. *Environmental Pollution,* 188**,** 132-143.

ZHONG, J., CAI, X.-M. & BLOSS, W. J. 2015. Modelling the dispersion and transport of reactive pollutants in a deep urban street canyon: Using large-eddy simulation. *Environmental pollution,* 200**,** 42-52.

ZHONG, J., CAI, X.-M. & BLOSS, W. J. 2016a. Coupling dynamics and chemistry in the air pollution modelling of street canyons: A review. *Environmental Pollution,* 214**,** 690-704.

ZHONG, J., CAI, X.-M. & BLOSS, W. J. 2016b. Modelling photochemical pollutants in a deep urban street canyon: application of a coupled two-box model approximation. *Atmospheric Environment,* 143**,** 86-107.

ZHONG, J., CAI, X.-M. & BLOSS, W. J. 2017. Large eddy simulation of reactive pollutants in a deep urban street canyon: Coupling dynamics with O3-NOx-VOC chemistry. *Environmental pollution,* 224**,** 171-184.

ZHONG, J., NIKOLOVA, I., CAI, X., MACKENZIE, A. R., ALAM, M. S., XU, R., SINGH, A. & HARRISON, R. M. 2020a. Neighbourhood-scale dispersion of traffic-induced ultrafine particles in central London: WRF large eddy simulations. *Environmental Pollution,* 266**,** 115223.

ZHONG, J., NIKOLOVA, I., CAI, X., MACKENZIE, A. R., ALAM, M. S., XU, R., SINGH, A. & HARRISON, R. M. 2020b. Traffic-induced multicomponent ultrafine particle microphysics in the WRF v3. 6.1 large eddy simulation model: General behaviour from idealised scenarios at the neighbourhood-scale. *Atmospheric Environment,* 223**,** 117213.

ZHONG, J., NIKOLOVA, I., CAI, X., MACKENZIE, A. R. & HARRISON, R. M. 2018. Modelling traffic-induced multicomponent ultrafine particles in urban street canyon compartments: Factors that inhibit mixing. *Environmental Pollution,* 238**,** 186-195.